

Copyright
by
Tz-Wei Wang
2010

**The Dissertation Committee for Tz-Wei Wang Certifies that this is the approved
version of the following dissertation:**

**Shear Performance of ASR/DEF Damaged Prestressed Concrete
Trapezoidal Box Bridge Girders**

Committee:

James O. Jirsa, Supervisor

Oguzhan Bayrak

Wassim M. Ghannoum

Harovel G. Wheat

Jinying Zhu

**Shear Performance of ASR/DEF Damaged Prestressed Concrete
Trapezoidal Box Bridge Girders**

by

Tz-Wei Wang, B.S.; M.S.

Dissertation

Presented to the Faculty of the Graduate School of

The University of Texas at Austin

in Partial Fulfillment

of the Requirements

for the Degree of

Doctor of Philosophy

The University of Texas at Austin

August, 2010

Dedication

To my parents

Acknowledgements

I would like to thank Dr. James O. Jirsa and Dr. Oguhan Bayrak, whose encouragement, guidance, and criticism helped bring the dissertation to a successful conclusion. I am also grateful to all the other committee members: Dr. Wassim M. Ghannoum, Dr. Harovel G. Wheat, and Dr. Jinying Zhu for all their comments on the dissertation.

I would like to thank Bryan Bindrich and Nancy Larson who worked on this project with me. This dissertation could not have been completed without their help. I also appreciate assistance and suggestions from my colleagues: Alejandro Avendaño, Andrew Moore, Catherine Hovell, and Dave Dunkman.

Technical assistance provided by the Ferguson Structural Engineering Laboratory staff is greatly appreciated. Andrew Valentine, Blake Stasney, Dennis Fillip, Eric Schell, and Mike Wason were always willing to provide me with their help and guidance. I could not have completed the tests without their assistance. The research and writing of this article were made possible by funding from the Texas Department of Transportation.

Lastly but not least, I would like to thank my family who always give me support physically and emotionally and Chun-Yi Shih for her love and belief in me.

Shear Performance of ASR/DEF Damaged Prestressed Concrete Trapezoidal Box Bridge Girders

Publication No. _____

Tz-Wei Wang, Ph.D.

The University of Texas at Austin, 2010

Supervisor: James O. Jirsa

Concrete bridges in Texas have developed large cracks in bent caps and pretensioned trapezoidal bridge girders. The bridges show premature concrete deterioration due to alkali-silica reaction (ASR) and delayed ettringite formation (DEF). There is concern that deterioration due to ASR/DEF may lead to a loss of structural capacity. However, there are no quantitative guidelines to relate the level of concrete deterioration due to ASR/DEF to structural performance. Using such guidelines, the need for rehabilitation of beams with ASR/DEF cracking can be assessed.

The goal of this research was to determine the shear capacity of pretensioned trapezoidal box girder specimens exhibiting varying degrees of ASR and/or DEF cracking and to use the shear testing results to evaluate the severity of the problem that may exist in Texas bridge structures. To achieve this goal, beams that were severely deteriorated due to ASR/DEF over a period of more than ten years were transported to the University of Texas for testing to failure. Both severely deteriorated and uncracked beams were tested in shear. The test results were used to evaluate the shear performance

of trapezoidal box beams affected by ASR/DEF. In addition, three different types of forensic analyses were conducted on the beams to understand the nature of the ASR/DEF cracks and severity of the deterioration.

After testing, it is found that the shear capacity of the test specimens was not significantly reduced even with heavy ASR/DEF cracking. Assessment using current US design provisions for bridges or buildings (ACI 318-08 and AASHTO LRFD 2008) and the proposed provision from an earlier project (TxDOT Project 5253) yielded conservative estimates of strength. Results from forensic analyses provided a qualitative indication of ASR/DEF damage but did not correlate with the observed levels of ASR/DEF deterioration.

Table of Contents

List of Tables	xv
List of Figures	xvii
CHAPTER 1 Introduction	1
1.1 Overview	1
1.2 Objectives and Scope	2
1.3 Organization	2
CHAPTER 2 Background	3
2.1 Overview	3
2.2 ASR/DEF Mechanism	3
2.2.1 Alkali-Silica Reaction (ASR)	3
2.2.2 Delayed Ettringite Formation (DEF)	5
2.3 Determination of Cause and Extent of Alkali-Silica Reaction and/or Delayed Ettringite Formation	6
2.4 Effect of Alkali-Silica Reaction and Delayed Ettringite Formation on Concrete Engineering Properties	8
2.5 Effect of Alkali-Silica Reaction and Delayed Ettringite Formation on Structural Capacities of Concrete Structures	9
2.5.1 Reinforced Concrete Beams	9
2.5.1.1 Flexural Strength	9
2.5.1.2 Shear Strength and Anchorage	10
2.5.2 Prestressed Concrete Beams	12
2.5.2.1 Flexural Strength	12
2.5.2.2 Shear Strength and Anchorage	12

2.5.3	Dapped End Beams.....	13
2.5.4	Summary.....	14
2.6	Recent Study in Japan.....	15
2.7	Research in Texas.....	18
2.8	Summary.....	19
CHAPTER 3 Test Specimens.....		21
3.1	Overview.....	21
3.2	Test Specimens.....	21
3.2.1	Background.....	21
3.2.2	Delivery of Test Specimens.....	22
3.2.3	General Information of Beams.....	23
3.2.3.1	Nomenclature.....	25
3.2.3.2	General Geometric Information.....	26
3.2.3.3	Steel Layout.....	28
3.2.3.4	Condition Survey.....	28
3.2.4	Details of Test Specimens.....	33
3.2.4.1	RF-3R-9-A.....	33
3.2.4.2	RF-3R-9-C.....	36
3.2.4.3	RF-3R-12-A.....	38
3.2.4.4	MLL-9-34-A.....	41
3.2.4.5	RF-1R-1-C.....	43
3.3	Material Properties.....	47
3.3.1	Concrete Strength.....	47

3.3.1.1	Deck Strength.....	47
3.3.1.2	Beam Cores.....	48
3.3.2	Reinforcing Bars	51
3.4	Summary	52
CHAPTER 4	Experimental Program.....	54
4.1	Deck Casting.....	54
4.2	Testing Set-up	56
4.3	Instrumentation	59
4.3.1	Load Cells and Bearing Plates	59
4.3.2	Linear Potentiometers	60
4.4	Test.....	61
4.5	Summary	62
CHAPTER 5	Experimental Results.....	63
5.1	Overview.....	63
5.2	Results of Web Shear Test.....	63
5.2.1	RF-3R-9-A	66
5.2.2	RF-3R-9-C	71
5.2.3	RF-3R-12-A	76
5.2.4	MLL-9-34-A	83
5.2.5	RF-1R-1C.....	91
5.3	Discussion.....	97
5.4	Summary	109
CHAPTER 6	Assessment with Code Provisions.....	110

6.1	Overview.....	110
6.2	Background of Strut-and-Tie Modeling.....	110
6.3	Elements of Strut-and-Tie Models.....	111
6.3.1	Struts	111
6.3.2	Ties.....	112
6.3.3	Nodes	112
6.3.4	Proportioning STM Elements	115
6.3.4.1	Proportioning a CCC Node.....	115
6.3.4.2	Proportioning a CCT Node	116
6.3.4.3	Proportioning a CTT Node	119
6.3.4.4	Proportioning a Strut.....	120
6.3.4.5	Proportioning a Tie	120
6.4	Concrete Efficiency Factors in Current STM Specification	121
6.5	Shear Capacity by Strut-and-Tie Modeling	126
6.6	Sample Calculation (RF-3R-9-C)	130
6.7	Calculation Results	148
6.7.1	One-Panel Model	148
6.7.2	Combination Model	151
6.7.3	Discussion	154
6.8	Summary	156
CHAPTER 7 Forensic Analysis		158
7.1	Overview.....	158
7.2	Petrographic Analysis	158

7.3	Beam Autopsies	163
7.3.1	Epoxy Injection and Cutting Tools	163
7.3.2	Observations	165
7.3.3	Discussion	175
7.4	Elastic Rebound Test	178
7.5	Summary	182
CHAPTER 8 Summary and Conclusions		184
8.1	Summary	184
8.2	Conclusions	185
8.3	Future Work	187
APPENDIX A Beam Information		188
A.1	Standard Drawing	188
A.2	Shop Drawing	198
A.2.1	RF-1R-1	198
A.2.2	RF-2R-6	203
A.2.3	RF-3R-9	208
A.2.4	RF-3R-12	213
A.2.5	MLL-9-34	218
APPENDIX B Concrete Mix Design		226
B.1	392-03-95-R	226
B.2	392-12-95	227
APPENDIX C Prestress Loss and Compression Block		228
C.1	Commonly Used Parameters	228

C.2	Prestress Loss.....	229
C.2.1	RF-3R-9	229
C.2.2	RF-3R-12	231
C.2.3	MLL-9-34	233
C.2.4	RF-1R-1	235
C.3	Depth of Rectangular Stress Block.....	237
C.3.1	Design Strength.....	237
C.3.1.1	RF-3R-9-A	237
C.3.1.2	RF-3R-9-C.....	238
C.3.1.3	RF-3R-12-A	239
C.3.1.4	MLL-9-34-A.....	240
C.3.1.5	RF-1R-1-C.....	241
C.3.2	Core Strength	242
C.3.2.1	RF-3R-9-A	242
C.3.2.2	RF-3R-9-C.....	243
C.3.2.3	RF-3R-12-A	244
C.3.2.4	MLL-9-34-A.....	245
C.3.2.5	RF-1R-1-C.....	246
APPENDIX D	Calculations for Strut-and-Tie Models.....	247
D.1	RF-3R-9-A	248
D.1.1	Design Strength.....	248
D.1.1.1	One-Panel Model	254
D.1.1.2	Combination Model	268

D.1.2	Core Strength	289
D.1.2.1	One-Panel Model	289
D.1.2.2	Combination Model	290
D.2	RF-3R-9-C	291
D.2.1	One-Panel Model	294
D.2.2	Combination Model	295
D.3	RF-3R-12-A	296
D.3.1	One-Panel Model	299
D.3.2	Combination Model	300
D.4	MLL-9-34-A	301
D.4.1	One-Panel Model	304
D.4.2	Combination Model	305
D.5	RF-1R-C.....	306
D.5.1	One-Panel Model	309
D.5.2	Combination Model	310
APPENDIX E	Petrographic Analysis.....	312
REFERENCES	339
VITA.....		345

List of Tables

Table 2.1 Details of test specimen	10
Table 3.1 Description of the test beams.....	22
Table 3.2 Concrete mixture and strength of the beams	24
Table 3.3 Basic information of the beams	24
Table 3.4 Labeling of each segments.....	25
Table 3.5 Beam geometric properties	28
Table 3.6 Summary of condition survey	32
Table 3.7 Air temperatures at cast	32
Table 3.8 Deck cylinder strength	47
Table 3.9 Summary of core strengths (ksi).....	50
Table 3.10 Steel stresses at critical points	52
Table 4.1 Detail setup of the web shear test	58
Table 5.1 Dimensions of beam set-up.....	64
Table 5.2 Summary of test results.....	99
Table 6.1 Efficiency Factors for a CCC node.....	123
Table 6.2 Efficiency Factors for a CCT node.....	124
Table 6.3 Efficiency Factors for a CTT node	126
Table 6.4 Available length and corresponding bond stress	142
Table 6.5 Shear capacity computed by one-panel model using design strength	149
Table 6.6 Shear capacity computed by one-panel model using core strength/0.85	149
Table 6.7 Shear capacity computed by combination model using design strength	152
Table 6.8 Shear capacity computed by combination model using core strength/0.85....	152
Table 6.9 Failure modes from combination model using design strength.....	152
Table 6.10 Failure modes from combination model using core strength/0.85	153
Table A.1 RF-1R-1 reinforcing bars list.....	198
Table A.2 RF-2R-6 reinforcing bars list.....	203
Table A.3 RF-3R-9 Reinforcing bars list.....	208
Table A.4 RF-3R-12 Reinforcing bars list.....	213
Table A.5 MLL-9-34 Reinforcing bars list.....	218
Table D.1 Member forces in the one panel model (RF-3R-9-A).....	289
Table D.2 Node 1 check (RF-3R-9-A)	289
Table D.3 Member forces in the combination model (RF-3R-9-A)	290
Table D.4 Node 1 and T3 check (RF-3R-9-A)	291
Table D.5 Member forces in the one panel model (RF-3R-9-C).....	294
Table D.6 Node 1 check (RF-3R-9-C).....	294
Table D.7 Member forces in the combination model (RF-3R-9-C)	295
Table D.8 Node 1 and T3 check (RF-3R-9-C)	296
Table D.9 Member forces in the one panel model (RF-3R-12-A).....	299
Table D.10 Node 1 check (RF-3R-12-A)	299
Table D.11 Member forces in the combination model (RF-3R-12-A)	300
Table D.12 Node 1 and T3 check (RF-3R-12-A)	301

Table D.13 Member forces in the one panel model (MLL-9-34-A).....	304
Table D.14 Node 1 check (MLL-9-34-A).....	304
Table D.15 Member forces in the combination model (MLL-9-34-A)	305
Table D.16 Node 1 and T3 check (MLL-9-34-A)	306
Table D.17 Member forces in the one panel model (RF-1R-1-C).....	309
Table D.18 Node 1 check (RF-1R-1-C).....	309
Table D.19 Member forces in the combination model (RF-1R-1-C)	310
Table D.20 Node 1 and T3 check (RF-1R-1-C)	311

List of Figures

Figure 2.1 Thin section image, showing some typical diagnostic features	4
Figure 2.2 Ettringite growth around aggregate and in cracked matrix (Thomas et al. 2008)	5
Figure 2.3 Total height of shear testing specimen vs. the number of the specimens.....	15
Figure 2.4 (a) Damaged pier (b) Fractured reinforcement (Miyagawa 2006)	16
Figure 2.5 Presumed mechanism of damages to steel bars (Miyagawa 2006)	17
Figure 2.6 Expansion on the repaired bent caps at US 183 and IH-35 interchange, Austin, Texas (Deschenes et al. 2009)	19
Figure 3.1 (a) Specimens on tractor-trailers arriving at laboratory (b)Three specimens stored in the laboratory (c) Rented mobile crane.....	23
Figure 3.2 An example for specimen labeling.....	25
Figure 3.3 Non-composite beam cross section	26
Figure 3.4 Top surface of a non-composite beam.....	27
Figure 3.5 Composite beam cross section.....	27
Figure 3.6 (a) Void floatation in RF-3R-12-C (b) Plywood	29
Figure 3.7 Longitudinal crack in the web portion.....	30
Figure 3.8 Cracking level (a) Negligible (b) Light (c) Moderate (d) Heavy	31
Figure 3.9 Layout of transverse reinforcement and prestressing strands (RF-R-9-A&C and RF-3R-12-A)	34
Figure 3.10 Web and top flange thickness.....	35
Figure 3.11 Moderately damaged end region of RF-3R-9-A	35
Figure 3.12 Horizontal cracks in the hollow section	36
Figure 3.13 RF-3R-9-C Top flange thickness.....	37
Figure 3.14 Moderately damaged end region of RF-3R-9-C.....	38
Figure 3.15 Void floatation in RF-3R-12-A	39
Figure 3.16 End region of RF-3R-12-A.....	40
Figure 3.17 Horizontal crack propagating from plywood	40
Figure 3.18 Cut surface of MLL-9-34-A	41
Figure 3.19 Layout of transverse reinforcement and prestressing strands (MLL-9-34-A).....	42
Figure 3.20 Minor cracking condition on MLL-9-34-A	43
Figure 3.21 Layout of transverse reinforcement and prestressing strands (RF-1R-1-C)..	45
Figure 3.22 RF-1R-1-C web flange thickness	46
Figure 3.23 Epoxy coated in the end region of RF-1R-1C	46
Figure 3.24 Horizontal cracks in the testing region.....	47
Figure 3.25 Core locations at dapped end and web	49
Figure 3.26 Reinforcement locations.....	51
Figure 3.27 Stress-strain relationship of tested bars	52
Figure 4.1 Formwork ready for concrete placement.....	55
Figure 4.2 Casting of beam RF-3R-9-C (Bindrich, 2009).....	55
Figure 4.3 End view of test setup.....	57
Figure 4.4 Side view o test set-up (a) Dapped end test (b) Web shear test	58

Figure 4.5 Beam ready for testing.....	59
Figure 4.6 Support at the end (a) North (b) South.....	60
Figure 4.7 Seven inch diameter inset counter bored into the top steel plate	60
Figure 4.8 Linear potentiometer (a) At support (b) At surface of the beam.....	61
Figure 5.1 Simulation of a beam test	64
Figure 5.2 Specimen displacements and deformations.....	65
Figure 5.3 Calculation of shear strain.....	66
Figure 5.4 RF-3R-9-A pre-existing cracks (west side).....	67
Figure 5.5 East side of RF-3R-9-A (a) Location of the new diagonal crack and spall concrete (b) Faulting.....	67
Figure 5.6 West side of RF-3R-9-A.....	68
Figure 5.7 RF-3R-9-A load-deflection plot	69
Figure 5.8 RF-3R-9-A average strains vs. measured shear	70
Figure 5.9 RF-3R-9-A shear strain (γ) vs. measured shear	71
Figure 5.10 Horizontal cracks (a) East side (b) West side (c) Crack opening on east side	72
Figure 5.11 Location of first new diagonal cracks (a) West side (b) East side	73
Figure 5.12 Diagonal cracks at failure (west).....	73
Figure 5.13 RF-3R-9-C load-deflection plot	74
Figure 5.14 RF-3R-9-C average strains vs. measured shear.....	75
Figure 5.15 RF-3R-9-C shear strain (γ) vs. applied shear	76
Figure 5.16 Shear span of RF-3R-12-A (west side)	77
Figure 5.17 Cracks caused by dapped end tests (a) North end (b) South end	78
Figure 5.18 Diagonal cracks and cold joint sliding	78
Figure 5.19 Concrete spalling and bent stirrup at failure.....	79
Figure 5.20 RF-3R-12-A load-deflection plot	80
Figure 5.21 RF-3R-12-A average strains vs. measured shear	81
Figure 5.22 RF-3R-12-A shear strain (γ) vs. measured shear	82
Figure 5.23 Cut section of RF-3R-12-A	83
Figure 5.24 Pre-existing crack conditions (a) Horizontal cracks in test region (west), (b) Long span (west), (c) Diagonal cracks in test region (east), and (d) Long span (west).....	84
Figure 5.25 (a) Horizontal crack in the southwest side (b) Crack sliding in the west side	85
Figure 5.26 Crack Pattern at failure (east).....	86
Figure 5.27 MLL-9-34-A load-deflection plot	87
Figure 5.28 MLL-9-34-A average strains vs. measured shear (test region).....	88
Figure 5.29 MLL-9-34-A average strains vs. measured shear (long span)	89
Figure 5.30 MLL-9-34-A shear strain (γ) vs. measured shear (test region).....	90
Figure 5.31 MLL-9-34-A shear strain (γ) vs. measured shear (long span)	91
Figure 5.32 Crack condition before testing (a) West (b) East	92
Figure 5.33 Prefailure crack pattern (west).....	93
Figure 5.34 Prefailure crack pattern (east).....	93
Figure 5.35 Crack pattern at failure (west).....	94

Figure 5.36 RF-1R-1-C load-deflection plot	95
Figure 5.37 RF-1R-1-C average strains vs. measured shear	96
Figure 5.38 RF-1R-1-C shear strain (γ) vs. measured shear	97
Figure 5.39 Comparison of load-deflection relationship	99
Figure 5.40 Relationship of $V_{\text{crack}}/V_{\text{test}}$ vs. damage level	100
Figure 5.41 Comparison of crack patterns	101
Figure 5.42 Comparison of average diagonal strains	102
Figure 5.43 Comparison of average vertical strains	103
Figure 5.44 Relationship of V_{test} vs. cracking level	104
Figure 5.45 Cracking pattern in end block and web	106
Figure 5.46 Comparison of maximum shear strains (γ_{max})	108
Figure 6.1 Prismatic and bottle-shaped struts	112
Figure 6.2 Classification of nodes	113
Figure 6.3 Resolution of forces on a node	113
Figure 6.4 Stresses on hydrostatic and non-hydrostatic nodes (Thompson, 2002)	114
Figure 6.5 Difference between hydrostatic and non-hydrostatic nodes (Bircher et al. 2008)	115
Figure 6.6 CCC node	116
Figure 6.7 CCT node	117
Figure 6.8 CCT node	118
Figure 6.9 U stirrups	119
Figure 6.10 CTT node	120
Figure 6.11 Reinforcement cross a strut (ACI 318 2008)	122
Figure 6.12 Back face of a CCT node (a) bearing of an anchor plate (b) bonding stress	124
Figure 6.13 Superimposed truss model (Brown et al. 2006)	127
Figure 6.14 Strut-and-tie model for a deep beam (fib 1999)	128
Figure 6.15 Representative number vs. shear span-to-depth ratio (adopted from Brown et al. 2006)	129
Figure 6.16 RF-3R-9-C elevation, cross section, and debonding schedule	131
Figure 6.17 Sketch of (a) One-panel model and (b) two-panel model	132
Figure 6.18 Close-up of the web	132
Figure 6.19 Proportioning the applied load on bearing plate	134
Figure 6.20 Determination the location of the vertical tie (Member 34) in the shear span	135
Figure 6.21 (a) One-panel model and (b) Two-panel model	136
Figure 6.22 A close-up for the one-panel model	137
Figure 6.23 A close-up for the multi-panel model	138
Figure 6.24 A close-up for the Node 1	139
Figure 6.25 Bottom bearing plate	140
Figure 6.26 Relationship between steel stress and development length (AASHTO LRFD 2008)	142
Figure 6.27 A close-up for Node 2	145
Figure 6.28 Top bearing plate	146

Figure 6.29 Comparison of test to computed shear capacities using design strength.....	150
Figure 6.30 Comparison of test to computed shear capacities using core strength/0.85	150
Figure 6.31 Comparison of test to computed shear capacities using design strength.....	153
Figure 6.32 Comparison of test to computed shear capacities using core strength/0.85	154
Figure 6.33 Bottle-shaped strut.....	156
Figure 6.34 Chamfer and plywood in the web portion	156
Figure 7.1 Location of the cores	159
Figure 7.2 (a) ASR distressed fine aggregate (b) Highly distress fine aggregate (Morgan 2010)	160
Figure 7.3 (a) Ettringite filled micro cracks (b)Ettringite filled gap around fine aggregate (Morgan 2010)	160
Figure 7.4 (a) General crack orientation within cores (Morgan 2010) (b) Restraint in the core.....	162
Figure 7.5 Comparison of reactive particles throughout the length of the cores.....	163
Figure 7.6 (a) Grey epoxy coating (b) Port at the large crack (c)Epoxy injection (d) Finished overview	164
Figure 7.7 Diamond wire saw	165
Figure 7.8 Locations of the cut sections	166
Figure 7.9 Overview and details of Section A.....	167
Figure 7.10 Elevation of the end block.....	168
Figure 7.11 Overview and details of Section B	170
Figure 7.12 Overview and details of Section C	172
Figure 7.13 Overview and details of Section D.....	173
Figure 7.14 Overview and details of Section E	174
Figure 7.15 Summary of the crack widths	176
Figure 7.16 Bulging in Section A	177
Figure 7.17 Relationship between expansion and restraint	177
Figure 7.18 Mechanism of elastic rebound test (Deschenes 2009)	178
Figure 7.19 Typical stress-strain relationship of steel	179
Figure 7.20 Locations of tested steel and cracking condition.....	180
Figure 7.21 Comparison of results from elastic rebound tests.....	181
Figure A.1 Standard reinforcement.....	189
Figure A.2 Standard beam section	190
Figure A.3 Standard plan	191
Figure A.4 Standard end detail (elevation).....	192
Figure A.5 Standard end detail	193
Figure A.6 Dapped end detail	194
Figure A.6 Standard section profile	195
Figure A.7 Standard section profile (continued).....	196
Figure A.8 Bearing and other details	197
Figure A.10 RF-1R-1 plan	199
Figure A.11 RF-1R-1 end details.....	200
Figure A.11 RF-1R-1 section profile.....	201

Figure A.12 RF-1R-1 section profile (continued).....	202
Figure A.13 Strands debonding schedule	203
Figure A.15 RF-2R-6 plan	204
Figure A.16 RF-2R-6 end details.....	205
Figure A.17 RF-2R-6 section profile	206
Figure A.18 RF-2R-6 section profile (continued).....	207
Figure A.19 RF-2R-6 strands debonding schedule.....	208
Figure A.20 RF-3R-9 plan	209
Figure A.21 RF-3R-9 end details.....	210
Figure A.22 RF-3R-9 section profile.....	211
Figure A.23 RF-3R-9 section profile (continued).....	212
Figure A.24 RF-3R-9 strands debonding schedule.....	213
Figure A.25 RF-3R-12 plan	214
Figure A.26 RF-3R-12 end details (elevation)	215
Figure A.27 RF-3R-12 section profile.....	216
Figure A.28 RF-3R-12 section profile (continued).....	217
Figure A.29 RF-3R-12 strands debonding schedule.....	218
Figure A.30 MLL-9-34 plan	219
Figure A.31 MLL-9-34 bars details	220
Figure A.32 MLL-9-34 end details (plan)	221
Figure A.33 MLL-9-34 end details (elevation).....	222
Figure A.34 MLL-9-34 section profile	223
Figure A.35 MLL-9-34 section profile (continued).....	224
Figure A.36 MLL-9-34 strands debonding schedule.....	225
Figure D.1 RF-3R-9-A Elevation, section, and debonding schedule	250
Figure D.2 RF-3R-9-A strut-and-tie model (a) One-panel (b) Two-panel	251
Figure D.3 Close-up of Node 1	256
Figure D.4 Close-up of Node 2.....	257
Figure D.5 Determination of tri-axial confinement factor of Node 1	264
Figure D.6 Determination of tri-axial confinement factor of Node 2.....	266
Figure D.7 Strut-and-tie model in the shear span (a) One-panel (b) Two-panel	269
Figure D.8 Close-up of Node 1 of the combination model.....	272
Figure D.9 Close-up of Node 2 of the combination model.....	274
Figure D.10 RF-3R-9-C Elevation, section, and debonding schedule.....	292
Figure D.11 RF-3R-9-C Strut-and-tie model in the shear span (a) One-panel (b) Two-panel	293
Figure D.12 RF-3R-12-A Elevation, section, and debonding schedule	297
Figure D.13 RF-3R-12-A Strut-and-tie model in the shear span (a) One-panel (b) Two-panel	298
Figure D.14 MLL-9-34-A Elevation, section, and debonding schedule.....	302
Figure D.15 RF-3R-12-A Strut-and-tie model in the shear span (a) One-panel (b) Two-panel	303
Figure D.16 RF-1R-1-C Elevation, section, and debonding schedule.....	307

Figure D.17 RF-3R-12-A Strut-and-tie model in the shear span (a) One-panel (b)Two-panel.....	308
--	-----

CHAPTER 1

Introduction

1.1 OVERVIEW

Premature concrete deterioration (PCD) has been a main durability issue of concrete structures in Texas due to alkali-silica reaction (ASR) and delayed ettringite deterioration (DEF). For bridges in Texas, the presence of alkali-silica reaction and delayed ettringite formation causes large cracks on the surface of the bridge girders and bent caps and raises the concern of the engineers of Texas Department of Transportation (TxDOT). Although the impact of the ASR/DEF deterioration on the structural capacity is not fully understood, it has been generally believed that ASR/DEF caused cracks related to the loss of the structural capacity.

In 1995, a group of pretensioned trapezoidal box beams were fabricated by Traylor Brothers for TxDOT for US 59 and the Katy Central Business District HOV structure. Five of these beams were rejected for various reasons including poor consolidation, void floatation, or incorrect end skew. Four of the beams, which were cast in July 1995, showed ASR/DEF related deterioration in different degrees after being retained in the contractor's yard for over fourteen years. And the fifth beam, which was cast in November 1995, showed very few cracks. These five beams are representative of the situation regarding pretensioned trapezoidal box beams in service on US 59 and on the Katy Central Business District HOV structure. Beams in the field deteriorate in a slower rate because bridge deck prevents the direct absorption of water, which is an essential factor of ASR and DEF.

There is a common consensus that the flexural strength is not remarkably affected by ASR/DEF deterioration. However the impact of the ASR/DEF deterioration on the shear capacity is still a controversial issue. Most specimens in the past research were fabricated in laboratory and were subjected to accelerated ASR/DEF deterioration; however, specimens that have practical size are rare. Furthermore, none of these

specimens suffered long-term ASR/DEF deterioration of more than ten years. The five beams in this research provide a great opportunity to further understand the impact of ASR/DEF on long-term shear performance of bridge girders.

1.2 OBJECTIVES AND SCOPE

The major objective of this study was to conduct shear testing on pretensioned trapezoidal bridge girder specimens suffering from ASR and/or DEF damage and use the results from the shear tests to evaluate the severity of the problems that exist in various locations in Texas.

To achieve this goal, TxDOT sponsored a study at the University of Texas at Austin through an interagency contract (IAC). The five pretensioned trapezoidal box girders mentioned previously were cut and sent to the Ferguson Structural Engineering Laboratory to conduct a large-scale shear testing program.

The testing program involved: (i) Prepare the transportation of the beams to the Ferguson Structural Engineering Laboratory, (ii) Design a test program, (iii) Load test both severely ASR and/or DEF cracked and uncracked beams, (iv) Inject epoxy in one beam and conduct an autopsy on the beam to understand the nature of the ASR/DEF caused cracks, (v) Use the testing results to evaluate the shear performance of the deteriorated trapezoidal box beams affected by ASR/DEF.

1.3 ORGANIZATION

In Chapter 2, all the background information related to the objectives of this study is presented. The details of test specimens are described in Chapter 3. Procedures and techniques used for shear tests are outlined within Chapter 4. Measurements and observations obtained from shear testing are discussed in Chapter 5. The evaluation of the shear capacities of the test specimens is presented in Chapter 6. Results of forensic analysis are discussed in Chapter 7. Finally, the work completed in this study and conclusion regarding the structural performance is summarized in Chapter 8.

CHAPTER 2

Background

2.1 OVERVIEW

In this chapter, basic mechanisms of alkali-silica reaction (ASR) and delayed ettringite formation (DEF) will be briefly explained. The methods for determining cause and extent of ASR and/or DEF used will be described. Thereafter, the research related to the effect of ASR and/or DEF on engineering properties and structural integrity of concrete will be reviewed in order to give readers basic background knowledge regarding ASR and/or DEF damage to concrete structures. Mitigation and prevention of ASR and/or DEF, although beyond the scope of the current study, will also be discussed briefly.

2.2 ASR/DEF MECHANISM

2.2.1 Alkali-Silica Reaction (ASR)

Aggregate containing certain constituents (e.g. reactive silica) may react with alkali hydroxide in the cement. The reactivity is potentially harmful only when it produces significant expansion (Mather 1975). This reaction is called alkali-aggregate reaction (AAR). Generally, there are two forms of AAR: alkali-silica reaction (ASR) and alkali-carbonate reaction (ACR). ACR is a reaction between alkalis and limestone aggregate containing calcite and clay and is more prevalent in Canada and China (Richardson 2002). ASR is of more concern and is more widespread elsewhere in the world. Therefore, the mechanism and effect of ASR on concrete will be discussed.

In 1930s, Thomas Stanton (Stanton 1940) observed several concrete structures in California and first recognized that ASR affects concrete structures and causes distress in concrete. ASR is the reaction between alkalis in the cement and the reactive silica in the aggregate. The chemical process can be separated into two steps:

1. Alkali + reactive silica \rightarrow alkali-silica gel
2. Alkali-silica gel + moisture \rightarrow expansion

Alkalis in the concrete pore solution react with the reactive silica in the aggregate and generate an alkali-silica gel product. The presence of alkali-silica gel does not necessarily cause deterioration in the concrete. However when the gel absorbs moisture from the environment, it will swell and cause pressures exceeding the tensile strength of the concrete and results in cracking on the concrete. A thin section image of concrete affected by ASR is shown in Figure 2.1. Several key characteristics of the ASR affected concrete can be seen.

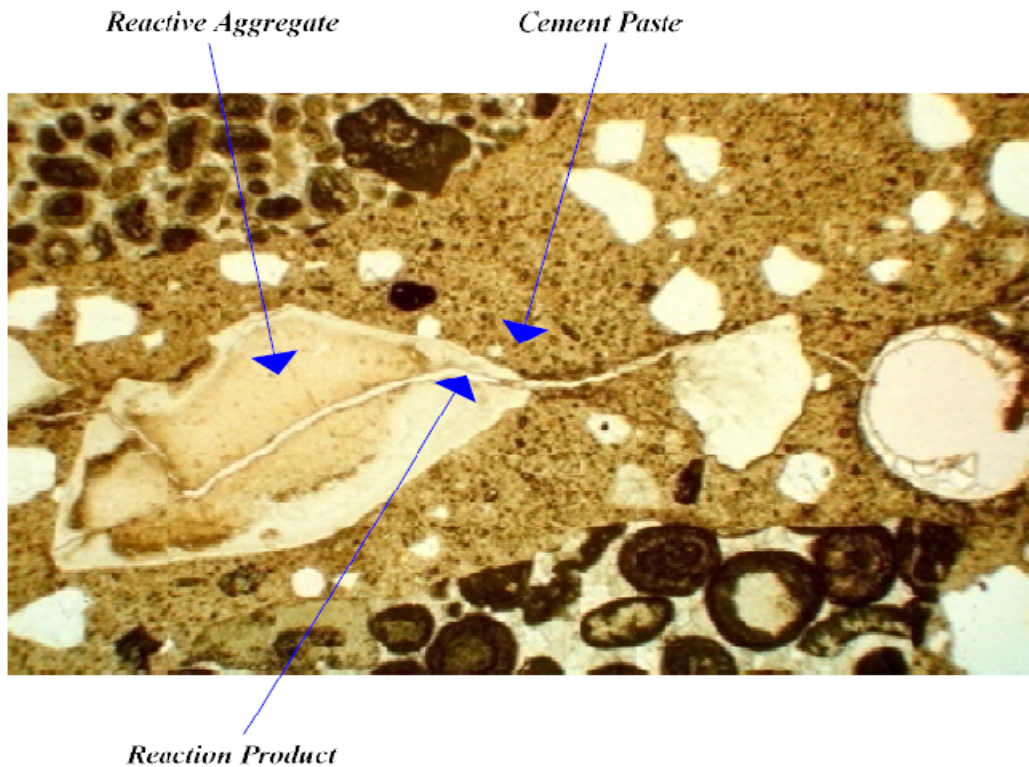


***Figure 2.1 Thin section image, showing some typical diagnostic features
(Folliard, 2007)***

From the mechanism described above, three factors essential to ASR can be summarized: (i) reactive silica in the aggregate, (ii) high alkali, which is usually provided

by cement, and (iii) sufficient moisture in the concrete. When these three conditions are satisfied, deleterious alkali-silica reaction will occur.

2.2.2 Delayed Ettringite Formation (DEF)

Delayed ettringite formation, DEF, is a form of sulfate attack that happens when the temperature during the early curing process exceeds 158°F. The ettringite formation during the early hydration process is a normal product and is not harmful to concrete durability. However when the temperature during hydration exceeds the threshold temperature (158°F), ettringite is not formed. Ettringite decomposes to hydrated calcium monosulphoaluminate (AF_m), releasing sulfates into pore solution. The sulfates do not react with tricalcium aluminate (C_3A) but are absorbed by calcium silicate hydrate (C-S-H). When the hydration process slows down and temperature in the concrete cools down to the ambient temperature, the sulfates attracted to the C-S-H gel will be slowly released back into cement pore solution. The released sulfates are available in the pore solution and can react with C_3A to form ettringite. The ettringite formed in the hardened concrete will expand and cause cracking (Bauer et al. 2006).

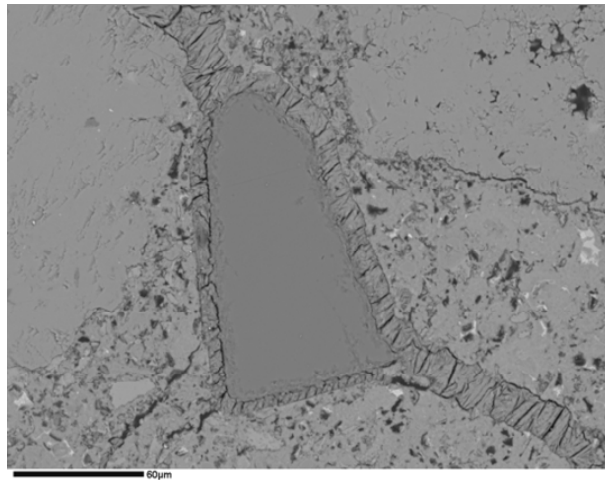


Figure 2.2 Ettringite growth around aggregate and in cracked matrix (Thomas et al. 2008)

DEF can only occur in concrete when the following three conditions are satisfied:
(i) The temperature during the early curing process exceeds 158°F; (ii) A DEF-

susceptible concrete mixture is used, and (iii) Sufficient moisture is present to drive and sustain the reaction (Folliard 2007). For the first condition, it is clear that the threshold value will vary in different mixture. Nonetheless, research conducted under TxDOT Project 0-4085 indicated that no DEF was observed when the temperature was less than this value (158°F). For the second condition, the research results from TxDOT Project 0-4085 indicated that some concrete mixtures will not exhibit DEF even if curing temperatures reach 200°F. For the third condition, DEF did not occur when the relative humidity was below 90 percent.

2.3 DETERMINATION OF CAUSE AND EXTENT OF ALKALI-SILICA REACTION AND/OR DELAYED ETTRINGITE FORMATION

A protocol developed by Folliard et al. in 2007 provides systematic guidance for engineers to evaluate a structure subject to ASR and/or DEF. The information which will be used in this study is briefly outlined here.

To evaluate a structure for the potential to develop ASR and/or DEF, a visual inspection is conducted and information/data (construction records, inspection reports, structure-specific information) for the target structure is collected.

If the structure exhibits ASR and/or DEF damage or may do so in the future, it is preferable to acquire information on concrete materials, mixture proportions, and inspection reports. In addition, it is recommended that construction dates and climatic data be collected. This information is important for evaluating the concrete temperature during curing, which could lead to DEF if it is greater than 158°F. The maximum temperature in the concrete can be estimated using ConcreteWorks, a software package developed as part of TxDOT Project 0-4563. This is a free software package at www.texasconcreteworks.com.

Visual inspection is another important component of the investigation, but it cannot be used for accurately predicting the cause and extent of ASR and/or DEF. However, it is useful when combined with other information/data from laboratory tests.

Basically, cracking patterns caused by ASR and/or DEF are usually very similar. DEF-caused cracking may have larger crack widths compared to ASR. Besides, there may be odd “buff” color or discoloration on concrete suffering from advanced DEF. Except for these two distinctions, the visual manifestation of these two distress mechanisms are alike.

Cracking observed in field structures affected by ASR and/or DEF is strongly affected by internal or external restraint and applied load (Folliard 2007). When ASR and/or DEF occur, concrete will expand in all direction, and if there is only minimal restraint in concrete, random or map cracking will appear on concrete surface. For a beam element, which is the main topic in this study, the main restraint is provided in the longitudinal direction by reinforcing steel or prestressed strand, therefore, the concrete will expand more in the transverse direction and exhibit horizontal cracking. In addition, ASR-produced gel may appear on concrete surfaces and result in surface staining.

One of the most important aspects for diagnosing ASR and/or DEF is petrographic evaluation. The evaluation should be conducted by a trained and experienced petrographer. In petrographic evaluation, the ASR and/or DEF diagnostic features can be identified as shown in Figure 2.1 and Figure 2.2. A trained petrographer should be able to identify these key features and distinguish ASR distress from DEF distress.

Strength and elastic modulus tests are also recommended. For strength, tensile strength is more sensitive to ASR and/or DEF than compressive strength is. Elastic modulus is also a parameter strongly affected by ASR and/or DEF. Sometimes it is difficult to extract a sufficient number of sound cores from the structure to perform these tests. In unpublished research, the Concrete Durability Center (CDC) at the University of Texas at Austin found that, on a single core, one could perform a stiffness damage test, followed by an elastic modulus test, followed by a compressive strength test. This method may be useful in the future when there are not enough cores for testing, however, it will not be used in this study.

There are other methods, for use in both field and laboratory studies, available for determining the cause and extent of ASR and/or DEF, but they are beyond the scope of this study and will not be employed.

2.4 EFFECT OF ALKALI-SILICA REACTION AND DELAYED ETTRINGITE FORMATION ON CONCRETE ENGINEERING PROPERTIES

Generally, it is difficult to distinguish whether cracks are caused by ASR, DEF or combination of the two distress mechanisms. Both ASR and DEF can cause internal expansion and cracking on the concrete surface. Because of the difficulty in telling the difference of the two distress mechanisms, TxDOT has adopted the term, premature concrete deterioration (PCD) to represent the effect of these two reactions. From a structural point of view, ASR and/or DEF lead to similar forms of distress. Based on the similarity of the visual manifestation, these two distress mechanisms will be discussed together in the following sections.

Many researchers made efforts to study the impact of ASR and/or DEF on the material behavior of concrete. The impact of ASR and/or DEF on the concrete mechanical properties is the effect of interplay between physical and chemical characteristics of the aggregates and concrete mixture. Therefore changes in various mechanical properties may occur at different rate. There is a consensus that changes in mechanical properties cannot be associated only with the level of expansion. They may also depend on the types of the reactive aggregates and the mechanism involved in the reaction (Swamy et al. 1988, Ahmed et al. 2003, and Giaccio et al. 2008).

Generally, most researchers have concluded that compressive strength and splitting tensile strength are not affected as much as direct tensile strength and elastic modulus (Swamy et al. 1988, Ahmed et al. 2003, and Smaoui et al. 2006).

2.5 EFFECT OF ALKALI-SILICA REACTION AND DELAYED ETTRINGITE FORMATION ON STRUCTURAL CAPACITIES OF CONCRETE STRUCTURES

Although engineering properties of concrete were shown by many researchers to be reduced through ASR and/or DEF, it is still an open question if reduction in engineering properties of concrete necessarily represents a reduction in the strength and integrity of a concrete structure. To judge if ASR and/or DEF reduce the strength of concrete structures, the assessment is sometimes based on material properties measured on extracted cores. This approach seems logical but Hobbs (1989) pointed out that this approach will underestimate the performance of concrete structures affected by ASR and/or DEF. Cores may expand after extraction because of the removal of structural restraint. Thus the properties measured by core tests may not be representative of the concrete member from which the cores were taken. Therefore, loading tests play a significant role in clarifying the reserve strength of ASR and/or DEF damaged structures.

In this section, the impact of ASR and/or DEF on the flexure and shear performance of concrete beam elements will be reviewed. Many studies of reinforced concrete beams damaged by premature concrete deterioration can be found in the literature, studies of prestressed concrete beams are relatively sparse. However, the research results obtained from reinforced concrete structures are still valuable for study of prestressed concrete beams.

2.5.1 Reinforced Concrete Beams

2.5.1.1 Flexural Strength

A report by The Institution of Structural Engineers indicated that the impact of the ASR on reinforced concrete structures can be minimal when the expansion is less than 6000 microstrain. A specimen with expansion above this level was reported to suffer a loss of flexural strength of up to twenty five percent (Kapitan 2006). A critical review done by the University of Bermingham also concluded that the flexural capacity is not

reduced by moderate expansion due to ASR (Clark 1989). Later, the same conclusion was also obtained from research reported by Fan (1998) and Monette (2002).

2.5.1.2 Shear Strength and Anchorage

Shear Strength of ASR damaged reinforced concrete structures is a more controversial issue. For beams without shear reinforcement, both of the studies conducted by Cope et al. (1990) and Bach et al. (1993) showed that the shear strength of reinforced concrete beams (5 in x 10 in. and 7 in. x 14 in.) without stirrups was not affected by ASR even with significant expansions. However Cope et al. also pointed out that due to the unpredictability of shear failure and ASR, the possibility of premature shear failure should not be ignored.

Ahmed et al. (1998) conducted a series of shear tests on sixteen reinforced concrete beams (3 in. x 5 in.) to investigate the static and fatigue shear strength of beams affected by ASR. They divided the sixteen beams into four groups based on shear reinforcement and end detailing (Table 2.1). ASR increased the shear strength both with and without shear reinforcement. The percentage of increase was 8.5% for singly reinforced and 11.5% for doubly reinforced beams, respectively. Beams with good end details (anchorage of bars) exhibited less expansion and an increase in the ultimate shear strength both with and without shear reinforcement. For fatigue shear strength, beams with ASR damage exhibited an increase in number of cycles to failure under repeated loading.

Table 2.1 Details of test specimen

S1	w/o stirrups and poor anchorage of longitudinal reinforcement
S2	w/o stirrups and good anchorage of longitudinal reinforcement
S3	with stirrups and poor anchorage of longitudinal reinforcement with compression reinforcement
S4	with stirrups and good anchorage of longitudinal reinforcement with compression reinforcement

Bach et al. (1993) also conducted shear tests of reinforced concrete beams with stirrups, and the results showed that the shear strength of the beams increased due to the prestressing effect caused by ASR expansion. A few pull-out tests of anchored bars were also performed in this study. The anchorage strength was reduced twenty to thirty percent due to ASR deterioration.

Deschenes et al. (2009) fabricated four nearly full-scale bent caps (21in x 42 in) with an ASR and/or DEF reactive concrete mixture and two with a non-reactive concrete mixture. In order to produce DEF deterioration in the reactive specimens, the four reactive specimens were subject to high temperature curing in excess of 158°F over twelve hours. After curing, the six specimens were subjected to outdoor exposure, frequent wet-dry cycles and, load conditioning. Three of the specimens (two reactive and one non-reactive) were used for six shear tests (two tests on each beam) within twelve months after the casting. The remaining three bent caps continue to be exposed outdoors and will be tested in the future. The shear capacities of the two reactive beams that exhibited low to moderate damage were higher than that of the non-reactive beam regardless of the shear span-to-depth ratio or deterioration level. The researchers pointed out that the confinement provided by the shear reinforcement plays a critical role in maintaining structural integrity.

For the non-reactive specimen, the applied shear causing diagonal shear cracking was approximately 33% of the ultimate shear capacity and corresponds to service level shear as defined by Birrcher et al. (2008). Diagonal shear cracking of the bent caps damaged by ASR/DEF appeared when the applied shear was around 75% of the ultimate shear capacity. The increase in load at first diagonal cracking of the ASR/DEF damaged bent caps was well above service level and close to shear capacity.

In contrast to the four studies above, Chana et al. (1992) conducted shear tests of sixteen reinforced concrete beams (4 in. x 8 in.) without shear reinforcement. Eight beams were cast with ribbed bars and eight were plain bars (poor anchorage). The results showed that the maximum reduction in shear strength of the beams due to ASR was 23% for ribbed bars and 30% for plain bars respectively. Chana et al. suggested that the small

difference in shear strength for beams with poor anchorage (plain bars) may be due to confinement of anchored bars provided by the reaction at the support.

Den Uijl and Kaptijn (2003) reported that a reduction of shear strength of flat slabs without shear reinforcement was observed. Six beams (20~24 in. x 25~30 in.) sawed from two bridges were loaded to failure (12 tests). Eight tests showed shear failure with an average capacity of 75% of the computed strength value from theoretical analysis.

From the studies reviewed, one can see that quite different opinions exist among researchers. The differing opinions have resulted in continued interest in studying the effect of ASR and/or DEF on concrete structures.

2.5.2 Prestressed Concrete Beams

Compared to studies of ASR and/or DEF damaged reinforced concrete beams, there is less research related to the ASR and/or DEF deterioration of prestressed concrete beams.

2.5.2.1 *Flexural Strength*

Clayton et al. (1990) tested twenty eight prestressed concrete I-beams (5 in. x 10 in. and 8 in. x 16 in.) affected by ASR (with and without stirrups) to flexural failure and reported that the capacity was not significantly reduced by ASR. Thereafter, Boenig et al. (2001) examined the flexural capacity of three full-scale salvaged ASR and/or DEF damaged prestressed box girders (48 in. x 27 in.). The results showed that the flexural capacity was not affected because the ASR and/or DEF deterioration was concentrated at the end region of the beam and no strand slip occurred.

2.5.2.2 *Shear Strength and Anchorage*

Clayton et al. (1990) also studied shear capacity of prestressed concrete I-beams and reported that the shear strength of beams with and without shear reinforcement drops about 20% when the expansion was 1000×10^{-6} . However, beams with shear reinforcement regain shear strength due to prestressing of the shear reinforcement when

ASR expansion reached 4000×10^{-6} . In contrast, beams without shear reinforcement did not show any further change. Clayton et al. also observed that shear cracks along the length of the beams resulted in transverse expansion that resulted in yielding of the shear reinforcement. They concluded that the average vertical compression stress on the concrete due to stressing of the stirrups by ASR expansion was about 2 MPa (290 psi). Restraint providing compression of 4 MPa (580 psi) was recommended for stopping ASR expansion. This observation closely corresponded to the conclusion made by Deschenes et al (2009), which concluded that 300 psi was generated by ASR expansion and 600 psi was recommended. Clayton et al. also reported no evidence that bond strength significantly decreased due to ASR deterioration. Loss of bond strength, however, may occur when ASR expansion leads to delamination or splitting of concrete in the anchorage zone.

Boenig et al. (2001) examined the shear capacity of the three ASR/DEF damaged prestressed box girders described in the last section. The results indicated that the shear capacity reduced 14% compared with that for undamaged girders. The authors pointed out a small reduction occurred because the ASR and/or DEF deterioration was primarily concentrated at the end regions of the girder.

2.5.3 Dapped End Beams

Bindrich (2009) conducted shear testing on the dapped ends of two salvaged prestressed trapezoidal box girders (36 in. x 54 in.) with moderate ASR and/or DEF deterioration. The results showed that the shear capacity of the two dapped end tests was greater than the capacity calculated from design codes (ACI, AASHTO, and PCI handbook). Both of the beams failed in bond-slip with shear failure, and the load capacity was at least 35% greater than the predicted load obtained from any of the code described above. Shear cracking caused by applied load usually aligned with existing ASR and/or DEF cracks. The lack of the new shear cracks caused by applied load provided little warning when the shear failure was imminent.

2.5.4 Summary

In Figure 2.3, the number of shear specimens versus total height of the specimen, h , is shown. The specimens are divided into two groups according to the beam height (h). It can be clearly seen that for most of the specimens tested in shear, $h < 20$ in. while only small number have $h > 20$ in. This is probably due to the cost, size of laboratory, duration of projects, etc. Most of the specimens greater than 20 inch were from salvaged beams fabricated by contractors (Boenig et al. and Bindrich) or sawn from in-service structures (den Uijl et al.). These salvaged beams or in-service structures were exposed to outdoor condition for at least nine years and provided researchers an opportunity to investigate shear capacity of full-scale specimens damaged by ASR and/or DEF. These specimens may be the most representative of the impact of ASR and/or DEF on shear capacity because they were full scale and were exposed to a natural environment while other small specimens were conditioned in the laboratory to accelerate the distress mechanism. It does not mean that the testing data from small specimens are not valuable, but it should be noted that *any strength test conducted on a specimen quantifies the performance of the material in relation to that method of test only and does not necessarily reflect the performance of the material in its structural context* (Clayton et al., 1990). Based on this point, full-scale testing is needed urgently for determine the impact of ASR and/or DEF on the shear capacity of concrete structures. In the current study h is 54 in. and a 14-year exterior exposure. Details will be described in the next chapter.

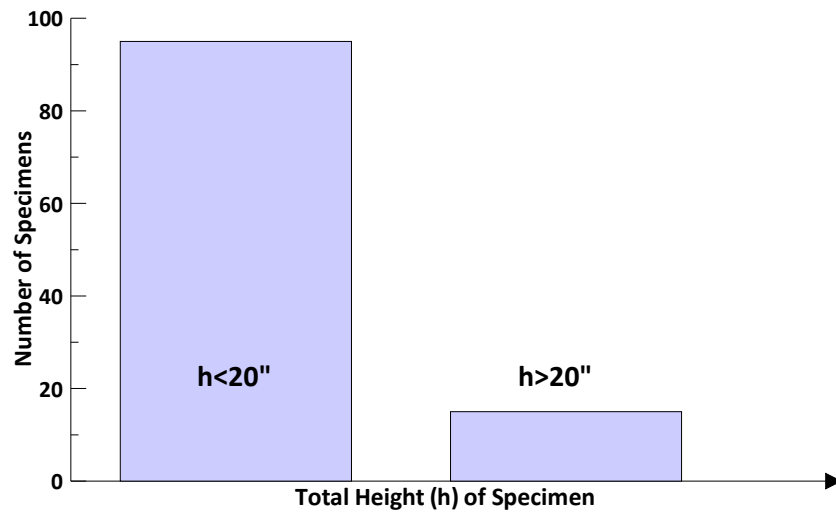


Figure 2.3 *Total height of shear testing specimen vs. the number of the specimens*

2.6 RECENT STUDY IN JAPAN

In Japan, several cases of ASR damaged structures were reported in 1970s. The appearance of ASR deterioration on the Hanshin Expressway in 1982 raised concern. Thereafter, many cases were reported in various types of concrete structures. Japanese researchers conducted a nationwide survey of test methods and countermeasures, and proposed methods for assessment and repair. As a result of that effort, fewer cases of ASR deterioration have been reported since 1990. To repair structures constructed in the 1970s and 1980s, engineers applied surface coating to prevent moisture penetration. However, these repair measures did not completely stop ASR expansion. In the late 1990s, shear reinforcement fractures were found. As a result, Japanese researchers began to investigate the fracture mechanism, to assess the safety of the damaged structures, and to develop methods for repair and strengthening.

There are currently thirty concrete structures showing reinforcement fracture due to ASR expansion. An example is shown in Figure 2.4. Japanese researchers (Miyagawa 2006) consider that the concrete structures are safe as long as the reinforcement is intact. However, when shear reinforcement fractures due to ASR expansion, structural strength may be reduced due to the loss of confinement.

As long as reinforcing steels are not broken due to ASR-caused expansion, the safety of a structure is considered not to be seriously compromised. However, the safety of a structure becomes questionable when the confinement of concrete becomes degraded due to the fracture of reinforcing steel bars.

A series of material tests and analyses were conducted to look into the effect of different bending radii of rebar, strain aging, stress-corrosion cracking, and hydrogen embrittlement on steel fracture. The result showed that rib shape and bending radius had a significant correlation with reinforcement fracture. A mechanism for reinforcement fracture was also reported (Figure 2.5).

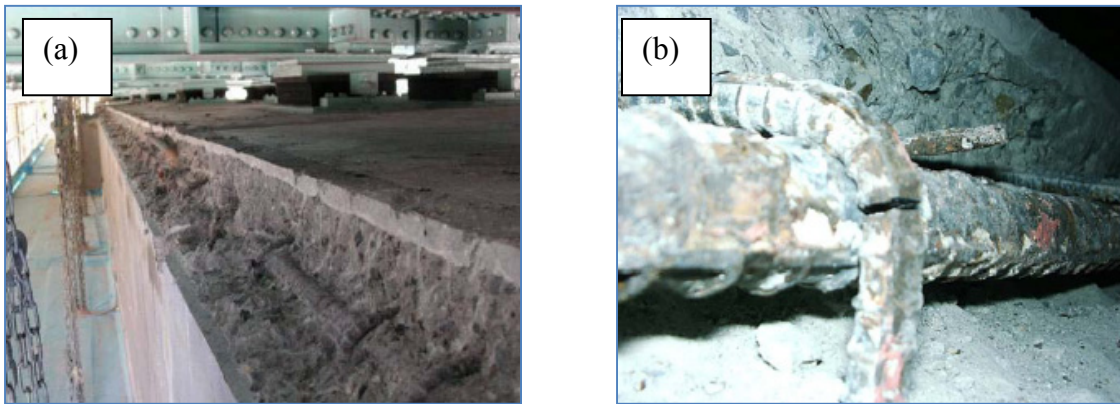


Figure 2.4 (a) Damaged pier (b) Fractured reinforcement (Miyagawa 2006)

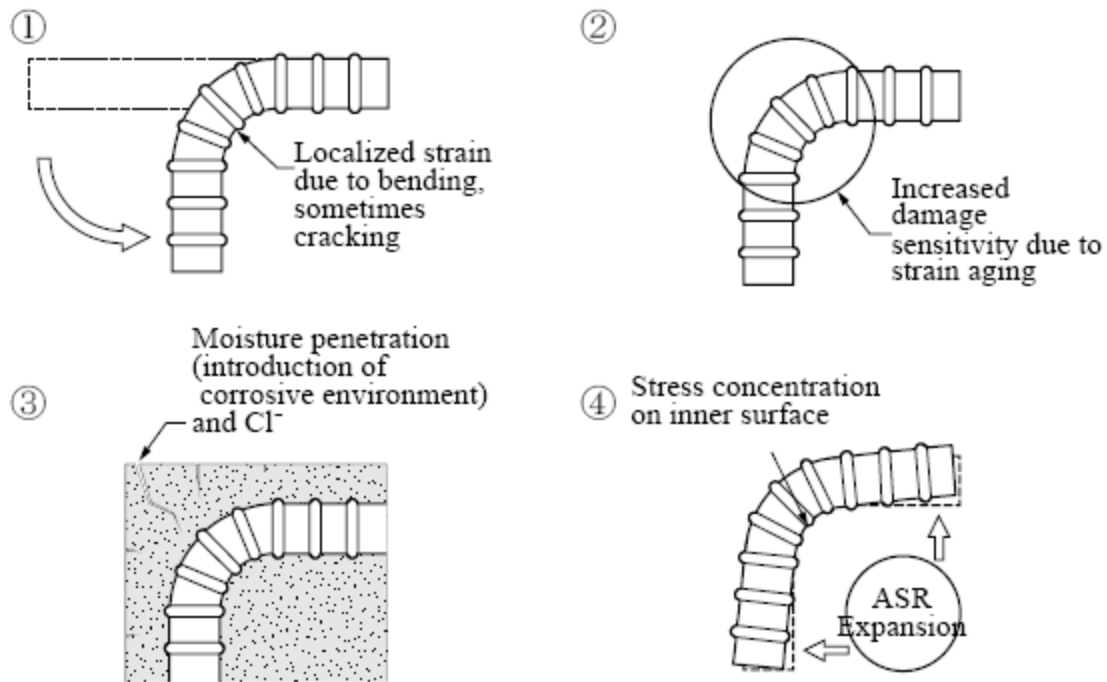


Figure 2.5 Presumed mechanism of damages to steel bars (Miyagawa 2006)

Inoue et al. (2008) studied the effect of rupture of shear reinforcement on shear capacity of reinforced concrete beams. It was found that rupture of the shear reinforcement has a larger influence on shear capacity of concrete than bond deterioration. However, the degree of reduction depends on the anchorage characteristics of the shear reinforcement in the ASR damaged reinforced concrete beams.

Mikata et al. (2008) also examined the effect of shear reinforcement fracture and deteriorated anchorage between concrete and steel bars on the capacity of prestressed concrete beams. The study showed that, for specimens with fractured anchorage and deteriorated bond strength, the truss mechanism provided by shear reinforcement cannot form, and a reduction in shear capacity was observed. These recent research results may change the common opinion that ASR deterioration of concrete structures is primarily a serviceability issue.

2.7 RESEARCH IN TEXAS

In late 1995, fifty six of sixty nine precast concrete box beams, which were fabricated in San Marcos, Texas, showed distress due to premature concrete deterioration. These distressed box beams motivated TxDOT starting to conduct research on premature concrete deterioration.

Boenig et al. (2002) conducted a field investigation to confirm and monitor existing cracks due to premature concrete deterioration and to examine crack widths and strength of the four distressed box beams described earlier. They developed a damage index to be used to predict the strength of the structural elements damaged by ASR and/or DEF. This method (damage index) was used by Bae et al. (2007) to examine the strength of ASR and/or DEF damaged High Mast Illumination Pole (HMIP) foundations in Houston area. Bae et al. concluded that the damage index can be used as qualitative method for severity of ASR and/or DEF deterioration but cannot be employed for estimating the reduction in capacity of ASR and/or DEF damaged shafts because the measured location, crack widths, and lengths are subjective. The HMIP tests showed no obvious loss in strength due to ASR and/or DEF damage. Another project on the strength of ASR and/or DEF damaged bent caps was described in 2.5.1.2.

TxDOT developed an ASR specification (initially as a TxDOT Special Provision to Item 421), which requires contractors to address ASR through performance or prescriptive requirements. Folliard et al. (2006) conducted comprehensive research in support of the new ASR specification. The report developed guidelines to prevent premature concrete deterioration and emphasized the benefits of prudent use of supplementary cementing materials (SCMs) to prevent concrete premature deterioration. A protocol of cause, extent, and future potential for damage due to ASR and/or DEF, which was introduced in section 2.3, was also developed (Folliard 2006).

To extend the service life of structures, mitigation countermeasures were also examined by Eskridge et al. (2005) and Burgher et al. (2008). Sealants were recommended for retarding ASR and/or DEF deterioration. However, sealants cannot

stop further ASR and/or DEF expansion. An example can be found on the repaired bent caps at US 183 and IH-35 interchange. The bent cap was sealed in 2006, but new damage was found by Deschenes et al. in 2008 (Figure 2.6). Although sealant slows down the progress of internal expansion, it fails to completely stop penetration of moisture. Since this area of knowledge is not directly related to the current study, no further discussion will be presented here but more detail can be found in Eskridge et al. (2005) and Burgher et al. (2008).

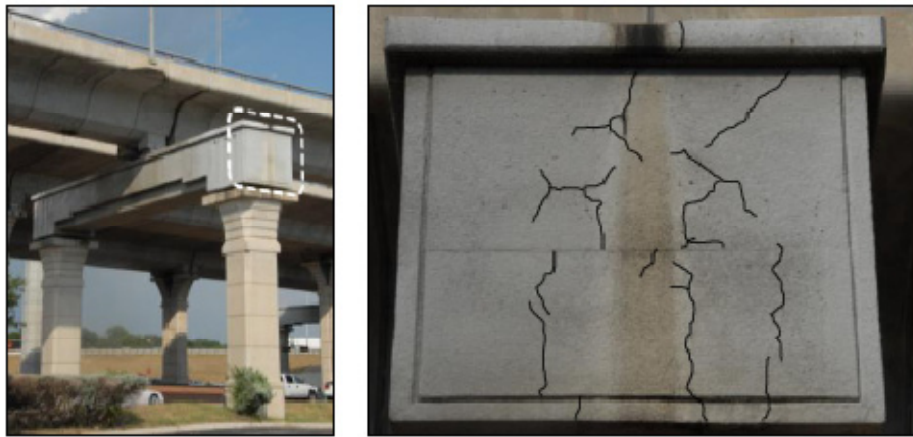


Figure 2.6 Expansion on the repaired bent caps at US 183 and IH-35 interchange, Austin, Texas (Deschenes et al. 2009)

2.8 SUMMARY

A brief literature review regarding alkali-silica reaction (ASR) and delayed ettringite formation (DEF) mechanisms and their effect on concrete was presented. While the chemical mechanisms of ASR and DEF are different, the physical manifestation on concrete structures is hard to distinguish. Internal expansion due to ASR and/or DEF can cause micro cracks in concrete. When these cracks appear on the surface of concrete, concrete shows map cracking or cracks that align according to the orientation of reinforcement restraining expansion.

For determining the cause and extent of ASR and/or DEF, both in-field work and laboratory work are important. Visual inspection is the first step to infer the cause and extent of distress of structures in the field. Visual inspection is not sufficient for

assessment of the cause and extent of ASR and/or DEF, but it is useful when associated with information collected from other tests. Petrographic evaluation is the most important method to determine ASR and/or DEF in the laboratory. This evaluation can identify the features of ASR and/or DEF but it has to be performed by trained and experienced petrographers.

Research about the effect of ASR and/or DEF on engineering properties of concrete was also reviewed. It was concluded that compressive strength and splitting tensile strength are not affected as much as direct tensile strength and elastic modulus. Expansion level is not the only indicator to evaluate the engineering properties affected by ASR and/or DEF, other factors, such as type of reactive aggregates and different mechanisms involved in the reaction also affect concrete engineering properties.

There is general agreement that the loss of flexural strength due to ASR and/or DEF is negligible. Shear strength of damaged concrete structures due to ASR and/or DEF is an area of more debate and study. Historically, most of the specimens affected by ASR and/or DEF for shear testing were small-scale and were placed in an artificial environment to accelerate the distress mechanism. The data are valuable but may not be representative of the real situation. Most in-service structures affected by ASR and/or DEF are large-scale and have been in service for several years, even several decades. To obtain the most representative data, full-scaling testing is required.

From recent studies, ASR and/or DEF damaged concrete structures with adequate shear reinforcement are safe as long as the shear reinforcement is intact. However, it was found in Japan that the safety may be reduced if the shear reinforcement fractures due to large expansion caused by ASR and/or DEF reactions.

For mitigating the ASR and/or DEF expansion of in-service structures, sealants were suggested to be used for preventing moisture penetration. However, this method has been shown to decelerate but not completely stop expansion. The use of supplementary cement materials (SCMs) was also strongly recommended for preventing ASR and/or DEF in new concrete structures.

CHAPTER 3

Test Specimens

3.1 OVERVIEW

Fifteen prestressed trapezoidal box beams were sent to Ferguson Structural Engineering Laboratory. In this chapter, background of these beams is first introduced. Then, general information is provided and visual inspection is conducted on the fifteen beams. Based on the results of visual inspection, five beams with various levels of cracking were selected for web shear test specimens. Cracking conditions and void floatation of the five specimens are described. In addition, material properties are also tested for the basis for evaluation of shear capacity of the specimens.

3.2 TEST SPECIMENS

3.2.1 Background

In 1995, prestressed trapezoidal box girders were fabricated by Traylor Brothers, Inc. for construction of the US59 corridor in Houston area. A number of beams were rejected for various reasons including void floatation, poor consolidation, and incorrect end skew. The rejected beams were not installed but stored in the contractor's precast yard. In September 2007, five of the rejected beams were cut into 3 pieces and sent to Ferguson Structural Engineering Laboratory (FSEL) at the University of Texas at Austin for examination of the damage and evaluation of the influence of ASR and/or DEF on the capacity of the beams. The basic information for the specimens and reason for rejection are summarized in Table 3.1. The beams were labeled according to the original nomenclature given by the contractor.

Table 3.1 Description of the test beams

Beam ID	Length (ft.)	Weight (ton)	Reason for Rejection
RF-3R-9	111.51	69.87	Floated void during concrete placement
RF-3R-12	111.22	69.71	Lack of consolidation
RF-1R-1	113.31	70.63	Concrete did not set in area of side and soffit
RF-2R-6	111.48	69.85	Floated void during concrete placement
MLL-9-34	101.66	65.52	Incorrect end skew

3.2.2 Delivery of Test Specimens

The original length and weight of the specimens ranged from 101 feet to 103 feet and 65 tons to 71 tons respectively (Table 3.1). Due to the limitation of the maximum lifting capacity of the crane in the laboratory (25 ton), each of the specimens was cut into three pieces in the precasting yard. After cutting, the specimens were shipped to UT on tractor-trailers (Figure 3.1(a)). Three segments from RF-3R-9 were unloaded in the laboratory (Figure 3.1(b)) for testing whereas the remaining twelve specimens were stored near the laboratory for future evaluation. A mobile crane was rented to lift the beams and place them near the laboratory (Figure 3.1(c)).

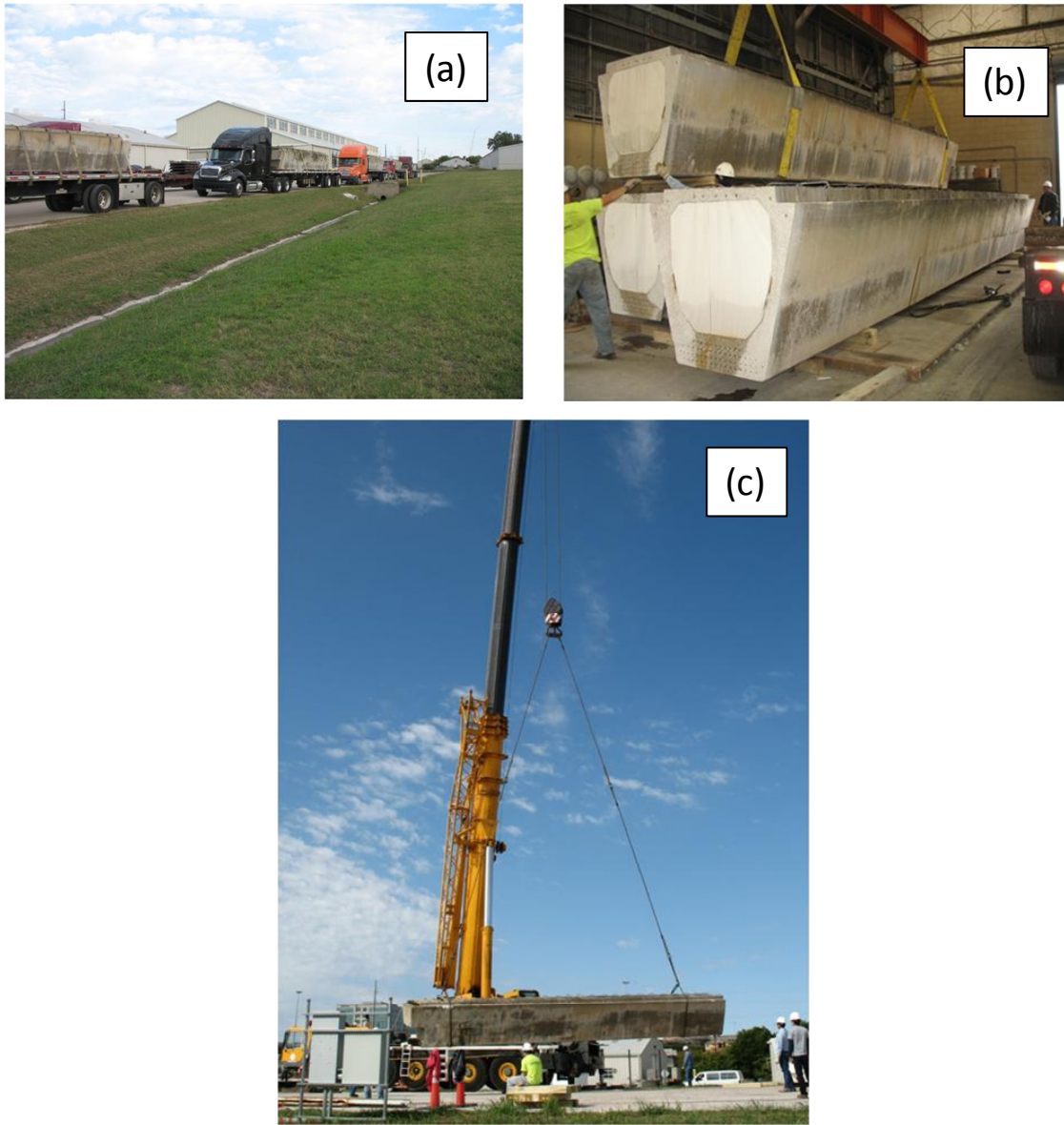


Figure 3.1 (a) Specimens on tractor-trailers arriving at laboratory (b) Three specimens stored in the laboratory (c) Rented mobile crane

3.2.3 General Information of Beams

The beams were designed for HS-20 loading in accordance with 1989 AASHTO standard specification. All reinforcement was specified as grade 60. All prestressing strands were low-relaxation 1/2-inch diameter, 270 ksi specified strength.

The casting date, concrete mixture, water-to-cement ratio (w/c), and concrete strength at critical points of manufacture of the five beams are presented in Table 3.2. In Table 3.3, details of prestressing steel are shown. Except for MLL-9-34, the beams were cast in the summer. MLL-9-34 was cast in late fall and had only minor cracking. The number of prestressing strands varies from beam to beam. Details of debonded tendons will be presented in 3.2.4. The details of mix design can be obtained in Appendix B.

Table 3.2 Concrete mixture and strength of the beams

Beam ID	Cast Date	Mix Design Number	w/c	Concrete Compressive Strengths			
				Release Req'd.	Release Actual	Design Req'd.	Design Actual
RF-3R-9	1995/7/6	392-3-95R	0.40	First Beam cast and rejected, No information available			
RF-3R-12	1995/7/8	392-3-95R	0.40	5810 psi	6340 psi @ 68.5 hrs	5810 psi	7550 psi @ 7 days
RF-1R-1	1995/7/26	392-3-95R	0.40	5989 psi	6620 psi @ 51 hrs	5989 psi	8320 psi @ 8 days
RF-2R-6	1995/7/28	392-3-95R	0.40	5413 psi	7050 psi @ 67 hrs	5811 psi	7080 psi @ 7 days
MLL-9-34	1995/11/9	392-12-95	0.29	5012 psi	5530 psi @ 23 hrs	5419 psi	8630 psi @ 7 days

Table 3.3 Basic information of the beams

Beam ID	Strand Count	Total Length (ft)	End Length (ft)	Weight per 3 piece (kip)	Note
RF-3R-9	62@1/2"	111.51	35.90	46.58	Dapped
RF-3R-12	62@1/2"	111.22	35.80	46.47	Dapped
RF-1R-1	64@1/2"	111.31	36.59	47.08	One Standard & dapped
RF-2R-6	56@1/2" +2 full debonded	101.81	35.89	46.56	Dapped
MLL-9-34	58@1/2"+2 full debonded	101.66	32.21	37.23	Skewed Dapped

3.2.3.1 Nomenclature

Since the beams were cut into segments, additional labeling is needed to represent each specimen. Three letters, A, B, and C are adopted with A and C indicating end segments and B indicating the center segment of each beam (Figure 3.2). Table 3.4 shows the names of the fifteen segments after labeling. Segments shaded are the test specimens in this study.

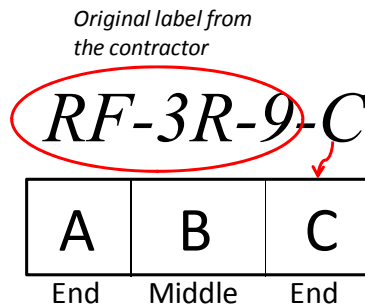


Figure 3.2 An example for specimen labeling

Table 3.4 Labeling of each segments

ID	Type	Reason For Rejection
RF-3R-9-A	Dap	Void Floated During Concrete Placement
RF-3R-9-B	Center	
RF-3R-9-C	Dap	
RF-3R-12-A	Dap	Lack of Consolidation
RF-3R-12-B	Center	
RF-3R-12-C	Dap	
RF-1R-1-A	Dap	Concrete did not set in area of side & soffit
RF-1R-1-B	Center	
RF-1R-1-C	Standard	
RF-2R-6-A	Dap	Void Floated During Concrete Placement
RF-2R-6-B	Center	
RF-2R-6-C	Dap	
MLL-9-34-A	Dap	Incorrect End Skew
MLL-9-34-B	Center	
MLL-9-34-C	Dap	

3.2.3.2 General Geometric Information

The cross section shown in Figure 3.3 and Table 3.5 was the same for all beams. However, the number of seven-wire 1/2 inch prestressing strands varied. The number of prestressing strands in the beams range from 58 to 64 with 22 to 24 debonded strands at each end. Details of the strands location is presented in Section 3.2.4 or Appendix A. Since the debonded prestressing strands result in a reduction in flexural capacity, flexure failure had to be avoided in the shear test. Therefore, a four inch thick deck was cast in the laboratory. Another advantage of the cast-in-place deck is that it provided a flat surface instead of a rough surface (Figure 3.4) for the loading plate. Details of the composite section with cast-in-place deck are provided in Figure 3.5 and Table 3.5. The deck raises the center of gravity and increases the weight of the beams over the allowable capacity (25 ton) of the crane in the laboratory. Hence, each beam had to be cut after testing was finished in order to move the segments with the laboratory crane.

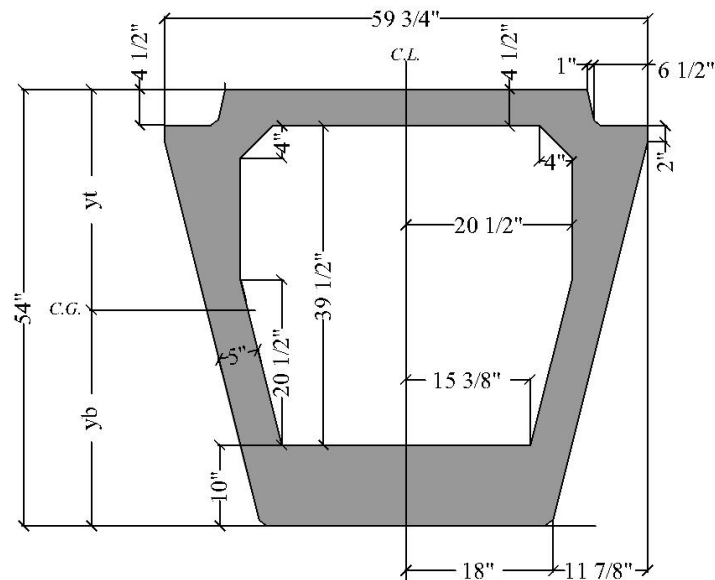


Figure 3.3 Non-composite beam cross section



Figure 3.4 Top surface of a non-composite beam

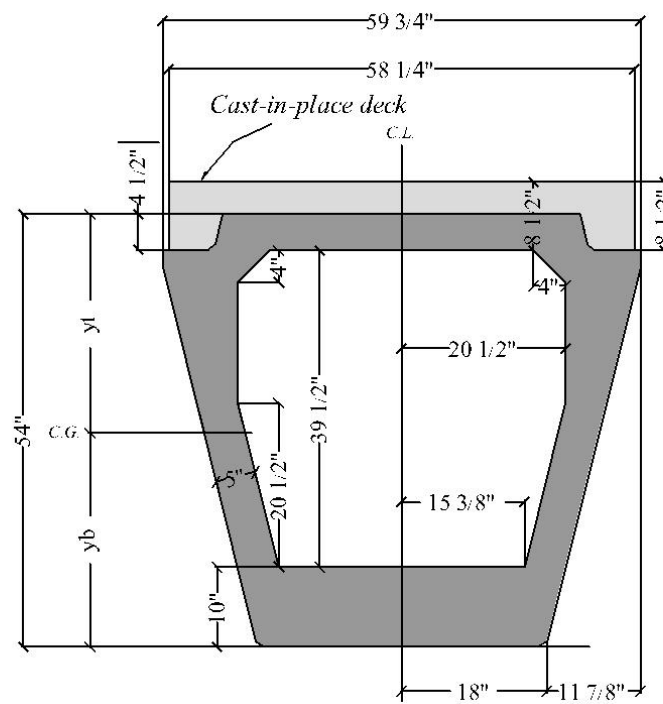


Figure 3.5 Composite beam cross section

Table 3.5 Beam geometric properties

Beam Properties		
Properties	Non-composite section (from construction documents)	Composite Section
y_b (in.)	26.71	32
y_t (in.)	27.29	26
Wt (lb/ft)	1154	1487
I (in ⁴)	404968	604241
Area (in ²)	1108	1428

3.2.3.3 Steel Layout

Generally arrangement of reinforcement is quite similar in all the beams. Dapped end blocks are not studied in this dissertation. Therefore end block reinforcement is presented in Appendix A. Stirrups were spaced at 5 inches from each end, the spacing was increased to 10 inches, and finally to 18 inches over the remaining length. Nine longitudinal compression bars were placed at the top flange. Reinforcement details can be seen in Appendix A.

3.2.3.4 Condition Survey

A visual inspection was conducted to evaluate the effect of ASR and/or DEF on the beams. The crack condition was observed to assess the level of damage of the beams. Except for MLL-9-34, map cracking and leaching were evident in the end regions of the beams.

Because the beams were cut into segments, the position of the void could be established. After inspection, it can be found that RF-3R-12-C had significant void movement that leads to significant difference between the web thickness (one is 3 inches and the other is 7 inches, see Figure 3.6(a)). Void in the box beams were created with plywood and Styrofoam. The plywood shown in Figure 3.6(b) was used to provide a reference plane for spacers to fix the void in the form. However, it can be seen that the plywood did not always fix the position of the Styrofoam, and the Styrofoam floated or

moved in the beam. Besides, the thickness (about 1/2 in.) of the plywood itself decreases the thickness of the web. Therefore, RF-3R-12-C was not selected to be tested.

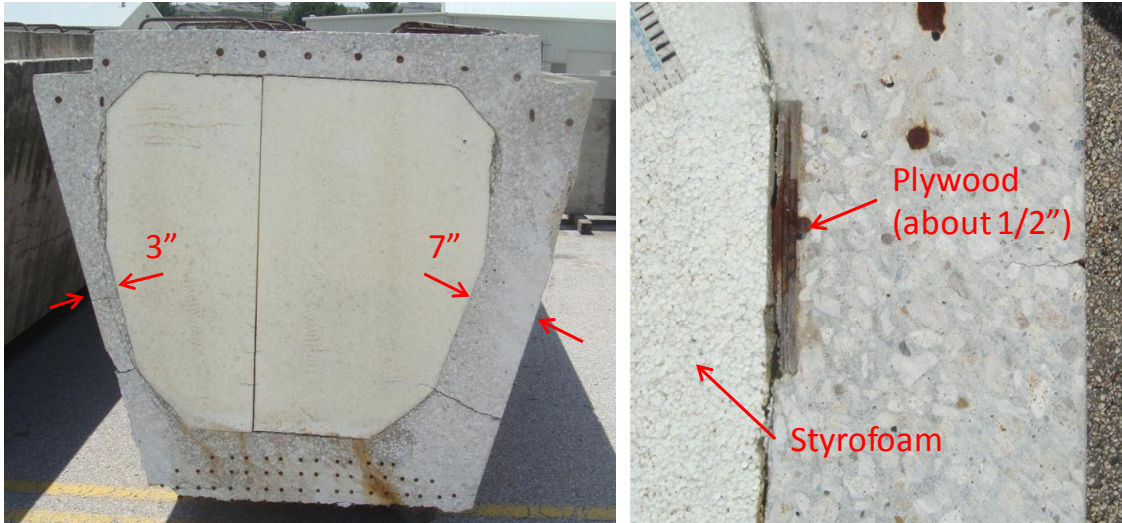


Figure 3.6 (a) Void floatation in RF-3R-12-C (b) Plywood

A longitudinal crack close to the location of the plywood can be found in most beams (Figure 3.7). Some longitudinal cracks extended through the length of the beams. The cause of the longitudinal crack may be attributed to a cold joint or expansion due to ASR and/or DEF. Generally, most cracks were concentrated at the end region. The only significant longitudinal cracking was found in or near the web portion.

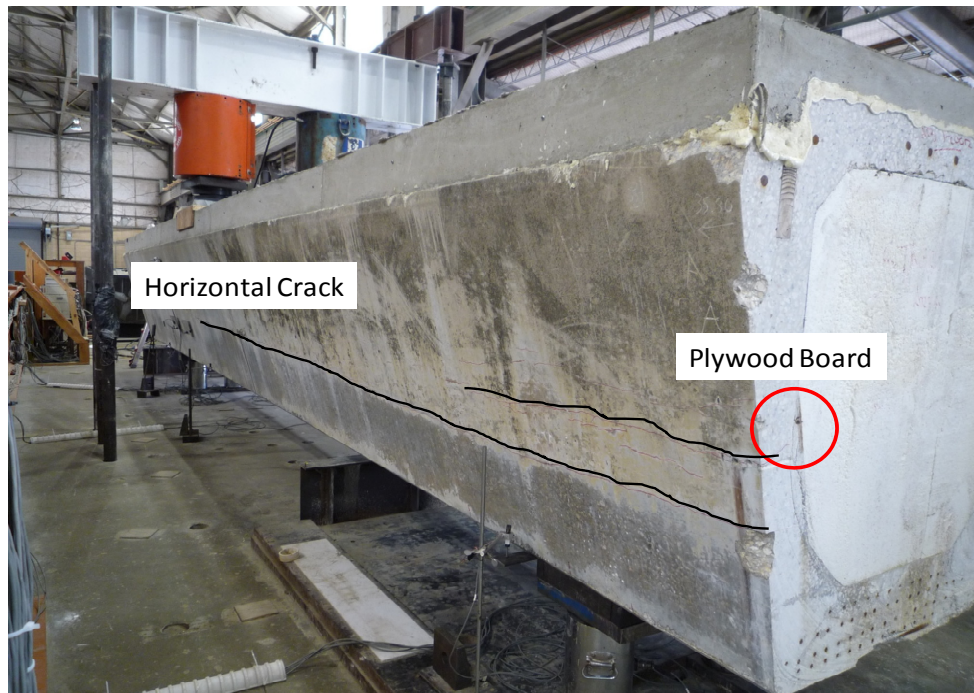


Figure 3.7 Longitudinal crack in the web portion

Cracking was defined based on visual inspection and was categorized into four levels: negligible, light, moderate, and heavy (Figure 3.8). Based on the cracking level, five beams in Table 3.6 were selected for web shear tests. These beams represent different levels of cracking and provide an opportunity to investigate the effect of ASR and/or DEF deteriorations on the shear capacity of the prestressed trapezoidal box beams. In addition, several beams were selected for forensic analysis only.

In Table 3.7, air temperature corresponding to the casting days is shown. The maximum air temperature was 100°F during the casting of the beam with heavy cracking (RF-1R-1) and was only 77°F during casting of the beam with the negligible cracking (MLL-9-34). The air temperature correlated well with the cracking levels determined by the visual inspection. DEF will occur when concrete curing temperature is greater than 158°F; for the beams cast in summer, the concrete temperature was likely to exceed the threshold value (158°F), causing more extensive cracking than the beam cast in late fall.



Figure 3.8 Cracking level (a) Negligible (b) Light (c) Moderate (d) Heavy

Table 3.6 Summary of condition survey

ID	Cracking Level	Void Floatation	Purpose			
			Shear Test		Petrographic Analysis	Elastic Rebound Test
			Dap	Web		
RF-3R-9-A	Moderate	Moderate	X	X		
RF-3R-9-B	Cold Joint Only					
RF-3R-9-C	Moderate	Light	X	X		
RF-3R-12-A	Light	None	X	X		
RF-3R-12-B	Longitudinal					
RF-3R-12-C	Heavy	Heavy				X
RF-1R-1-A	Heavy	Light	X		X	X
RF-1R-1-B	Longitudinal					
*RF-1R-1-C	Heavy	Light		X		
RF-2R-6-A	Moderate	Light			X	X
RF-2R-6-B	Cold Joint Only					
RF-2R-6-C	Light	None				
MLL-9-34-A	Negligible	None	X	X	X	X
MLL-9-34-B						
MLL-9-34-C	Negligible	None				
*RF-1R-1-C was also used for autopsy.						

Table 3.7 Air temperatures at cast

Beam ID	Cast Date	Max Temperature (°F)	Min Temperature (°F)
RF-3R-9	1995/7/6	93	82
RF-3R-12	1995/7/8	91	83
RF-1R-1	1995/7/26	100	90
RF-2R-6	1995/7/28	97	86
MLL-9-34	1995/11/9	77	64
From: www.wunderground.com			

3.2.4 Details of Test Specimens

Besides the general information included in 3.2.3, this section provides more specific information including debonding schedule, description of void floatation and crack patterns for the tested specimens.

Two types of shear tests – dapped end shear test and web shear test were conducted. This dissertation will deal only with the web shear tests. Therefore, only the details of specimens involved in the web shear test will be presented. For more information about dapped end tests, please refer to Larson (2010).

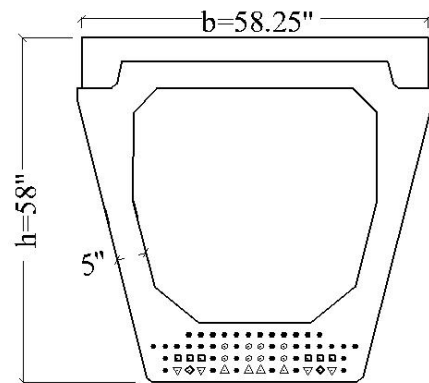
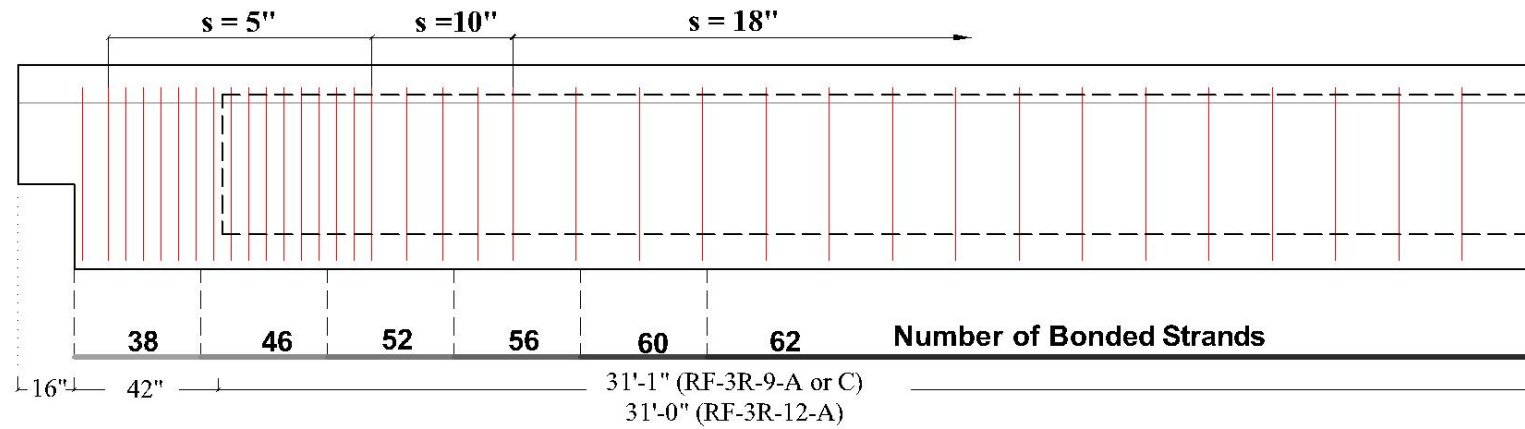
3.2.4.1 RF-3R-9-A

RF-3R-9-A had 62 prestressing strands, 38 were fully bonded strands. The strands were debonded in 3 ft increments. Strands with longer debonded length were located close to the side of beam. An elevation including transverse reinforcement and debonding schedule is shown in Figure 3.9.

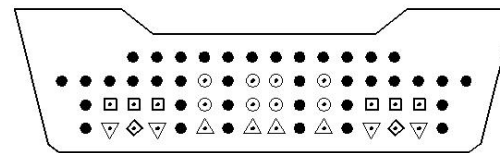
Moderate void floatation caused thickness of the web and top flange to vary from 4.5 in. to 6.325 in. and 3.5 in. to 4.325 in. respectively (Figure 3.10). Since void floatation changes over the length of the beam, precise web thickness cannot be determined with certainty. However, non-destructive tests showed that the sum of the two web thicknesses is generally 10 inches. The discrepancies between in the top flange became insignificant after the deck was cast in the laboratory.

A visual inspection revealed that the specimen had moderate cracking. Map cracking, which is a typical manifestation of ASR and/or DEF, was extensive in the end block region, where the curing temperatures were high. Width varied from hairline to 0.06 in. (Figure 3.11). Horizontal cracks in the hollow section appeared to form due to ASR and/or DEF expansions (Figure 3.12). The widest crack was observed close to the top of the beam near the end region. Diagonal cracks radiated from the bottom corner of the dapped end toward the mid-depth and gradually became horizontal along the length of the beam. Both sides of the beam showed similar damage. A dapped end shear test and a web shear test were conducted on this specimen.

Elevation (No Skew Dapped End)



Section Profile



Close-up of Strands

Debonding Schedule	
●	No Debonded
○	3'-0" FROM EA END
□	6'-0" FROM EA END
△	9'-0" FROM EA END
▽	12'-0" FROM EA END
◇	15'-0" FROM EA END

Debonding Schedule

Figure 3.9 Layout of transverse reinforcement and prestressing strands (RF-R-9-A&C and RF-3R-12-A)

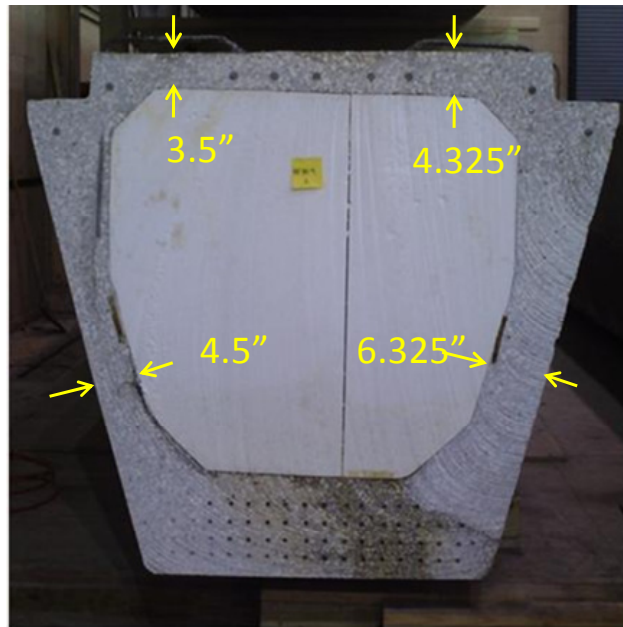


Figure 3.10 Web and top flange thickness

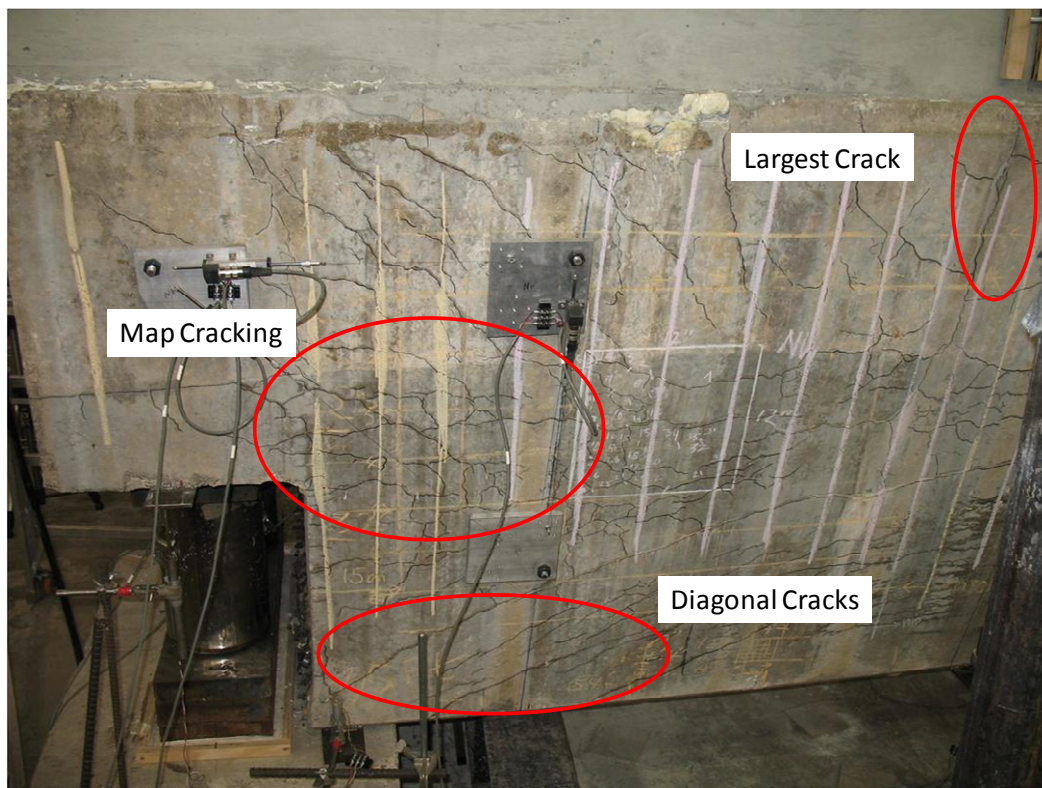


Figure 3.11 Moderately damaged end region of RF-3R-9-A

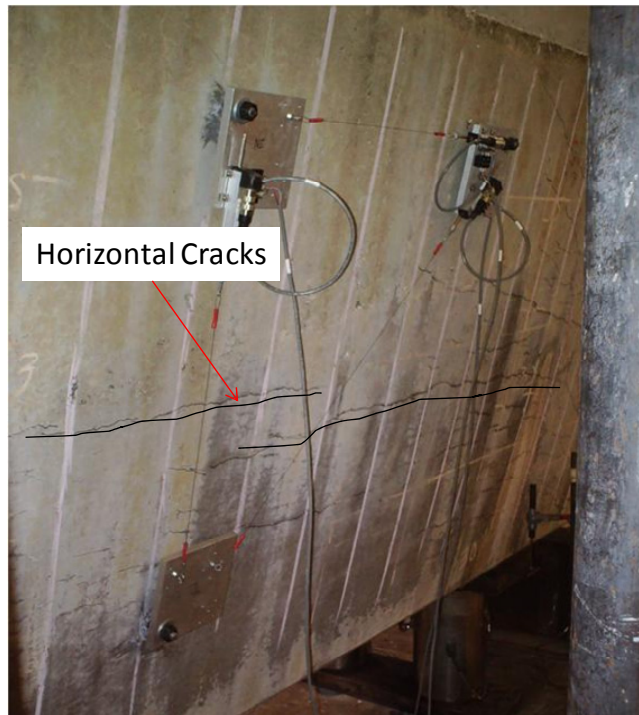


Figure 3.12 Horizontal cracks in the hollow section

3.2.4.2 RF-3R-9-C

RF-3R-9-C and RF-3R-9-A were from the same beam (RF-3R-9). Therefore the length, debonding schedule, and arrangement of transverse reinforcement were the same as RF-3R-9-A (Figure 3.9). From the observation on the cut surface, void floatation resulted top flange to vary only from 4.5 in. to 5.125 in. The thickness of both webs was 5 in. However, it should be noted that void movement may not be the same along the length of the beam (Figure 3.13).



Figure 3.13 RF-3R-9-C Top flange thickness

A visual inspection revealed that the specimen also had moderate cracking (Figure 3.14). Similar to RF-3R-9-A, map cracking was extensive in the end region and varied from hairline to 0.06 in. with horizontal cracks continuing into the hollow section. Diagonal cracks radiated from the bottom corner of the beam toward the mid-depth of the beam. The angle of the crack gradually became horizontal. Vertical cracks were also observed across the top of the beam. Both sides of the beams showed a similar crack pattern. A dapped end shear test and a web shear test were conducted on RF-3R-9-C.

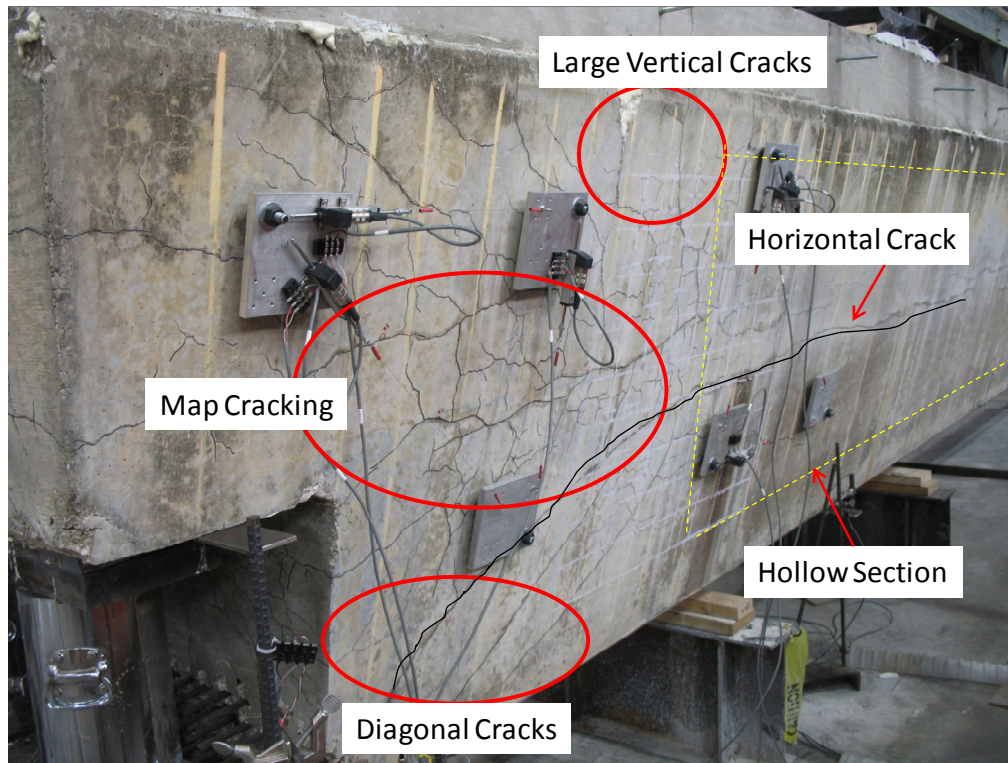


Figure 3.14 Moderately damaged end region of RF-3R-9-C

3.2.4.3 RF-3R-12-A

RF-3R-12-A had the same prestressing strand schedule as RF-3R-9 (Figure 3.9). Minor void floatation resulted in equal web thickness and constant top flange thickness. However, it should be noted that void floatation may vary along the length of the beam. RF-3R-12-C, which was cut from the other end of RF-3R-12, had void floatation that caused a 3 in. web thickness on one side and 7 in. on the other side (Figure 3.6(a)). A cut made after testing was completed also shows a large void floatation at the middle of specimen RF-3R-12-A (Figure 3.15).



Figure 3.15 Void floatation in RF-3R-12-A

From inspection of RF-3R-12-A, the cracking pattern was similar to the previous beams but noticeably less map cracking was observed in the end region and fewer diagonal cracks radiated from the bottom corner of the beam (Figure 3.16). The cracking level was determined as light. Poor consolidation of the concrete at the horizontal crack in the hollow section was observed. This poor consolidation at the construction joint may be due to insufficient vibration during construction. A horizontal crack propagated through the thin web section where plywood was used to position the Styrofoam. Poor consolidation during construction created a weak plane in the specimen (Figure 3.17), especially where the plywood holding the Styrofoam reduced the web thickness further. A dapped end shear test and a web shear test were conducted on RF-3R-12-A.

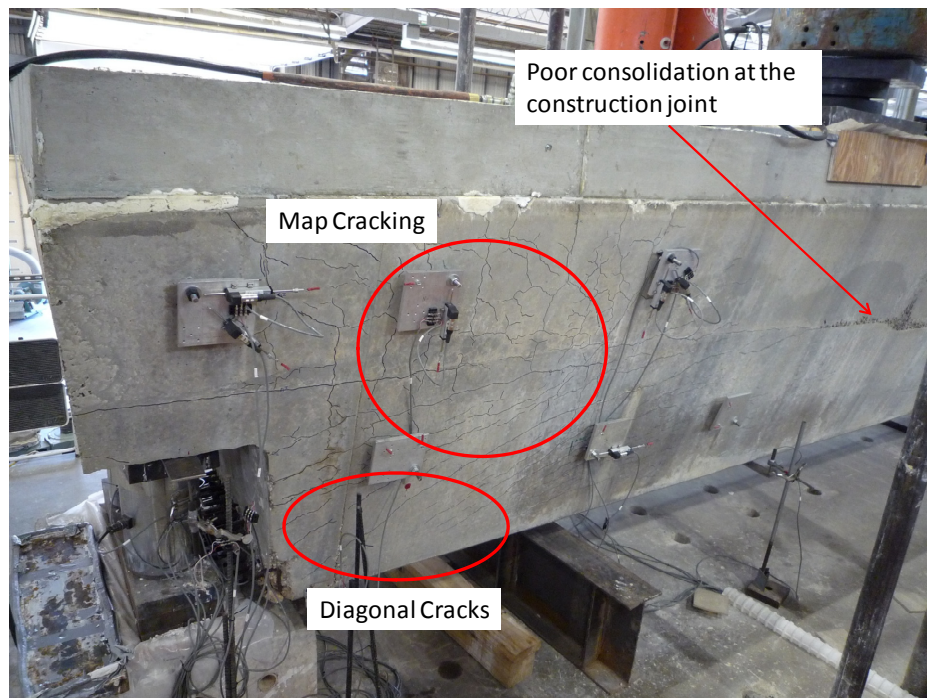


Figure 3.16 End region of RF-3R-12-A

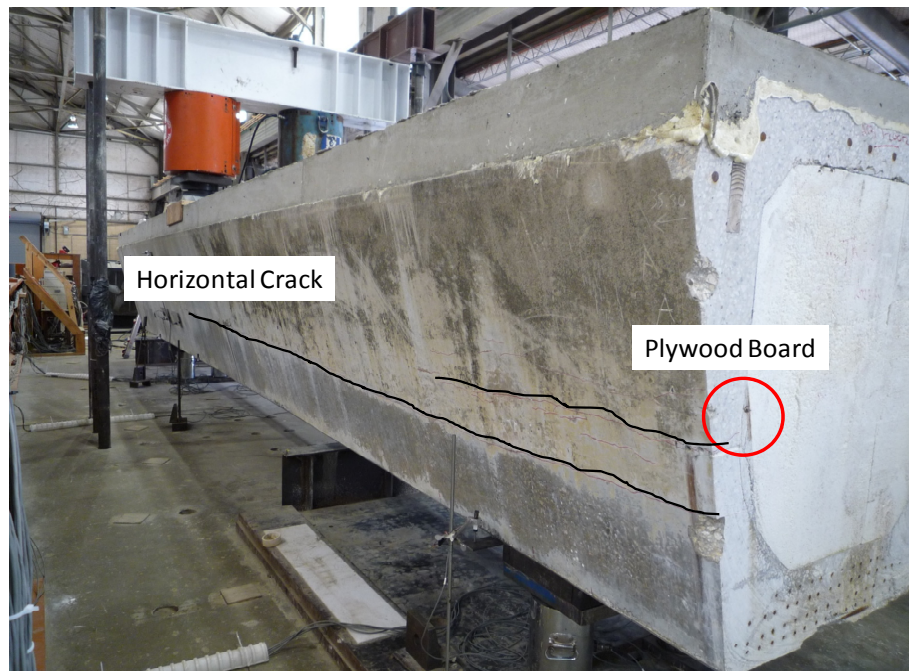


Figure 3.17 Horizontal crack propagating from plywood

3.2.4.4 MLL-9-34-A

Different from the previous three beams, MLL-9-34-A had a dapped end and an end skew of around 33 degree. MLL-9-34-A had 58 prestressing strands with 34 fully bonded. The arrangement of transverse reinforcement and the debonding schedule is presented in Figure 3.20.

From examination of the cut surface, little void floatation was found, and the thickness of web and top flange on each side was equal (Figure 3.18). The other end of the beam (MLL-9-34-C) also had a minimal void deviation. Thus, MLL-9-34-A may be assumed to have minimal void floatation.



Figure 3.18 Cut surface of MLL-9-34-A

A condition survey reveals that MLL-9-34-A had only negligible cracking (Figure 3.20). Minimal map cracking was concentrated in the east region, and only a couple of diagonal cracks radiated from the bottom corner of the beam on the east side. Minor horizontal cracks, observed in the previous specimens, were found at the mid-depth of the beam. Large vertical cracks were also observed (0.04 to 0.05 in.). However, due to minimal map cracking and significantly fewer diagonal cracks than all the previous specimens, MLL-9-34-A was taken as a control specimen (negligible cracking). Again, a dapped end shear test and a web shear test were conducted on this specimen.

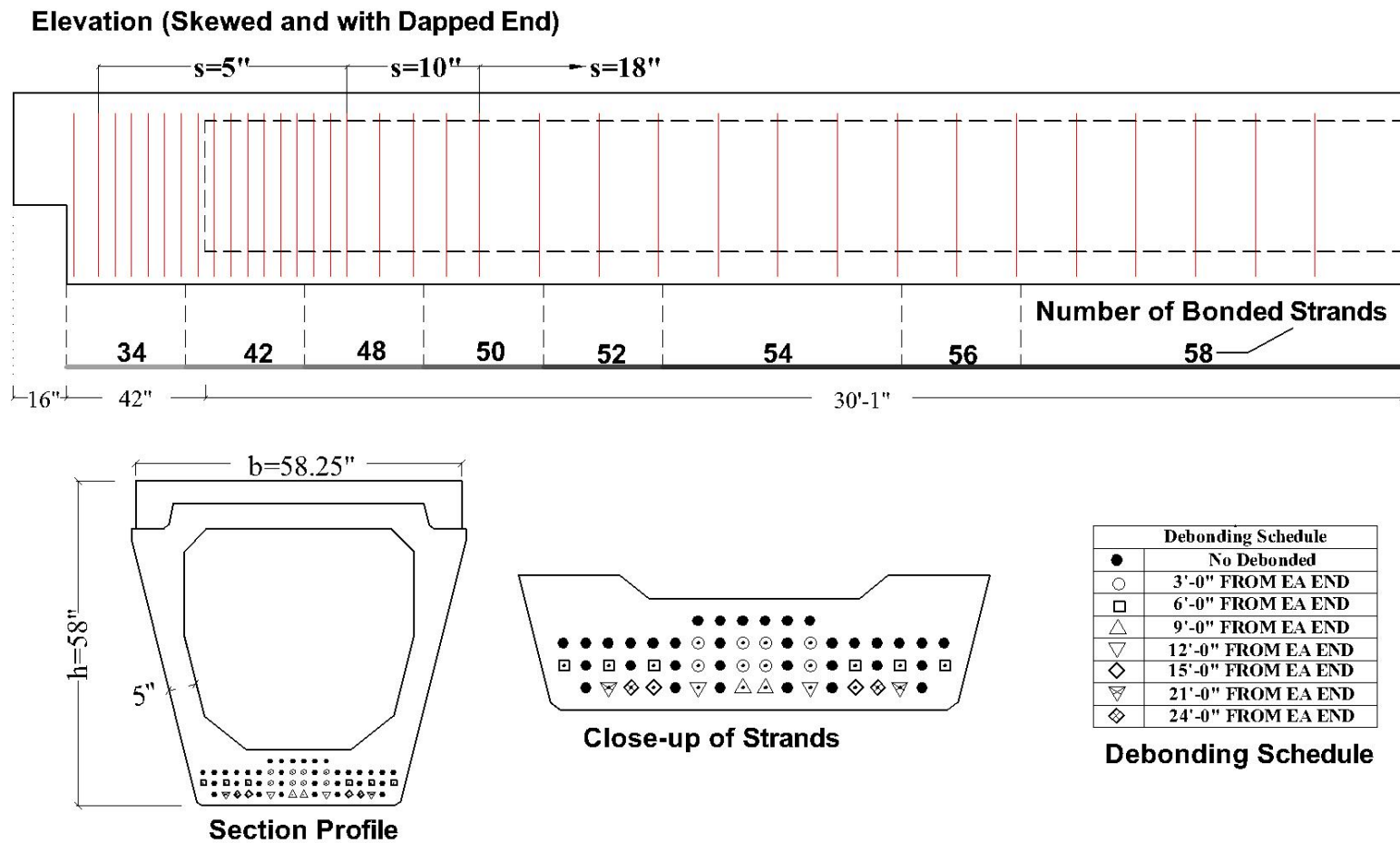


Figure 3.19 Layout of transverse reinforcement and prestressing strands (MLL-9-34-A)

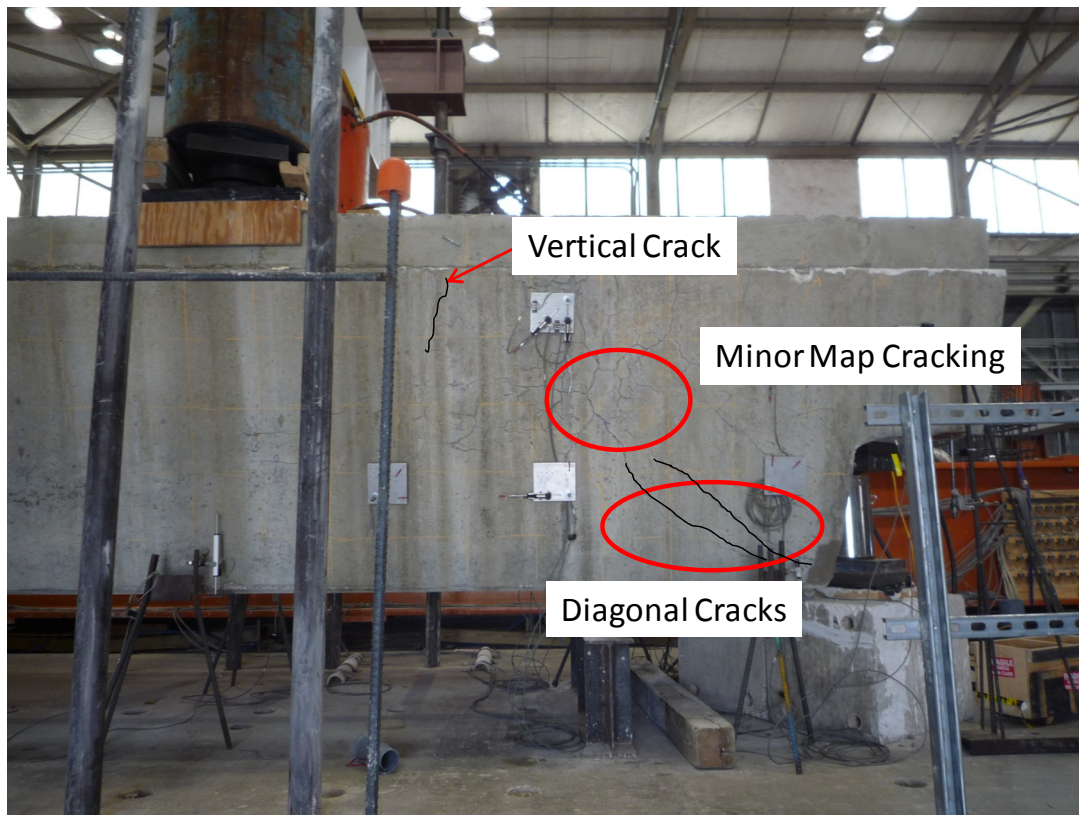


Figure 3.20 *Minor cracking condition on MLL-9-34-A*

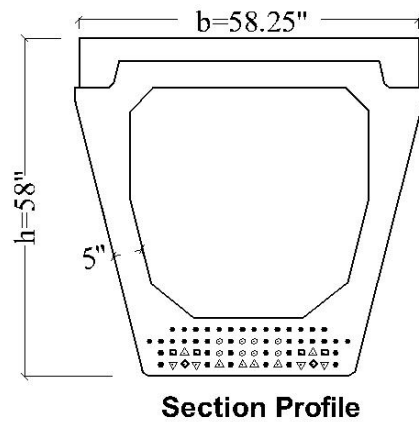
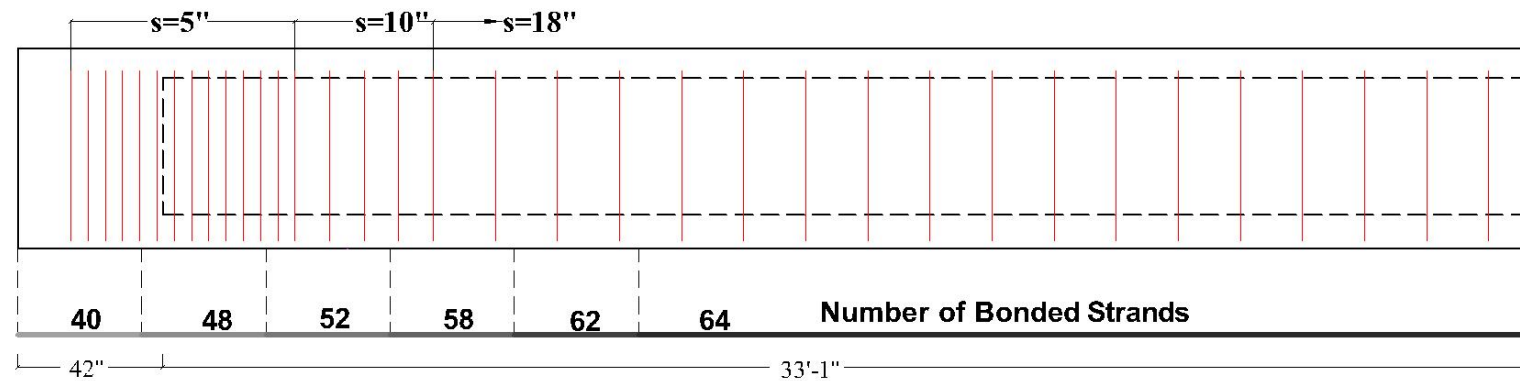
3.2.4.5 RF-1R-1-C

Unlike the previous specimens, RF-1R-1-C did not have a dapped end but a normal end block. The specimen had 64 prestressing strands, 40 fully bonded. The arrangement of transverse reinforcement and prestressing schedule is presented in Figure 3.21. Light void floatation resulted in web thickness varying from 4.5 in. to 5.5 in. (Figure 3.22). The thickness of the top flange was quite uniform.

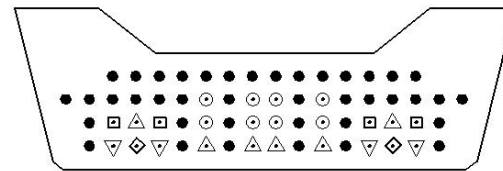
From a condition survey, RF-1R-1-C was categorized as a heavily cracked beam. Cracks on the damaged end block were coated with epoxy, and the end block was injected with epoxy before the specimen was moved into lab (Figure 3.23). The end block was later autopsied after all the shear tests were done. Therefore, no end shear test but only a shear test in the web portion was conducted. Numerous horizontal cracks with

widths up to 0.04 in. were observed in the test region (Figure 3.24). Because the testing region was away from the end block, no map cracking was observed in this portion.

Elevation (Normal End)



Section Profile



Close-up of Strands

Debonding Schedule	
●	No Debonded
○	3'-0" FROM EA END
□	6'-0" FROM EA END
△	9'-0" FROM EA END
▽	12'-0" FROM EA END
◇	15'-0" FROM EA END

Debonding Schedule

Figure 3.21 Layout of transverse reinforcement and prestressing strands (RF-1R-1-C)

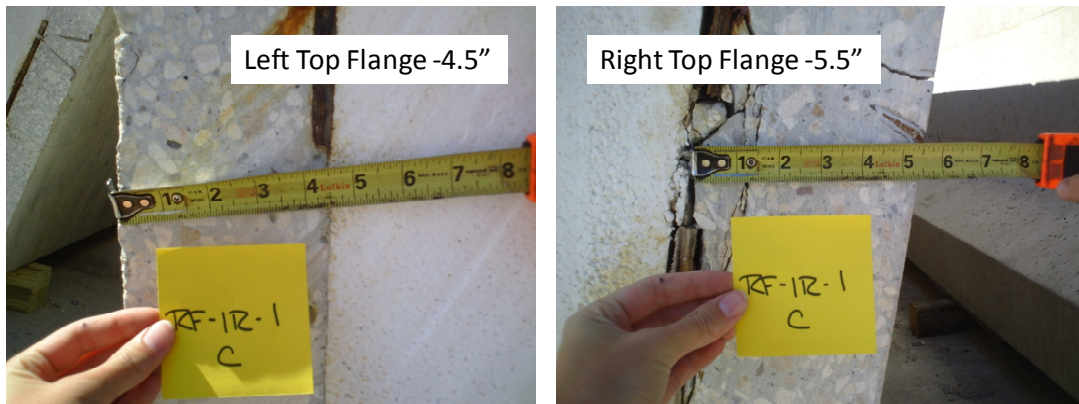


Figure 3.22 RF-1R-1-C web flange thickness

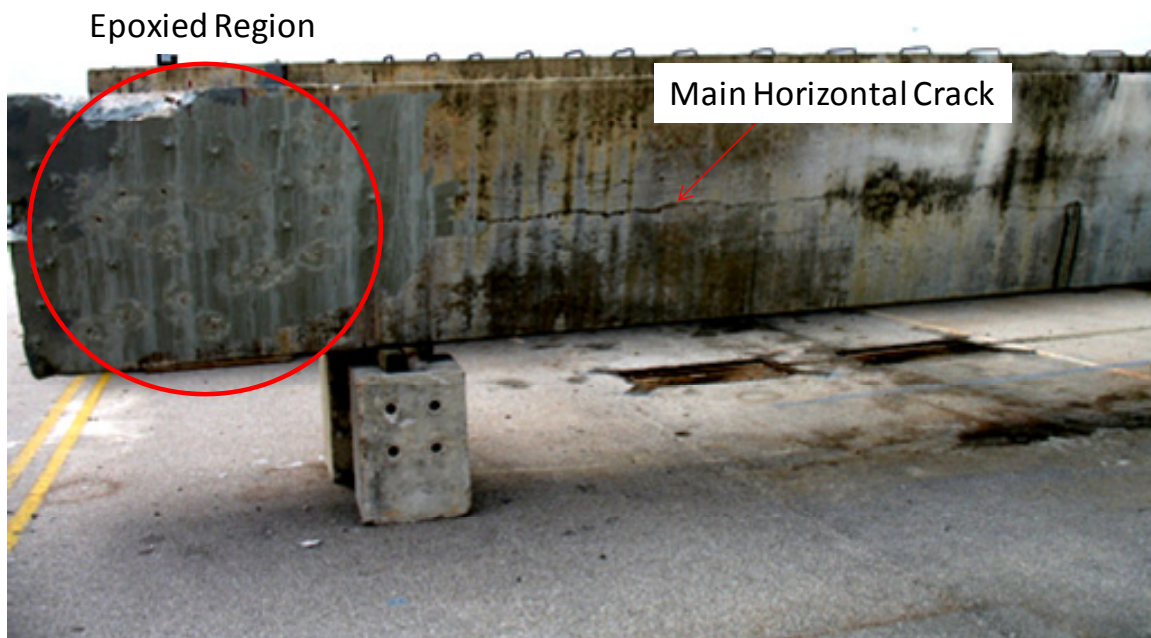


Figure 3.23 Epoxy coated in the end region of RF-1R-1C



Figure 3.24 Horizontal cracks in the testing region

3.3 MATERIAL PROPERTIES

3.3.1 Concrete Strength

3.3.1.1 Deck Strength

Four-inch diameter cylinders were cast with the deck to obtain the compressive strength of the deck. The cylinders were kept near the location of the beam and stripped at the same time as the formwork was removed. After each test, three to four cylinders were taken to be tested their compressive strength according to ASTM C39. The results are summarized in Table 3.8.

Table 3.8 Deck cylinder strength

	RF-3R-9-A	RF-3R-9-C	RF-3R-12-A	MLL-9-34-A	RF-1R-1C
Strength (ksi)	10.00*	6.99	9.05	8.43	7.95
*Strength of RF-3R-9-A was evaluated based on ACI 209					

3.3.1.2 *Beam Cores*

After finishing testing of each beam, the specimens were cored at the dapped ends and/or webs. The 3.75 in. diameter cores were tested in compression according to ASTM C42 in order to observe the impact of ASR and/or DEF deteriorations on concrete compressive strength. The core compressive strength provided an indication of in-situ concrete strength for calculating the shear capacity of the beam.

In order to maintain an aspect ratio of 1 to 2, the length of the extracted cores had to be greater than 7.5 inches. Any additional length was removed to obtain the desired aspect ratio. The dapped end of a beam is generally a heavily reinforced zone. Only the end face of the dapped end provides enough space between bars to extract a core with a desired dimension (Figure 3.25). The web portion is relatively unobstructed, but concrete damaged during the shear tests has to be avoided. Therefore, the cores extracted at webs were located on side face of the far end. All the cores were extracted from the end face of the dapped end or side face of the far end to represent concrete in ASR and/or DEF damaged zone and minor ASR and/or DEF damaged zone respectively. According to recommendation by ASTM C42, core tests having an average of 85 percent of the specific strength are realistic. It is not practical to expect core tests equivalent to specific strength since differences in size of specimens, conditions of curing, and procedures of extracting cores make equivalent values impossible. Furthermore, extraction removes the confinement of the cores and increases the micro cracks in the cores. Therefore the average of “original” core strength (f'_{core}) is divided by 0.85 to represent specific strength. This value ($f'_{core}/0.85$) will be used for evaluation of shear capacity of the beams in Chapter 6. The results of compression tests are summarized in Table 3.9. Seven-day required and measured strength are also included in the table for comparison purpose.

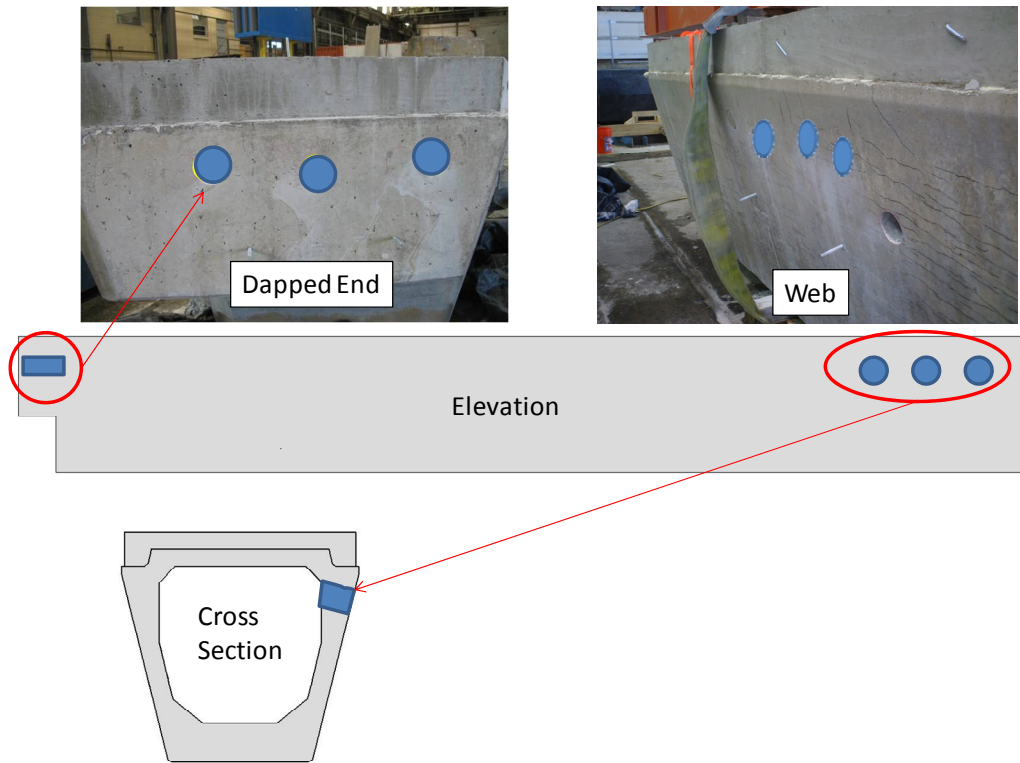


Figure 3.25 Core locations at dapped end and web

In the following discussion, core strength refers to $f'_{core}/0.85$. Comparing the core strengths among different levels of cracking, it can be found that there is not a distinct relationship between the web core strength and cracking level. However, dap core strength of RF-1R-1-A (heavily cracked) showed an apparently low strength compared to other beams with lower cracking levels. This reduction of compressive strength may be due to ASR and/or DEF deteriorations. No distinct relationship can be found between different locations. All core strengths are well above seven-day requirement. For beams with negligible to light cracks, core strengths increased about 17% compared to seven-day measured strengths except the core from the web of MLL-9-34. This relatively low strength may be due to preparation for the compression test. Seven-day required and measured strength are not available for RF-3R-9 (Table 3.2); however, it seems that similar requirements were applied to this beam. If the speculation is true, core strengths from RF-3R-9 A and C (Moderate cracking) seems to not have been affected by ASR

and/or DEF deteriorations. RF-3R-9-A and C were two ends of the same girder, but their core strength had a difference of 3.55 ksi. It was unexpected that they had such big difference since they were all from the same girder with moderate cracking. Therefore, to eliminate this difference, the core strength of RF-3R-9-A and C was averaged (10.07 ksi). For the beam with heavy cracking (RF-1R-1), the core strengths are less than seven-day measured strength by about 10%, indicating that extensive ASR and/or DEF cracks may reduce concrete compression strength. This observation also substantiates the classification of cracking level determined by visual inspection.

Although, the results of compression tests seem to give an indication of the level of ASR and/or DEF deterioration, core strength may be affected by procedures of extractions, cutting, or testing procedures; thus core strengths should not be taken as the only basis for evaluating the level of ASR and/or DEF deteriorations. Only load tests can provide a more accurate evaluation of the effect of ASR and /or DEF deteriorations on structural capacities.

Table 3.9 Summary of core strengths (ksi)

ID	MLL-9-34-A	RF-3R-12-A	RF-3R-9-A	RF-3R-9-C	RF-1R-1-A	RF-1R-1-C
Cracking Level	Negligible	Light	Moderate	Moderate	Heavy	Heavy
7-day Required	5.42	5.81	N/A	N/A	5.99	5.99
7-day Measured	8.63	7.55	N/A	N/A	8.32	8.32
Dapped End						
f'_{core}	7.89	8.15	10.06	7.05	5.44	N/A
$f'_{core}/0.85$	9.28	9.59	11.84	8.29	6.39	N/A
			Average=10.07 ksi			
Web						
f'_{core}	6.43	8.93	N/A	N/A	6.21	6.24
$f'_{core}/0.85$	7.56	10.51	N/A	N/A	7.31	7.34

3.3.2 Reinforcing Bars

Two #4 and one #6 reinforcing bars were removed from the solid end block of beam RF-1R-1-A to determine steel properties (Figure 3.26). Although RF-1R-1A was not tested in shear, the steel properties shall reflect those of the other beams. The measured steel properties provide a means of determining whether the steel met ASTM requirements, and provide values for assessing capacity of the beams. The steel stress-strain relationship is shown in Figure 3.27. From the test results (Table 3.10), it can be found that yield strength of the #4 bars was higher than nominal yield strength (60 ksi); therefore, it is conservative to use 60 ksi as design yield stress of the tie for transverse reinforcement in the beams. The actual yield strength (average = 69ksi) will be also used for comparison.

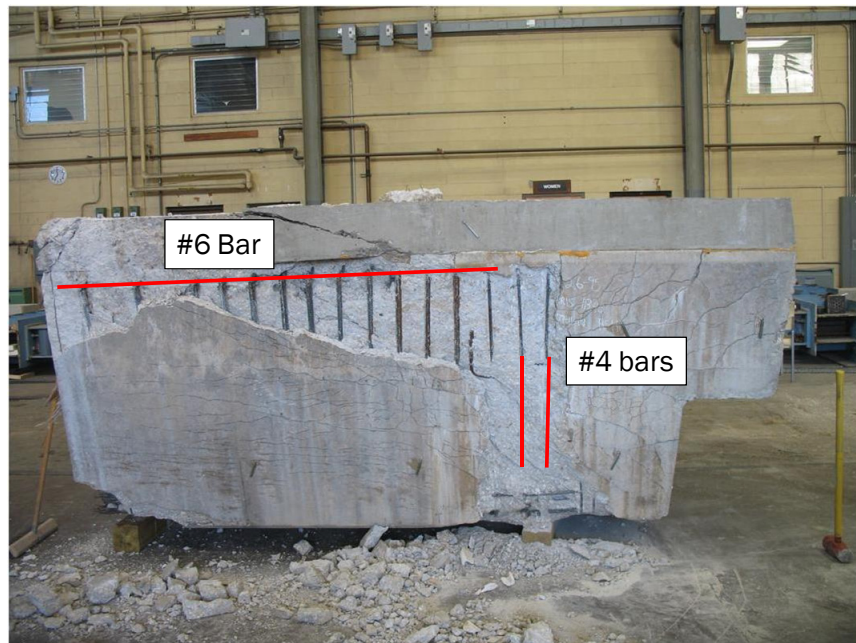


Figure 3.26 Reinforcement locations

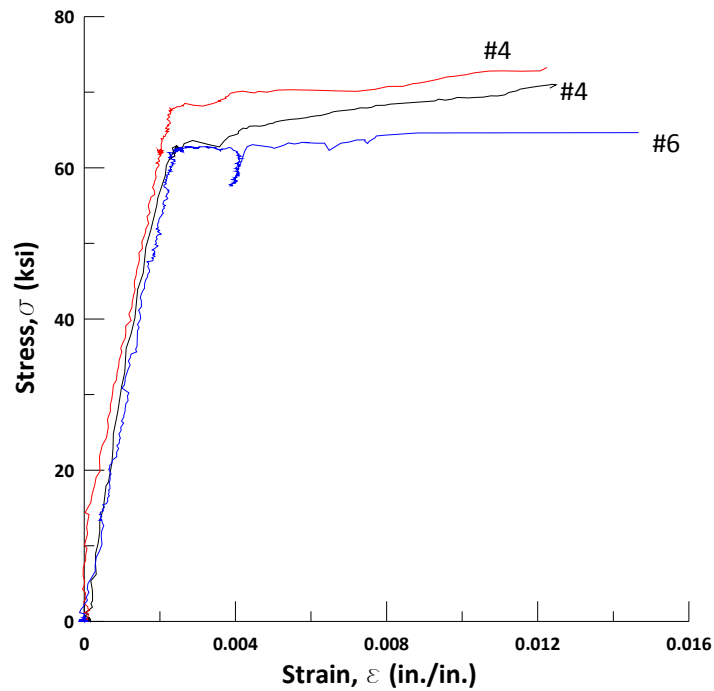


Figure 3.27 Stress-strain relationship of tested bars

Table 3.10 Steel stresses at critical points

	#4	#4	#6
■ @ Plateau	68	70	63
■ @ Fracture	96	96	104

3.4 SUMMARY

In this chapter, a general visual inspection was conducted on the fifteen beams with various levels of ASR and/or DEF deteriorations. According to their cracking conditions, they were categorized into four cracking levels: negligible, light, moderate, and heavy. Five of them were selected to be tested in shear to evaluate the shear capacity of beams with various levels of ASR and/or DEF deteriorations. Details, void floatation, and cracking patterns of these five beams were described. Besides, concrete strengths of the beams with different cracking levels and different locations (dapped end and web portion) were tested. Core strengths seem to reflect the cracking levels determined by

visual inspection. Long term compressive strength was reduced by ASR and/or DEF deteriorations. However, no distinct relationship is observed between the dapped end and the web portion. Steel properties were also tested in one beam (RF-1R-1-A). These material properties provide a basis for future evaluation of shear capacity of the test specimens in Chapter 6.

CHAPTER 4

Experimental Program

4.1 DECK CASTING

It was important to produce shear failure of the specimens. To achieve this goal, a 4-inch deck slab was added to the top of the beam. The additional deck slab has two advantages: (1) Increasing flexural capacity of the specimens, and (2) Providing a flat and even surface for load bearing plates.

Forms were fabricated so that the cast-in-place deck thickness was 4 inches above the top flange of the beam (Figure 3.5). The actual thickness of the deck of each specimen varied along the length of the beam depending on void floatation. Threaded rods were used to hold the forms in place. Since the deck thickness was 4 inches, only one layer of reinforcement was consisting of #4 bars spaced at 6 in. transversely and #5 bars spaced at 9 in. longitudinally was used (Figure 4.1).

The deck was cast with a concrete strength of 10 ksi. High strength concrete was used to permit testing the beam as soon as possible. The top of the beam was wetted before casting to prevent water in the fresh concrete from being absorbed by the beam. A screed was used to level the surface, and trowels were used to finish the surface near the load point (Figure 4.2).

The void floatation in beam RF-3R-9-C raised the longitudinal and shear transfer bars, resulting in several shear transfer bars extending above the formwork for the cast-in-place slab. Therefore, the shear transfer bars were cut and some of the original concrete in the flange had to be removed to provide at least two inches of cast-in-place deck above the top flange.



Figure 4.1 Formwork ready for concrete placement



Figure 4.2 Casting of beam RF-3R-9-C (Bindrich, 2009)

4.2 TEST SET-UP

The test set-up was designed for testing of large-scale specimens. Load was provided by two 2000-kip hydraulic rams. A 12-inch diameter spherical head connected to the bottom of the ram reacted against a steel plate grouted to the top of the beam so that a uniform bearing stress was produced. The rams reacted against a transverse steel spreader beam, which was held in place by longitudinal steel hold-down beams at each end. Each hold-down beam was anchored to the strong floor by three 3.5 inch diameter threaded rods (Figure 4.3).

All beams, except for RF-1R-1-A and RF-1R-1-C, were tested twice: first, to investigate the shear performance of the dapped end, and second, to investigate the shear performance of the web portion. After finishing the dapped end test, the beam was moved in the load frame in order to conduct the web shear test of the beam (Figure 4.4) at the selected shear span-to-depth ratio (a/d). For a beam subjected to point loading, the shear span (a) is defined as the distance between the support and the load point. All web shear tests had a shear span of about 99 inches. The effective depth (d), which is defined as the distance between the extreme compression fiber and the centroid of prestressing strands, is about 53.5 inches. Therefore shear span to depth ratio (a/d) of all the beams in web shear tests is 1.85. A beam shown in Figure 4.5 is in the test position. Only the web shear tests are discussed herein. Details of testing set-up of the web shear test are presented in Table 4.1.

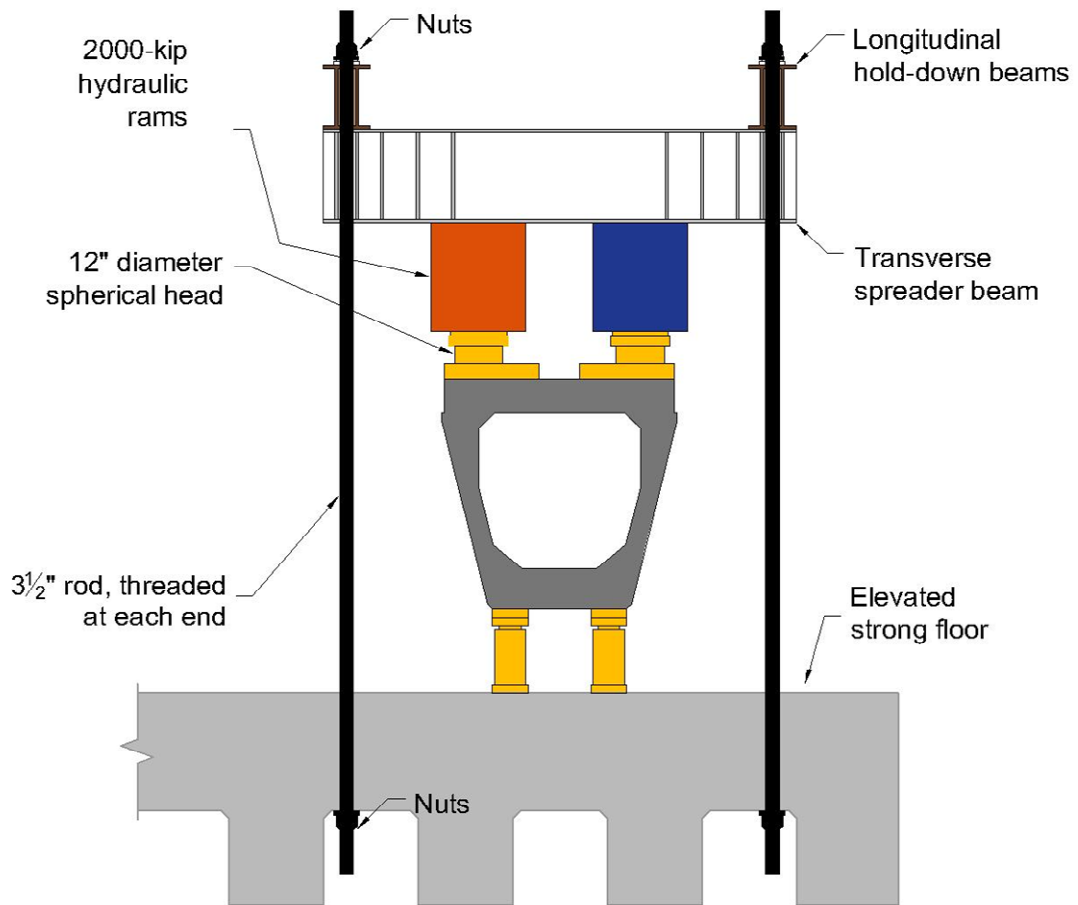
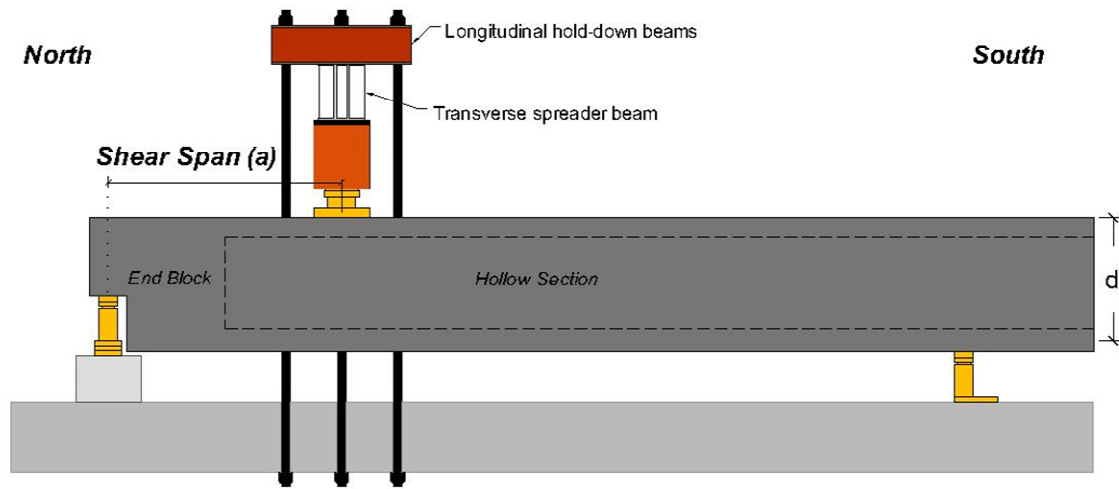
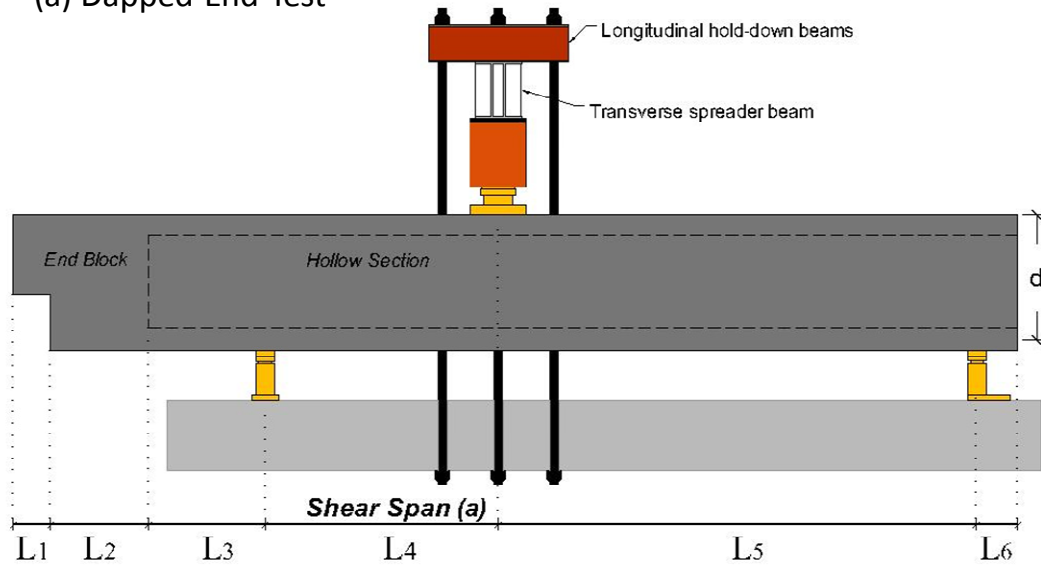


Figure 4.3 End view of test setup



(a) Dapped End Test



(b) Web Shear Test

Figure 4.4 Side view o test set-up (a) Dapped end test (b) Web shear test

Table 4.1 Detail setup of the web shear test

ID	L ₁ (in.)	L ₂ (in.)	L ₃ (in.)	L ₄ (in.)	L ₅ (in.)	L ₆ (in.)
RF-3R-9-A	16	42	0	99	249	24
RF-3R-9-C	16	42	57	99	198	18
RF-3R-12-A	16	42	42	99	201	71
MLL-9-34-A	16	42	42	99	137	83
RF-1R-1-C	0	42	28	99	224	47

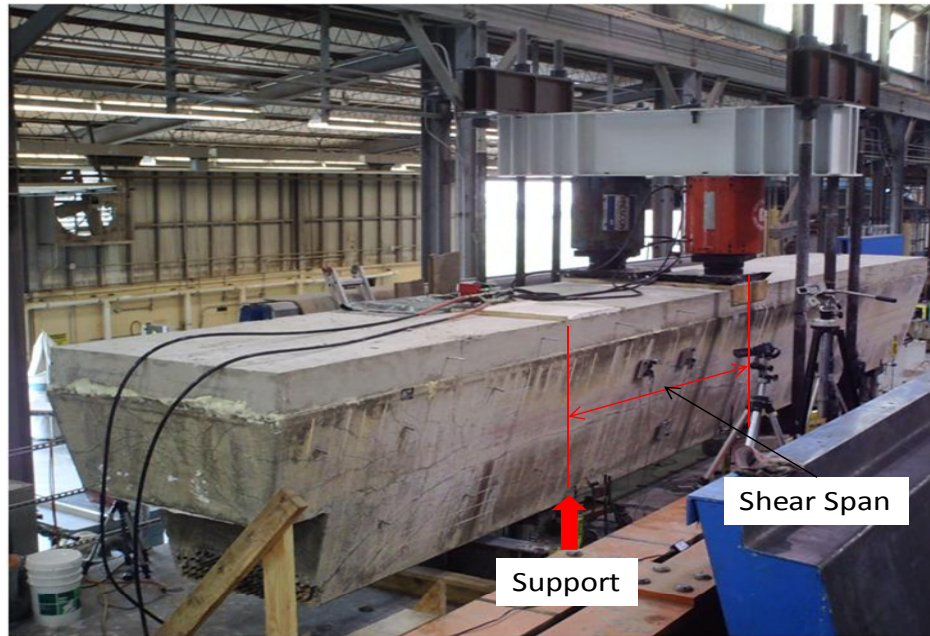


Figure 4.5 Beam ready for testing

4.3 INSTRUMENTATION

4.3.1 Load Cells and Bearing Plates

Four load cells were used to monitor the support reactions during the test. A 32"x9" steel plate was used to support the north end of the beam and two 16"x9" steel plates were used at the south end. The long direction of the steel plate at the north end was perpendicular to the length of the beam, whereas the long side of the steel plates at the south end was parallel to the length of the beam (Figure 4.6). The 2-inch steel plates on the top of the load cells contained corresponding 7-inch diameter inset counter bored 3/8 in. into the plates to fit the slightly convex surface on the top of the load cells (Figure 4.7). A 2.5-inch thick, 5-layer laminated elastomeric bearing pad, which has the same dimension as the corresponding steel plate, was used to distribute bearing stresses over the contact surface.

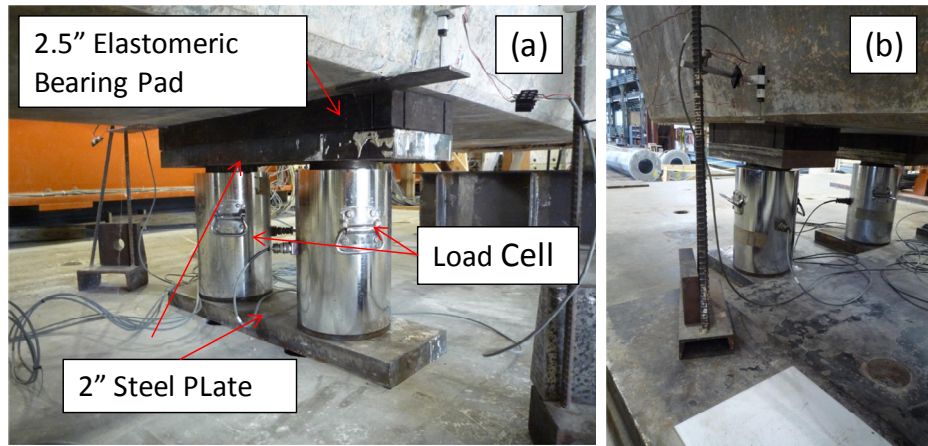


Figure 4.6 Support at the end (a) North (b) South

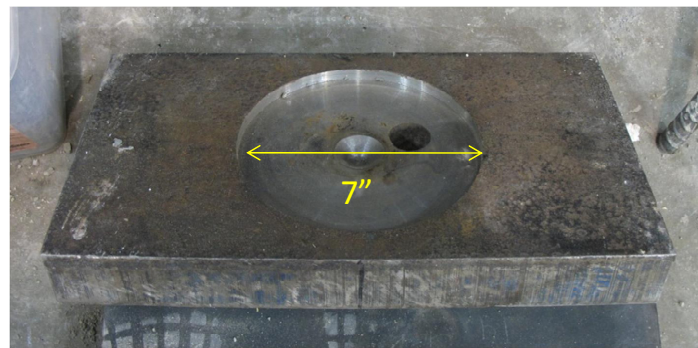


Figure 4.7 Seven inch diameter inset counter bored into the top steel plate

4.3.2 Linear Potentiometers

Linear potentiometers were used to measure deflections and crack opening during testing. Deflections were measured at three different locations – at the supports and at the load point. The potentiometers rested on steel plates glued to the bottom of the beam to protect the linear potentiometer from spalling concrete (Figure 4.8(a)).

Linear potentiometers were also used to measure the crack opening on the concrete surface during testing and to determine shear deformation. Three linear potentiometers were attached to aluminum plates arranged to form a 45-degree right triangle with a leg length around 2 ft. To attach the aluminum plates to the beam, three 1/2-inch holes were drilled into the concrete. One-half inch threaded rods were then set into the holes using epoxy. The plates were positioned on the surface so that the

transducers were in a plane parallel to the surface of the beam. Then piano wire was attached to the plates and the linear potentiometers to form a 45-degree triangle. The complete assembly is shown in Figure 4.8(b). Using this method, relative movements between any two rods was captured, and crack opening across vertical, horizontal or diagonal wires could be measured by the linear potentiometers. The same setup was attached to each side of the beam.

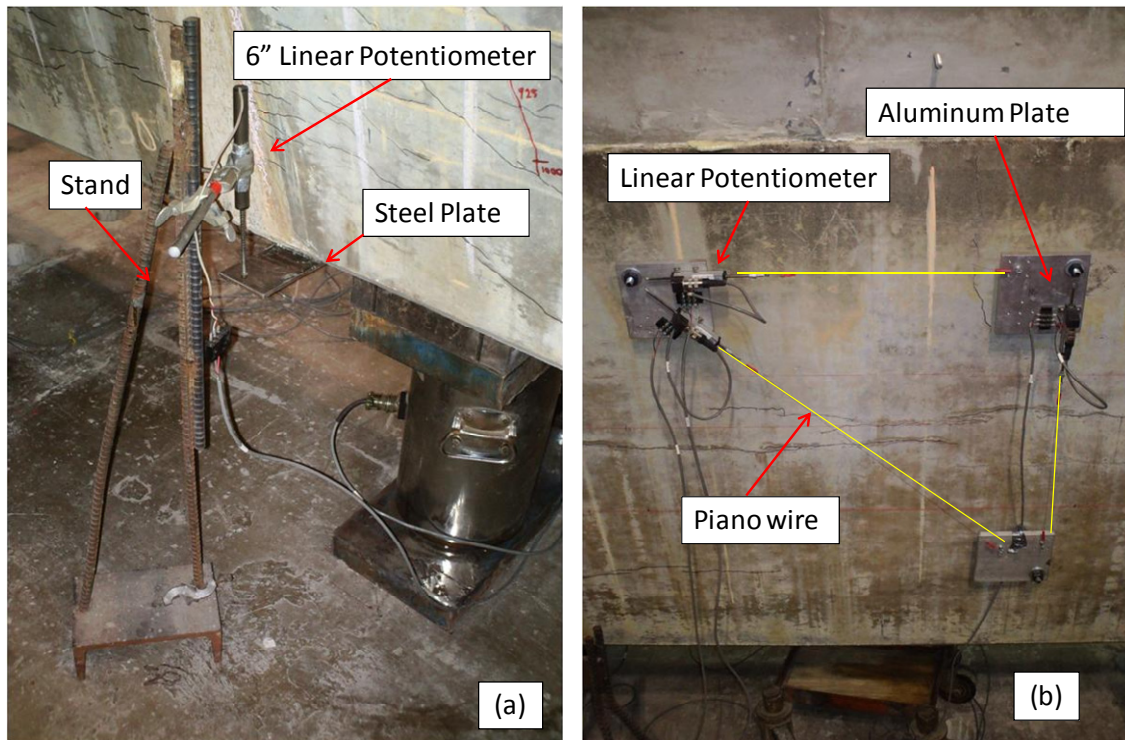


Figure 4.8 Linear potentiometer (a) At support (b) At surface of the beam

4.4 TEST

Existing cracks due to ASR and/or DEF were marked before the shear test commenced. Photos and videos were taken for a record of the test. Each beam was monotonically loaded to failure in increments of 50 to 100 kips at the initial stage of the test and 25 to 50 kips after the first shear cracks appeared in order to observe crack propagation and record critical load. Width of selected cracks was measured and any recorded.

4.5 SUMMARY

In this chapter, details of the web shear test were presented. Procedures of constructing cast-in-place deck were first described. Then, details of testing setup were shown. Set-up of load cells and linear potentiometers were also mentioned. Test results are detailed in Chapter 5.

CHAPTER 5

Experimental Results

5.1 OVERVIEW

The results of web shear tests will be presented in terms of ultimate shear capacity and load-deformation (deflection and strain) response. The results will be compared to assess the impact of ASR and/or DEF cracking on prestressed trapezoidal box beams.

5.2 RESULTS OF WEB SHEAR TEST

Before presenting the test results, the shear load and deflection need to be defined. The shear reported includes the beam self weight, testing frame weight, and the load applied by hydraulic rams. The self weight of the beam and load imposed by the testing frame were not measured by the load cells but can be computed and added to the applied load. Figure 5.1 shows that a beam test can be simulated as a simply supported beam subjected to distributed loads (self weight) and two concentrated loads (weight of testing frame and applied load). The critical section was defined at the center of the test region (shear span) that was 99 in. long for all tests. Dimensions of each beam are summarized in Table 5.1. The ultimate test shear (V_{test}) reported is defined as the combination of the shear contributed from self weight, testing frame, and applied load. Dead load deformation was estimated by adjusting the curve to a zero origin.

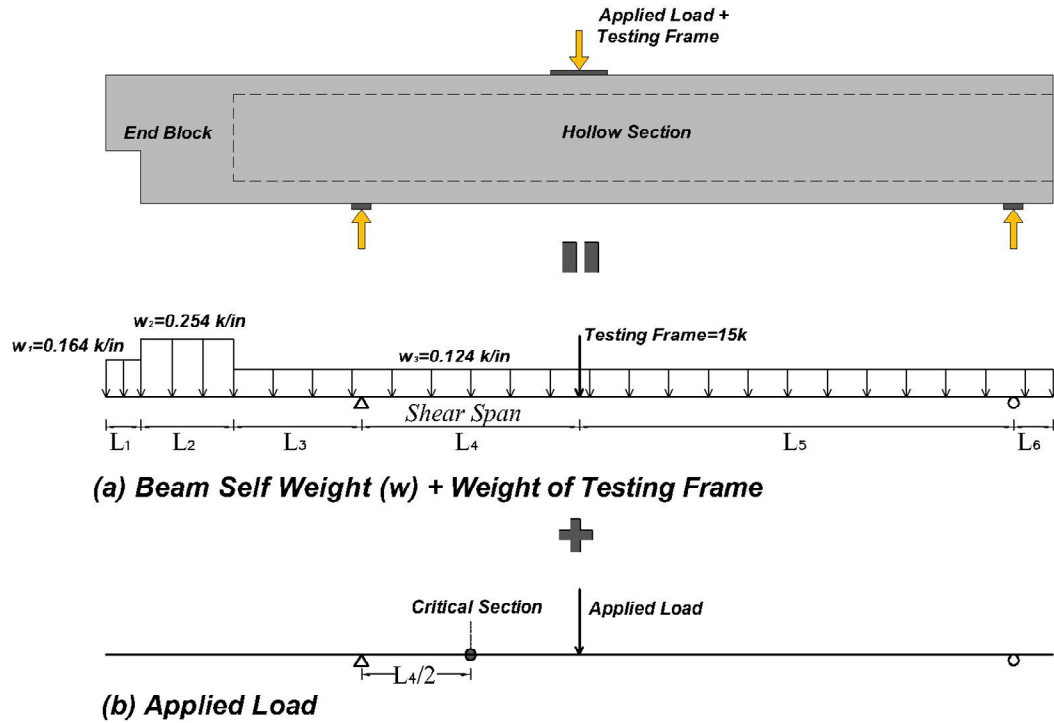


Figure 5.1 Simulation of a beam test

Table 5.1 Dimensions of beam set-up

	L_1 (in.)	L_2 (in.)	L_3 (in.)	L_4 (in.)	L_5 (in.)	L_6 (in.)
RF-3R-9-A	16	42	0	99	249	24
RF-3R-9-C	16	42	57	99	198	18
RF-3R-12-A	16	42	42	99	201	71
MLL-9-34-A	16	42	42	99	137	83
RF-1R-1-C	0	42	28	99	224	47

Deflection under the load point relative to supports (Δ_{BEAM}) was obtained by taking the average of the deflections measured by two linear potentiometers under the load point and subtracting the rigid body motion of the beam (Figure 5.2).

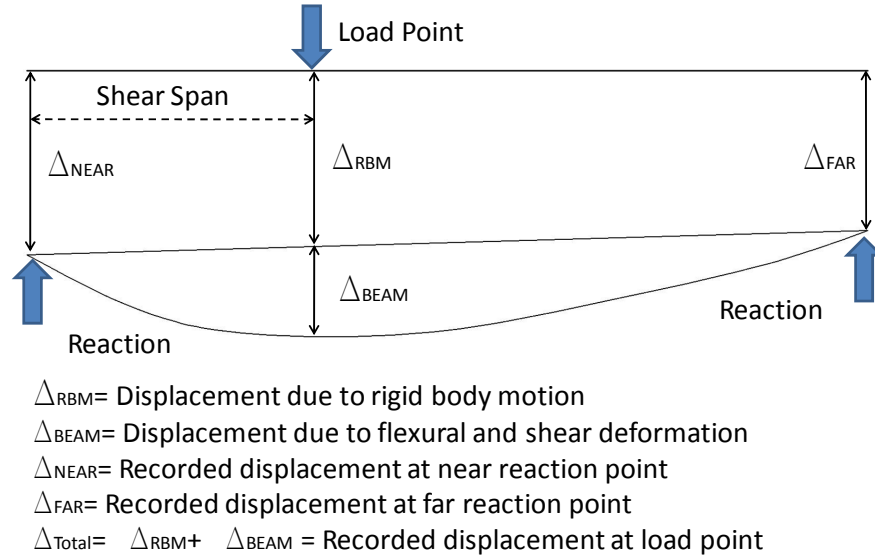


Figure 5.2 Specimen displacements and deformations

“Average” Horizontal, vertical, and diagonal strains can be calculated through dividing the deformation measured by linear potentiometers in the corresponding direction by the distance between the nuts for positioning the aluminum plates (Figure 4.8(b)). Average is emphasized because the strains calculated in this way are based on the distance between the threaded rods embedded in concrete (Δ_x , Δ_y , and Δ_{Diag}). Therefore, the calculated strains are average strain but not exact strains in the cracking position. Shear strain (γ_{xy}) was calculated based on the distortion of right angle of the triangle formed by three linear potentiometers (Figure 5.3). If the average horizontal and vertical strains are taken as ϵ_x and ϵ_y , the maximum shear strain can be obtained through the following equation:

$$\frac{\gamma_{max}}{2} = \sqrt{\left(\frac{\epsilon_x - \epsilon_y}{2}\right)^2 + \left(\frac{\gamma_{xy}}{2}\right)^2}$$

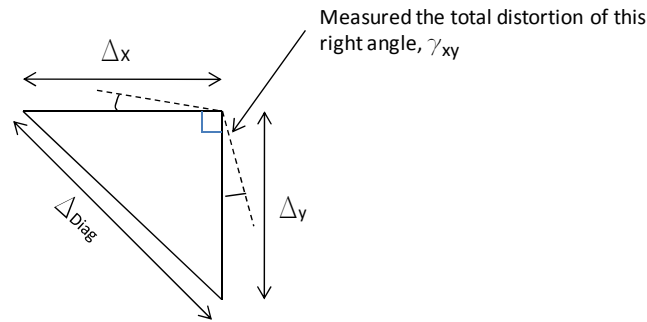


Figure 5.3 Calculation of shear strain

5.2.1 RF-3R-9-A

Beam RF-3R-9-A was considered subjected to moderate cracking due to ASR and/or DEF. The shear span-to-depth ratio is 1.85. Because this was the second test on the beam (the dapped end was tested first), the test region was selected to avoid any influence of the cracks caused by the dapped end test. Most cracks existing before testing were horizontal and the maximum width was smaller than 0.005 inches (Figure 5.4). Concrete cracking could be heard and when the first new diagonal crack (width of 0.016 in.) appeared on the east side (Figure 5.5(a)) at a shear of 314 kips. When the shear reached 373 kips, a new diagonal crack (0.013 in. width) appeared in the west face and connected with existing horizontal cracks (Figure 5.6). This diagonal crack was considered the main diagonal crack because only few new diagonal cracks were observed after the first diagonal crack appeared. When the applied load was increased, the diagonal and existing horizontal crack widths expanded. The maximum measured width of the diagonal crack and existing horizontal crack was around 0.04 inches and 0.025 inches respectively. In addition, the diagonal crack extended in both directions toward the load point and the support. When the applied load reached 600~618 kips, some concrete spalled from the west side, and faulting (an offset across the crack) was observed (Figure 5.5(b)). Finally, the strand slip was observed and the concrete started crushing at the bottom of the east side (Figure 5.5(b)) at a shear of 676 kips, beyond which, load on the beam could not be increased. The failure mode of RF-3R-9-A was determined to be compression strut crushing.



Figure 5.4 RF-3R-9-A pre-existing cracks (west side)

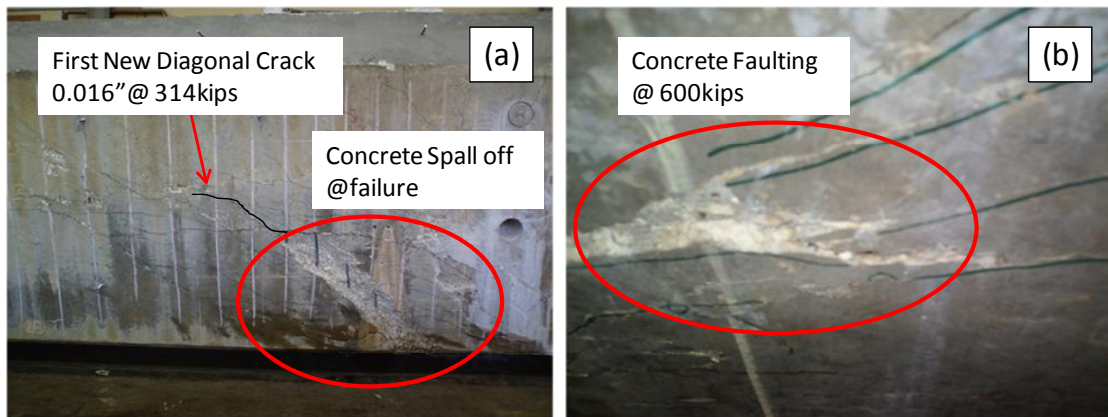


Figure 5.5 East side of RF-3R-9-A (a) Location of the new diagonal crack and spall concrete (b) Faulting

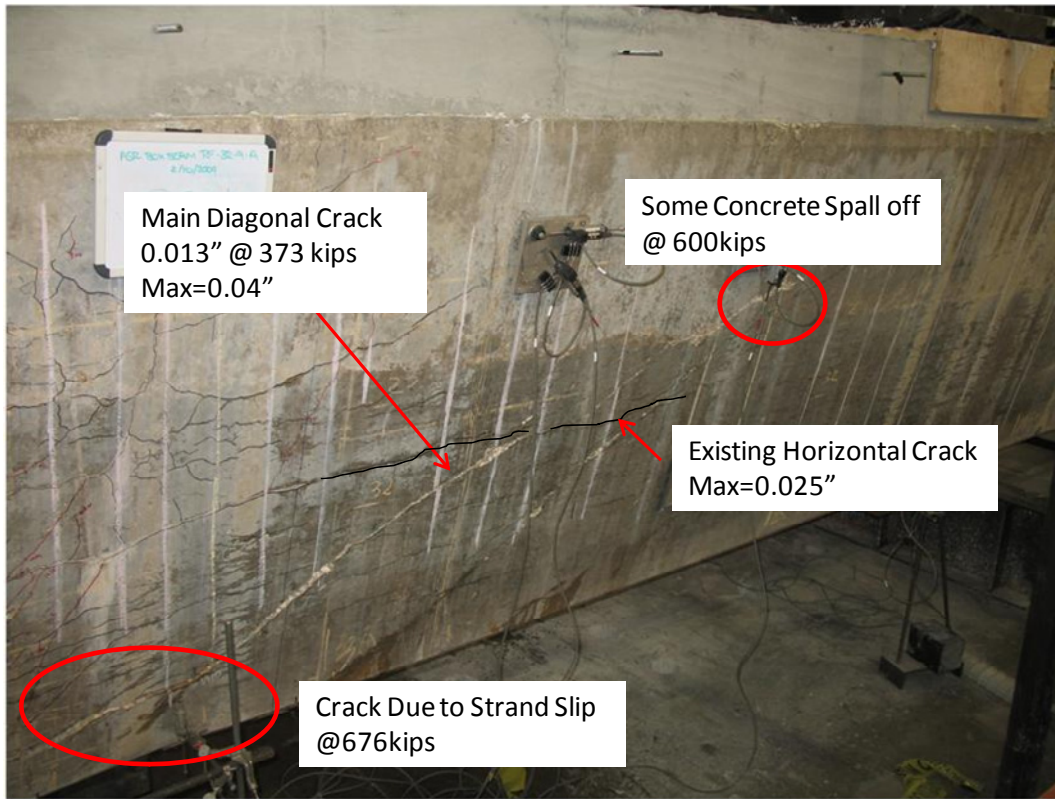


Figure 5.6 West side of RF-3R-9-A

In Figure 5.7, the relationship between applied shear load and deflection is shown. It can be seen that the stiffness remained nearly constant before the first new shear crack developed and the stiffness of the beam gradually decreased until failure occurred.

The measured shear deformation in the shear span provides information on the concrete cracking and stirrup deformation. From Figure 5.8, it can be seen that strain in the diagonal and vertical direction is more significant than in the horizontal direction. The average horizontal strain changed very little throughout the test. Small average diagonal and vertical strain was recorded before the first new diagonal crack appeared. Average vertical strain exceeded nominal yield strain (0.002) of the stirrups, indicating that yielding is likely to have occurred before failure. Shear strains were also plotted and a similar trend can be observed. The shear strain (γ_{xy}) and the maximum shear strain (γ_{max}) are almost identical.

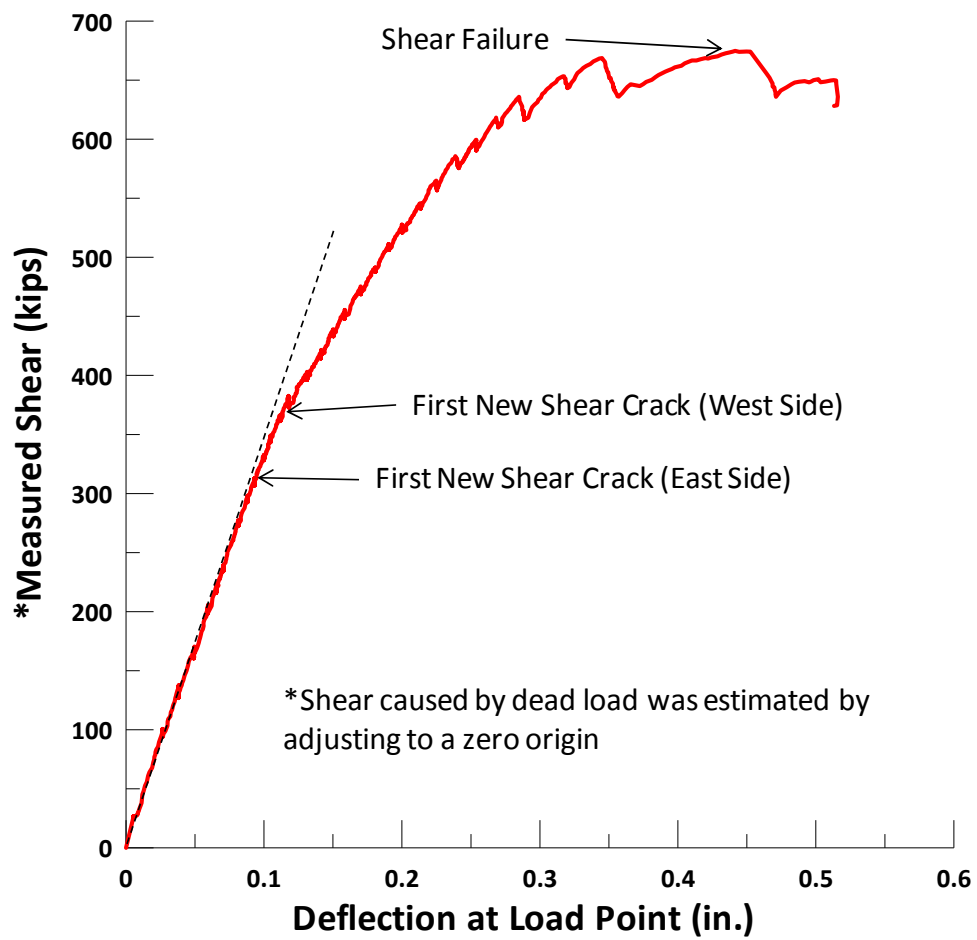


Figure 5.7 RF-3R-9-A load-deflection plot

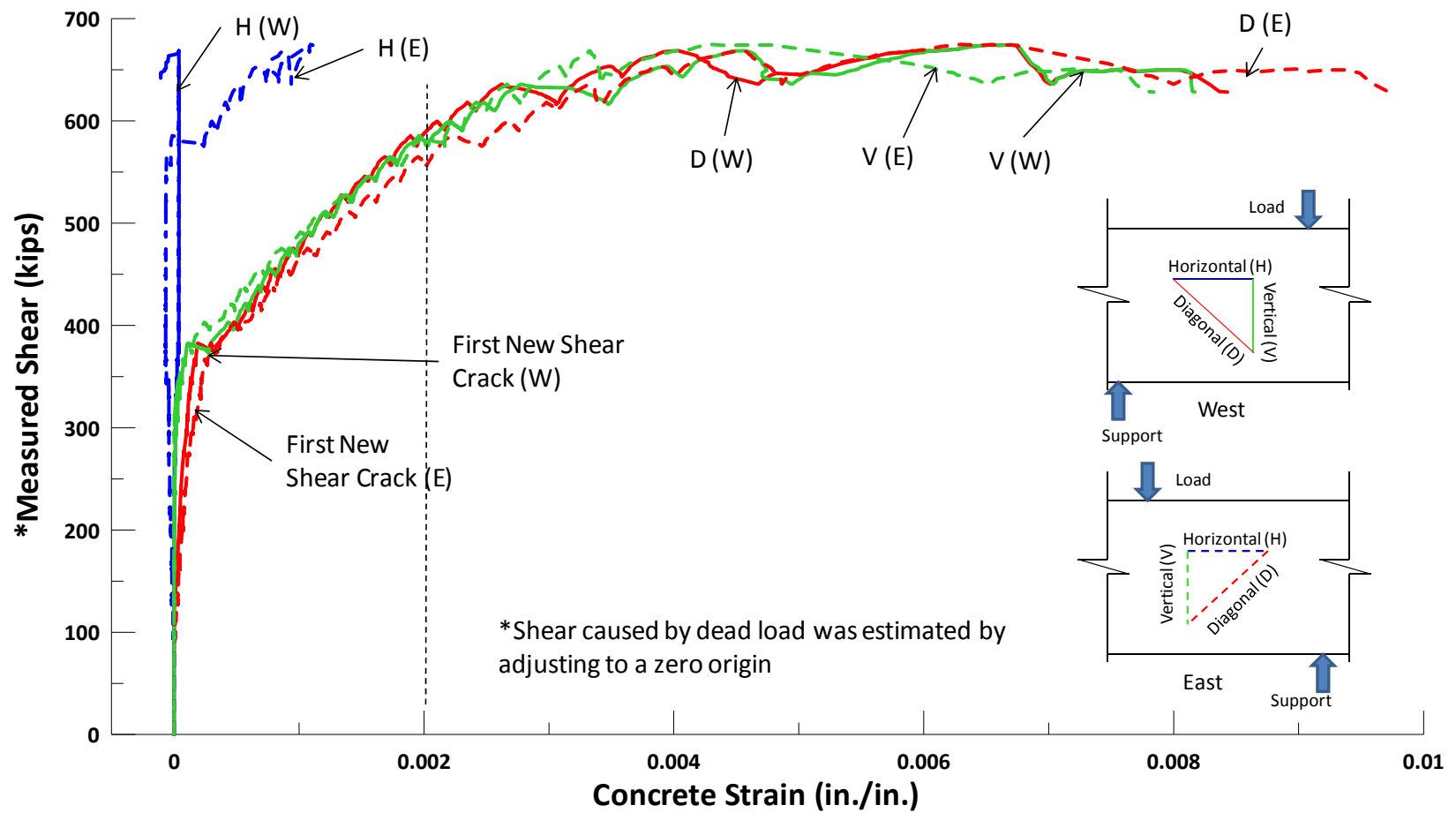


Figure 5.8 RF-3R-9-A average strains vs. measured shear

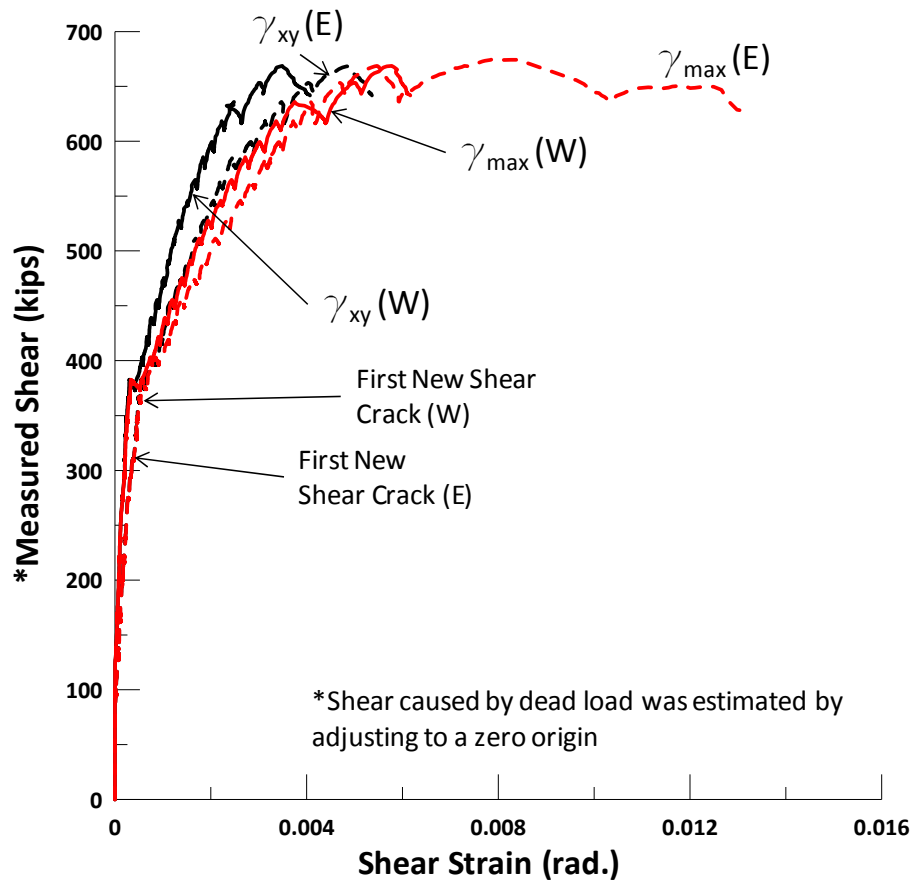


Figure 5.9 RF-3R-9-A shear strain (γ) vs. measured shear

5.2.2 RF-3R-9-C

RF-3R-9-C was cut from the opposite end of beam RF-3R-9. ASR and/or DEF cracking was considered to be moderate, similar to that of RF-3R-9-A. The shear span-to-depth ratio was 1.85 for the web shear test. As before, the web shear test was the second test of the specimen, and hence the test region was selected to avoid cracks caused by the dapped end test.

Only horizontal cracks distributed within the shear span were observed before testing. A primary horizontal crack was found on the east and west side with a width of 0.05 and 0.04 inches respectively (Figure 5.10). The width of the primary horizontal crack on the east side was up to 0.06 in. at a shear of 200 kips and kept widening as shear

increased while that on the west side did not change significantly. The first new diagonal crack of 0.005 in. appeared on the west and east side at a shear of 326~342 kips (Figure 5.11). These diagonal cracks were considered as the main diagonal cracks because very few new diagonal cracks were found after the first one appeared. The diagonal cracks widened gradually to 0.05 in. and connected with the main horizontal cracks, extending toward the load point and support as the shear increased to 542 kips. At the same time, the primary horizontal crack on the east side widened to 0.08 in. After this load, the crack widths were not measured for reasons of safety. Loading continued until the beam failed suddenly and loudly when the shear reached 660 kips. A couple of new diagonal cracks appeared at failure (Figure 5.12). Unlike beam RF-3R-9-A, no concrete crushing occurred, and the failure mode was denoted as a shear tension failure.

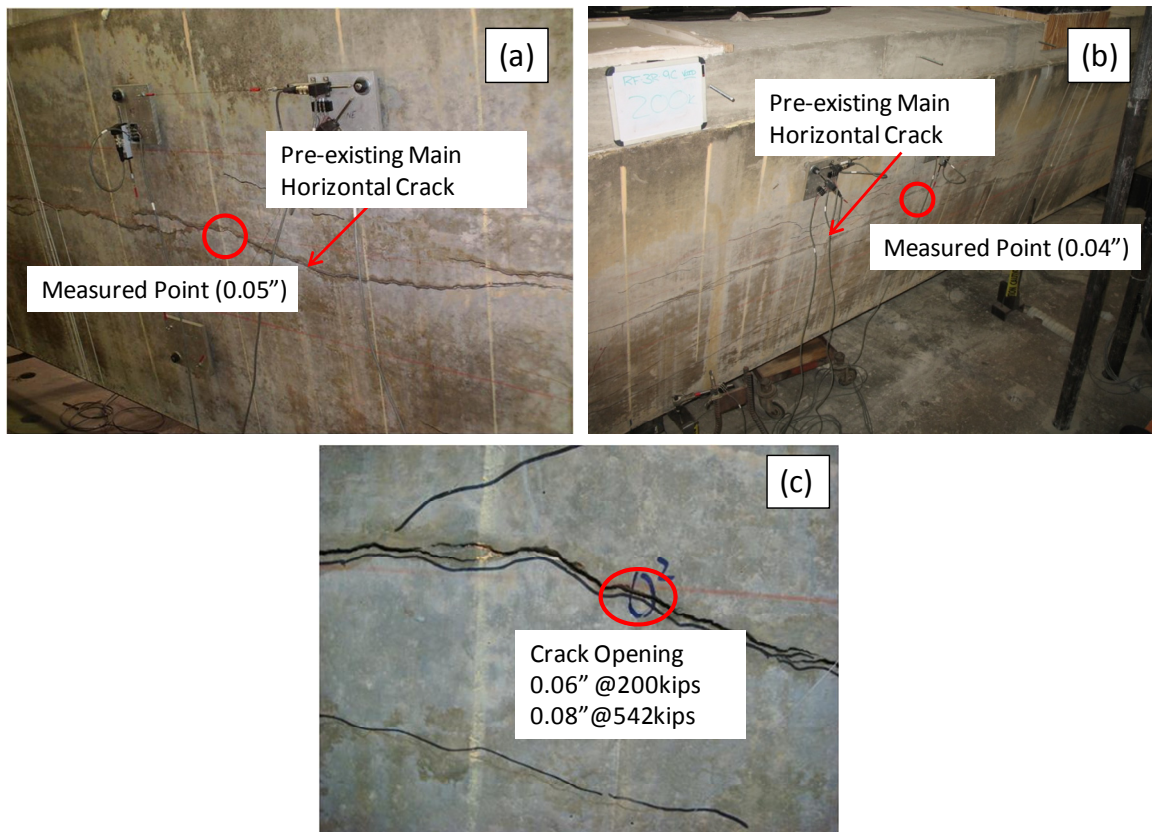


Figure 5.10 Horizontal cracks (a) East side (b) West side (c) Crack opening on east side

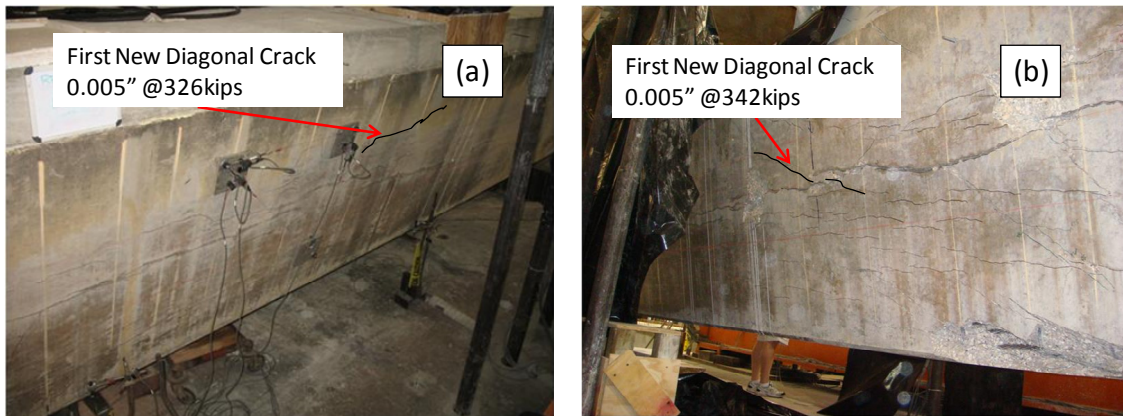


Figure 5.11 Location of first new diagonal cracks (a) West side (b) East side

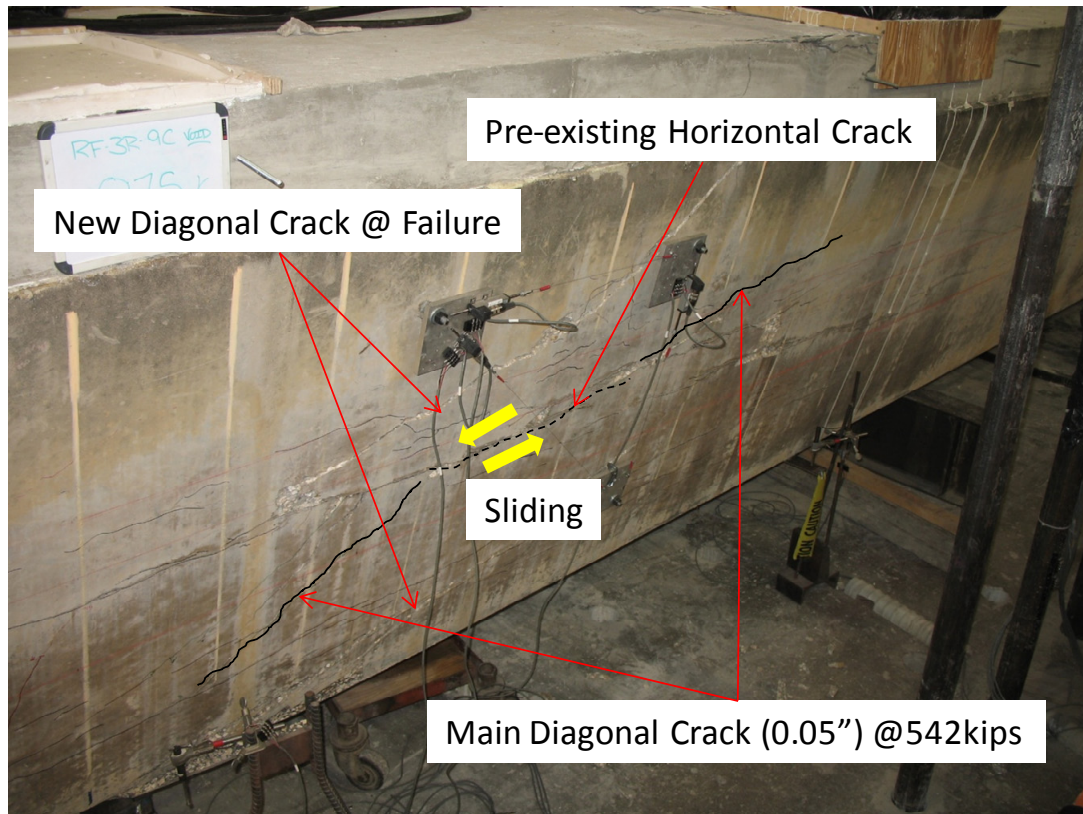


Figure 5.12 Diagonal cracks at failure (west)

The shear-deflection relationship of RF-3R-9-C is shown in Figure 5.13. Only minor changes in stiffness were observed before the first new diagonal crack appeared due to the widening of the existing horizontal cracks. After the first new diagonal crack

appeared, the stiffness of the beam decreased gradually until failure. The deflection at maximum shear was about 0.35 in. Similar to RF-3R-9-A, the shear-concrete strain relationship (Figure 5.14) showed that the average horizontal strain was much smaller than the average diagonal and horizontal strain. The increases in horizontal strain that occurred about 520 kips may be due to sliding of the beam. Significant change in the vertical and diagonal strain indicates the opening of the horizontal and diagonal cracks. The average vertical strain was greater than the nominal yield strain of the stirrup, stirrup yielding is likely to have occurred before failure. Shear strains (Figure 5.15) exhibited similar trends.

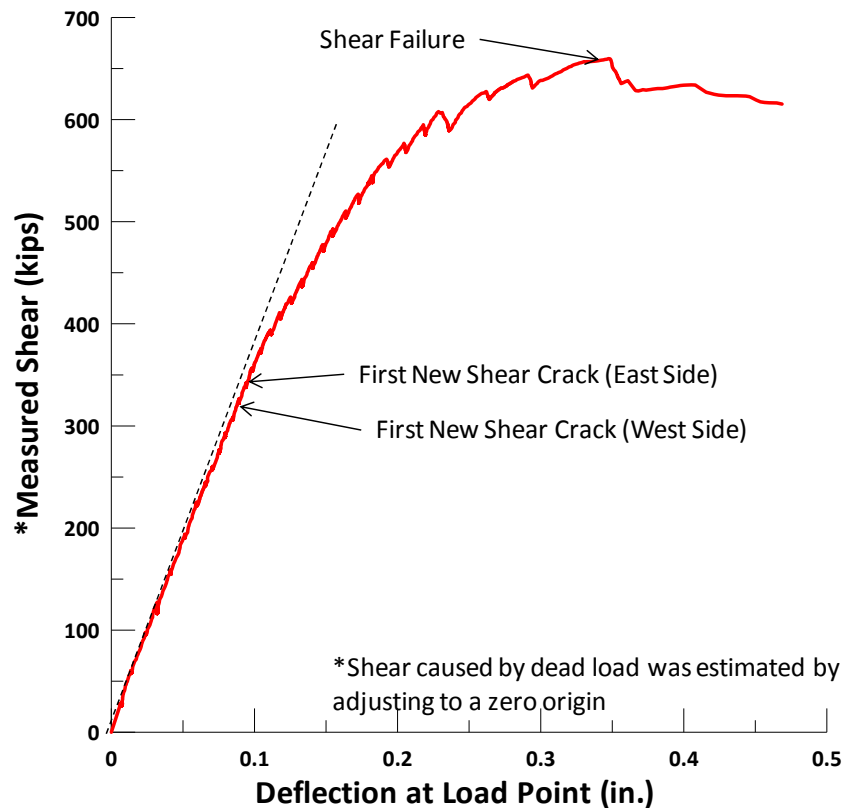


Figure 5.13 RF-3R-9-C load-deflection plot

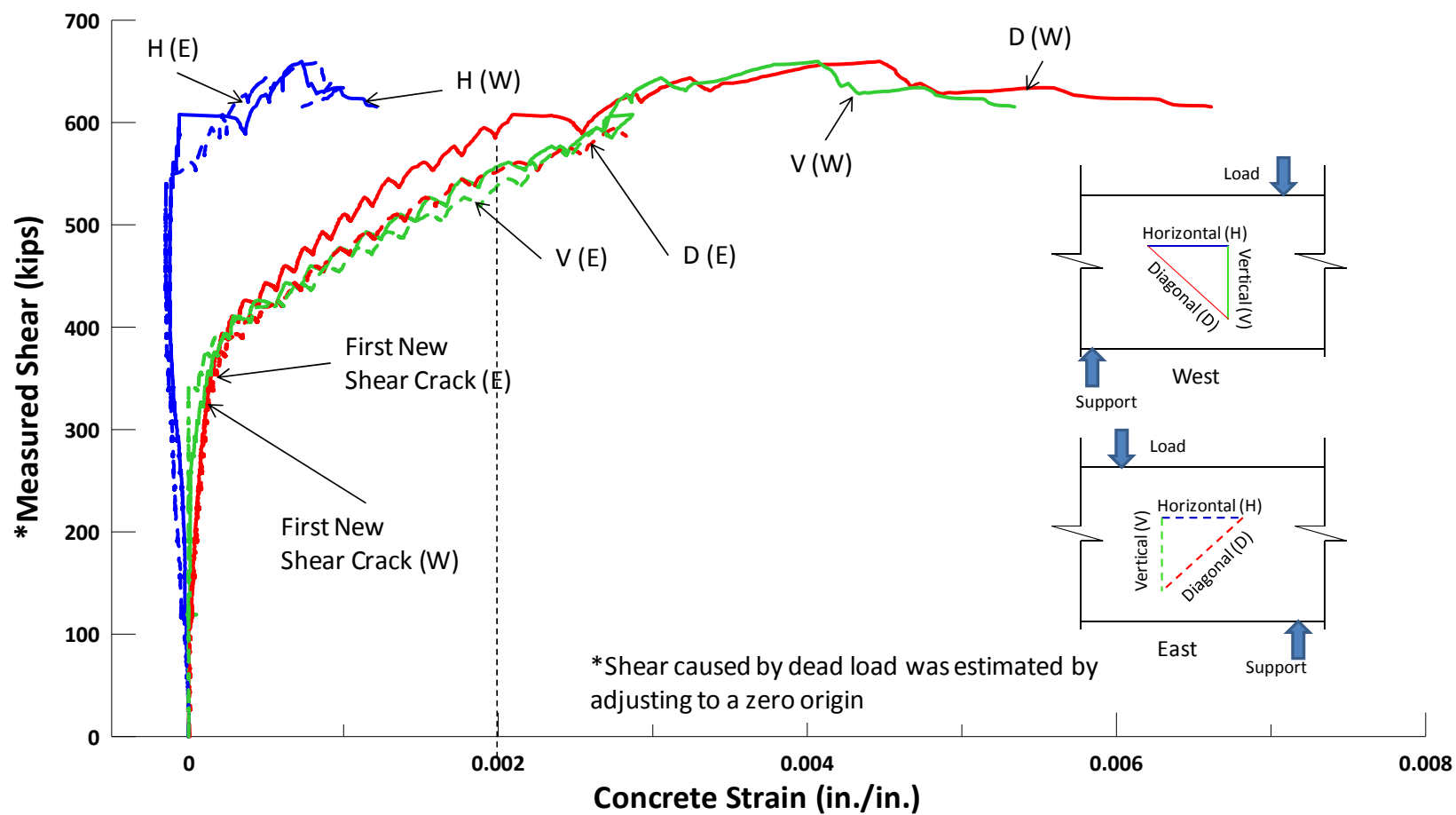


Figure 5.14 RF-3R-9-C average strains vs. measured shear

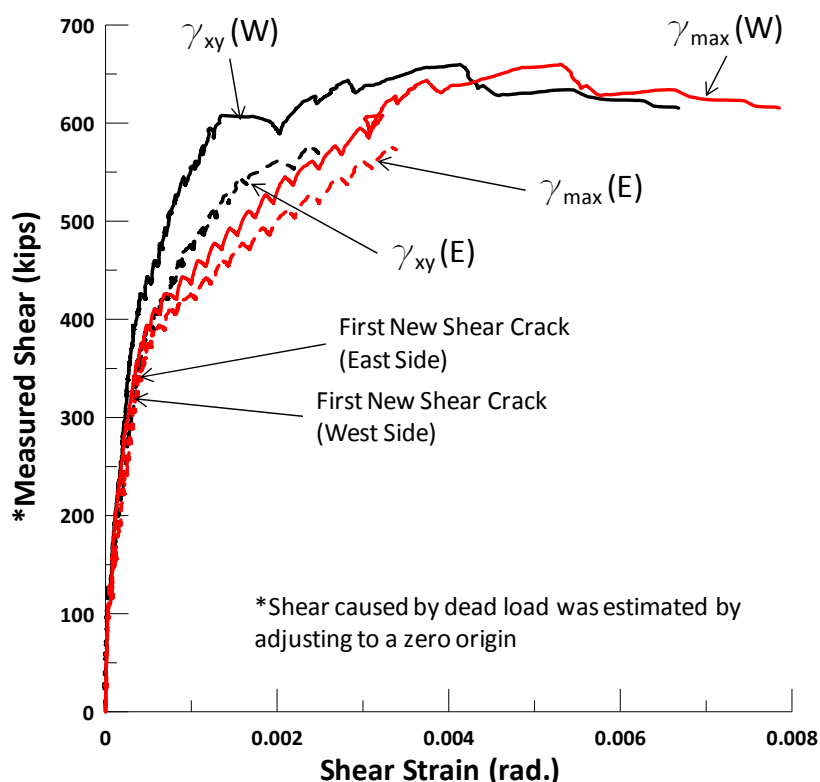


Figure 5.15 RF-3R-9-C shear strain (γ) vs. applied shear

5.2.3 RF-3R-12-A

RF-3R-12-A was defined as a lightly cracked beam before testing. The dapped end of the beam was tested before the web shear test was conducted. The test region had a large main horizontal crack on each side along with some small cracks up to 0.016 in. wide (Figure 5.16). In addition, there were some existing diagonal cracks with widths from less than 0.005 in. to 0.016 in. in the test region that occurred during the dapped end test (Figure 5.17). However, these diagonal cracks did not change noticeably throughout the shear test. The horizontal crack in the west side was the result of poor consolidation of the concrete during construction, which was likely a result of cold joint. It was difficult to define the crack width and qualitative observations will be reported.

A minor expansion of ASR and/or DEF cracking (about 0.013 in.) was observed at a shear of 224 kips (Figure 5.16), but no new diagonal cracks appeared at this time.

The first new diagonal crack was found on both west and east side with an inclination of about 20 degrees when the shear reached 260 kips. Unlike RF-3R-9-A and RF-3R-9-C, more new diagonal cracks propagated after the first one appeared (Figure 5.18). When the shear reached 358 kips, sliding and a small amount of concrete spalling at the cold joint on the west side was observed. When the shear reached 509 kips, more concrete at the cold joint spalled. The diagonal cracks near the cold joint had a maximum width of up to 0.04 in. at this load (Figure 5.18). As load increased, several pieces of concrete spalled off at the cold joint. When the shear reached a maximum of 573 kips, there was no significant failure but the load began to drop. Therefore, RF-3R-12-A was denoted as a cold joint failure. After the test, a large concrete segment separated near the cold joint, and a slightly bent stirrup due to the sliding of the cold joint was observed (Figure 5.19).

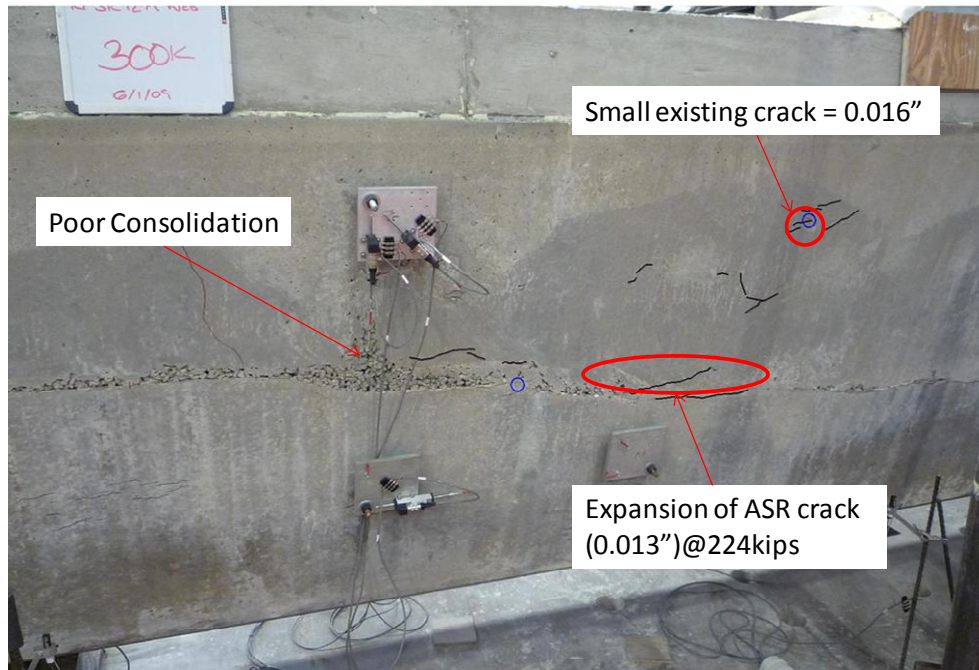


Figure 5.16 Shear span of RF-3R-12-A (west side)

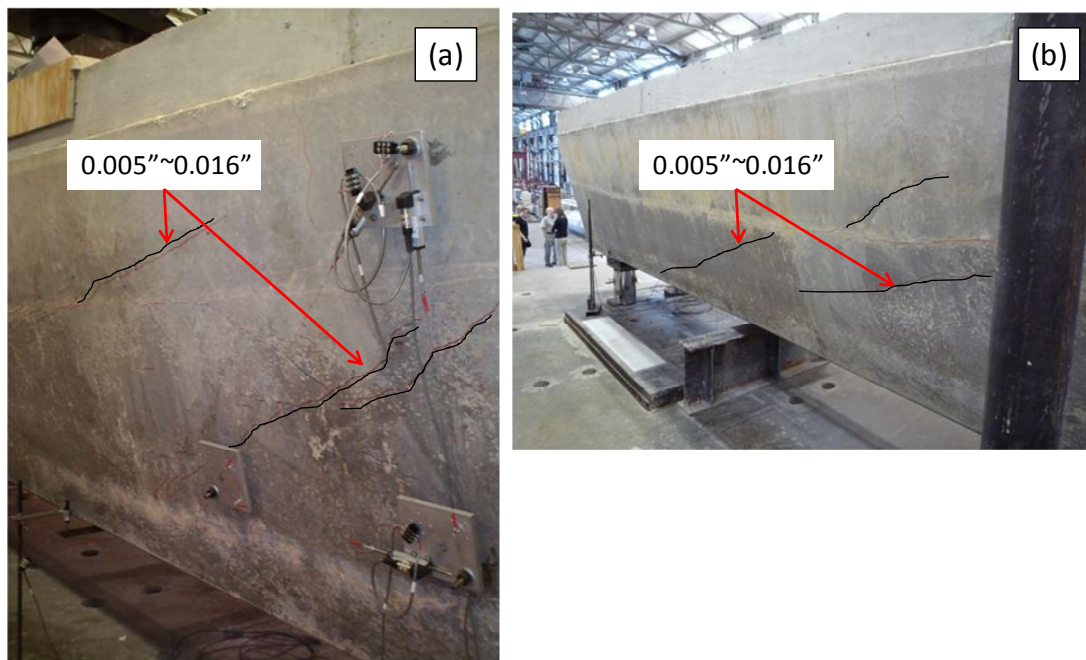


Figure 5.17 Cracks caused by dapped end tests (a) North end (b) South end

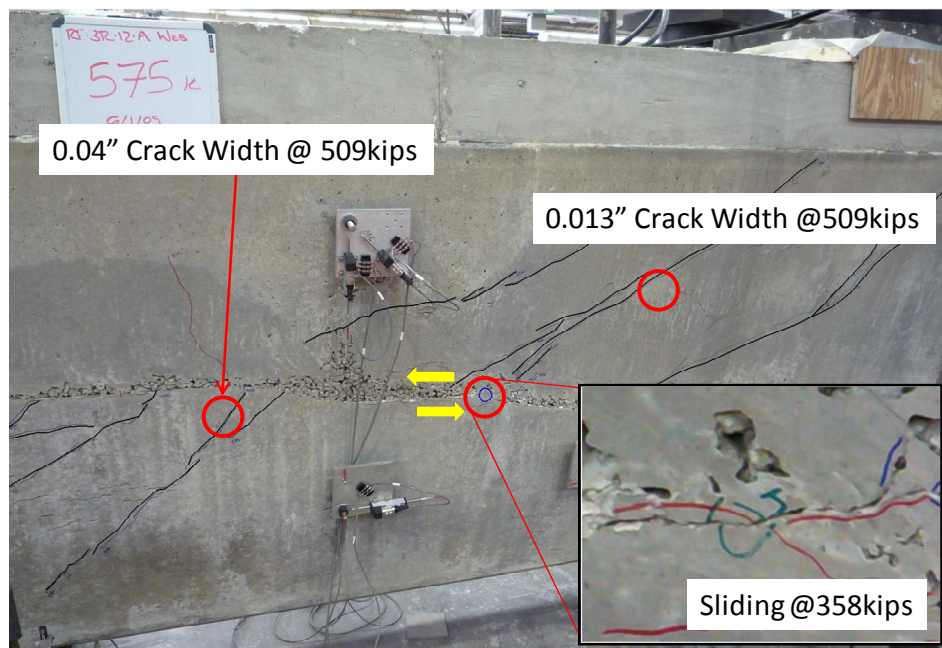


Figure 5.18 Diagonal cracks and cold joint sliding

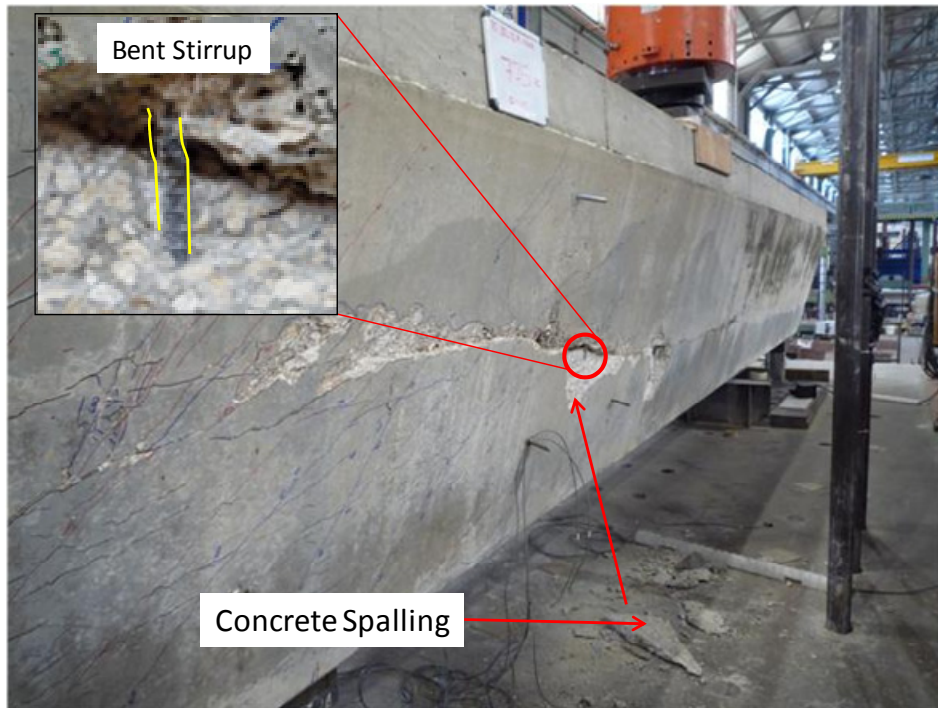


Figure 5.19 Concrete spalling and bent stirrup at failure

In Figure 5.20, the relationship between applied shear and load point deflection of RF-3R-12-A is shown. It can be noticed that the beam stiffness decreased before the first shear crack appeared probably due to the sliding along the cold joint. The ultimate shear (573 kips) was smaller than that of RF-3R-9-A and RF-3R-9-C, indicating that the cold joint may have reduced the shear strength even though this beam did not have as many ASR and/or DEF cracks as RF-3R-9-A and RF-3R-9-C. In Figure 5.21, average measured concrete surface strains are shown. Diagonal and vertical strain in the west side was larger than the east side because the cold joint weakened the west side of the beam. Average vertical strains greater than 0.002 indicates stirrups likely yielded before failure. Larger shear strain was revealed on the west side as can be seen in Figure 5.22.

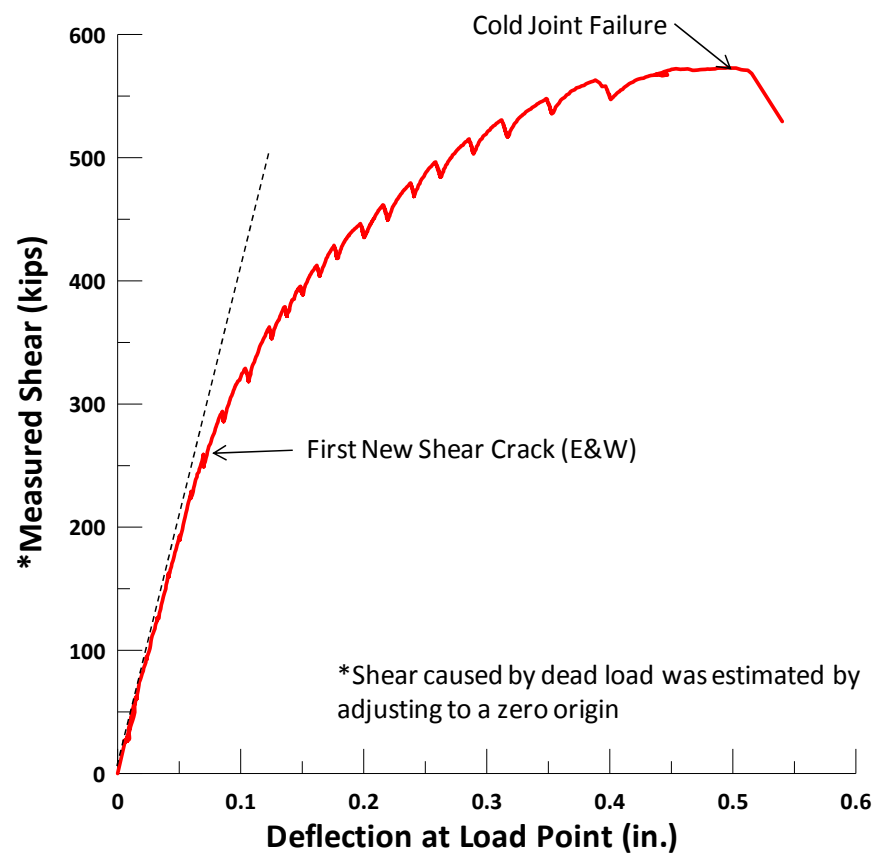


Figure 5.20 RF-3R-12-A load-deflection plot

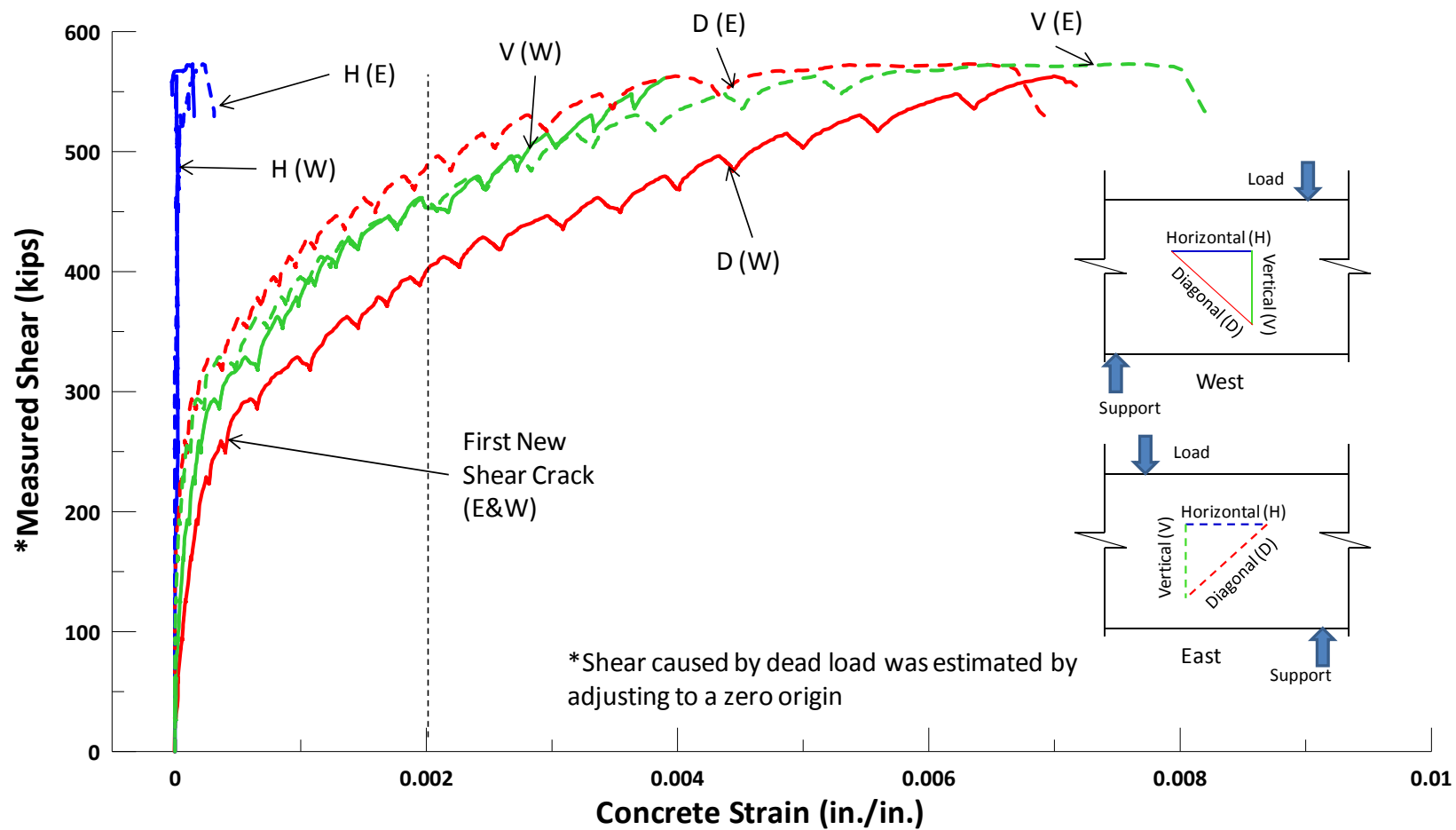


Figure 5.21 RF-3R-12-A average strains vs. measured shear

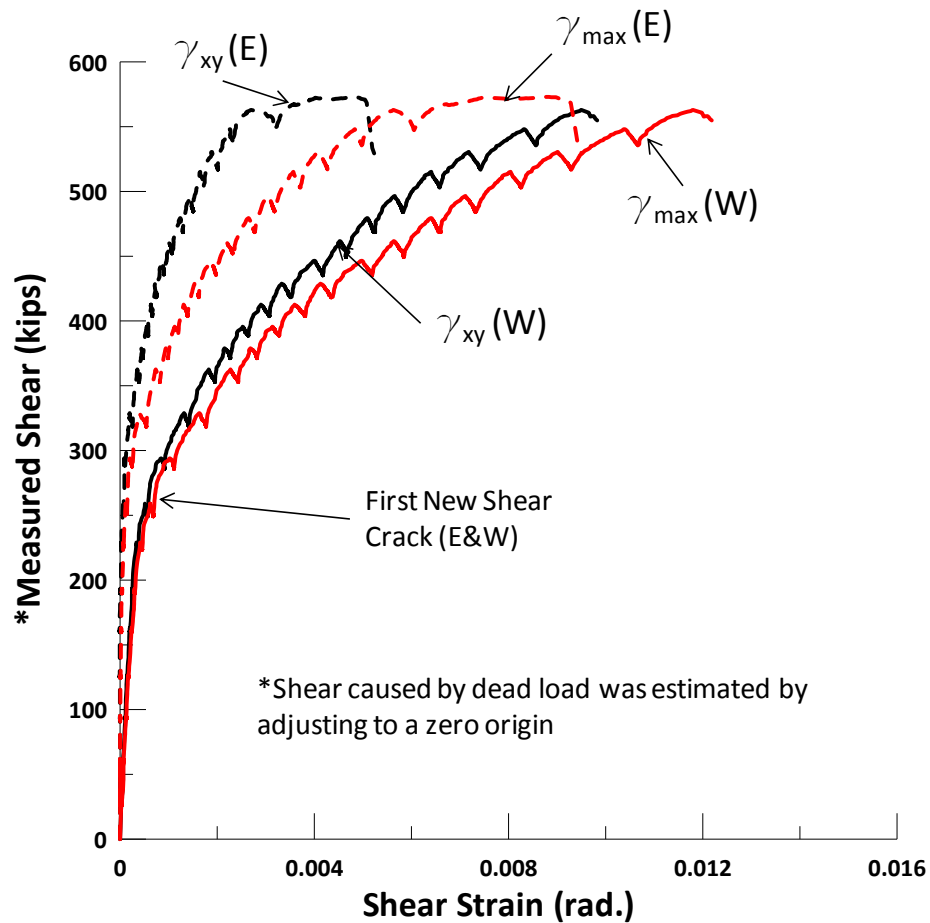


Figure 5.22 RF-3R-12-A shear strain (γ) vs. measured shear

After testing, the beam was cut in half for removal from the laboratory. From the cut section shown in Figure 5.23, it was found that the web thickness (2.5 in.) in the west side was much thinner than the east side (7.5 in.). However, a pretest survey did not indicate such a huge difference between the thicknesses of the two sides. It is apparent that the void floatation was not the same along the beam and helps to explain why strains in the west side were greater than those in the east side.



Figure 5.23 Cut section of RF-3R-12-A

5.2.4 MLL-9-34-A

MLL-9-34-A was defined as a beam with negligible cracking before testing. A main horizontal crack can also be found near the mid-depth of the test region, but cracking (width of 0.009 in.) was not as severe as RF-3R-12-A. The horizontal crack was larger (width of 0.05 in.) in the long span (Figure 5.24(a) and (b)). The beam had a skewed end and the length of the side was different. Besides, the previous dapped end test also caused some diagonal cracking in the test region and the long span of the beam. The crack width of these diagonal cracks was up to 0.025 in. in east side (Figure 5.24(c) and (d)). To monitor the cracks and shear strains in the long span, one more set of linear potentiometers was installed in each side of the beam as shown in Figure 5.24(b).



Figure 5.24 Pre-existing crack conditions (a) Horizontal cracks in test region (west), (b) Long span (west), (c) Diagonal cracks in test region (east), and (d) Long span (west)

Some small opening of the pre-existing cracks was observed before the first diagonal crack appeared. The first new diagonal crack during the test occurred in the east side at a shear of 194 kips. As load was increased, more diagonal cracks can be observed in the east side. The first new diagonal crack did not form in the west side until the shear reached 310 kips. The diagonal cracks extended to ward the top plate and the support when the load increased. The pre-existing horizontal crack in the west side expanded

noticeably, especially in the long span (Figure 5.25(a)). Cracking noises accompanied sliding of the horizontal crack as shear increased to 484 kips (Figure 5.25(b)). The horizontal crack in the southwest face widened to 0.12 in., the widest crack width observed in this test. After the sliding occurred, the concrete started to crush and the load could not be increased. The maximum shear was 610 kips. Generally, diagonal cracks in the east side were distributed more extensively than in the west side (Figure 5.26).

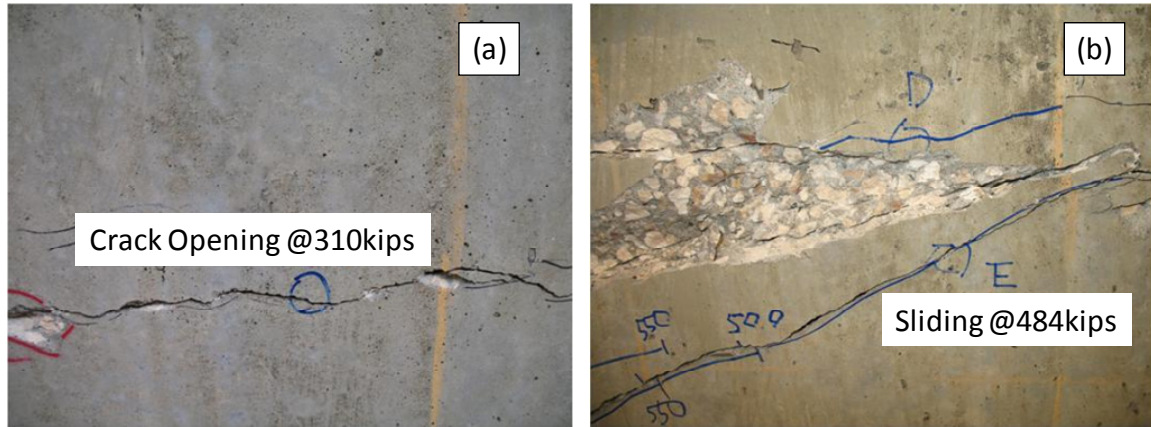


Figure 5.25 (a) Horizontal crack in the southwest side (b) Crack sliding in the west side



Figure 5.26 Crack Pattern at failure (east)

In Figure 5.27, the relationship between measured shear and load point deflection of MLL-9-34-A is shown. The stiffness decreased before the first new shear crack appeared. This may be due to the opening of the existing crack, or horizontal or diagonal cracks that formed during the dapped end test. The deflection at the load point was about 0.4 in. when failure occurred. In Figure 5.28 and Figure 5.29, average concrete surface strains in the test region and in the long span are shown. As before, average horizontal strain was always small compared to the strain in other directions. The average vertical strain in the test region was greater than 0.002 before failure, indicating likely yielding of stirrups. Negative stiffness of the west vertical strain found in the long span may be due to the compression or the slippage of the instrumentation. Diagonal strain in test region did not change significantly before the first new diagonal crack appeared, whereas in long span the strain gradually increased from the beginning of the test, showing that the pre-existing horizontal and diagonal cracks in long span opened before the first new diagonal

crack appeared. This trend can also be observed in shear strains (Figure 5.30 and Figure 5.31), especially at the west side in long span (Figure 5.31).

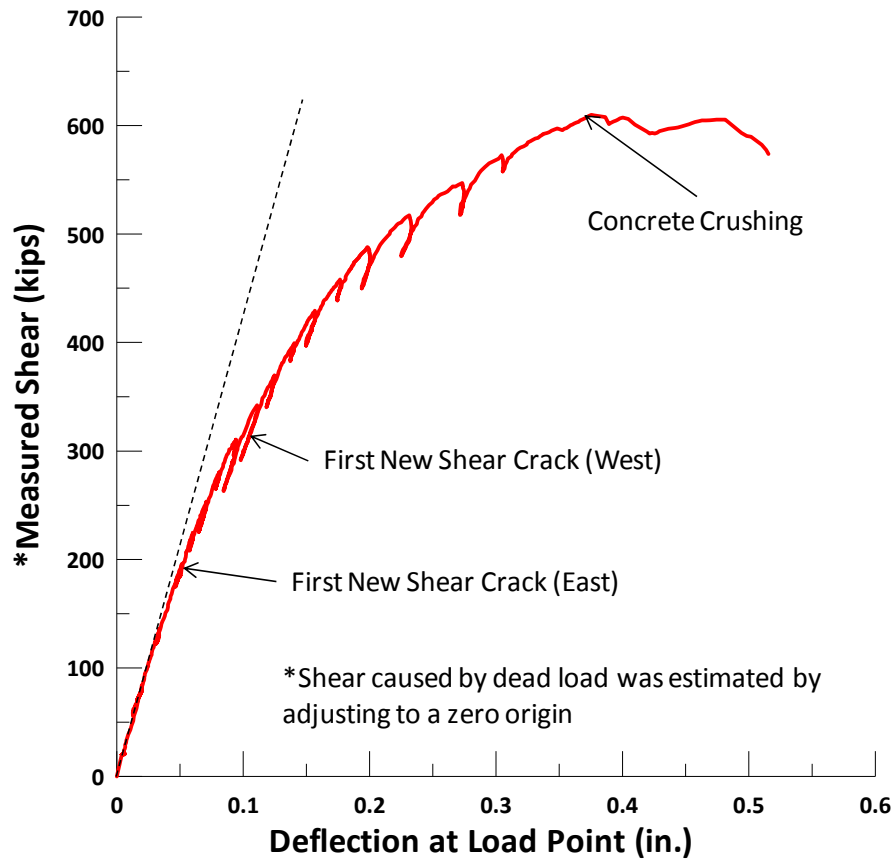


Figure 5.27 MLL-9-34-A load-deflection plot

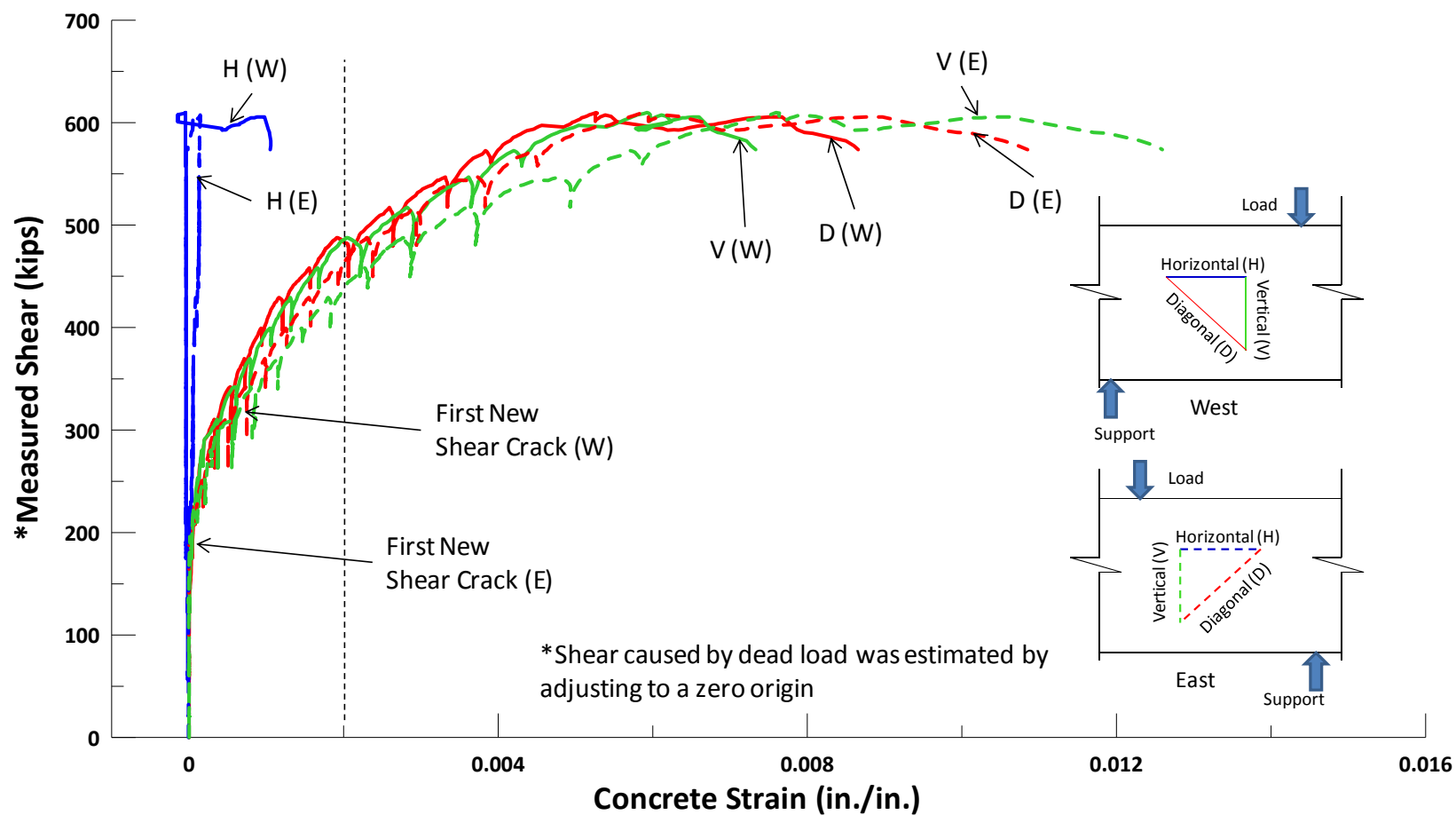


Figure 5.28 MLL-9-34-A average strains vs. measured shear (test region)

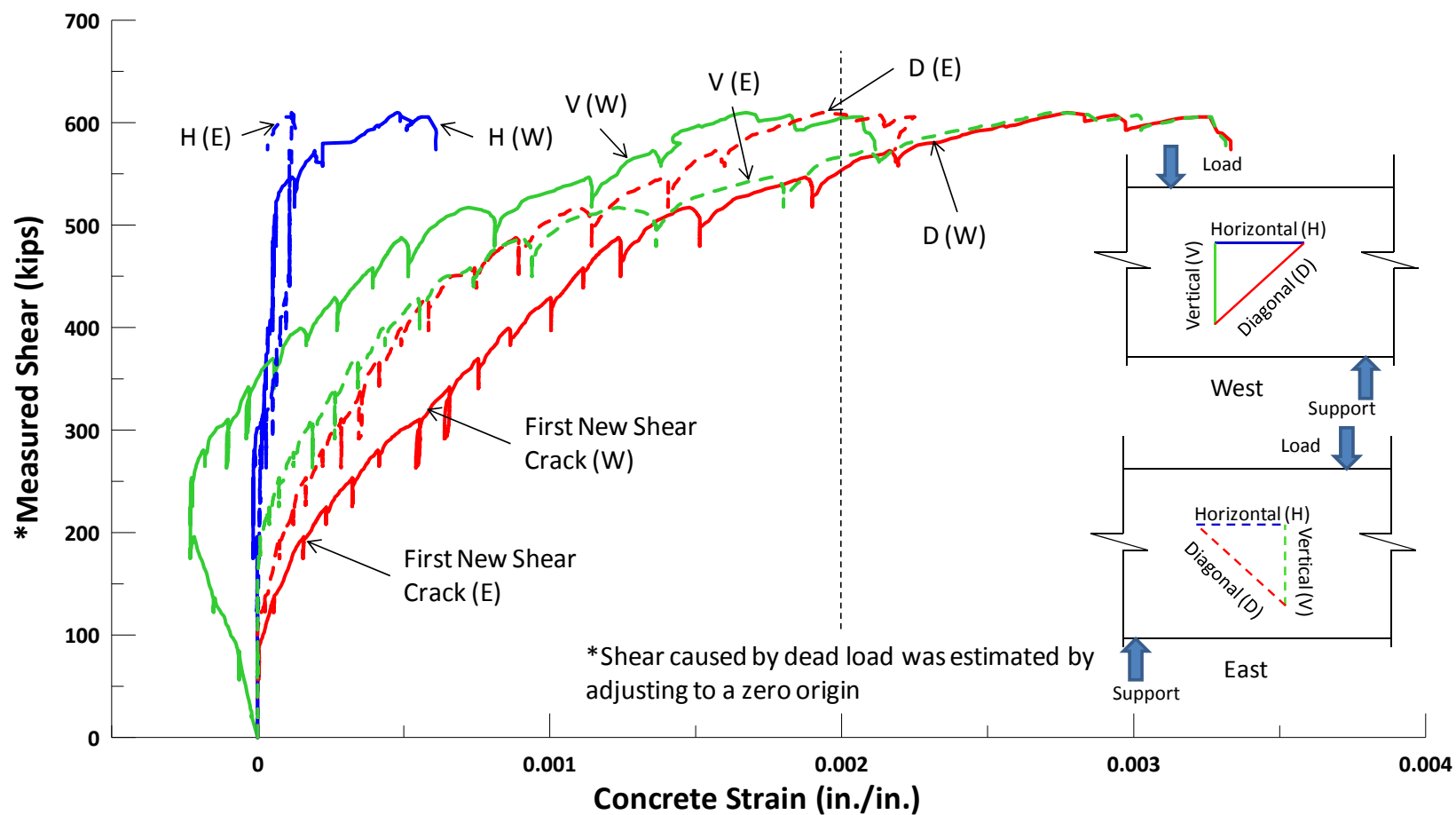


Figure 5.29 MLL-9-34-A average strains vs. measured shear (long span)

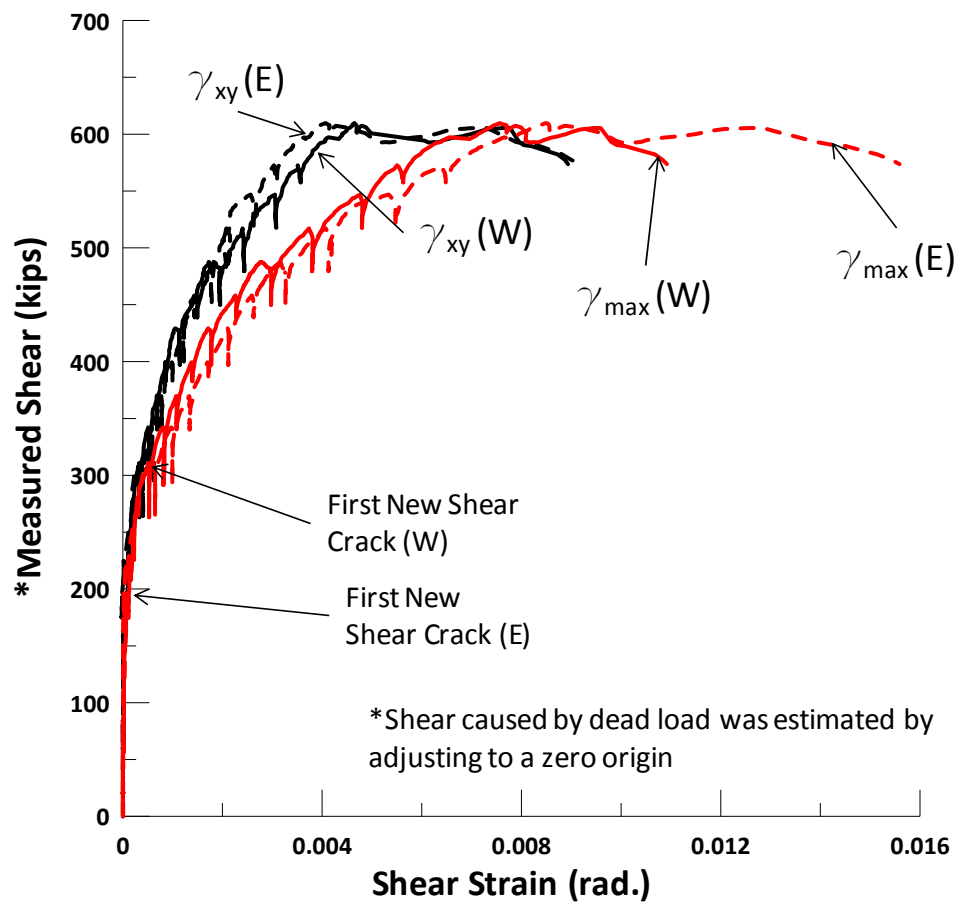


Figure 5.30 MLL-9-34-A shear strain (γ) vs. measured shear (test region)

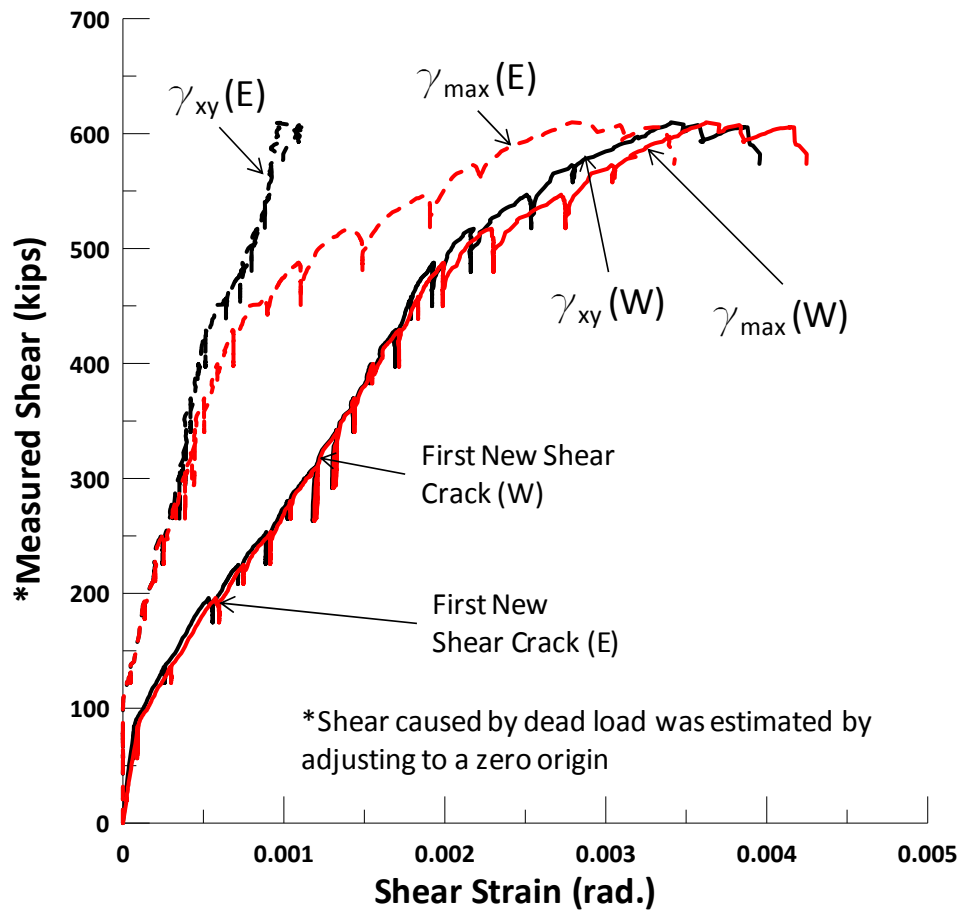


Figure 5.31 MLL-9-34-A shear strain (γ) vs. measured shear (long span)

5.2.5 RF-1R-1C

RF-1R-1C was defined as heavily cracked. There was a main horizontal crack through the mid-depth of the test region in the each side. The maximum width of the horizontal cracks was 0.04 in. in the west side (Figure 5.32). In addition, many more small horizontal cracks can be observed in the test region than were observed in the previous tests. The first new diagonal crack (around 25 degrees) appeared in the west and east side at a shear of 373 kips, much later than MLL-9-34-A. The diagonal cracks expanded to connect the horizontal cracks and extended toward top plate and support, but only a few distinct new diagonal cracks appeared after these first diagonal cracks occurred even though failure was imminent (Figure 5.33). The width of diagonal cracks

was 0.125 in. in the west side and 0.06 in. in the east side before failure, respectively. When the shear reached 477 kips, an opening of up to 0.125 in. can be observed at the main horizontal cracks in east and west faces. Furthermore, there was faulting and sliding at the cracks (Figure 5.33 and Figure 5.34). As load was increased, water trapped in the beam leaked out from the diagonal cracks and cracking noises could be heard. The beam started to crush and the maximum shear reached 624 kips. Several new diagonal cracks appeared at failure (Figure 5.35).

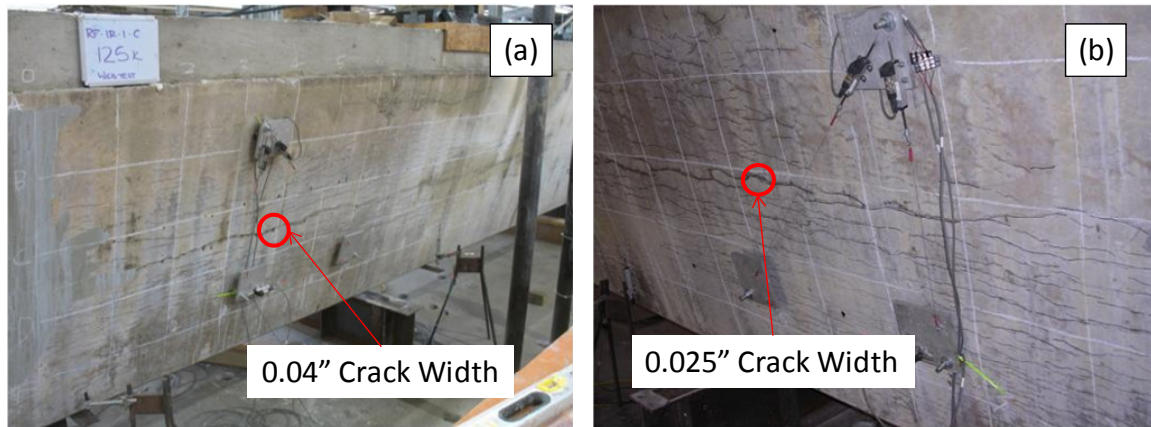


Figure 5.32 Crack condition before testing (a) West (b) East

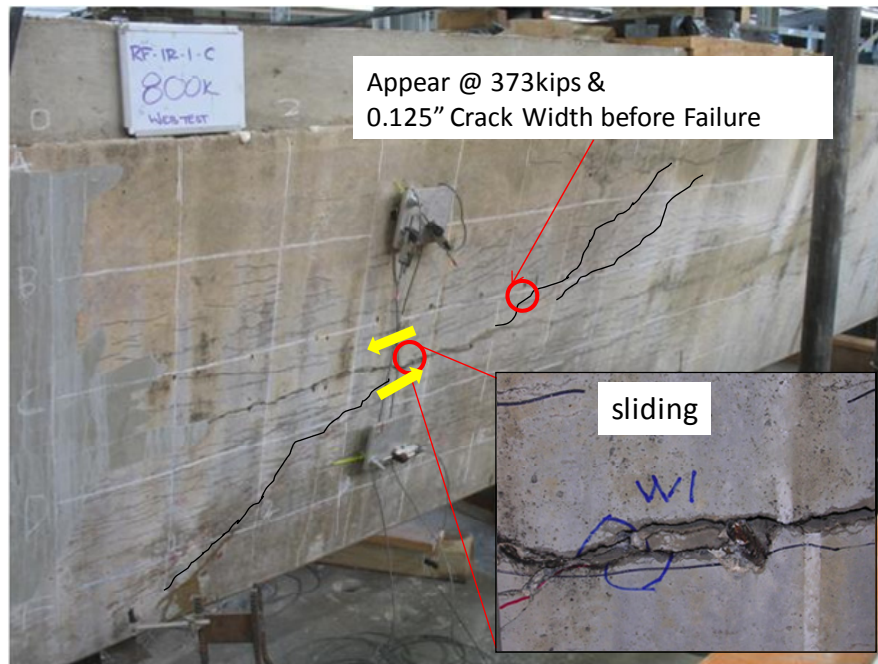


Figure 5.33 Prefailure crack pattern (west)

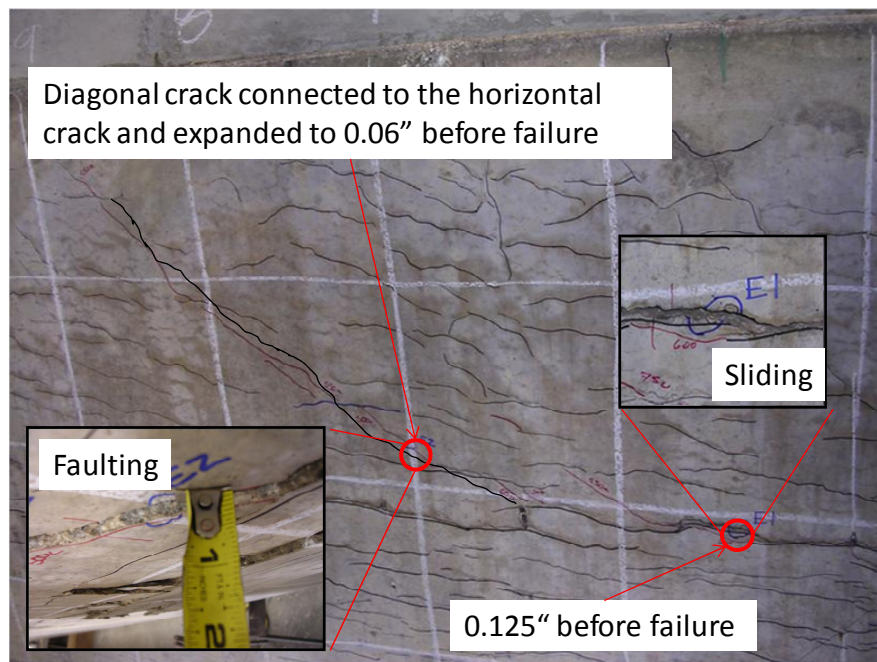


Figure 5.34 Prefailure crack pattern (east)

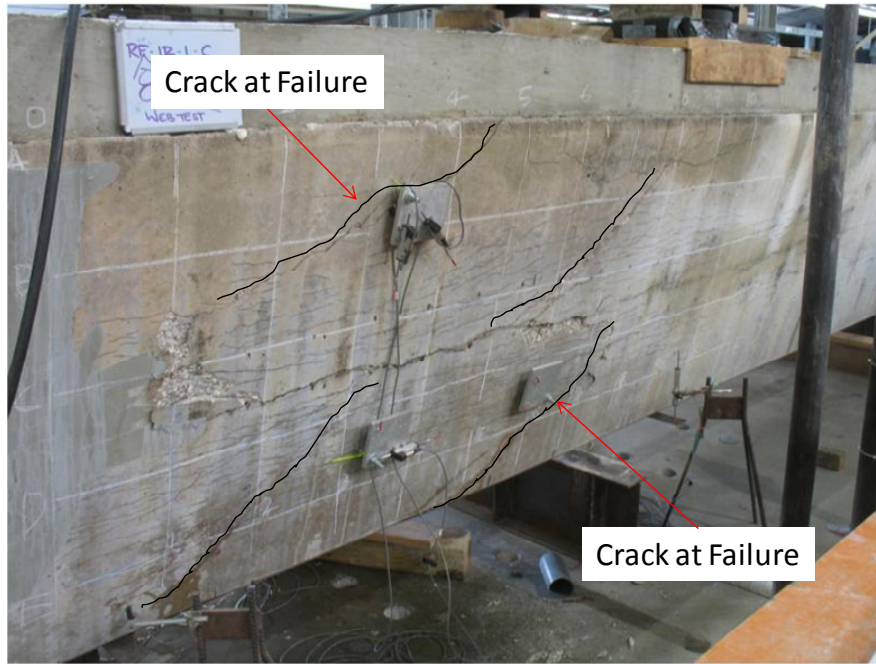


Figure 5.35 Crack pattern at failure (west)

In Figure 5.36, the relationship between applied shear and load point deflection of RF-1R-1-C is shown. Stiffness was slightly reduced before the first new diagonal crack occurred as a result of expansion of pre-existing cracks. The deflection plateaued before failure. In Figure 5.37, average concrete surface strains are shown. Average horizontal strain was still small throughout the test. Diagonal and vertical strain changed slightly before the first new diagonal crack appeared due to expansion of the pre-existing cracks. The average vertical strain also exceeded 0.002, indicating likely yielding of the stirrup before failure. Similarly, shear strains did not change significantly before the first new diagonal crack occurred (Figure 5.38).

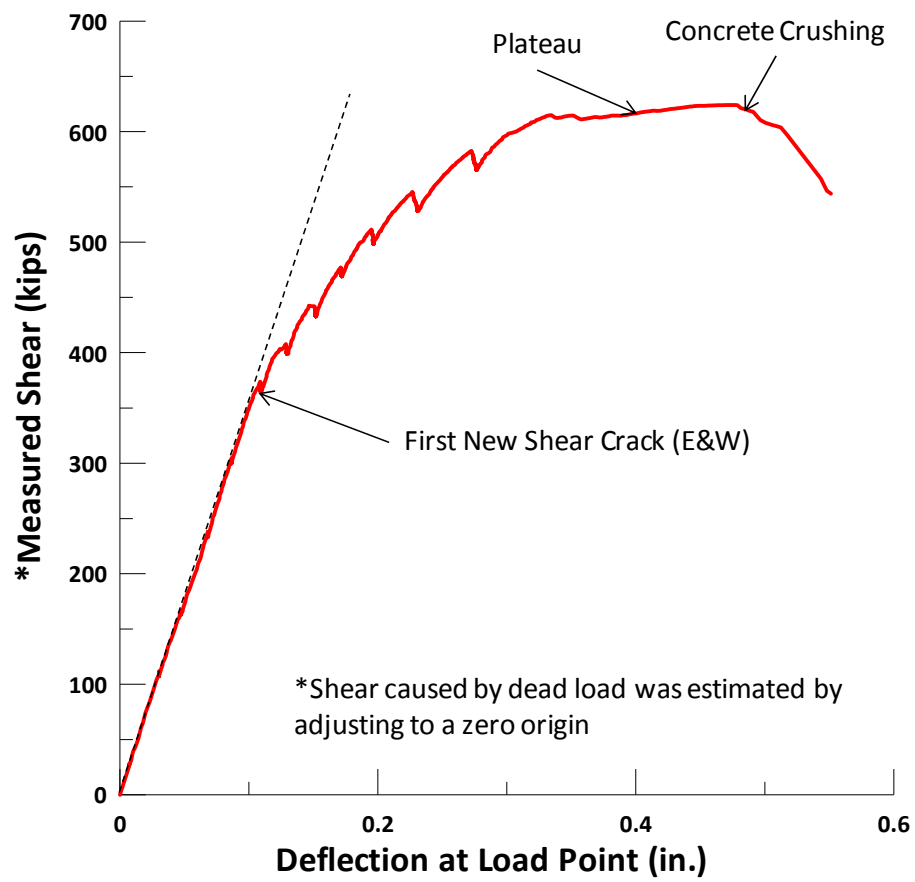


Figure 5.36 RF-1R-1-C load-deflection plot

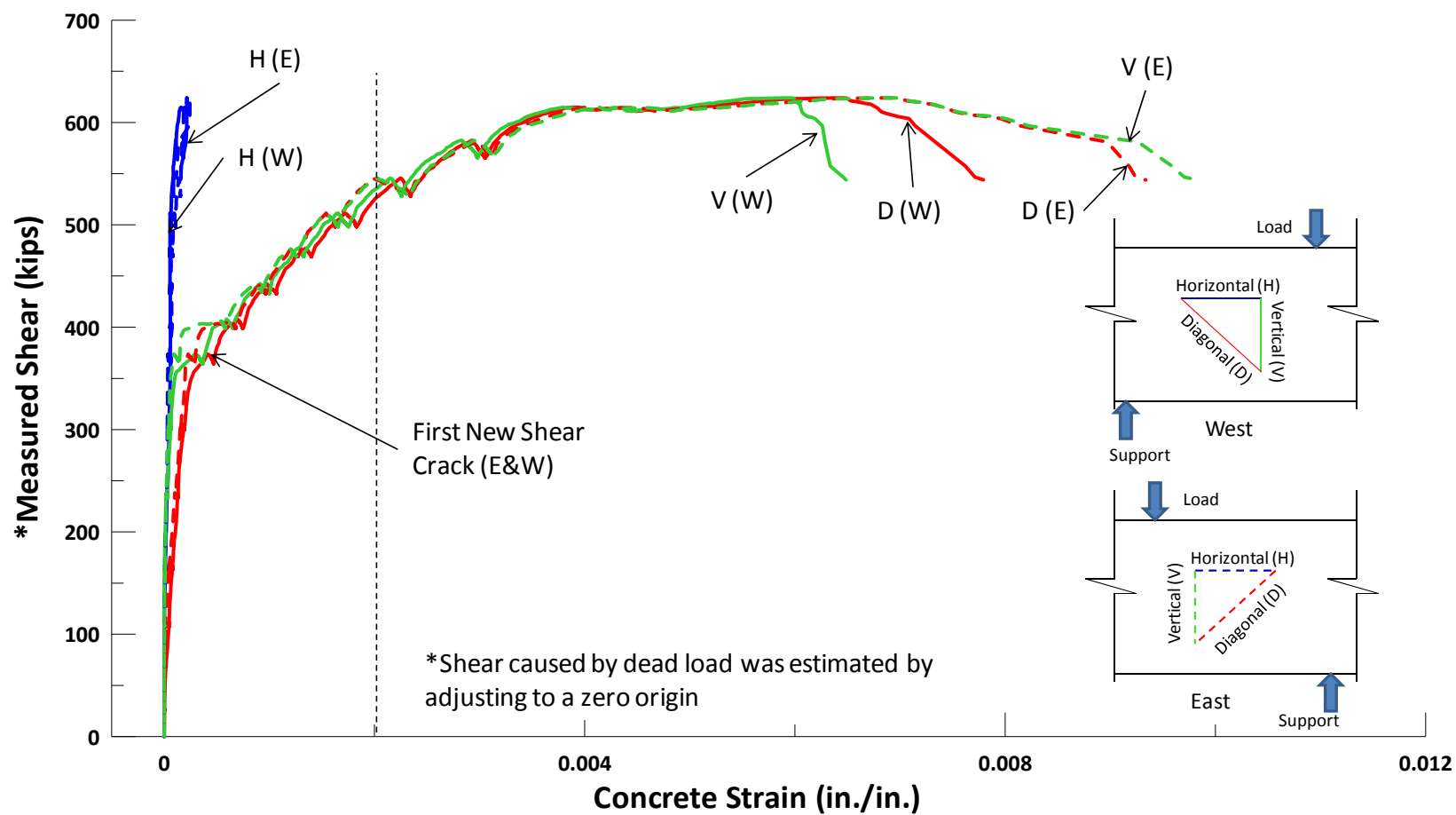


Figure 5.37 RF-1R-1-C average strains vs. measured shear

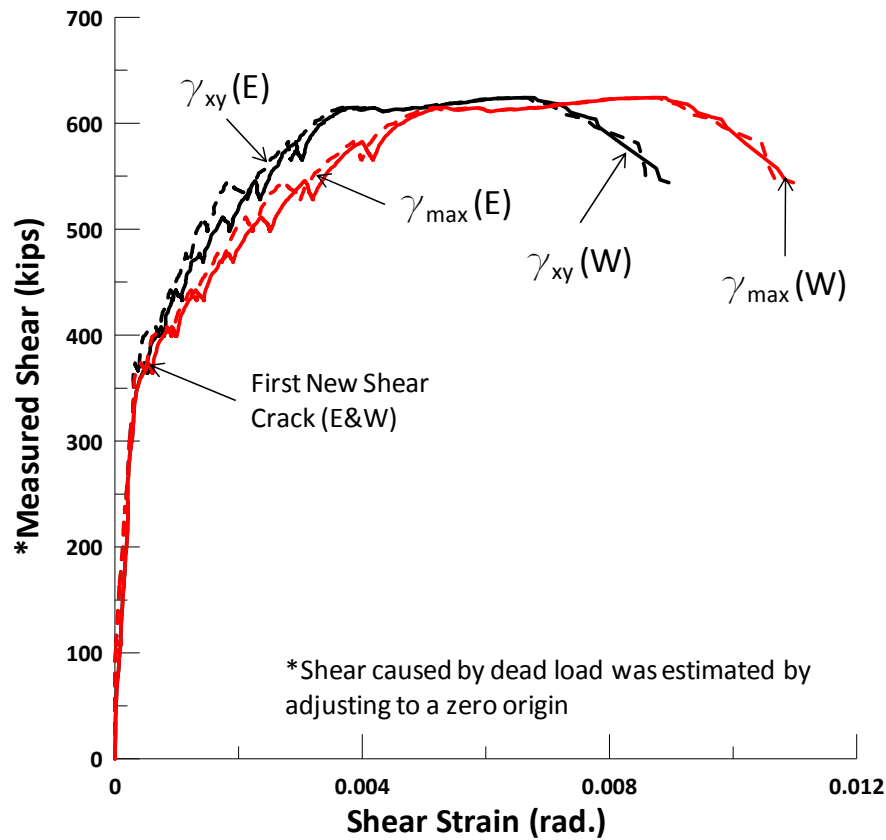


Figure 5.38 RF-1R-1-C shear strain (γ) vs. measured shear

5.3 DISCUSSION

A comparison of the measured shear vs. load point deflection of all the specimens is shown in **Figure 5.39**. RF-3R-12-A (light cracking) and MLL-9-34-A (negligible cracking) exhibited a larger deformation compared to the other three beams (moderate to heavy cracking). RF-3R-12-A had the lowest shear capacity due to early failure at the cold joint. Therefore, RF-3R-12-A should not be considered when assessing the effect of ASR and/or DEF on the prestressed trapezoidal box beams. MLL-9-34-A was a beam with negligible cracking and can be used as a control specimen for comparing test results. The plot shows that, except for RF-3R-12-A, MLL-9-34-A had the lowest shear capacity of the four remaining specimens, 10% lower than the beam with highest shear capacity (RF-3R-9-A, moderate cracking). The beam with heavy cracking had slightly higher

capacity than MLL-9-34-A but about 8% lower than RF-3R-9-A. In sum, the beams with moderate cracking had the highest shear capacity, and the beams with negligible and heavy cracking had similar shear capacity.

In Table 5.2, the shear load (V_{crack}) at “new” visible cracking is compared with the ultimate shear load (V_{test}). The beam with heavy cracking (RF-1R-1-C) had a higher ratio of “new” visible cracking load to ultimate shear load (V_{crack}/V_{test}). The relationship between cracking level and V_{crack}/V_{test} is summarized in Figure 5.40. The results indicate the more ASR and/or DEF cracking, the higher the ratio of V_{crack}/V_{test} . The more ASR and/or DEF cracking, the higher the shear before new diagonal cracks form. In the more highly cracked beams, existing cracks are opening before new cracks form. Beams with a high ratio of V_{crack}/V_{test} gave little warning of failure. According to the report by Deschenes (2009), ASR and/or DEF deteriorations induce tensile strains and stresses in reinforcement. The stresses in the reinforcement provide prestress force and cause compression in the concrete due to a self-equilibrated system. Therefore ASR and/or DEF induced compression in the concrete causes a delay in new diagonal cracking. The test results in the current study further substantiate this finding and indicate that defined cracking levels are proportional to ASR and/or DEF induced compression. The results also indicate that defined cracking levels are proportional to severity of ASR and/or DEF deteriorations as implied by first visible cracking load.

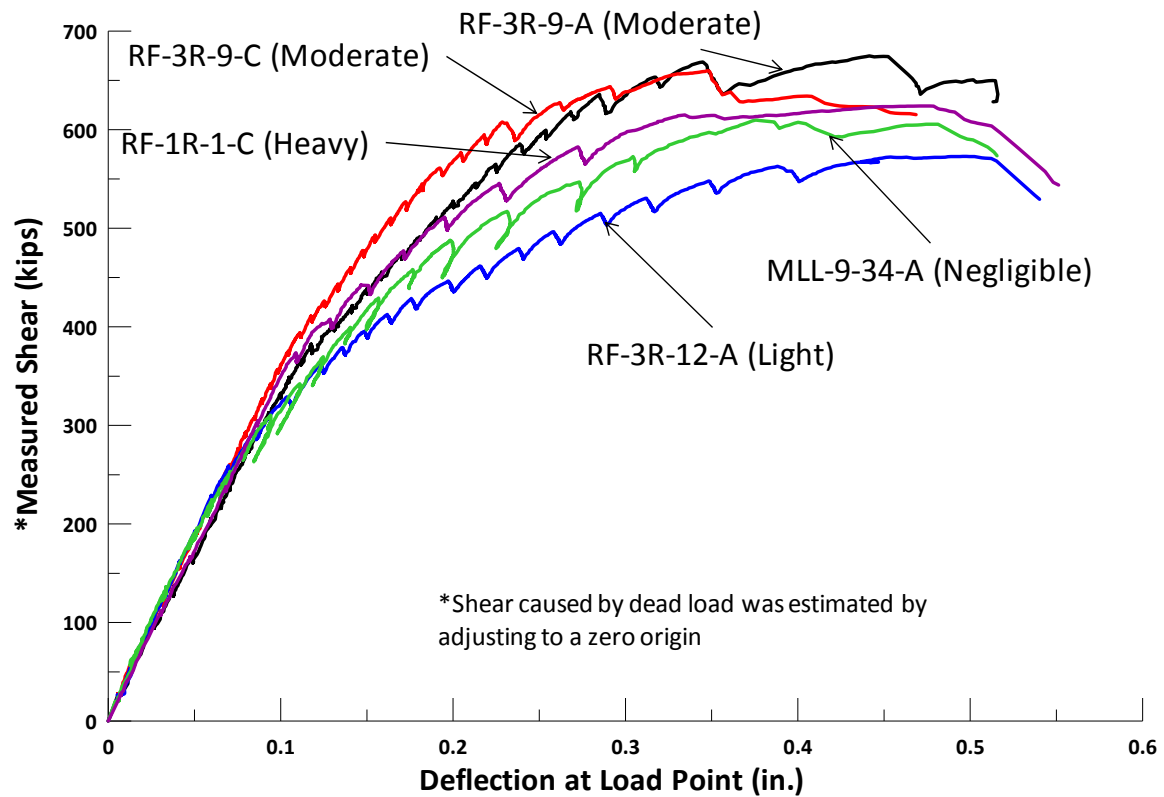


Figure 5.39 Comparison of load-deflection relationship

Table 5.2 Summary of test results

Beam ID	Cracking	V_{crack} (kips)	% of V_{test}	V_{test} (kips)	Failure Mode
MLL-9-34-A	Negligible	183	30	610	Strut Crushing
RF-3R-12-A	Light	260	45	573	Cold Joint
RF-3R-9-A	Moderate	313	47	673	Strut Crushing
RF-3R-9-C	Moderate	326	49	660	Shear Tension
RF-1R-1-C	Heavy	373	60	624	Strut Crushing

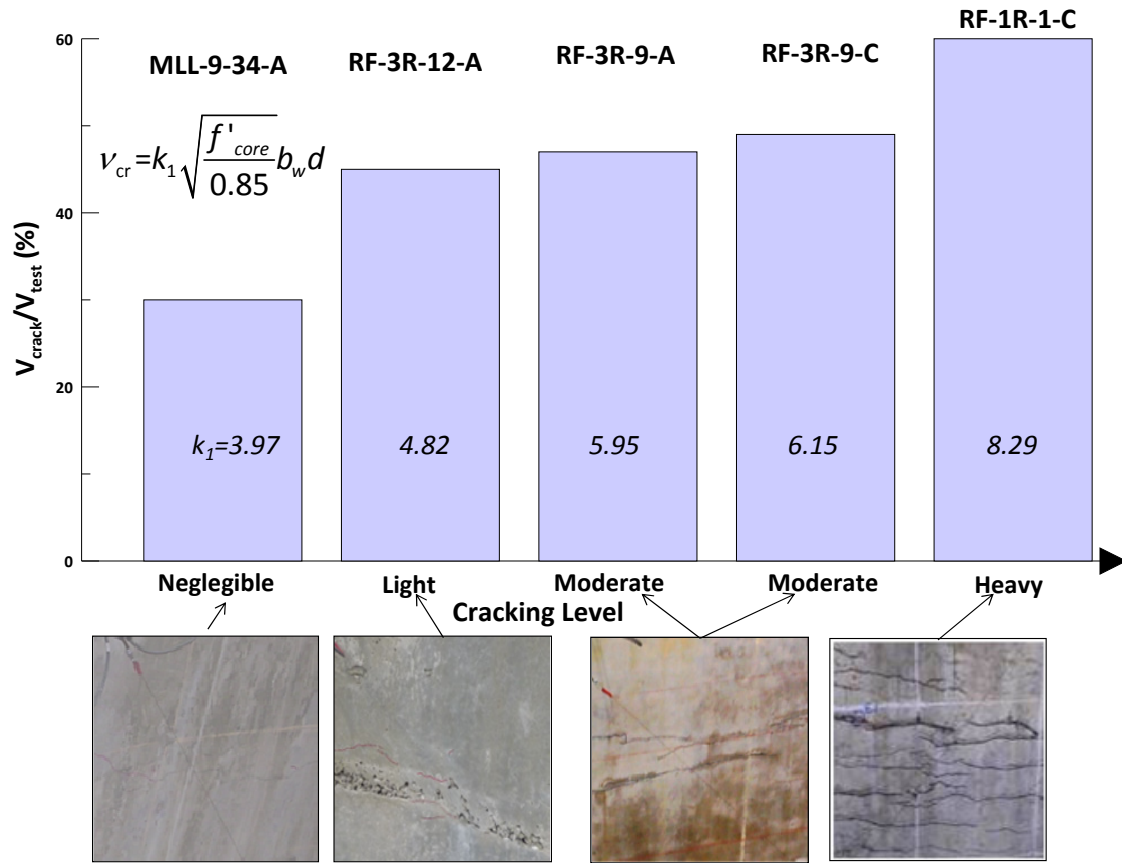


Figure 5.40 Relationship of V_{crack}/V_{test} vs. damage level

It is interesting to compare the crack pattern between the beams with low cracking level and high cracking level. From Figure 5.41, it is clear that beams with low ASR and/or DEF cracking exhibited more shear cracking before failure. On the contrary, beams highly cracked by ASR and/or DEF generated few new diagonal cracks, and diagonal cracking formed primarily by connecting existing ASR and/or DEF cracks and there was very little warning of failure.

In Figure 5.42 and Figure 5.43, the average diagonal strains and the average vertical strains in each beam are shown. All of the beams had an average vertical strain greater than 0.002 before failure, indicating likely yielding of stirrups before failure. However, only RF-3R-9-C exhibited a shear tension failure mode. The average vertical strains in RF-3R-12-A and MLL-9-34-A were larger at a given shear than the other three

beams. V_{crack} of lightly cracked beams was generally lower than that of more highly damaged beams.

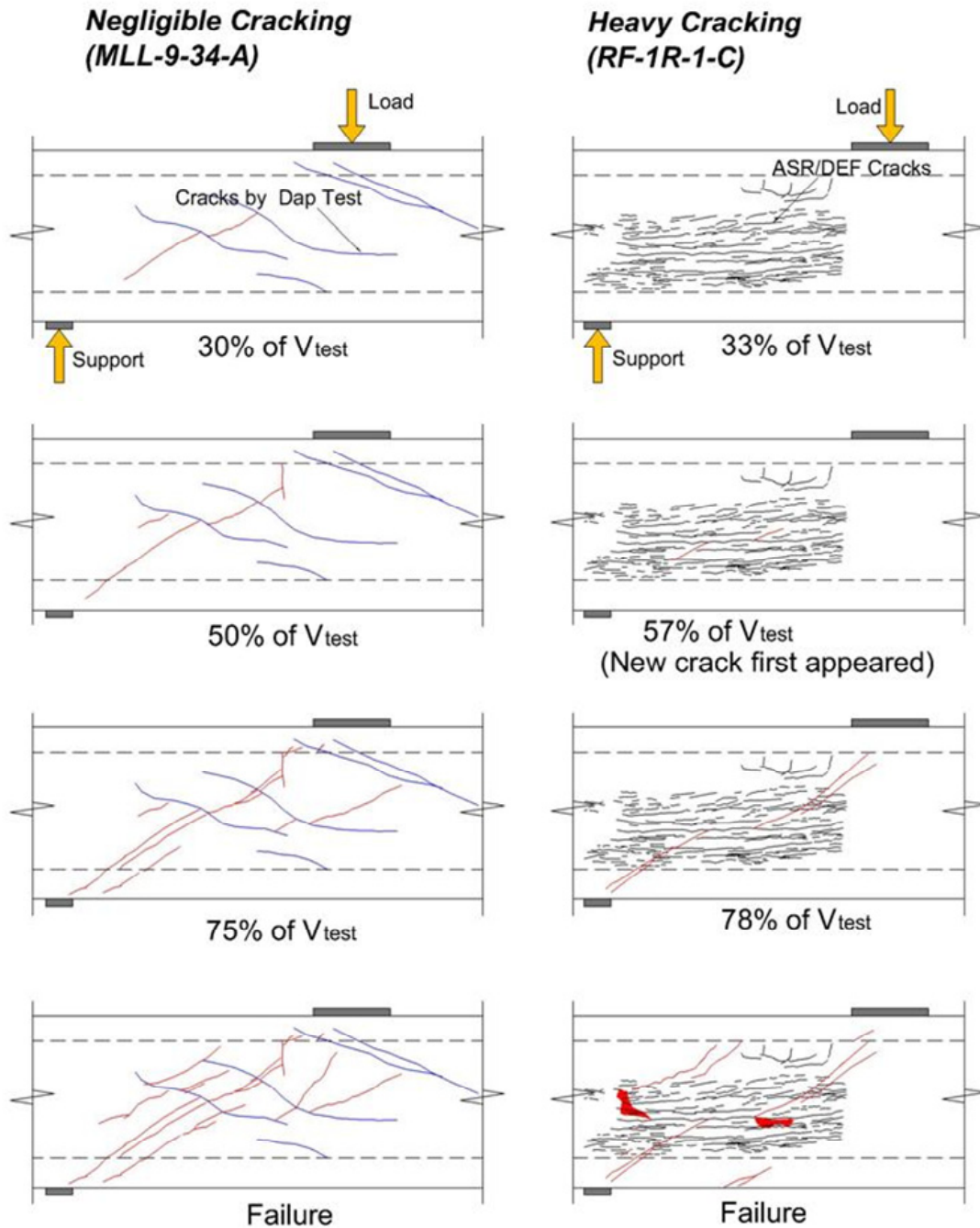


Figure 5.41 Comparison of crack patterns

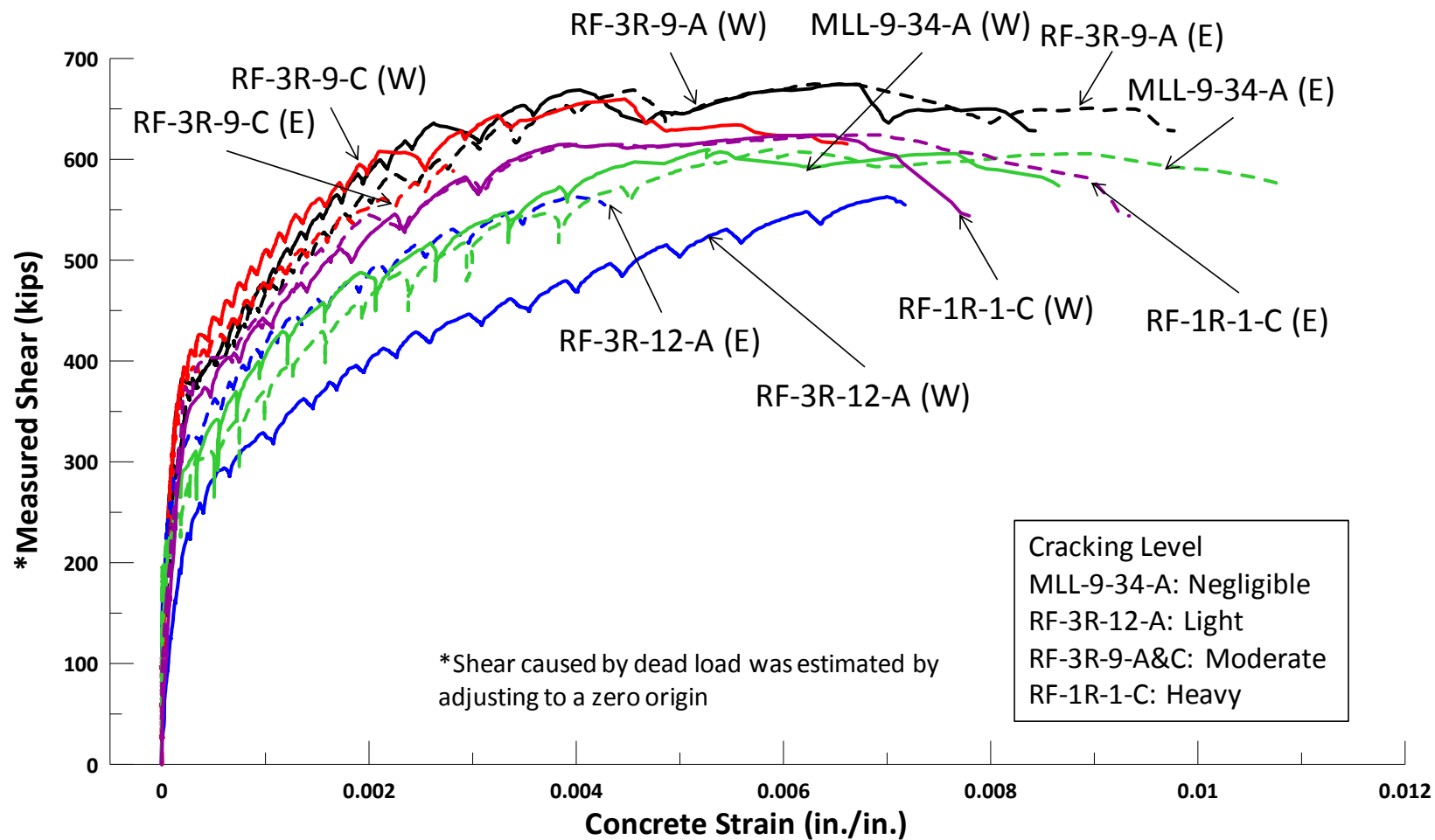


Figure 5.42 Comparison of average diagonal strains

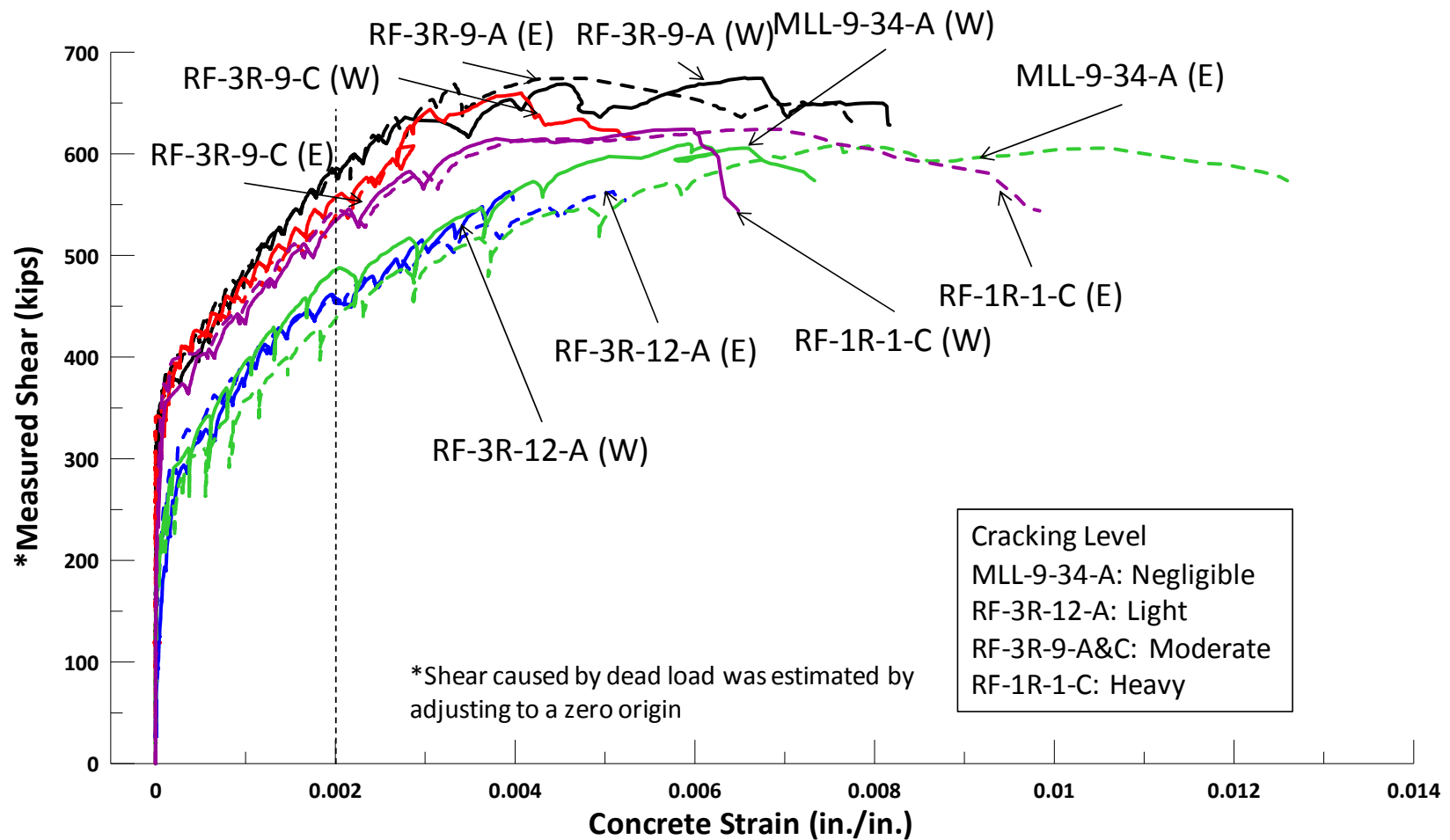


Figure 5.43 Comparison of average vertical strains

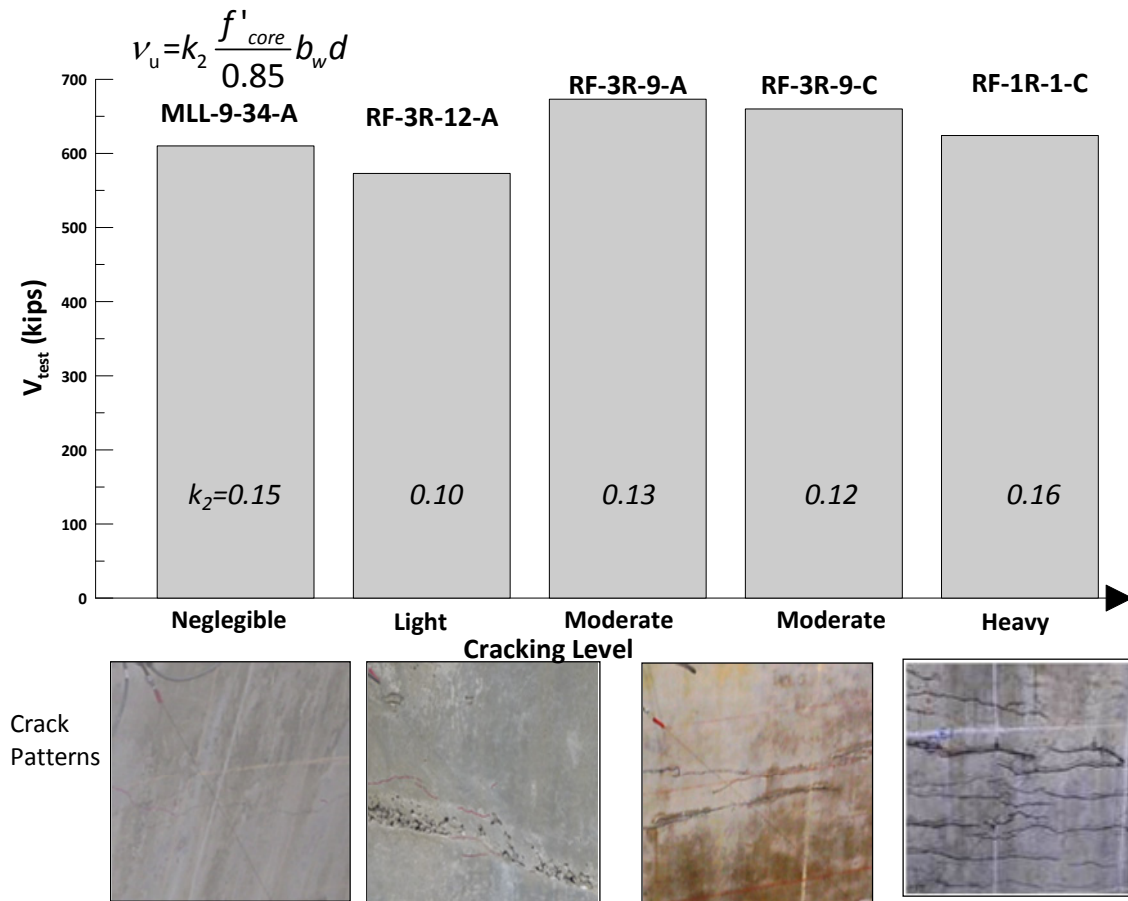


Figure 5.44 Relationship of V_{test} vs. cracking level

In Figure 5.44, the relationship of the ultimate shear capacity vs. ASR and/or DEF cracking level is shown. There was no clear relationship found between the shear capacity and ASR and/or DEF cracking level. The beams with moderate cracking (RF-3R-9-A and C) had higher capacity than all the other beams. However, these differences are more likely due to experimental scatter and other deficiencies in the beams rather than ASR and/or DEF cracking. Sample pictures for various cracking levels in Figure 5.40 and Figure 5.44 did not show distinct differences in cracking levels. This is because for a beam subjected to ASR and/or DEF deterioration, the cracking is usually concentrated at the end block. In Figure 5.45, cracking patterns in end block and web are compared.

The failure mode of each specimen is shown in Table 5.2. Three of the five test specimens failed in strut crushing. One failed in shear tension, and the other failed due to

poor cold joint. This result indicates that the main failure mode for the deep beam with a shear span-to-depth ratio of 1.85 is strut crushing, corresponding to the results reported by Birccher et al. (2008) that direct strut is the main failure mechanism of the reinforced concrete deep beams (shear span-to-depth ratio < 2.0). However, the specimen with shear tension failure is of interest for investigating an appropriate strut-and-tie model to accurately predict the shear capacity and the failure mode of the prestressed trapezoidal box beams. This part will be discussed in Chapter 6.

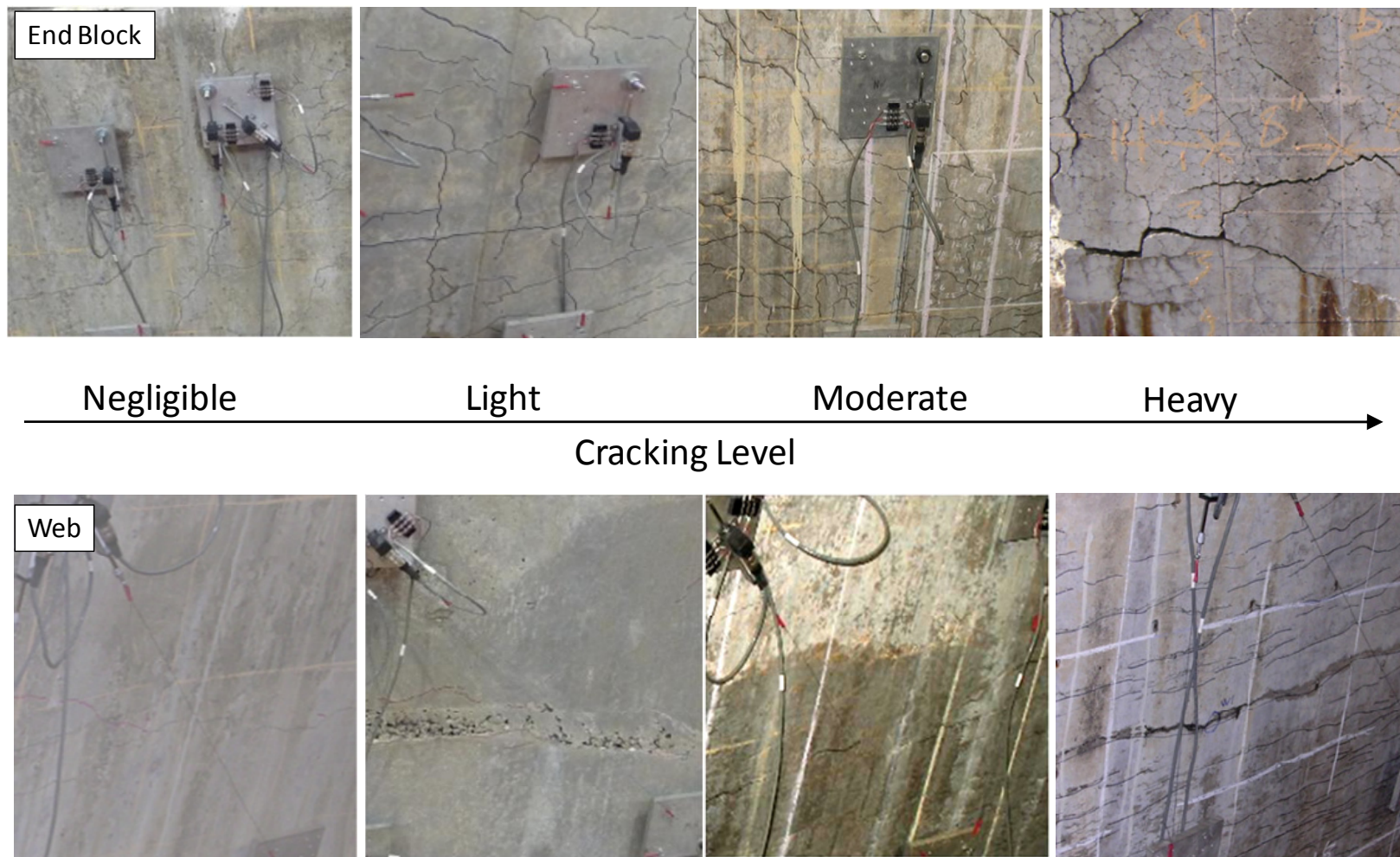


Figure 5.45 Cracking pattern in end block and web

From Figure 5.46, it can be observed that RF-3R-12-A exhibited the most deformation, indicating that the cold joint significantly affected the behavior of the beam. The two beams with lower cracking (RF-3R-12-A and MLL-9-34-A) exhibited larger deformation than the other three beams with moderate cracking to heavy cracking.

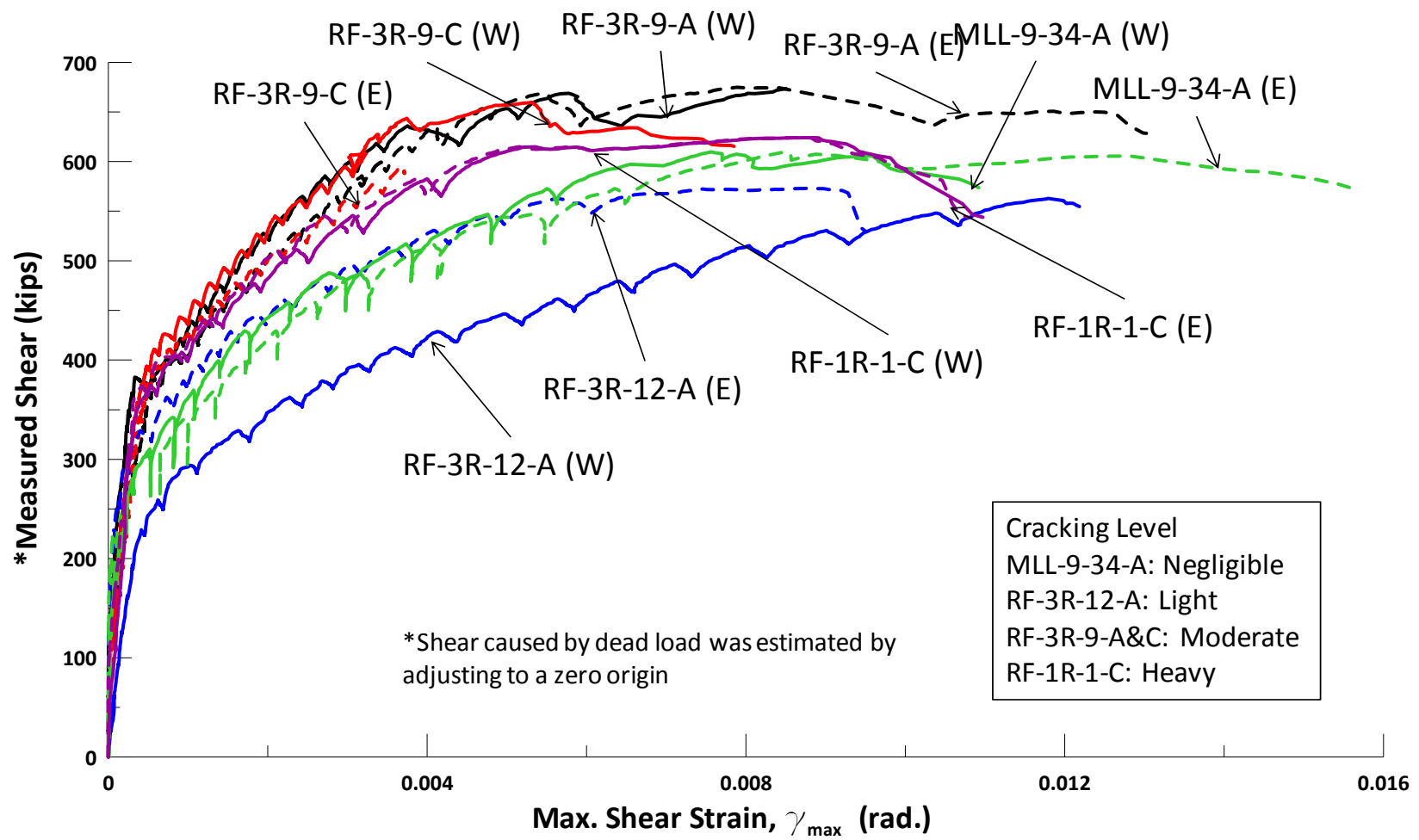


Figure 5.46 Comparison of maximum shear strains (γ_{max})

5.4 SUMMARY

In this chapter, the results of the web shear tests for five prestressed trapezoidal box beams with low to high ASR and/or DEF damage were presented. The results showed that the beams with higher cracking level had a higher load when new diagonal cracks formed. Highly cracked beams also had fewer new diagonal cracks compared to less cracked beams. These two observations indicate that beams with more ASR and/or DEF cracking may provide very little warning before failure occurs. Therefore, beams with ASR and/or DEF cracking that are in service should be monitored at regular intervals.

No distinct reduction of shear capacity was observed even in the specimen with heavy cracking. The main failure mode for the prestressed trapezoidal box deep beams with a shear span-to-depth ratio of 1.85 is strut crushing. One of the specimens – RF-3R-12-A, had a severe cold joint. The test results showed that failure occurred along the cold joint because there was a weak plane in web of the beam. In addition, a wood spacer used to position the Styrofoam void in the beam floated and resulted in unequal web widths in the beam. These two factors (cold joint and thin flange) caused a premature failure in RF-3R-12-A.

CHAPTER 6

Assessment with Code Provisions

6.1 OVERVIEW

The beams in this study were all tested with a shear span-to-depth ratio of 1.85. Beams with such shear span-to-depth ratios less than two are considered as deep beams in ACI 318-08 and AASHTO LRFD 2008. According to these provisions, a deep beam should be designed using strut-and-tie modeling. In order to examine the shear capacities of the beams with ASR and/or DEF deteriorations that were tested in this study, strut-and-tie models were used to evaluate the shear capacities following procedures in AASHTO LRFD design provision, ACI 318-08 building code provision, and a provision proposed in TxDOT Project 5253. A brief introduction of strut-and-tie modeling and differences between these provisions are presented first. Then two different types of strut-and-tie models – one-panel models and combination models will be utilized to examine the shear capacities of the test specimens. A sample calculation will then be presented to demonstrate the philosophy underlying the strut-and-tie model. Finally, a comparison of the procedures will be used to develop a simple and conservative method for determining the shear capacities of the specimens tested.

6.2 BACKGROUND OF STRUT-AND-TIE MODELING

Strut-and-tie modeling (STM) is a design method for simplifying the complex state of stresses within reinforced and prestressed concrete members to a set of stress paths. Structures are modeled as truss structures. The stress paths correspond to the axis of the truss members. Truss members that are in compression are called *struts* while those in tension are called *ties*. The intersections of these elements are called *nodes*. Struts, ties, and nodes comprise a strut-and-tie model. Forces in struts, ties, and nodes can be determined from statics and should not exceed their ultimate strength. The ultimate strength of these elements (strut, tie, and nodes) is determined from empirical observation.

Combining the empirical strengths of these elements with the truss model, a strut-and-tie model can be developed.

STM is very useful when designing structures in which plane sections do not remain plane, such as deep beams, dapped ends, corbels, and post-tensioned anchorage zones. The behavior of these elements does not conform to flexural behavior and kinematic compatibility usually causes difficulty during analysis. STM neglects kinematic compatibility, but considers equilibrium and constitutive relationships. The constitutive relationships are established from empirical observations of struts, ties, and nodes to determine their yield or ultimate strength conditions. Therefore, a solution using STM is a lower bound solution, which means that computed capacity from a strut-and-tie model is always less than or at most equal to the structure's actual capacity. This conservatism is the most important advantage of STM. Since the stresses applied to the elements in a strut-and-tie model cannot exceed their yield or plastic capacity, the strut-and-tie model not only provides an estimate of capacity but also the failure mode.

6.3 ELEMENTS OF STRUT-AND-TIE MODELS

Before applying strut-and-tie modeling to predict ultimate shear capacities, each component of a strut-and-tie model is examined here.

6.3.1 Struts

Struts are the elements that carry compression within the strut-and-tie model. The basic strut is prismatic with uniform cross section over its length. The compression zone in a beam's flexural region is an example of a prismatic strut (Figure 6.1).

Another major type of strut in a strut-and-tie model is bottle-shaped, which means that the strut spreads laterally along its length, generating tensile stresses transverse to the strut. These tensile stresses may cause cracking along the strut length, and therefore transverse reinforcement should be provided in order to control cracking. More research related to crack-control reinforcement can be found in TxDOT Project 5253 (Bircher et al. 2008). Bottled-shaped struts are usually simplified to prismatic struts, but this

simplification does not eliminate the fact that tensile stresses exist due to the spreading of the struts. Therefore, crack-control reinforcement is required.

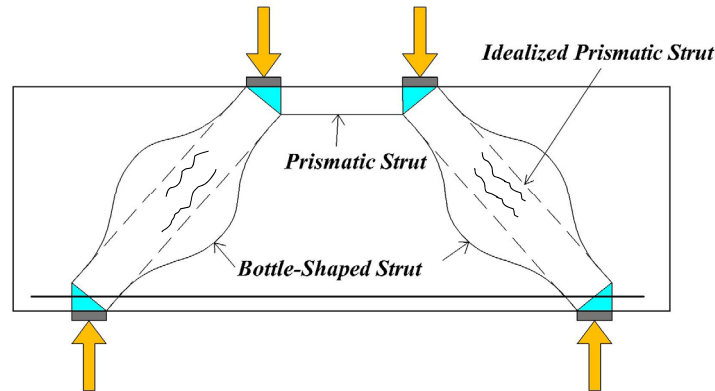


Figure 6.1 *Prismatic and bottle-shaped struts*

6.3.2 Ties

Ties are the elements that carry tension in a strut-and-tie model, and represent reinforcing or prestressing steel. Therefore, the shape of ties is much more straightforward than struts. The allowable stresses of ties are usually yielding strength of steel. Location of a tie should correspond to the centroid of the steel that the tie represents.

6.3.3 Nodes

Nodes are defined as points in a strut-and-tie model where the axes of struts, ties, and concentrated forces acting on the joints intersect. Nodal zones consist of the volume of concrete at a node that is assumed to transfer strut-and-tie forces through the node (ACI 318, 2008). In the following discussion nodal zones are referred to as nodes. Based on the elements that frame into nodes, nodes can be categorized into three major types – CCC, CCT, and CTT nodes where C stands for compression and T, tension (Figure 6.2). If there are more than three elements framing into a node, additional elements are required to combine with other elements to get resulting forces so that the node is subjected to three forces as shown in Figure 6.3.

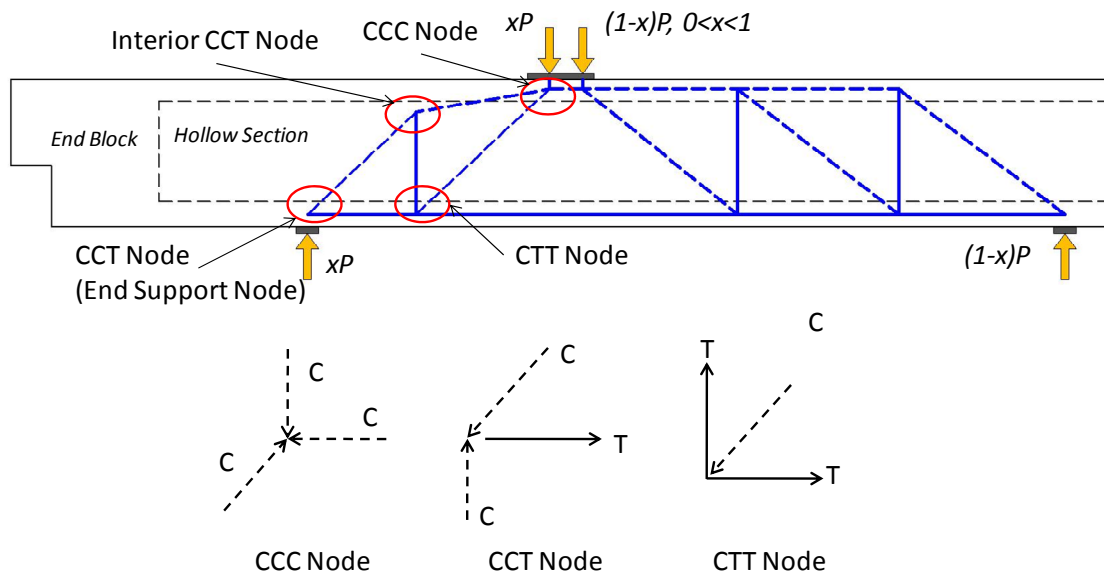


Figure 6.2 Classification of nodes

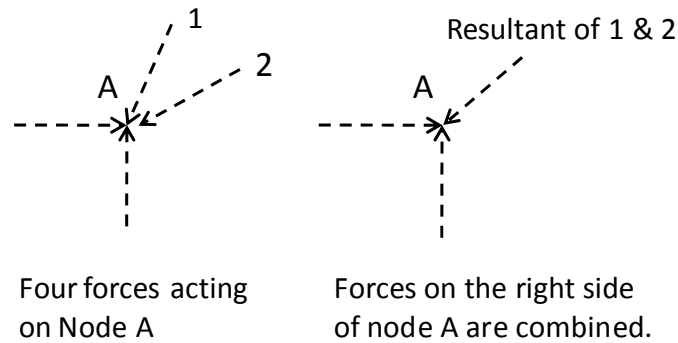


Figure 6.3 Resolution of forces on a node

According to the state of stresses on nodes, nodes can be categorized as hydrostatic nodes or non-hydrostatic nodes. Hydrostatic nodes are subjected to equal stresses on each face of the node. Because the stresses are normal to the surface, there are no shear stresses at the node and the ratio of the area of the face is equal to the applied force. In contrast, non-hydrostatic nodes are loaded with unequal stresses on each face of the nodes.

The main advantage of hydrostatic stresses is simplicity in dimensioning nodes. However, when the strut angle becomes shallower (larger shear span-to-depth ratio),

hydrostatic nodes can result in unrealistically large dimensions of back face and strut-to-node interface (Figure 6.5). However, the size of non-hydrostatic nodes only slightly decreases and more closely reflects the actual stresses in the nodal region. Therefore, non-hydrostatic nodes will be used for all STMs in this study. More details for hydrostatic and non-hydrostatic nodes can be found in TxDOT Project 5253 (Bircher et al. 2008).

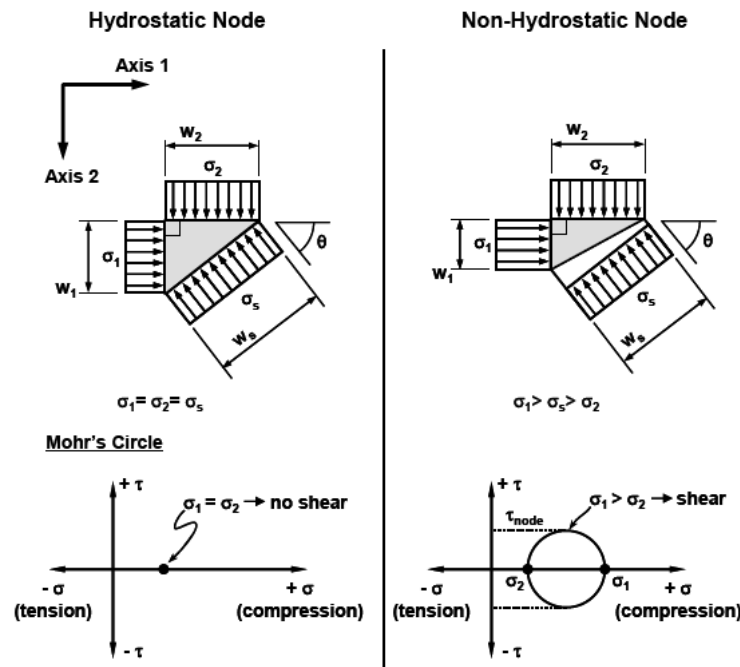


Figure 6.4 Stresses on hydrostatic and non-hydrostatic nodes (Thompson, 2002)

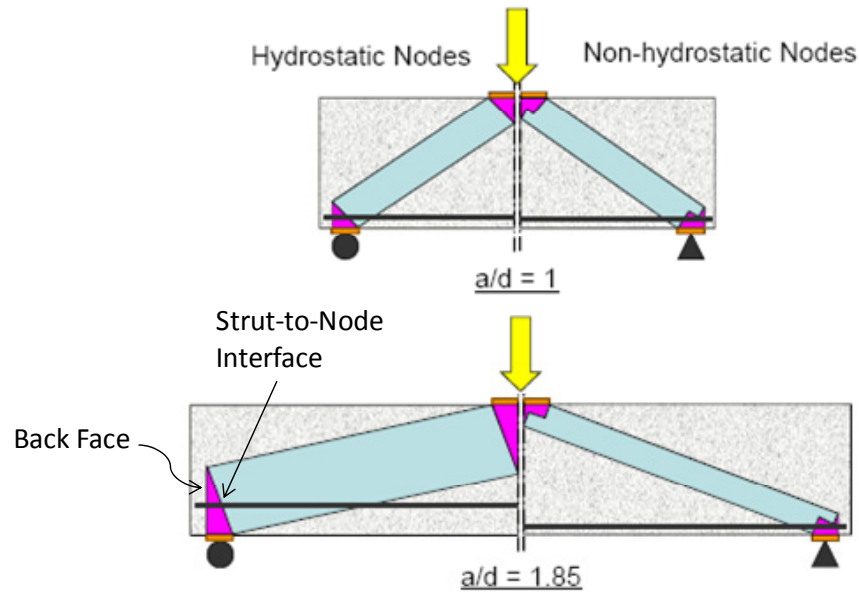


Figure 6.5 *Difference between hydrostatic and non-hydrostatic nodes (Birrer et al. 2008)*

6.3.4 Proportioning STM Elements

The techniques for node proportioning have been well established by previous researchers. Generally, the proportioning techniques used herein are the same as that employed in TxDOT Project 5253. The principal of node proportioning introduced in this section is used to evaluate the beams in this study.

6.3.4.1 Proportioning a CCC Node

CCC nodes always appear at the load point of the specimens in this study (Figure 6.2). Frequently, it is easier for calculation to split the load into two parts according to the reactions in the two supports. For the beam shown in Figure 6.2, the applied load, P , is split into xP and $(1-x)P$ according to the reactions in the two supports. Referring to the CCC node shown in the figure, the close-up of the node is presented in Figure 6.6. The length of the bearing face is set equal to xl_b where l_b is the bearing plate length. The height of the back face, h_n , is assumed to be equivalent to the depth of the rectangular stress block obtained from flexural analysis. This assumption may not be valid within a

D-region; however, this assumption is well-established in practice and is conservative. The procedures to obtain h_n is explained in 6.6. The length of the strut-to-node interface, w_{int} , is determined based on the length of the bearing face (xl_b), height of the back face (h_n), and the angle of the strut framing into the strut-to-node interface. The length of the strut-to-node interface can be obtained by the following equation:

$$w_{int} = xl_b \sin \Phi + h_n \cos \Phi \quad (6-1)$$

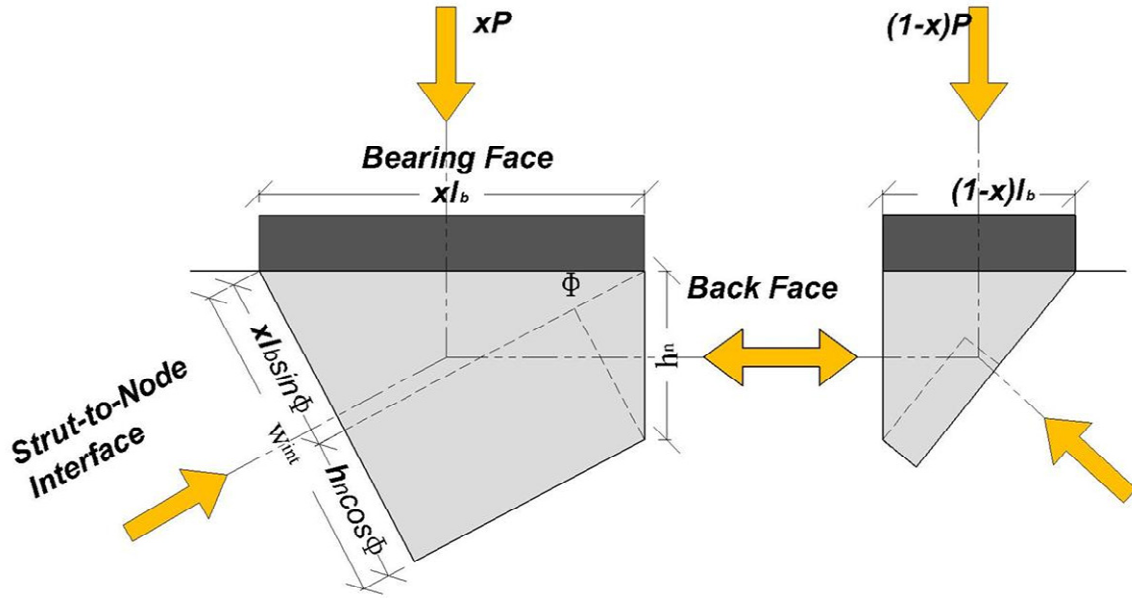


Figure 6.6 CCC node

6.3.4.2 Proportioning a CCT Node

The CCT node shown in Figure 6.2 is magnified and presented in Figure 6.7. This node at the end support of the beam may be referred to as an end support node. The bearing face of a CCT node has the same dimension as the bearing plate (l_b). The height of the back face (h_n) is taken as twice of the distance from centroid of the bonding prestressing strands to the extreme tension fiber of the beam. The width of the strut-to-node interface (w_{int}) can be also determined by Equation 6-1 with $x=1$.

$$w_{int} = l_b \sin \Phi + h_n \cos \Phi$$

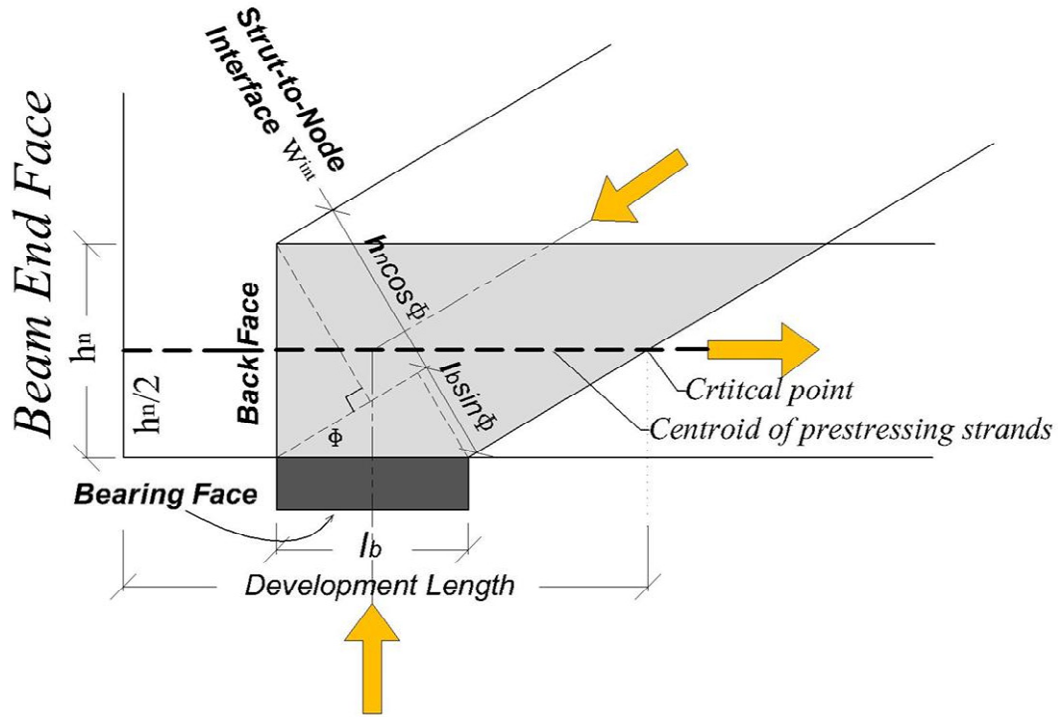


Figure 6.7 CCT node

Another interior CCT node can be seen in Figure 6.2. It is reasonable to assume that the diagonal struts in the beam will fan out and engage several stirrups (Figure 6.8). It is difficult and impractical to proportion such an interior node. The node faces that the fanning struts frame into can be imagined very wide; therefore, it is not necessary to check the imaginary strut-to-node interface. However the strength of the tension tie has to be ensured. According to recommendations by Wight and Parra-Montesinos (2003), the number of the stirrups involved in the vertical tie can be determined by the minimum angle between strut and tie, i.e. 25 degree. In the specimens tested in this study, the stirrups are provided by pairs of U-stirrups tied together with a 16 in. splice (Figure 6.9). According to 5.11.2.6.4 of AASHTO LRFD (2008), pairs of U-stirrups that are placed to form a closed unit can be considered properly anchored and spliced if length of laps is not less than $1.7l_d$ where l_d is the development length for bars in tension. For No.11 bar and smaller:

$$l_d(\text{in.}) = \frac{1.25 A_b f_y}{\sqrt{f'_c}} \geq 0.4 d_b f_y \quad (\text{AASHTO 5.11.2.1.1})$$

Where

A_b = area of bar (in^2) = 0.2 in^2

f_y = specified yield strength of reinforcing bars (ksi) = 60 ksi

f'_c = specified concrete strength at 28 days

d_b = diameter of bar (in.)

The stirrups used in this study are #4 bars and concrete strength is around 5 ksi.

Thus

$$l_d = \frac{1.25 \cdot 0.2 \cdot 60}{\sqrt{5}} = 6.7 \text{ in.} < 0.4 \cdot 0.5 \cdot 60 = 12 \text{ in.}$$

$$\therefore l_d = 12 \text{ in.}$$

The required length of splice ($1.7l_d$) for the test specimens is around 20 in. and is greater than that provided (16 in.). However, no anchorage failure of the stirrups was observed during the tests; therefore, it seems reasonable to assume that the U-stirrups provided sufficient anchorage and splice length for the vertical tie. As long as sufficient anchorage of the reinforcing bars is provided, the interior CCT node can be taken as a smeared node and it is not necessary to check the stresses on the node.

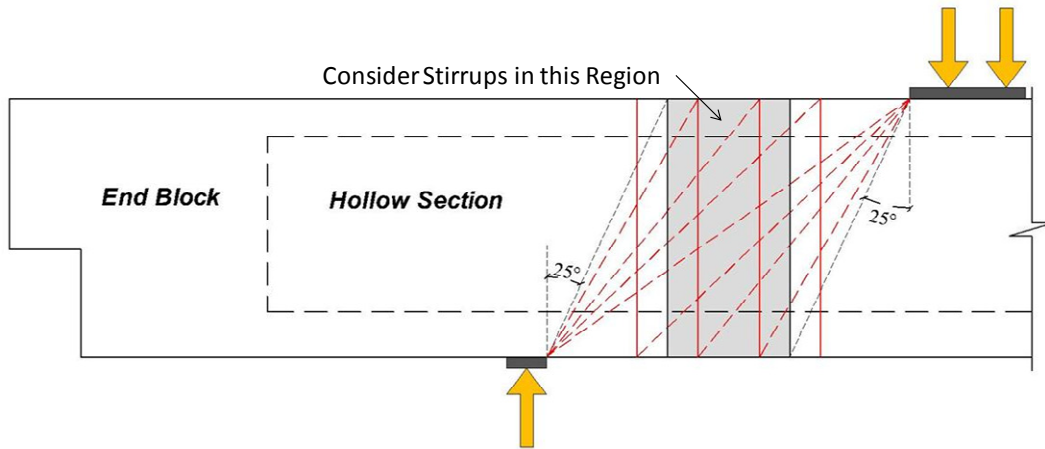


Figure 6.8 CCT node

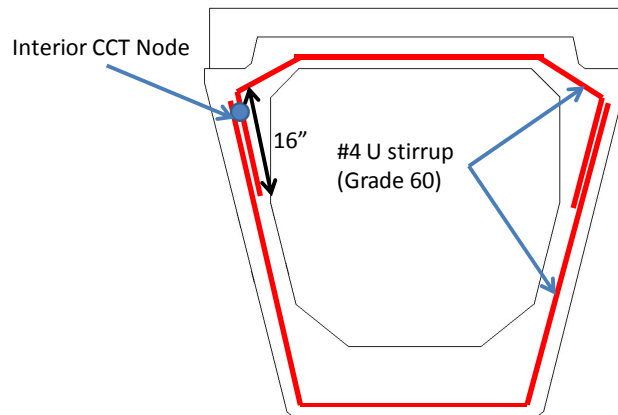


Figure 6.9 U stirrups

6.3.4.3 Proportioning a CTT Node

The CTT node shown in Figure 6.2 is magnified and presented in Figure 6.10. This type of node is also an interior node, which is not bounded by a bearing plate. To proportion such a node, the number of the stirrups can be first determined in the same way as was done for the interior CCT node. After determining the number of the stirrups involved, the dimension of the exterior face, l_a , can be determined as the distance between two outermost stirrups plus $12d_b$ as recommended by AASHTO LRFD (2008), where nominal d_b is the diameter of the stirrup. The back face, h_n , of the node is calculated the same way as for an end support CCT node. Finally, the width of the strut-to-node interface can be determined as the CCC and end support CCT nodes. In fact, the CTT node is an interior node. Forces from the compression field fan out or smear and are equilibrated by vertical and horizontal tension ties. Therefore, as long as the strength of the stirrups is sufficient, the CTT node can be considered as a smeared node and does not need to be checked.

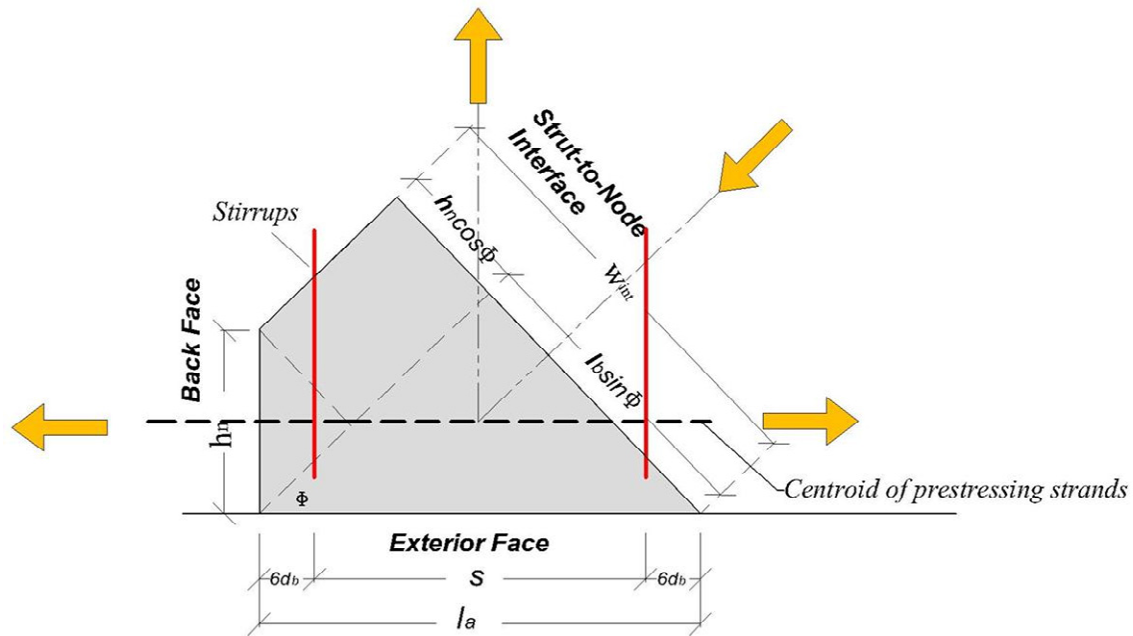


Figure 6.10 CTT node

6.3.4.4 Proportioning a Strut

Struts can be prismatic and bottle-shaped (Figure 6.1). Prismatic struts usually occur in the compression zone of a beam's flexure region. Most struts in strut-and-tie models are bottle-shaped, and forces concentrate and bear on the strut-to-node interfaces. Therefore, the highest stress always occurs at the strut-to-node interface. The critical proportions of a strut are based on the width of the strut-to-node interface. Therefore the critical capacity of a strut is considered equivalent to the capacity of the strut-to-node interface (Birccher et al. 2008).

6.3.4.5 Proportioning a Tie

Location and direction of a tie should correspond to the centroid and the direction of the steel that the tie represents. Proper bar distribution, spacing, development deserve the most consideration. Ties must be properly anchored in the nodal zone. ACI 318 allows the development length to be conservatively taken from the beam end face to the critical point for the bonded tendons (Figure 6.7).

6.4 CONCRETE EFFICIENCY FACTORS IN CURRENT STM SPECIFICATIONS

In this section, the concrete efficiency factors in current US provisions - ACI 318-08 and AASHTO LRFD (2008), and in TxDOT Project 5253 are briefly summarized. In current US provisions, ACI 318-08 and AASHTO LRFD (2008) assign different efficiency factors for the strut and the strut-to-node interface. This inconsistency confuses engineers when determining the capacity of the strut-to-node interface. However, based on recent experimental work done under TxDOT Project 4371 (Brown et al. 2006), it was concluded that for beams with short shear spans, failure typically occurred at the interface between a node and a strut. This observation supports the opinion recognized by *fib* (1999) that the critical stress in a strut is at the strut-to-node interface. Therefore, the efficiency factors for the strut-to-node interface as defined by ACI 318-08 and AASHTO LRFD (2008) are substituted by those used for the strut and are tabulated in Table 6.1 to Table 6.3. The new efficiency factors proposed in TxDOT Project 5253 incorporate ACI 318-08, AASHTO LRFD (2008), and *fib* (1999) provisions and are also presented in the tables.

CCC Node

The efficiency factors for the three faces of a CCC node are listed in Table 6.1. The back face and bearing face efficiency factors are the same for all three methods (i.e. 0.85). At the back face, the stress limit ($0.85f'_c$) is the same as that for flexural analysis. In TxDOT Project 5253, this efficiency factor was also used for the back face. Similarly, ACI 318-08 and AASHTO LRFD (2008) limit the bearing capacity of unconfined concrete to $0.85f'_c$ and the efficiency factors on a bearing face in these two provisions are consistent. In TxDOT Project 5253, this value was adopted for the efficiency factor at the bearing face.

For the efficiency factor for the strut-to-node interface, ACI 318-08 considers the minimum steel ratio to control the tension force due to the spreading of the strut (Figure 6.11).

$$\sum \frac{A_{si}}{b_s s_i} \sin \alpha_i \geq 0.003 \quad (6-2)$$

Struts with steel ratio satisfying the equation above are given a higher efficiency factor (0.64), whereas those without reinforcement satisfying the equation are given a lower efficiency factor (0.51). AASHTO LRFD uses the same efficiency factors (0.85) for the strut-to-node interface of CCC nodes. TxDOT Project 5253 proposes that the efficiency factor assigned to the strut-to-node interface decreases as the compressive strength of concrete increases. It also requires that the steel ratio should be greater than 0.003 in horizontal and vertical directions respectively; therefore, it is more stringent than ACI 318-08. For the strut without steel ratio satisfying the minimum requirement, the efficiency factor is taken as 0.45.

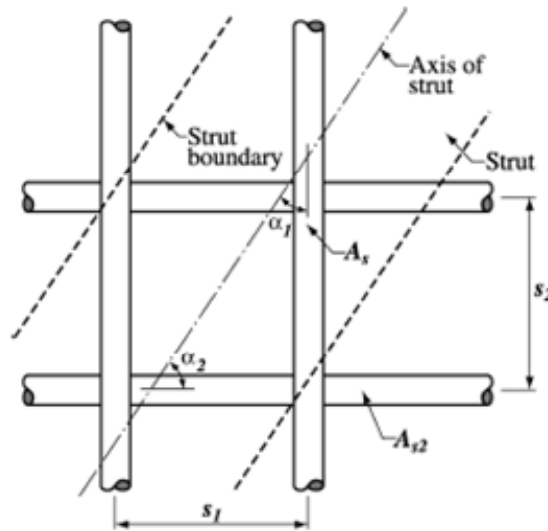


Figure 6.11 Reinforcement cross a strut (ACI 318 2008)

Table 6.1 Efficiency Factors for a CCC node

Node Face	Design Code	Efficiency Factors
Back Face	ACI 318-08	$0.85 \times 1 = 0.85$
	AASHTO LRFD (2008)	0.85
	TxDOT Project 5253	0.85
Bearing Face	ACI 318-08	$0.85 \times 1 = 0.85$
	AASHTO LRFD (2008)	0.85
	TxDOT Project 5253	0.85
Strut-to-Node Interface	ACI 318-08	$0.85 \times 0.75 = 0.64$ when $\rho > \rho_{min}^*$ $0.85 \times 0.60 = 0.51$ when $\rho < \rho_{min}^*$
	AASHTO LRFD (2008)	0.85
	TxDOT Project 5253	$0.45 \leq 0.85 - f'_c / 20 \text{ksi} \leq 0.65$
* ρ_{min} is minimum steel ratio defined in section A3.3 of ACI 318-08 A3.3		

CCT Node

The efficiency factors for the three faces of a CCT node are listed in Table 6.2. The efficiency factors in a CCT node are generally smaller than those in a CCC node because the presence of tensile stress reduces the effective compressive strength of the concrete. Stress resisted by the back face of a CCT node may be attributed to bearing from an anchor plate or anchorage of the tie reinforcement. In ACI 318-08 and AASHTO LRFD (2008) provisions, the tension force from the tie is taken as a concentrated load on the back face of a CCT node whether the stress is distributed by an anchor plate or is developed through bond along the tie reinforcement. However, in *fib* (1999) the anchorage length and bearing pressure at the support often govern the node dimension. This implies that the stress caused by bonding of an anchored bar will not govern the capacity of the back face of a CCT node. Accordingly, TxDOT Project 5253 distinguishes the source of stress on the back face of a CCT node (i.e. anchor plate and

bonding of the tie reinforcement, Figure 6.12). The efficiency factor for the back face proposed in study TxDOT Project 5253 is for an anchor plate.

Table 6.2 Efficiency Factors for a CCT node

Node Face	Design Code	Efficiency Factors
Back Face	ACI 318-08	$0.85 \times 0.80 = 0.68$
	AASHTO LRFD (2008)	0.75
	TxDOT Project 5253	0.70
Bearing Face	ACI 318-08	$0.85 \times 0.80 = 0.68$
	AASHTO LRFD (2008)	0.75
	TxDOT Project 5253	0.70
Strut-to-Node Interface	ACI 318-08	$0.85 \times 0.75 = 0.64$ when $\rho > \rho_{\min}^*$ $0.85 \times 0.60 = 0.51$ when $\rho < \rho_{\min}^*$
	AASHTO LRFD (2008)	$\frac{1}{0.8 + 170\varepsilon_1} \leq 0.85$
	TxDOT Project 5253	$0.45 \leq 0.85 - f'_c / 20 \text{ksi} \leq 0.65$
* ρ_{\min} is minimum steel ratio defined in section A3.3 of ACI 318-08 A3.3		

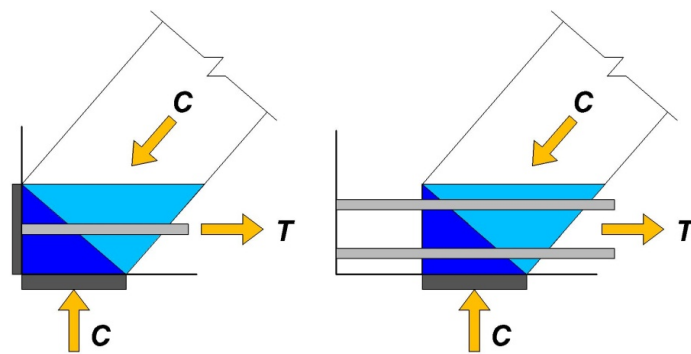


Figure 6.12 Back face of a CCT node (a) bearing of an anchor plate (b) bonding stress

In ACI 318-08, the efficiency factors at the strut-to node interface of CCC and CCT nodes are the same. In TxDOT Project 5253, the efficiency factor assigned to the CCC strut-to-node interface can also be assigned to CCT strut-to-node interface. Rather than using the amount of steel cross the strut, AASHTO LRFD (2008) determines the efficiency factor at the strut-to-node interface based on the tensile strain in the direction of the adjoining tensile tie. The efficiency factor is based on the Modified Compression Field Theory developed by Vecchiano and Collins (1986). The calculation procedures are based on the following two equations in AASHTO LRFD (2008):

The Efficiency factor

$$v = \frac{1}{0.8 + 170\varepsilon_l} \leq 0.85 \quad (AASHTO 5.6.3.3.3-1)$$

$$\varepsilon_l = \varepsilon_s + (\varepsilon_s + 0.002) \cot^2 \phi \quad (AASHTO 5.6.3.3.3-2)$$

Where

ϕ = the smallest angle between the compressive strut and the adjoining tie

ε_s = the tensile strain in the concrete in the direction of the tension tie

The efficiency factor reduces as the tensile strain in the concrete in the direction of the tension tie increases. The tie strain increases as the angle between strut and tie decreases. As a result, tensile strain increases as the strut becomes shallow. The tie force also depends on the compression force in the strut; therefore, the tie force, the strut force, and efficiency factor have to be iterated until the solution converges.

CTT Node

The efficiency factors for the three faces of a CTT node are listed in Table 6.3. Generally, the efficiency factors for a CTT node are smaller than those of a CCT node because of the presence of an additional tension stress. Because transverse reinforcement is usually distributed over a length of the longitudinal reinforcement in beams (Figure 6.10), a CTT node is typically considered a “smeared” node if bars are anchored properly. Schlaich et al. (1987) mentioned that “*for wide concrete stress fields joining each other or with tensile ties, which consist of many closely distributed reinforcing bars, the*

deviation of forces may be smeared (or spread).” Besides, as long as the strength of anchorage in a smeared node is ensured, concrete stresses in smeared node are not critical.

Table 6.3 Efficiency Factors for a CTT node

Node Face	Design Code	Efficiency Factors
Back Face	ACI 318-08	$0.85 \times 0.60 = 0.51$
	AASHTO LRFD (2008)	0.65
	TxDOT Project 5253	N/A
Exterior Face	ACI 318-08	$0.85 \times 0.60 = 0.51$
	AASHTO LRFD (2008)	0.65
	TxDOT Project 5253	N/A
Strut-to-Node Interface	ACI 318-08	$0.85 \times 0.75 = 0.64$ when $\rho > \rho_{\min}^*$ $0.85 \times 0.60 = 0.51$ when $\rho < \rho_{\min}^*$
	AASHTO LRFD (2008)	$\frac{1}{0.85 + 170 \epsilon_1} \leq 0.85$
	TxDOT Project 5253	N/A
* ρ_{\min} is minimum steel ratio defined in section A3.3 of ACI 318-08 A3.3		

6.5 SHEAR CAPACITY BY STRUT-AND-TIE MODELING

Strut-and-tie modeling is a powerful method for designing reinforced and prestressed concrete because it considers the stress paths in a truss mechanism. However, variations of strut-and-tie models can result from different decisions made by engineers. As a result, any strut-and-tie model can be analyzed but some may be better than others in terms of material usage, constructability, or mode of failure. A good strut-and-tie model should realistically reflect the stress paths in a structure. In this study, the shear capacity of ASR and/or DEF cracked prestressed trapezoidal box beams was calculated using two types of strut-and-tie models – single-panel models (Figure 6.13(a)) and combination models (a one-panel model plus a two-panel model, Figure 6.13(c)).

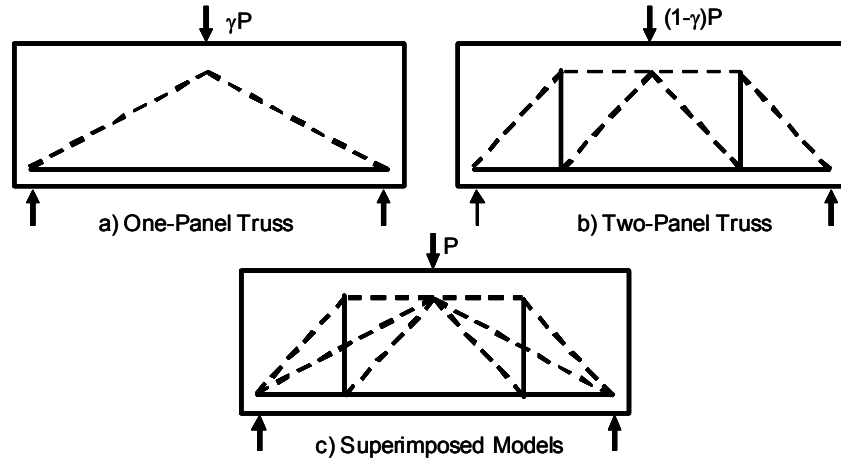


Figure 6.13 Superimposed truss model (Brown et al. 2006)

The results obtained from TxDOT Project 5253 indicated that for a reinforced concrete beam with shear span-to-depth ratio smaller than two, the effect of transverse reinforcement is not significant, and a single-panel model is appropriate. It is simple, appropriately accounts for stress concentrations in the nodal zone, and is consistent with dominant shear transfer mechanism. However, when the shear span-to-depth ratio is greater than two, the single-panel model is not appropriate and a sectional shear model is recommended. Besides, results reported in TxDOT Project 5253 showed that for a shear span-to-depth ratio of 1.85 (equal to that was used in the current study), it can be argued that overlapping of a single-panel model and a two-panel model should be used. With a shear span-to-depth ratio (1.85), the single-panel model was considered to part (γ) of the total applied load and the two-panel model carried the remaining part ($1-\gamma$) of the total applied load. The effect of transverse reinforcement is considered using the two-panel model.

According to *fib* (1999), a load near a support of a beam may be transferred directly to support by an inclined strut (Figure 6.14). The transverse reinforcement may be designed to take a portion of the load according to the following equation.

$$\frac{F_1}{F} = \frac{\frac{2a}{z} - 1}{3} \quad (fib \ 6.34)$$

shear capacity. The data plotted using the results from Brown et al. are in good agreement with the test results reported by TxDOT Project 5253. When the shear span-to-depth ratio is 1.85, it is reasonable to allocate about 2/3 of the total applied load to the one-panel model and the remaining 1/3 of the total applied load to the two-panel model. Hence, in the calculations for combination models of the beams in this study, these ratios were used.

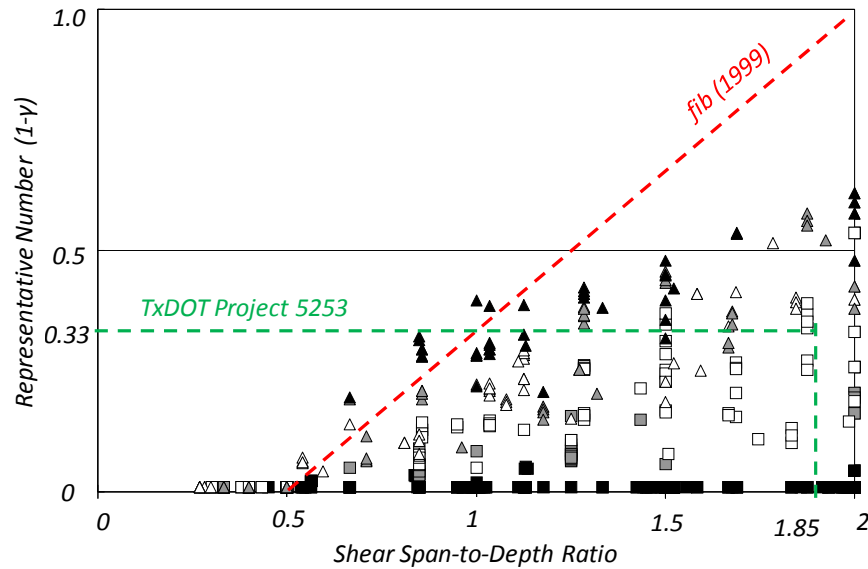


Figure 6.15 Representative number vs. shear span-to-depth ratio (adopted from Brown et al. 2006)

It should be noted that all test results or design provisions mentioned above do not specifically consider deep beams with trapezoidal box sections. Difficulties arise for such beams when determining nodal zone dimension. Calculations for one-panel models are simple and straightforward. Therefore, for sake of brevity, all calculations for one-panel model are given in Appendix D. A sample calculation for a combination model according to AASHTO LRFD (2008) is performed in the next section. By following this sample calculation, the reader is more likely to understand the application of the strut-and-tie model. The reason that AASHTO LRFD (2008) was chosen for the sample calculation is because the efficiency factors of strut-to-node interface of CCT node in AASHTO LRFD (2008) are obtained through iteration and are more complicated than those using ACI 318-08 and TxDOT Project 5253. Except for concrete efficiency factors, the procedures

using these provisions are similar, and the provisions in Appendix D can be more easily understood after reviewing the sample calculation.

6.6 SAMPLE CALCULATION (RF-3R-9-C)

Beam RF-3R-9-C was taken as an example to predict shear capacity by a combination model (one-panel and two-panel) according to AASHTO LRFD 2008 Specification. Before starting calculation, some general properties of the specimen which will be used in the following calculation are listed below for the reader easy to follow.

Design compressive strength $f'_c = 5.81$ ksi

$\beta_1 = 0.76$ (AASHTO 5.7.2.2)

Elastic modulus of prestressed steel, $E_p = 29000$ ksi

Nominal tensile strength of prestressed steel $f_{pu} = 270$ ksi

Nominal yield strength of prestressed steel $f_{py} = 0.9 f_{pu} = 243$ ksi (low-relaxation)

Nominal diameter of prestressed steel $d_{bs} = 0.5$ in.

Number of strands = 62

Total span = 297 in.

Shear span = 99 in.

Experimental shear capacity (V_{exp}) = 660 kips.

RF-3R-9-C Elevation (No Skew Dapped End)

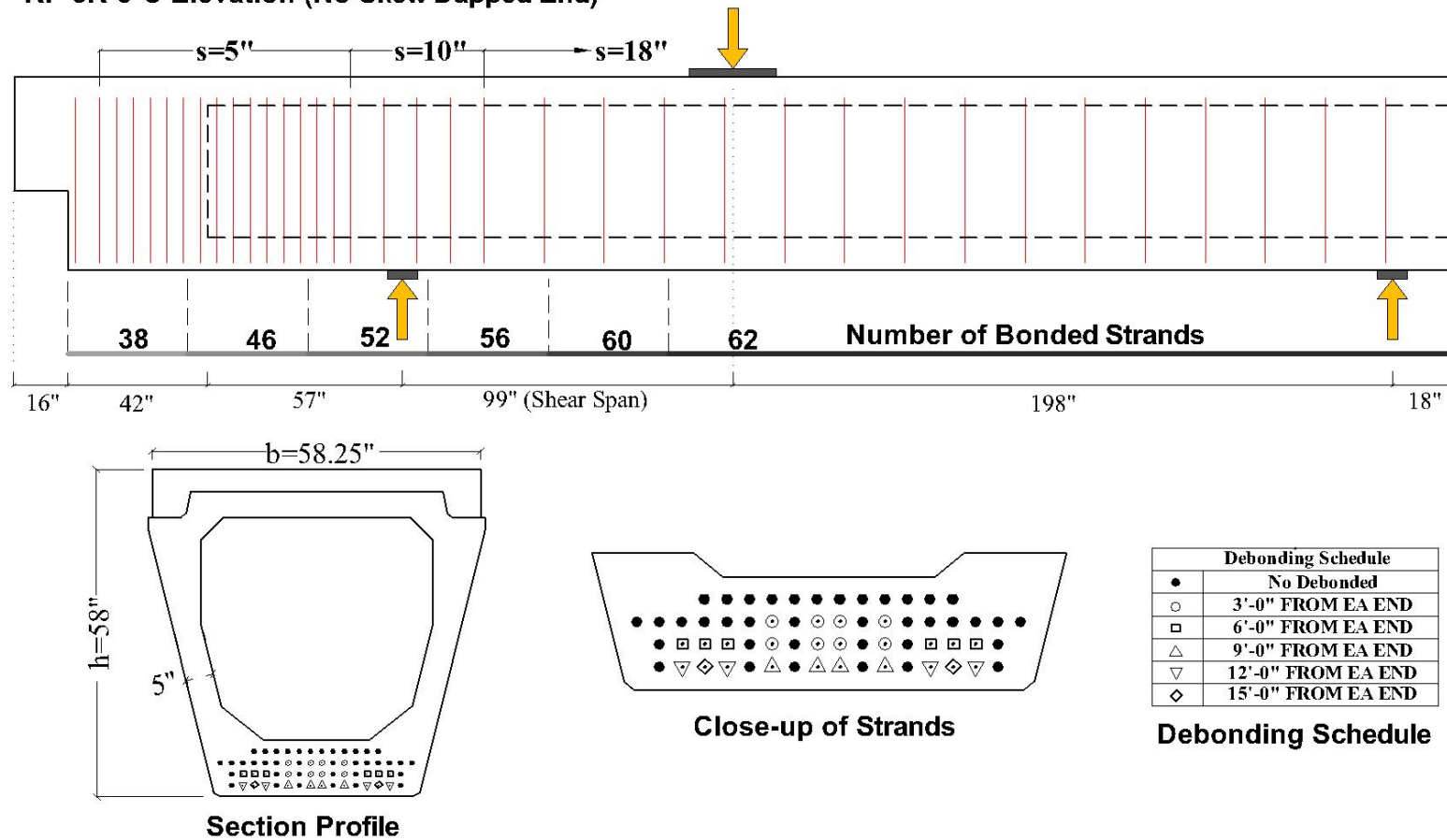


Figure 6.16 RF-3R-9-C elevation, cross section, and debonding schedule

In Figure 6.17, a sketch of the one-panel model and two-panel model is shown. Solid lines in the model stand for compression members whereas dashed lines stand for tension members. Nodes with the same labels have the same locations in the one-panel model and the two-panel model. From the classification of nodes in the shear span (Figure 6.2), Node 1 is an end support CCT node, Node 2 a CCC node, Node 3 an interior CCT node, and Node 4 a CTT node.

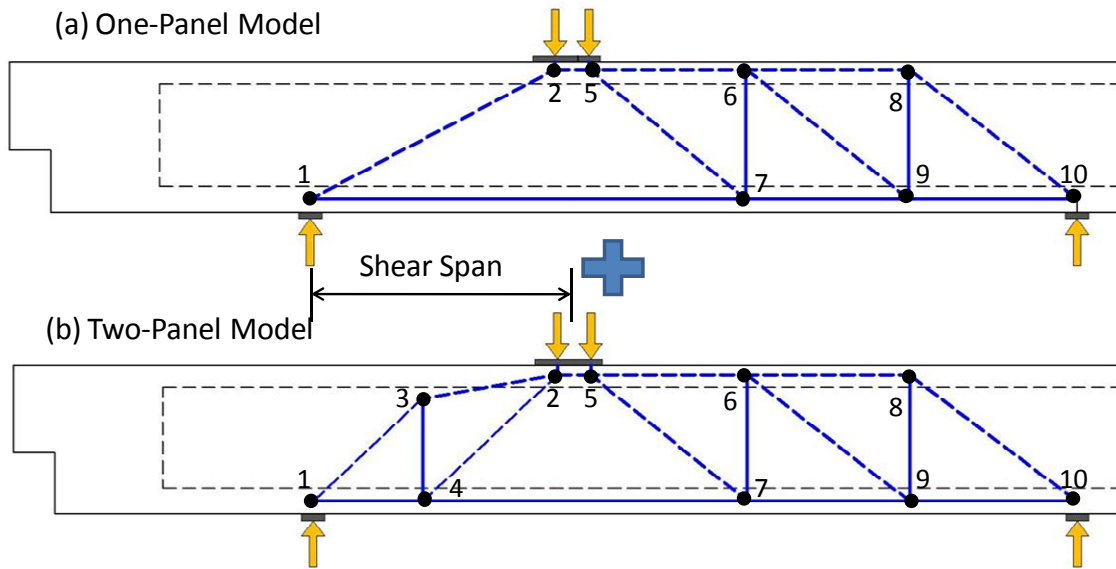


Figure 6.17 Sketch of (a) One-panel model and (b) two-panel model

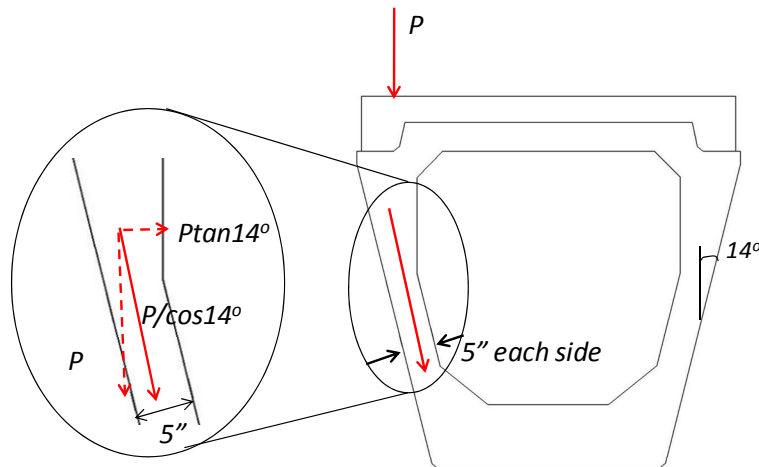


Figure 6.18 Close-up of the web

The cross section of the specimen is trapezoidal and the web is not perpendicular to the top and bottom flange (Figure 6.18). This inclination is very small (only 3% difference) and negligible; therefore, in the following calculations, this inclination will be neglected.

Back Face of the CCC Node

In order to determine the location of the top chords in the models, a rectangular stress block can be used to determine the back face of the CCC Node (Node 2) as mentioned in 6.3.4.1 (Figure 6.6). Although the beam may be far from flexure failure, it is conservative to determine the concrete compression block in this manner. From AASHTO LRFD (2008), the following equation can be used.

$$k=2\left(1.04-\frac{f_{py}}{f_{pu}}\right)=0.28 \quad (AASHTO 5.7.3.1.1-2)$$

$$c=\frac{A_{ps}f_{pu}}{0.85f'_c\beta_1b+\frac{kA_{ps}f_{pu}}{d_p}}=10.02 \text{ in.} \quad (AASHTO 5.7.3.1.1-4)$$

$$f_{ps}=f_{pu}\left(1-k\frac{c}{d_p}\right)=256 \text{ ksi} \quad (AASHTO 5.7.3.1.1-1)$$

Where A_{ps} was taken as the total area of the strands that are fully developed at the load point. Fifty-six strands were fully developed at the load point. Hence A_{ps} is 8.568 in² and d_p , the distance between the top of the beam and the centroid of 56 prestressing strands, was 52.86 in. The depth of the rectangular compression block was $\beta_1c = 7.62$ in. ACI 318-08 can also be used to determine the compression block.

$$f_{ps}=f_{pu}\left\{1-\left(\frac{\gamma_p}{\beta_1}\right)\left(\frac{\rho_p f_{pu}}{f'_c}+\frac{d(\omega-\omega')}{d_p}\right)\right\} \quad (ACI 18-3)$$

Where ω and ω' were zero because there was no non-prestressed steel and compression steel was neglected, γ_p was 0.28 because f_{py}/f_{pu} was 0.9, and ρ_p was the ratio of A_{ps} to bd_p ,

$$\rho_p=\frac{A_{ps}}{bd_p}=\frac{8.568}{58.25 \cdot 52.86}=0.002783$$

Thus

$$f_{ps}=270 \left[1 - \left(\frac{0.28}{0.76} \right) \left(0.002783 \cdot \frac{270}{5.81} \right) \right] = 257 \text{ ksi}$$

Then the depth of the rectangular stress block can be calculated as below

$$\frac{A_{ps}f_{ps}}{0.85bf'_c} = \frac{8.568 \cdot 257}{0.85 \cdot 58.25 \cdot 5.81} = 7.66 \text{ in.}$$

Comparing the value obtained from ACI to that from AASHTO LRFD (7.66 v.s. 7.62), the difference is negligible. The depth of the compression block in all beams will be calculated based on AASHTO LRFD (2008). The mid-depth of the compression block ($\beta_1 c/2$) is taken as the location of top chords (struts) of the strut-and-tie model, while the d_p is the axis of the bottom chords (ties). A unit applied load is assumed first. The unit load in the strut-and-tie model is separated into two forces according to the proportion of the reaction at each end. Each force acts on a length of top bearing plate according to the percentage of the total applied load (Figure 6.19). Member forces are then based on a unit applied load (1 kip). To get the real force in any member, the member force in the model can be obtained by multiplying the force due to unit load by the applied load to get the force in that member. For example, if the applied load is 500 kips, the left reaction is 334 kips or 500 be multiplied by 0.667. Only a direct strut and a horizontal tension tie are needed. Based on the above information, the one-panel model for RF-3R-9-C can be determined.

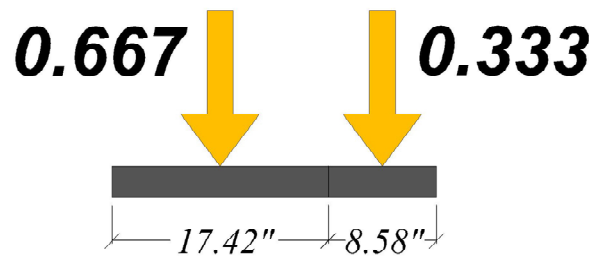


Figure 6.19 Proportioning the applied load on bearing plate

For the two-panel model, to determine the location of the vertical tie (member 34 in Figure 6.17(b)), the number of stirrups involved in member 34 has to be defined according to 6.3.4.2. Only one stirrup is located in the region defined and shown

in Figure 6.20. The vertical tie is located at the axis of the stirrup. Once the locations of the top chord, the bottom chord, and the vertical tie in the shear span are obtained, the two-panel model in the shear span can be analyzed.

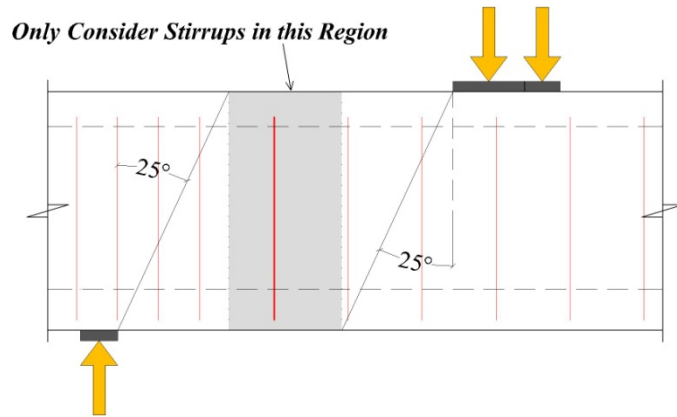


Figure 6.20 Determination the location of the vertical tie (Member 34) in the shear span

The truss models in the long span are determined by the forces in the top chord (member 25 in the both models) and bottom chord (member 17 in the one-panel model and member 47 in the two-panel model), and the forces in the bottom chord and top chord are only affected by the distance between them (i.e. inner lever arm). Since this distance is the same in the both models, the member forces in the long span will be the same, and hence the model in the long span will not be changed. Based on this observation, the model in the long span is independent of the selection of the model in the shear span being considered. The member forces in the long span can be easily obtained by summing the forces in each model. From inspection of the analytical results and from the experimental results, there are no struts, ties, or nodes critical in the truss model in the long span; therefore in the following calculation, only the model in the shear span will be considered (Figure 6.21).

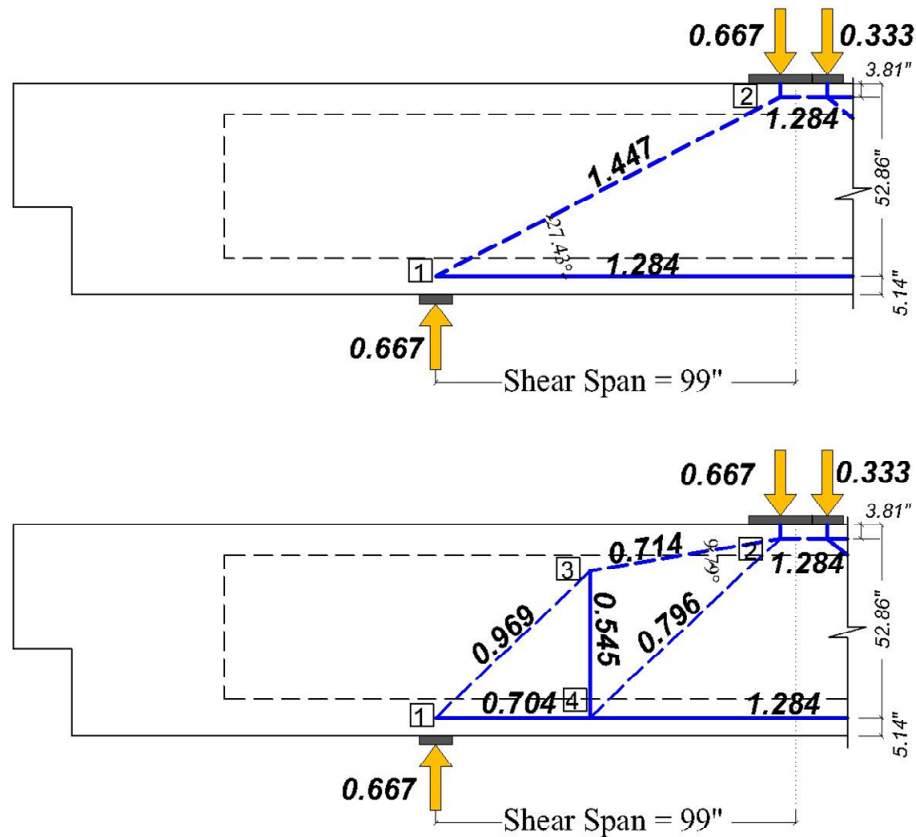


Figure 6.21 (a) One-panel model and (b) Two-panel model

Once forces from the unit load on the one-panel model and the two-panel model in the shear span have been determined, the next step is to apportion the applied load to the one-panel and two-panel models. According to the discussion in 6.5, this proportion (one-panel to two-panel) may be determined as two, i.e. the one-panel model carries twice the load that of the two-panel model.

Calculation Procedure

In order to determine the critical shear capacity of RF-3R-9-C, it is easy to try an arbitrary applied load first. The applied load that causes first failure in any element of either model is the computed ultimate load. Then the predicted shear capacity can be calculated according to statics. For sake of brevity, only the last step of trial-and-error is presented here.

Assume the total applied force is 132 kips. Therefore the applied forces in the one-panel model and two-panel model are:

$$P_d = 132 \times 2/3 = 88 \text{ kips} \quad \text{One-panel (direct strut) model}$$

$$P_m = 132 \times 1/3 = 44 \text{ kips} \quad \text{Two-panel (multi-panel) model}$$

Based on the load that each model carries, the member forces in the two models can be calculated. The forces in the truss models in the shear span are shown in Figure 6.22 and Figure 6.23.

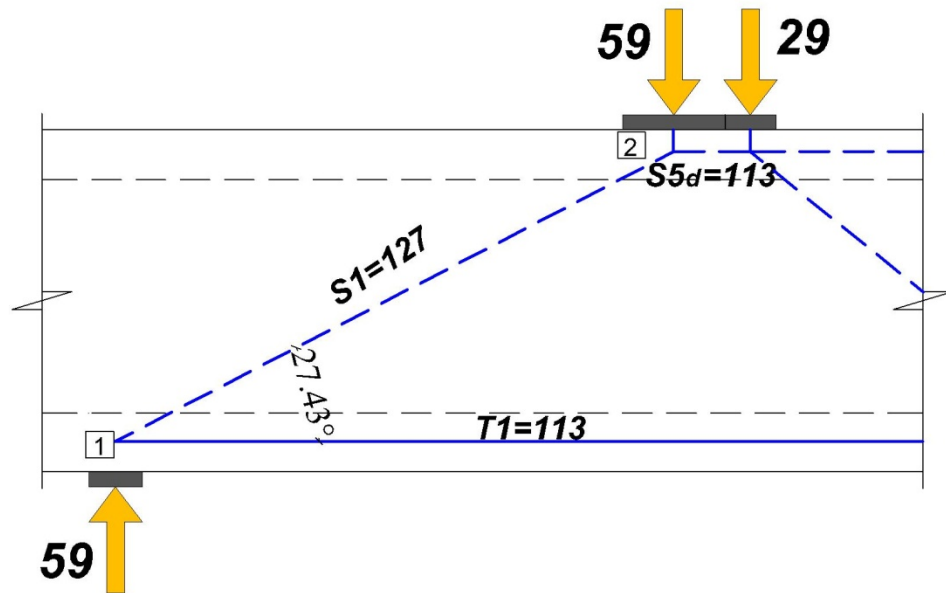


Figure 6.22 A close-up for the one-panel model

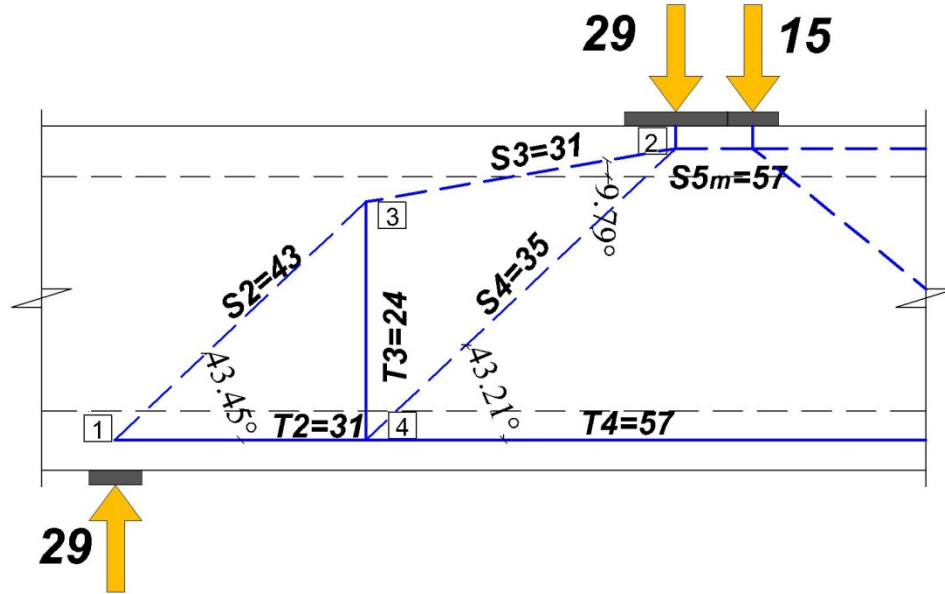


Figure 6.23 A close-up for the multi-panel model

At this point, an examination of the combination model can commence. When checking a strut-and-tie model, every critical element and nodal face should be checked. Besides, one should notice that when checking a strut (or strut-to-node interface) of the combination model, it is necessary to consider the two individual models at the same time. For example, even though S1 (Figure 6.22) and S2 (Figure 6.23) are considered adequate by calculation in individual model, one cannot say that the structure is safe. They must be considered together.

Node 1 (End Support CCT node)

The forces on Node 1 in Figure 6.22 and Figure 6.23 are combined as shown in Figure 6.24. Force acting on each face of this combined node is obtained by summing up corresponding forces on individual node. The force acting on the strut-to-node interface is the resultant of S1 and S2 and thus the load can be calculated as following:

$$\text{Load } S_{1_2} = \sqrt{(S_{1x} + S_{2x})^2 + (S_{1y} + S_{2y})^2} = 169 \text{ kips}$$

where

$$S_{1x}=127 \times \cos(27.43^\circ)=113 \text{ kips}$$

$$S_{2x}=43 \times \cos(43.45^\circ)=31 \text{ kips}$$

$$S_{1y}=127 \times \sin(27.43^\circ)=59 \text{ kips}$$

$$S_{2y}=43 \times \sin(43.45^\circ)=29 \text{ kips}$$

The angle of $S_{1,2}$ is the angle of the resultant force acting on the strut-to-node interface.

$$\phi_{1,2}=\tan^{-1}\left(\frac{S_{1y}+S_{2y}}{S_{1x}+S_{2x}}\right)=31.43^\circ$$

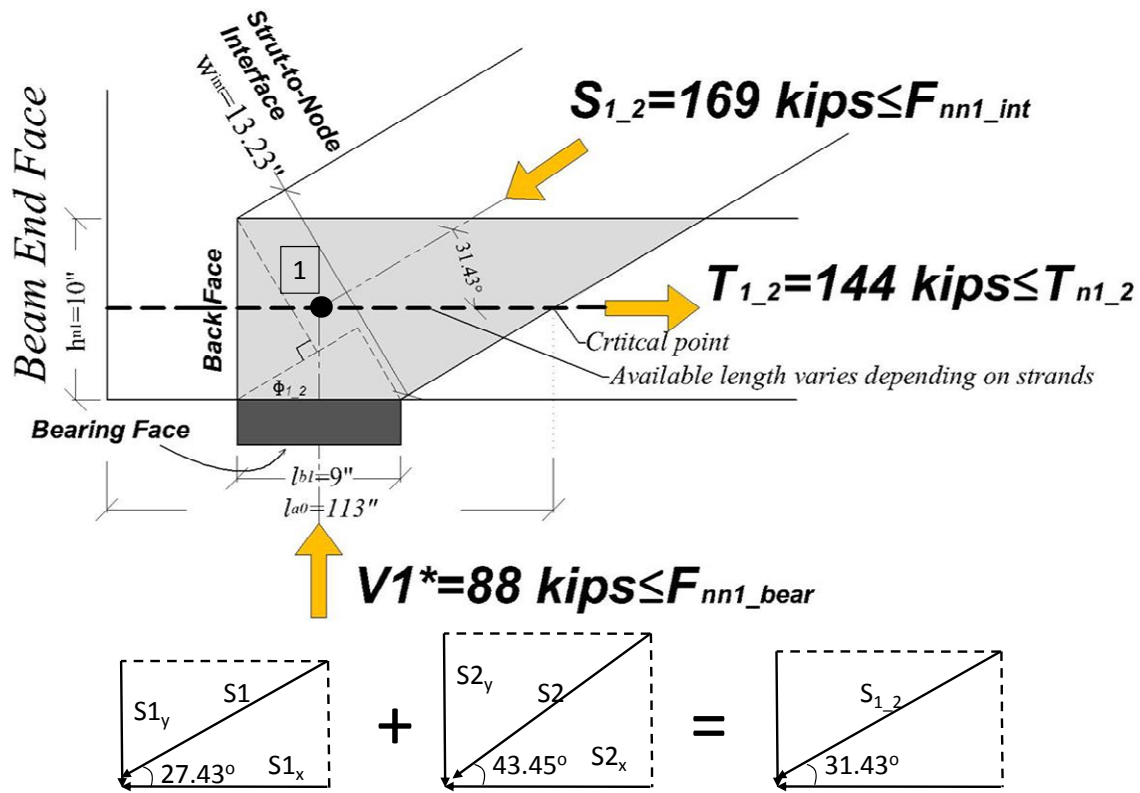


Figure 6.24 A close-up for the Node 1

The combined Node 1 is proportioned as a non-hydrostatic node. The length of bearing face of the CCT node (l_{b1}) has the same dimension as the bottom bearing plate (9 in.). The height of back face of the node (h_{n1}) is taken as twice of the distance from centroid of the bonding prestressing strands in the nodal zone (56 strands) to the extreme tension fiber of the beam. The distance of the centroid of the prestressing strands to the

extreme tension fiber is 5.14 inches. Twice this distance exceeds the thickness of the bottom flange (10 in.) in the test beam. Therefore the length of the back face is taken as the thickness of the bottom flange, 10 inches. According to the length of the bearing plate and the height of the back face, the width of the strut-to-node interface (w_{int1}) is determined as 13.23 inches by Equation 6-1:

$$w_{int1} = l_{b1} \sin \Phi_{1_2} + h_{n1} \cos \Phi_{1_2}$$

The CCT node proportioning is now complete. Since the dimension of Node 1 and forces acting on each face of Node 1 has been obtained, the check of the nodal zone can begin.

Bearing Face

Load $V1^* = 59 + 29 = 88$ kips

Efficiency Factor $v = 0.75$

$f_{ce} = v f'_c = 0.75 \times 5.81 = 4.36$ ksi

The size of the bottom bearing plate is 9 in. by 32 in (Figure 6.25). Thus

Capacity $F_{nn1_bear} = 4.36 \times (9 \times 32) = 1255$ kips > 88 kips O.K.



Figure 6.25 Bottom bearing plate

Back Face

Although there is no anchor plate at the back face of the CCT node, AASHTO LRFD (2008) and ACI 318-08 do not distinguish the source of stress on the back face of

a CCT node (i.e. anchor plate and bonding of the tie reinforcement). Therefore, the back face is still checked in the following manner.

$$T_{1_2}=144 \text{ kips}$$

$$f_{ce}=4.36 \text{ ksi}$$

$$\text{Capacity } F_{nnl_back}=f_{ce} \times h_n \times 32 \text{ in.}=4.36 \times 10 \times 32=1394 \text{ kips} > 144 \text{ kips} \quad \text{O.K.}$$

The anchorage from the critical point also has to be checked. The following equation for the full development length may be used

$$l_d = \kappa \left(f_{ps} - \frac{2}{3} f_{pe} \right) d_{bs} \quad (AASHTO 5.11.4.2-1)$$

Where

$$\kappa=1.6 \text{ for pretensioned members with a depth greater than 24 in.}$$

$$f_{ps}=260 \text{ ksi as defined previously}$$

$$f_{pe}=164.6 \text{ ksi as defined in Appendix C}$$

$$d_{bs}=\text{nominal strand diameter, 0.5 in.}$$

Thus

$$l_d = 1.6 \left(260 - \frac{2}{3} \times 165.7 \right) \times 0.5 = 117 \text{ in.}$$

The relationship between steel stress and the length strands are bonded can be idealized as Figure 6.26. This idealized correlation can be used to analyze the strand stress at the section within the transfer length and development length. From Figure 6.26, it can be inferred that the steel stress ($f(l_{px})$) of the strands developed through boundary at the critical point is related to the available length (x) according to the debonding schedule. The relationship can be described using the following equations.

$$f(l_{px}) = \begin{cases} \frac{l_{px}}{60d_{bs}} f_{pe} & \text{if } l_{px} < 60d_{bs} \\ f_{pe} + \frac{l_{px} - 60d_{bs}}{l_d - 60d_{bs}} (f_{ps} - f_{pe}) & \text{if } 60d_{bs} < l_{px} < l_d \\ f_{ps} & \text{if } l_{px} > l_d \end{cases}$$

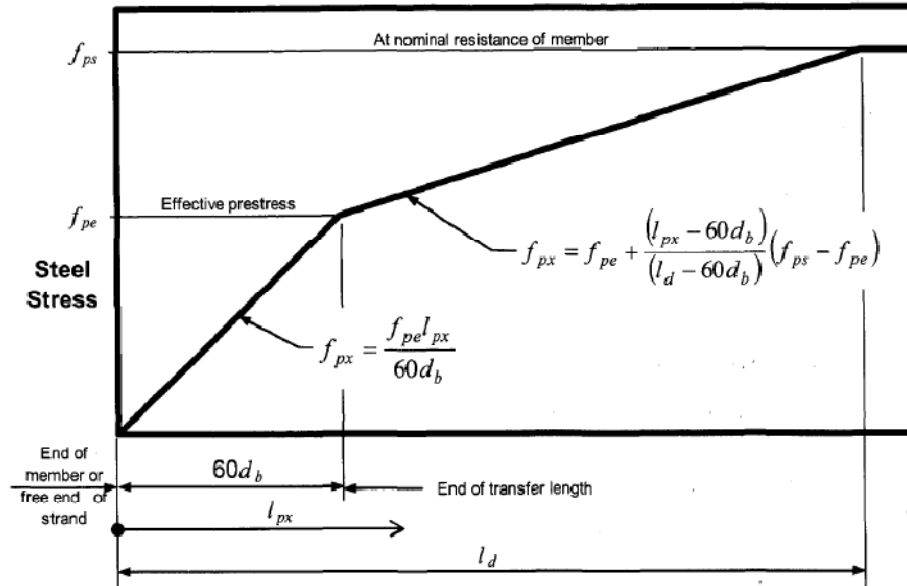


Figure 6.26 Relationship between steel stress and development length (AASHTO LRFD 2008)

Table 6.4 Available length and corresponding bond stress

The Origin of the Bonded Strands	Number	Available Length (l _{px}), (in.)	Bond Stress (ksi)
End	38	113 (l _{a0})	252
3 ft	8	77	214
6 ft	6	41	176
9 ft	4	5	27

Fifty six strands are bonded at the critical point, and their available lengths can be determined from their bonded length according to the relationship shown above. The available length and calculated steel stress are shown in Table 6.4. With this information, the adequacy of the tie at the critical point can be examined.

$$\text{Load} = T_{1_2} = 144 \text{ kips}$$

$$\begin{aligned} \text{Tie Capacity} &= 0.153 \times (38 \times 252 + 8 \times 214 + 6 \times 176 + 4 \times 27) \\ &= 1904 \text{ kips} > 144 \text{ kips} \quad \text{O.K.} \end{aligned}$$

The calculated tie capacity is even greater than $T1+T4=113+57=170$ kips. Therefore the adequacy of tie T1 is confirmed.

Strut-to-Node Interface

In order to obtain the efficiency factor (v), the following four equations are solved by iteration:

$$\begin{aligned} \text{Tie tensile strain } \epsilon_s &= \frac{F_{nn1_int} \cos(\phi_{1_2})}{A_{ps} E_{ps}} \\ &= \frac{320.4 \cos(31.4^\circ)}{(56 \times 0.153) \times 29000} = 1.100 \times 10^{-3} \\ \text{Tensile strain } \epsilon_l &= \epsilon_s + (\epsilon_s + 0.002) \cot^2 \phi_{1_2} \\ &= 1.1 \times 10^{-3} + 1.1 \times 10^{-3} \cot^2(30.43^\circ) = 9.402 \times 10^{-3} \end{aligned}$$

(AASHTO 5.6.3.3.3-2)

$$\text{Efficiency Factor } v = \frac{1}{0.8 + 170 \epsilon_l} = 0.36 < 0.85$$

(AASHTO 5.6.3.3.3-1)

$$\text{Capacity } F_{nn1_int} = 0.36 \times 5.81 \times 10 \times 13.23 = 320.4 \text{ kips} > 169 \text{ kips} \quad \text{O.K.}$$

Because of the box section, it is more difficult to choose an exact thickness of the strut-to-node interface than in the case of a rectangular section. Thus the thickness of the strut-to-node interface is taken as 10 inches, which is the thinnest part of the web portion of the test beam. As a result, the calculation will be very conservative. Besides, AASHTO LRFD specifies separate factors when determining the capacity of strut and strut-to-node interface. The efficiency factor used above is for a strut. The concrete efficiency factor for a CCT node in AASHTO LRFD (2008) is 0.75. Assume the strut has the smallest width at the strut-to-node interface (i.e. the same width as strut-to-node interface). The calculation performed above is conservative, and therefore there is no need to check the strut further.

Node 2 (CCC node)

Node 2 is a CCC node and exists in both the one-panel and two-panel model. Therefore, similar to Node 1, it is necessary to combine corresponding forces in

individual model into one node. The superposition technique is similar as that in Node 1. Forces acting on the bearing face and back face can be obtained in a straightforward manner. The force at the strut-to-node interface is the resultant of S1, S3, and S4. Similar calculations to those performed for the strut-to-node interface of Node1 can be applied to get the resultant force of S1, S3, and S4.

$$\text{Load } S_{1_3_4} = \sqrt{(S_{1x} + S_{3x} + S_{4x})^2 + (S_{1y} + S_{3y} + S_{4y})^2} = 191 \text{ kips}$$

Where

$$S_{1x} = 113 \text{ kips}$$

$$S_{3x} = 31 \times \cos(9.79^\circ) = 31 \text{ kips}$$

$$S_{4x} = 35 \times \cos(49.5^\circ) = 26 \text{ kips}$$

$$S_{1y} = 59 \text{ kips}$$

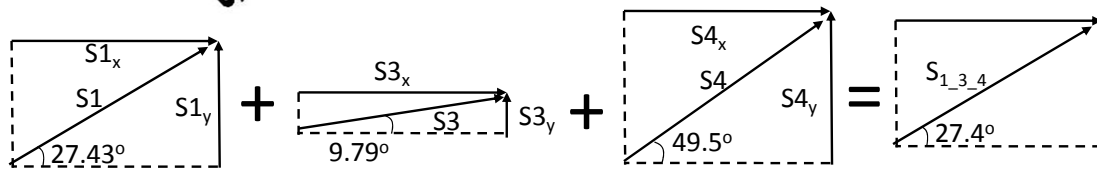
$$S_{3y} = 31 \times \sin(9.79^\circ) = 5 \text{ kips}$$

$$S_{4y} = 35 \times \sin(43.21^\circ) = 24 \text{ kips}$$

The angle of the resultant force acting on the strut-to-node interface is the angle of the resultant force.

$$\phi_{1_3_4} = \tan^{-1} \left(\frac{S_{1y} + S_{3y} + S_{4y}}{S_{1x} + S_{3x} + S_{4x}} \right) = 27.4^\circ$$

The combined Node 2 is also proportioned as a non-hydrostatic node. The length of the top bearing plate (26 in.) was shown in Figure 6.19. According to the proportioning of the applied load, the length (l_{b2}) of the bearing face for Node 2 is 17.43 in. The height of back face of the node (h_{n2}) is taken as the height of rectangular stress block calculated previously for the back face of the CCC node; that is 7.62 in. Using the length of the bearing face and the height of the back face, the width of the strut-to-node interface (w_{int2}) is 14.78 in., which can be determined as was done for Node 1 (Equation 6-1). The configuration of Node 2 is shown in Figure 6.27. All faces of Node 2 can now be checked.



Bearing Face

Efficiency Factor $v=0.85$

Two plates have a shaded bearing area in Node 2 as shown in (Figure 6.28).

145

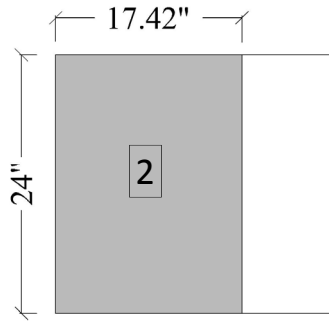


Figure 6.28 Top bearing plate

Back Face

Load (S5)=113+57=170 kips

$f_e=4.94$ ksi

Capacity $F_{nn2_back}=f_e \times (2 \times 4.63 \times 24) = 1805 \text{ kip} > 170 \text{ kips}$ O.K.

Strut-to-Node Interface

Load (S_{1_3_4})=191 kips

$f_e=4.94$ ksi

Capacity $F_{nn2_int}=2 \times 0.85 \times f'_c \times (14.78 \times 24) = 3505 \text{ kips} > 191 \text{ kips}$ O.K.

The efficiency factor used here is 0.85. Because Node 2 is a CCC node, it is not subjected to a principal tensile strain. According to the commentary in AASHTO LRFD (2008), the concrete in this situation can resist a compressive stress of $0.85f'_c$.

Node 3 (CCT node)

Node 3 is a node only appearing in the two-panel model. In the other words, the load carried by Node 3 is not as great as Node 1 and Node 2, which carry the load from both the one-panel and two-panel model. In addition, Node 3 is an interior CCT node as classified in 6.3.4.2. In Node 3, the node faces that the fanning struts bear against do not need to be checked. As long as the anchorage of the tension tie is sufficient, Node 3 can be taken as a smeared node. Hence Node3 is not critical in this specimen and will not be checked in calculations for all the other beams.

Node 4 (CTT node)

As mentioned in 6.3.4.3, Node 4 is classified as a CTT node and is usually considered as a smeared node; hence, it is typically not a critical node. Based on this reason, it can be directly concluded that Node 4 is not critical in this specimen and will not be checked in calculations for all the other beams.

Vertical Tie (T3)

Load=24 kips

Only one stirrup is included in the vertical tie (T3) and the capacity of T3 is:

$$\text{Capacity } T_{n3} = 1 \times 2 \times A_{s,\#4} \times f_y = 1 \times 2 \times 0.2 \text{ in}^2 \times 60 \text{ ksi} = 24 \text{ kips}$$

The load on T3 reaches its capacity. Thus the failure load is governed by T3 and the calculated shear capacity (V_{cal}) is

$$V_{cal} = (P_d + P_m) \times \frac{\text{Total Span} - \text{Shear Span}}{\text{Total Span}} = 132 \times \frac{297 - 99}{297} = 88 \text{ kips}$$

The failure mode is shear tension failure, as was observed in the test, and the ratio of experimental shear (660 kip) to calculated shear is:

$$\frac{V_{exp}}{V_{cal}} = 7.49$$

The sample calculation for the combination model above was done according to AASHTO LRFD 2008. Calculations according to the other two provisions (ACI 318-08 and TxDOT Project 5253) can be performed in a similar manner. The main difference is the concrete efficiency factors used, which have been introduced in 6.4. The calculation of steel stress due to bond along the tendon in ACI 318-08 is also different from AASHTO LRFD 2008, but anchorage is not critical in this study. Besides, it should be noted that TxDOT Project 5253 explicitly allows a triaxial confinement factor to be used when checking nodal zones. Details of that application are given in Appendix D. It is easier to calculate the one-panel model because there is no need to consider two forces acting at the same location. Detailing calculation for one-panel for various provisions can be found in Appendix D.

6.7 CALCULATION RESULTS

6.7.1 One-Panel Model

In 6.5 and 6.6, the strut-and-tie model in this study was explained and a sample calculation was given. In this section, calculated capacities in the one-panel and combination model using AASHTO LRFD (2008), ACI 318-08, and TxDOT Project 5253 are compared. Detailed calculations are given in Appendix C and Appendix D. In Table 6.5 and Table 6.6, the results are based on the one-panel model using two values of concrete strength and steel strength, the design strength (f'_c) and core concrete strength divided by 0.85 ($f'_{core}/0.85$). Both values of concrete strength yield conservative computed shear strengths of the beams. Because $f'_{core}/0.85$ was always higher than f'_c , shear capacities based on $f'_{core}/0.85$ is always higher than those based on f'_c . It can be seen that AASHTO LRFD yielded the most conservative estimation while the procedures in TxDOT Project 5253 gave the most accurate results. The TxDOT Project 5253 approach explicitly allows triaxial confinement factors to be used when checking CCC and CCT nodes. However, even the highest calculated shear capacity is 47% lower than experimental shear capacity (V_{test}/V_{5253} of RF-3R-12-A in Table 6.6).

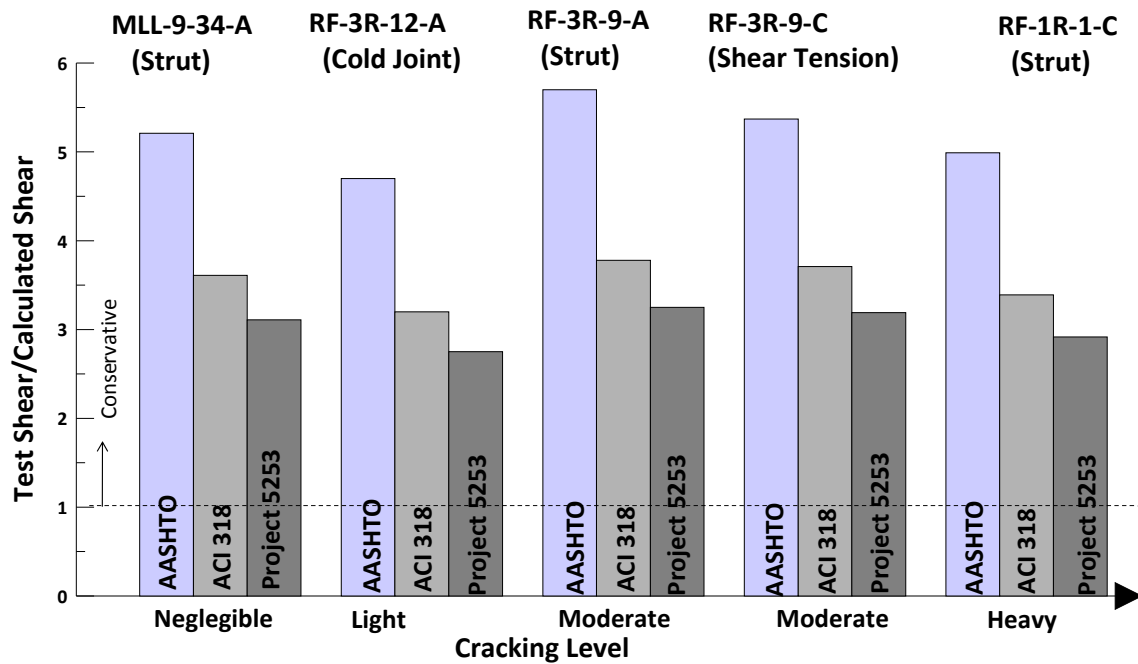
All failure modes predicted by the one-panel model are strut crushing. This was because the support in the shear span of each beam was 56 to 96 inches from the nearest end face. This distance was enough to develop the required forces in the prestressing strands. Since strut crushing always governed the failure mode, the shear capacities were highly affected by concrete strength. For design strength, it can be seen that the ratio of test shear to calculated shear based on the same provision was higher because of a similar low design concrete strength of 5 ksi (Figure 6.29) while for core strength the ratio was lower (Figure 6.30). Comparing the identified failure modes to those observed, it can be seen that for three of the five beams, the same mode resulted. The other two beams had a cold joint failure (RF-3R-12-A) and shear tension failure (RF-3R-9-C) respectively.

Table 6.5 Shear capacity computed by one-panel model using design strength

Beam ID	Test	AASHTO LRFD 2008		ACI 318-08		TxDOT Project 5253	
	V_{test} (kips)	V_{AASHTO} (kips)	$\frac{V_{test}}{V_{AASHTO}}$	V_{ACI} (kips)	$\frac{V_{test}}{V_{ACI}}$	V_{5253} (kips)	$\frac{V_{test}}{V_{5253}}$
MLL-9-34-A	610	117	5.21	169	3.61	196	3.11
RF-3R-12-A	573	122	4.70	179	3.20	208	2.75
RF-3R-9-A	673	118	5.70	178	3.78	207	3.25
RF-3R-9-C	660	123	5.37	178	3.71	207	3.19
RF-1R-1-C	624	125	4.99	184	3.39	214	2.92
Note: All predicted failure modes are strut crushing							

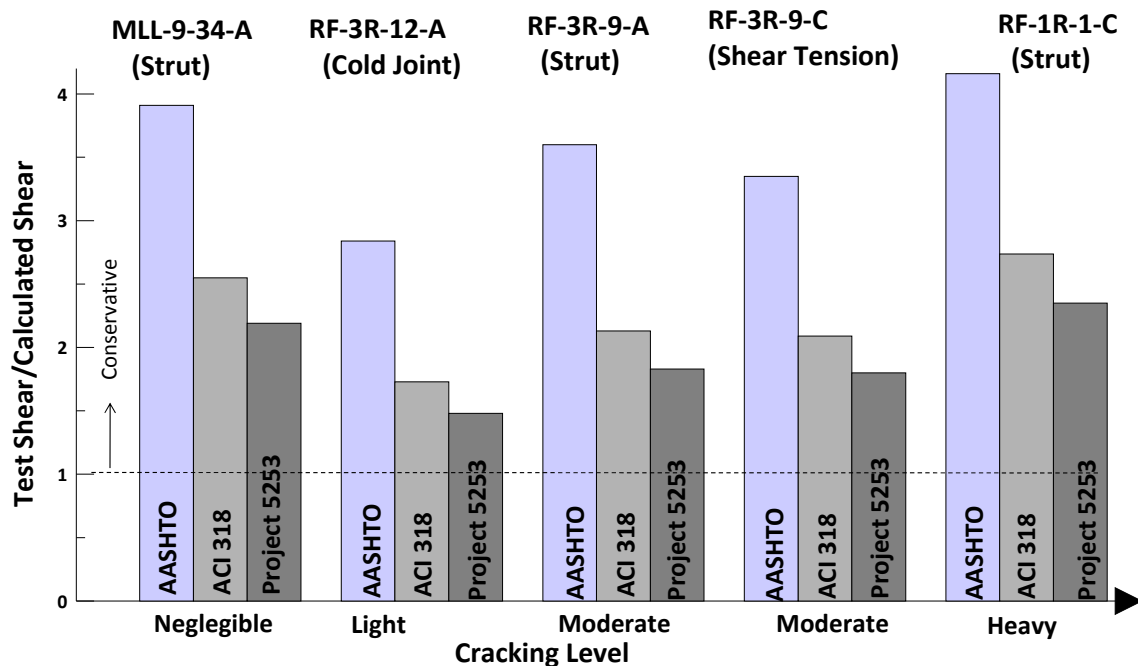
Table 6.6 Shear capacity computed by one-panel model using core strength/0.85

Beam ID	Test	AASHTO LRFD 2008		ACI 318-08		TxDOT Project 5253	
	V_{test} (kips)	V_{AASHTO} (kips)	$\frac{V_{test}}{V_{AASHTO}}$	V_{ACI} (kips)	$\frac{V_{test}}{V_{ACI}}$	V_{5253} (kips)	$\frac{V_{test}}{V_{5253}}$
MLL-9-34-A	610	156	3.91	239	2.55	278	2.19
RF-3R-12-A	573	202	2.84	332	1.73	386	1.48
RF-3R-9-A	673	187	3.60	316	2.13	368	1.83
RF-3R-9-C	660	197	3.35	316	2.09	368	1.80
RF-1R-1-C	624	150	4.16	228	2.74	265	2.35
Note: All predicted failure modes are strut crushing							



*All predicted failure modes are Strut Crushing.
Failure modes in parentheses are test failure modes.

Figure 6.29 Comparison of test to computed shear capacities using design strength



*All predicted failure modes are Strut Crushing.
Failure modes in parentheses are test failure modes.

Figure 6.30 Comparison of test to computed shear capacities using core strength/0.85

6.7.2 Combination Model

In Table 6.7 and Table 6.8, the results based on the combination model using design concrete strength (f'_c) and nominal steel strength (60 ksi) and core concrete strength divided by 0.85 ($f'_{core}/0.85$) and tested steel strength (69 ksi) are shown. Both concrete strengths resulted in conservative calculated strengths. Differing from one-panel model, the identified failure mode is not necessarily strut crushing. Shear tension failure due to a vertical tie (Figure 6.20) occurred when there was not enough transverse reinforcement to support the two-panel model of the combination model. In Table 6.9 and Table 6.10, the identified failure modes to test failure modes for f'_c and $f'_{core}/0.85$ are compared. It can be found that when f'_c is used, strut crushing is likely to occur especially when AASHTO LRFD 2008 is applied. This is because concrete efficiency factors used for strut-to-node interface are more conservative than those of the other provisions when the strut angle is shallow. In this study, all the struts were inclined at about 30 degrees. A shear tension failure mode prevailed over a strut failure when $f'_{core}/0.85$ was used. The stirrups that constitute the vertical tie (Figure 6.20) cannot support the two-panel model when the concrete strut capacity in the combination model is based on higher concrete strength. Therefore, even though higher concrete strength is used, the computed shear does not increase because the vertical tie fails first.

In Figure 6.31 and Figure 6.32, the ratio of test shear to calculated shear is presented. It can be seen that the differences among these three provisions are not as apparent as in the one-panel model. This is because shear tension failure governs in most cases, and hence different concrete strengths make little difference in calculation. Generally, the combination model is more conservative than the one-panel model. The lowest test/computed shear capacity is 1.63 (V_{test}/V_{5253} of RF-3R-9-A in Table 6.8).

Table 6.7 Shear capacity computed by combination model using design strength

Beam ID	Test	AASHTO LRFD 2008		ACI 318-08		TxDOT Project 5253	
	V_{test} (kips)	V_{AASHTO} (kips)	$\frac{V_{test}}{V_{AASHTO}}$	V_{ACI} (kips)	$\frac{V_{test}}{V_{ACI}}$	V_{5253} (kips)	$\frac{V_{test}}{V_{5253}}$
MLL-9-34-A	610	146	4.18	187	3.26	196	3.11
RF-3R-12-A	573	155	3.69	194	2.95	194	2.95
RF-3R-9-A	673	161	4.18	206	3.27	239	2.82
RF-3R-9-C	660	88	7.50	88	7.50	88	7.50
RF-1R-1-C	624	163	3.83	185	3.37	185	3.37

Table 6.8 Shear capacity computed by combination model using core strength/0.85

Beam ID	Test	AASHTO LRFD 2008		ACI 318-08		TxDOT Project 5253	
	V_{test} (kips)	V_{AASHTO} (kips)	$\frac{V_{test}}{V_{AASHTO}}$	V_{ACI} (kips)	$\frac{V_{test}}{V_{ACI}}$	V_{5253} (kips)	$\frac{V_{test}}{V_{5253}}$
MLL-9-34-A	610	193	3.16	235	2.60	235	2.60
RF-3R-12-A	573	237	2.40	237	2.40	237	2.40
RF-3R-9-A	673	250	2.69	363	1.86	413	1.63
RF-3R-9-C	660	106	6.26	106	6.26	106	6.26
RF-1R-1-C	624	194	3.22	217	2.88	217	2.88

Table 6.9 Failure modes from combination model using design strength

Beam ID	Test	AASHTO LRFD 2008	ACI 318-08	TxDOT Project 5253
MLL-9-34-A	Strut	Strut	Strut	Shear Tension
RF-3R-12-A	Cold Joint	Strut	Shear Tension	Shear Tension
RF-3R-9-A	Strut	Strut	Strut	Strut
RF-3R-9-C	Shear Tension	Shear Tension	Shear Tension	Shear Tension
RF-1R-1-C	Strut	Strut	Shear Tension	Shear Tension

Table 6.10 Failure modes from combination model using core strength/0.85

Beam ID	Test	AASHTO LRFD 2008	ACI 318-08	TxDOT Project 5253
MLL-9-34-A	Strut	Strut	Shear Tension	Shear Tension
RF-3R-12-A	Cold Joint	Shear Tension	Shear Tension	Shear Tension
RF-3R-9-A	Strut	Strut	Strut	Shear Tension
RF-3R-9-C	Shear Tension	Shear Tension	Shear Tension	Shear Tension
RF-1R-1-C	Strut	Shear Tension	Shear Tension	Shear Tension

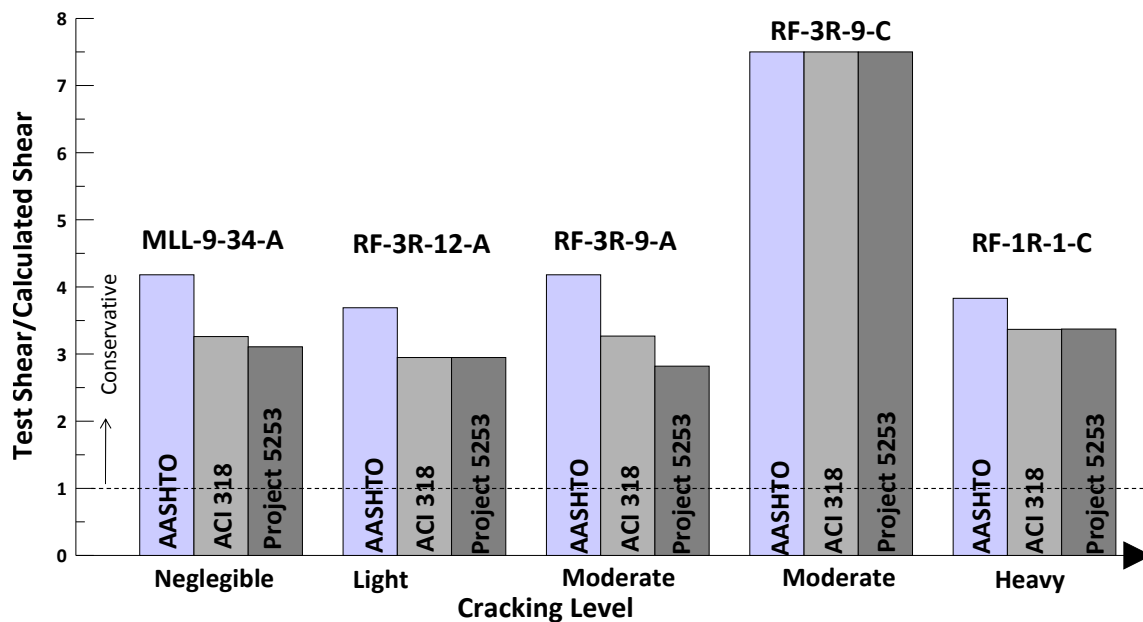


Figure 6.31 Comparison of test to computed shear capacities using design strength

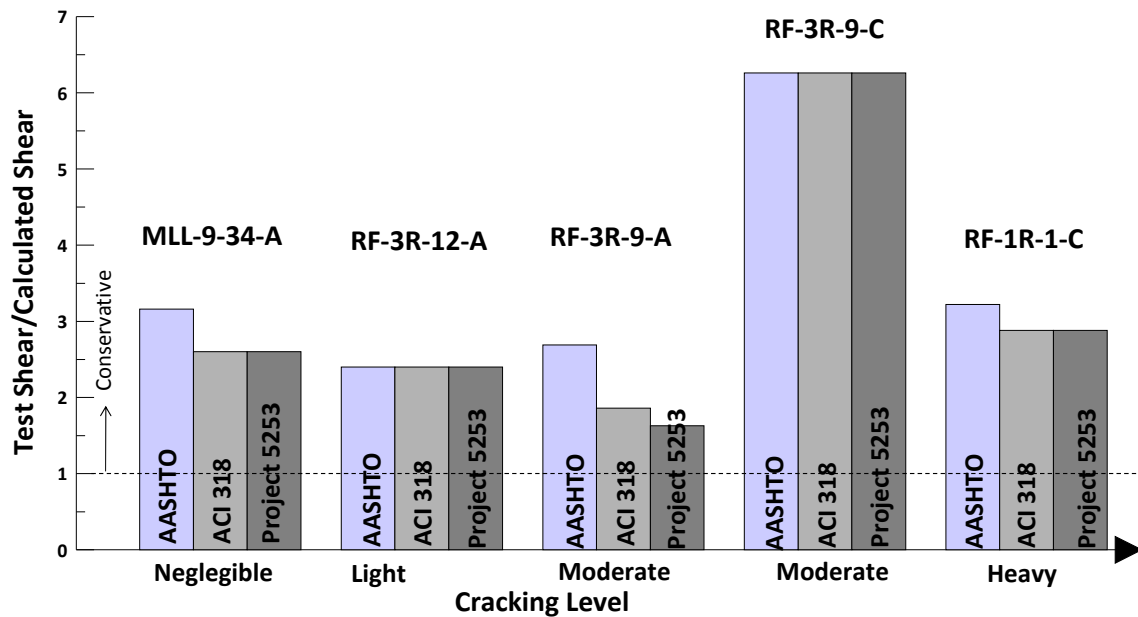


Figure 6.32 Comparison of test to computed shear capacities using core strength/0.85

6.7.3 Discussion

From the analysis results presented in 6.7.1 and 6.7.2, it was found that both one-panel and combination models yielded conservative calculations regardless of the provisions used or the concrete strength and steel strength. The two models resulted in a similar degree of conservatism when design concrete strength and nominal steel strength were used. However, the one-panel model generally gave a more accurate result when core strength/0.85 was used. One of the main reasons for using the combination model in this study was to correctly identify failure modes, but after the calculations were completed, it was found that not only the failure mode was not correctly identified, but the computed shear was much lower than measured. Shear calculated from the combination model was more conservative than that from the one-panel model. This result is in agreement with the recommendations from TxDOT Project 5253 that a one-panel model was suitable for deep beams when the shear span-to-depth ratio was smaller than two. Although the one-panel model in this study correctly identified the failure mode in only three of the five specimens, the failure mode was not critical as long as conservative estimate of strength is obtained. Another advantage of the one-panel model

was its convenience. Superposition of two elements was not required when the one-panel model was utilized, and hence calculation was simpler than for the combination model.

Comparing the three provisions used in this study, TxDOT Project 5253 provision yielded the most accurate results when a one-panel model was utilized. The average ratio of test-to-calculated shear was about 1.93. This ratio was higher than the average ratio (around 1.60) reported in TxDOT Project 5253 for the reinforced concrete deep beam database used in that study.

From the discussion above, the provision of TxDOT Project 5253 may seem more attractive than the other two. However, one should note that concrete efficiency factors in TxDOT Project 5253 were developed based on reinforced concrete deep beam tests. No experimental results were available for prestressed concrete deep beams. Therefore, this proposed provision should be used with caution especially when analyzing ASR and/or DEF damaged prestressed box beams.

Another point to consider is the calculation for the capacity of the strut-to-node interface. A strut that extends from load point to support is bottle-shaped (Figure 6.1). This means that the width of a strut increases in the mid-length of the strut. The width that was used throughout this study was at the end of the strut for checking both strut and strut-to-node interface, and should be conservative.

Definition of the strut thickness was also a difficult issue in this study. According to the section profile of the beam, the web thickness varied along the depth (Figure 6.33). Chamfer at the bottom corner of the hollow section made the total thickness at the strut-to-node interface greater than the minimum ten inches wide used in calculations, and increases the complexity of the state of stress in this region. In addition, plywood used to position the Styrofoam void was found in the web portion in these specimens (Figure 6.34). The plywood not only failed to position Styrofoam as it was expected to do, causing void floatation along the length of the beam, but also decreased the thickness of the web by about 1/2 in. Based on the situation described above, the thickness was chosen as the minimum thickness (10 in. or 5 in. each side) and, as a result, makes the computed shear strength more conservative.

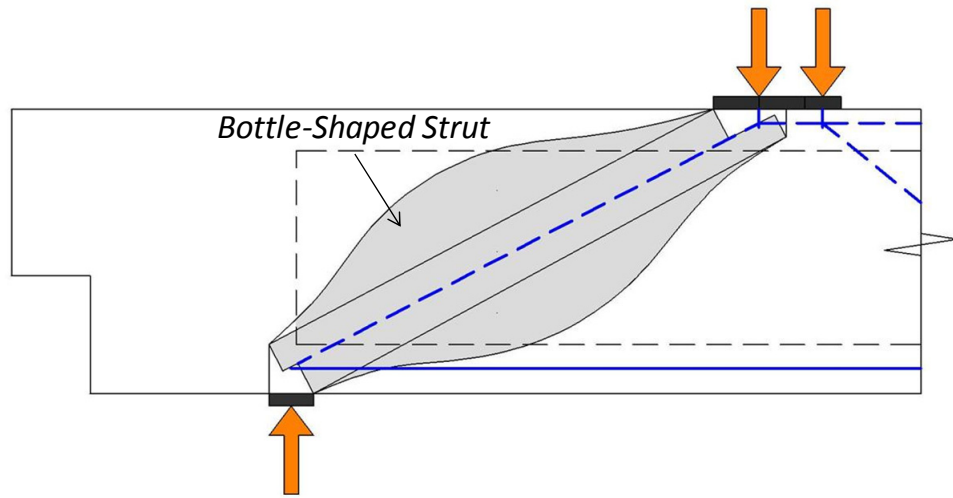


Figure 6.33 Bottle-shaped strut

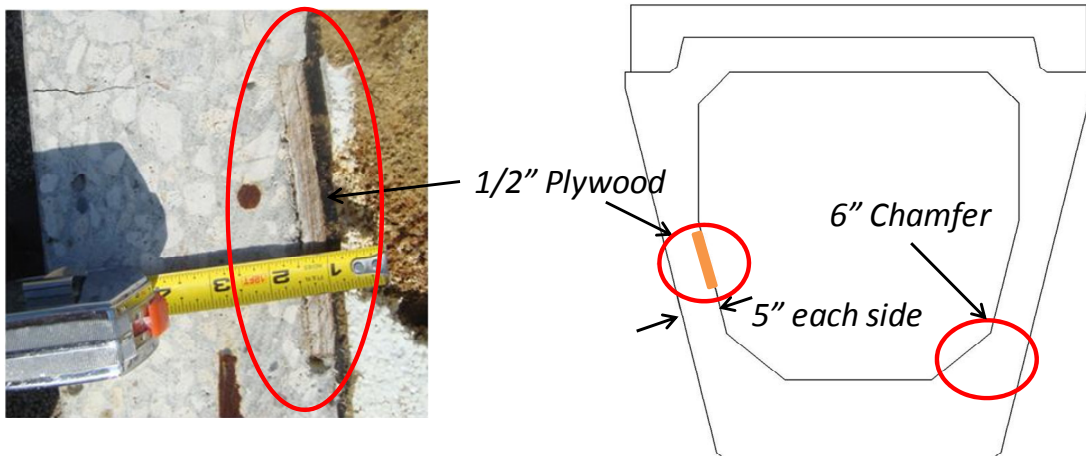


Figure 6.34 Chamfer and plywood in the web portion

6.8 SUMMARY

In this chapter, two types of strut-and-tie models were used to estimate the shear capacities of five prestressed trapezoidal box beams. The models were calculated based on three provisions – AASHTO LRFD (2008), ACI 318-08, and TxDOT Project 5253. A brief introduction of strut-and-tie models and efficiency factors used in various codes was first presented. Then, a sample calculation was given to provide insight to the determination of the strength from the strut-and-tie models. Both design concrete strength with nominal steel strength and core strength with tested steel strength were examined.

The results showed that all the strut-and-tie models yielded a conservative strength for either concrete strength. The results also showed that a one panel model using core strength and tested steel strength according to TxDOT Project 5253 gave the most accurate but still conservative computation. However, TxDOT Project 5253 should be used with caution in prestressed concrete elements because this proposed provision was developed based on reinforced, not prestressed, concrete deep beam tests. Difficulties in determining the width and thickness of the strut and strut-to-node interface were also discussed and calculations were based on minimum observed dimensions.

CHAPTER 7

Forensic Analysis

7.1 OVERVIEW

Three different forensic analyses were conducted on beams that had varying degrees of ASR and/or DEF damage. First, cores were extracted from three ASR and/or DEF damaged beams for petrographic analysis. Petrographic analysis provided a means of assessing (a) whether ASR or DEF was the main distress mechanism in the beams, (b) damage progression from the surface into the concrete, and (c) damage severity in each core. Second, one heavily cracked beam was sliced to determine the width and extent of cracks in the region of the beam where temperature effects during early curing were most pronounced. Finally, an elastic rebound test was used to investigate if ASR and/or DEF expansions caused yielding of the transverse reinforcement.

7.2 PETROGRAPHIC ANALYSIS

Nine cores extracted from the end region of the beams with varying levels of cracking were sent to the TxDOT Concrete Laboratory for petrographic analysis. The location of cores and the cracking condition are presented in Figure 7.1. RF-2R-6-A was not tested in shear in this study. The level of cracking of RF-2R-6-A was considered as between MLL-9-34-A (negligible cracking) and RF-1R-1-A (Heavy cracking) from a visual inspection. Therefore RF-2R-6-A was defined as a beam with moderate cracking.

There were three main objectives of the petrographic analysis: (i) to document ASR and/or DEF micro structural damage and determine the contributions of ASR and/or DEF deterioration, (ii) to compare micro structural damage in cover and core concrete, thereby characterizing the crack networks, and (iii) to compare damage severity between all samples. The results of the petrographic analysis are briefly presented in this section.

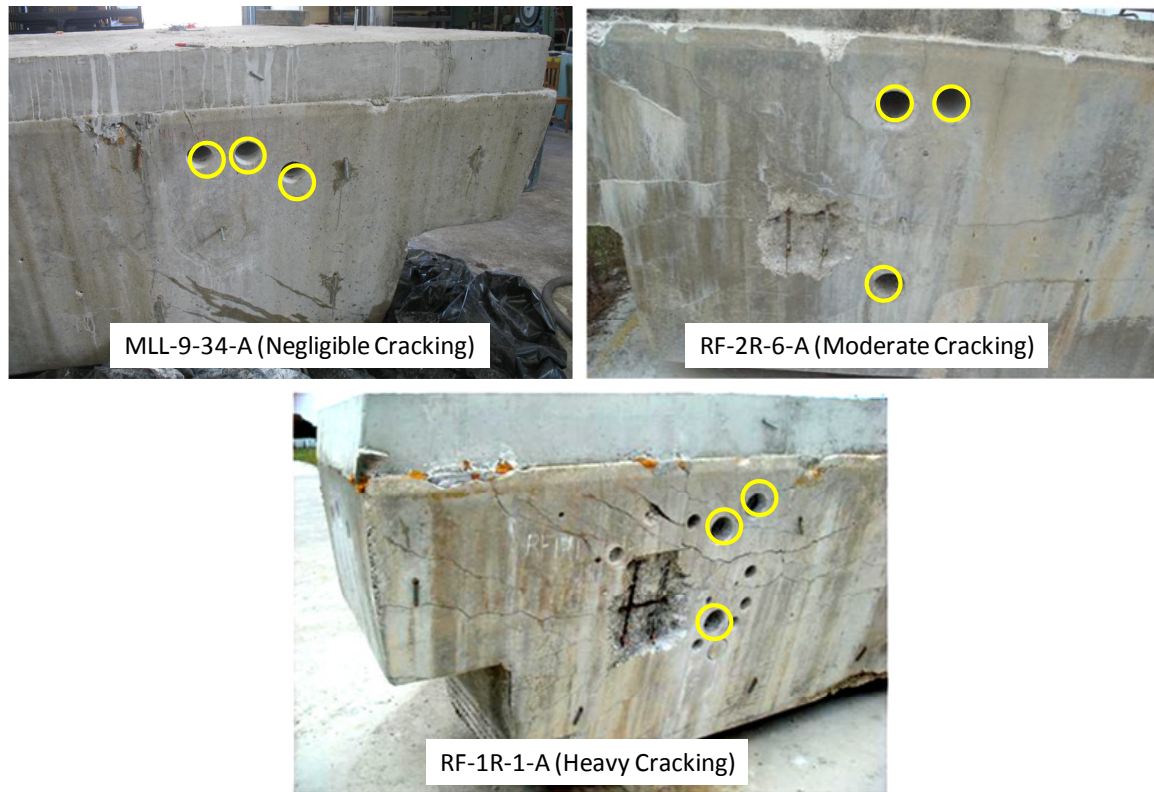


Figure 7.1 Location of the cores

After thorough review of lapped section images, scanning electron microscope (SEM) and spectral analysis, TxDOT Concrete Laboratory personnel concluded that *all cores had suffered significant distress from ASR (Figure 7.2). “Although ettringite was found filling most of micro cracks formed by ASR (Figure 7.3) and in many of the air voids and some discrete nests within the paste, the cases of gapping around aggregates (Figure 7.3(b)) due to paste expansion by DEF were limited. Therefore, it is inconclusive whether DEF contributed to the distress (Morgan 2010).”* Besides, several cores included a piece of reinforcing bar because the end blocks were heavily reinforced. A coating of ettringite was observed where the rebar had dislodged, indicating either debonding occurred that formed a large enough gap between rebar and paste for ettringite precipitation or settlement gaps or thermal cracks may have occurred.

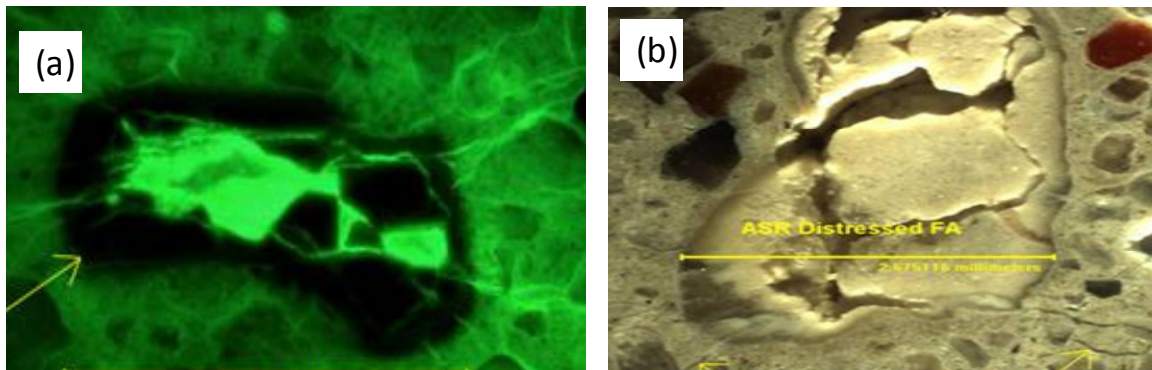


Figure 7.2 (a) ASR distressed fine aggregate (b) Highly distress fine aggregate (Morgan 2010)

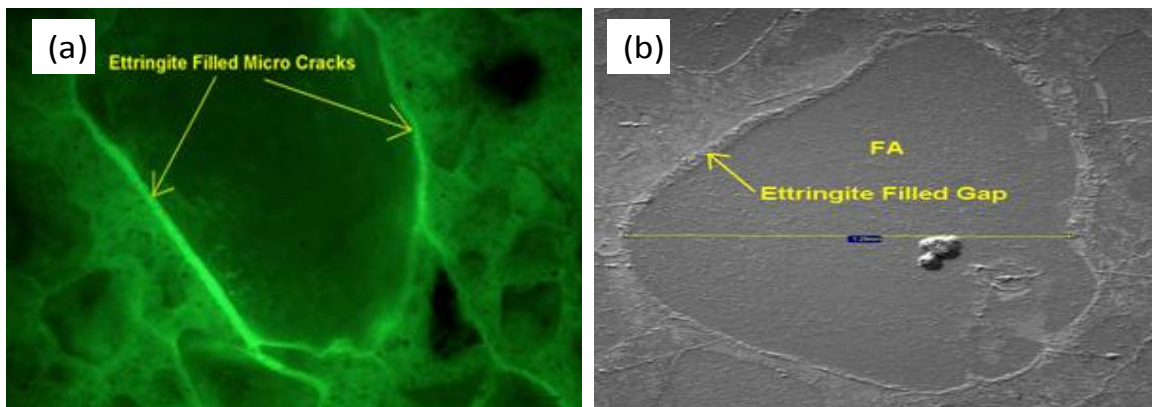


Figure 7.3 (a) Ettringite filled micro cracks (b) Ettringite filled gap around fine aggregate (Morgan 2010)

In 2004, forensic analysis on beam RF-1R-1 was conducted by the Concrete Durability Center at the University of Texas at Austin (Folliard et al. 2004). They observed that the end region had already expanded and had little potential expansion whereas the middle of the beam exhibited much higher potential expansion. From scanning electron microscopy, they found that the amount of ettringite and gapping suggested DEF to be the main cause of deterioration. It is likely that ASR occurred first throughout the beam and then triggered DEF in some portions. The conclusion reported by Folliard and Drimalas is different from that of the TxDOT Concrete Laboratory. One possible reason for this difference may be the process for core preparation for petrographic analysis in TxDOT Concrete Laboratory, during which some ettringite was washed away (Folliard 2010).

However, this is not the first time that two independent laboratories reached different conclusions. In 1999, TxDOT conducted a round-robin investigation of 56 ASR and/or DEF damaged prestressed box beams. Five participants conducted the evaluation on both distressed and undistressed box beams. Three of the participants attributed the main distress mechanism to DEF while the other two participants reported ASR to be the primary distress mechanism. All of the participants found the existence of both ASR and DEF (Lawrence et al. 1999).

Although ASR and DEF have unique chemical processes, the structural effects are very similar. Both ASR and DEF can cause volumetric expansion and micro cracks in the concrete material. Due to the similarities of micro structural damage caused by ASR and DEF, the structural effects of ASR and DEF can be considered the same whether ASR or DEF is the main distress mechanism.

The cores were extracted horizontally from the end region and were perpendicular to the axis of the beam. To study damage progression over the length of the cores, a sketch representing the cracking and orientation observed in the cores is shown in Figure 7.4(a). The most obvious feature shown in Figure 7.4(a) is the orientation of the cracks perpendicular to the surface in the 2 in. cover. Micro cracks are parallel to the surface in the region beyond the cover, indicating that high local stresses were imposed by the reinforcement in the end region of the beam. Because the end region of the beam was heavily reinforced with transverse and longitudinal steel, and the direction of the least restraint is perpendicular to the steel, the least restraint should occur in the direction perpendicular to the surface (Figure 7.4(b)). The absence of parallel cracking within the first two inches away of the concrete indicates that the cover concrete plays a passive role. It can be inferred that cracking on surface is a result of structural expansion.

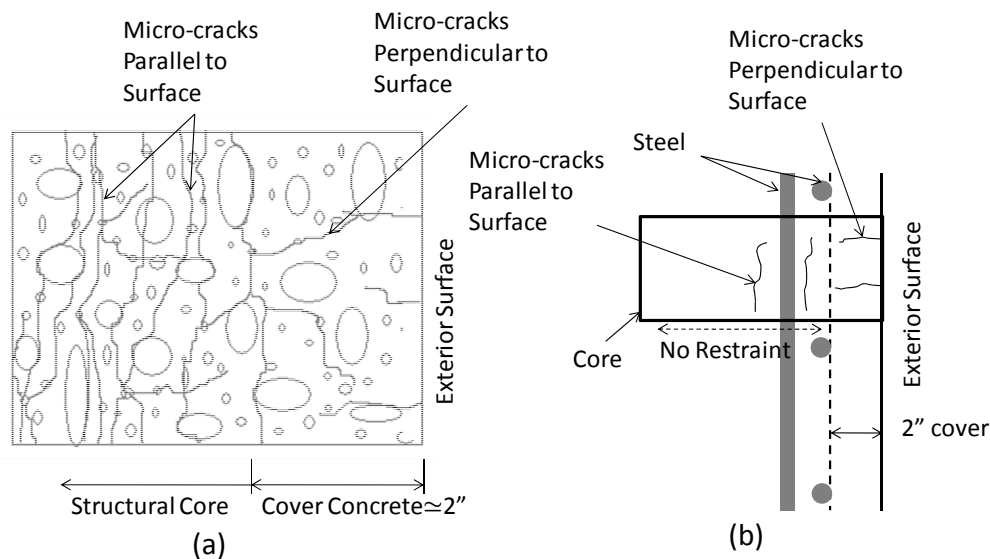


Figure 7.4 (a) General crack orientation within cores (Morgan 2010) (b) Restraint in the core

After examination of micro cracking, TxDOT personnel were asked to qualitatively study the damage severity in each core, comparing micro structural damage between each core. Reactive particles were counted during stereoscopic evaluation and averaged within three sections: 0~4 in., 4~8 in., and 8+in. (Figure 7.5). Identification of reactive particles was based on level and characteristics of distress, gel formation, dissolution, crack orientation, and discoloration. Part of the identification was also dependent on the petrographer's experience. The constituent of the reactive particles was primarily crystalline quartz (Morgan 2010). From Figure 7.5, it can be observed that average number of reaction particles in any section is lower in the beam with negligible cracking than in the other two beams. For the sections from 0~4 in. and 8+ in., cores extracted from the beam with moderate cracking had more reactive particles than the beam with heavy cracking. In summary, the number of reactive particles in the middle part (4~8 in.) revealed a similar trend as the cracking level while those in the end parts (0~4 in. and 8+ in.) did not show good agreement with the cracking level.

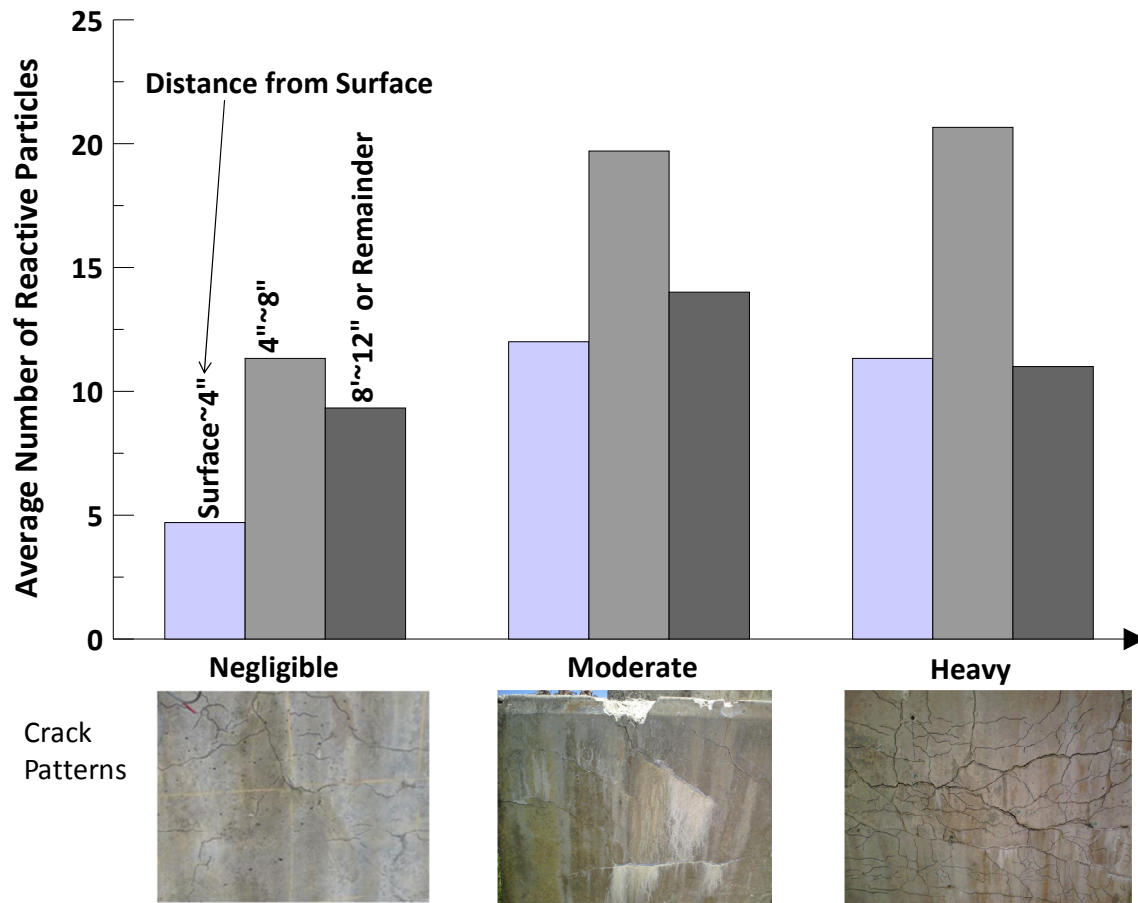


Figure 7.5 Comparison of reactive particles throughout the length of the cores

7.3 BEAM AUTOPSIES

7.3.1 Epoxy Injection and Cutting Tools

To investigate the crack pattern caused by ASR and/or DEF, an autopsy was conducted on beam RF-1R-1-C. The autopsy was conducted after finishing the web shear test on the beam. In order to facilitate the investigation, the beam was injected with epoxy in the solid end block and a small part of the hollow section. The surface of the beam was coated with epoxy having a grey color (Figure 7.6(a)) so that the epoxy that was injected into the cracks would not exude from the cracks. The injected epoxy was black to contrast with seal coat. The epoxy was injected into the beam through ports shown in Figure 7.6(b) and (c). The ports were placed over large cracks (Figure 7.6(c)) and

distributed over the surface of the beam to let the epoxy fill the cracks as much as possible. An overview of the beam after injection is shown in Figure 7.6(d).

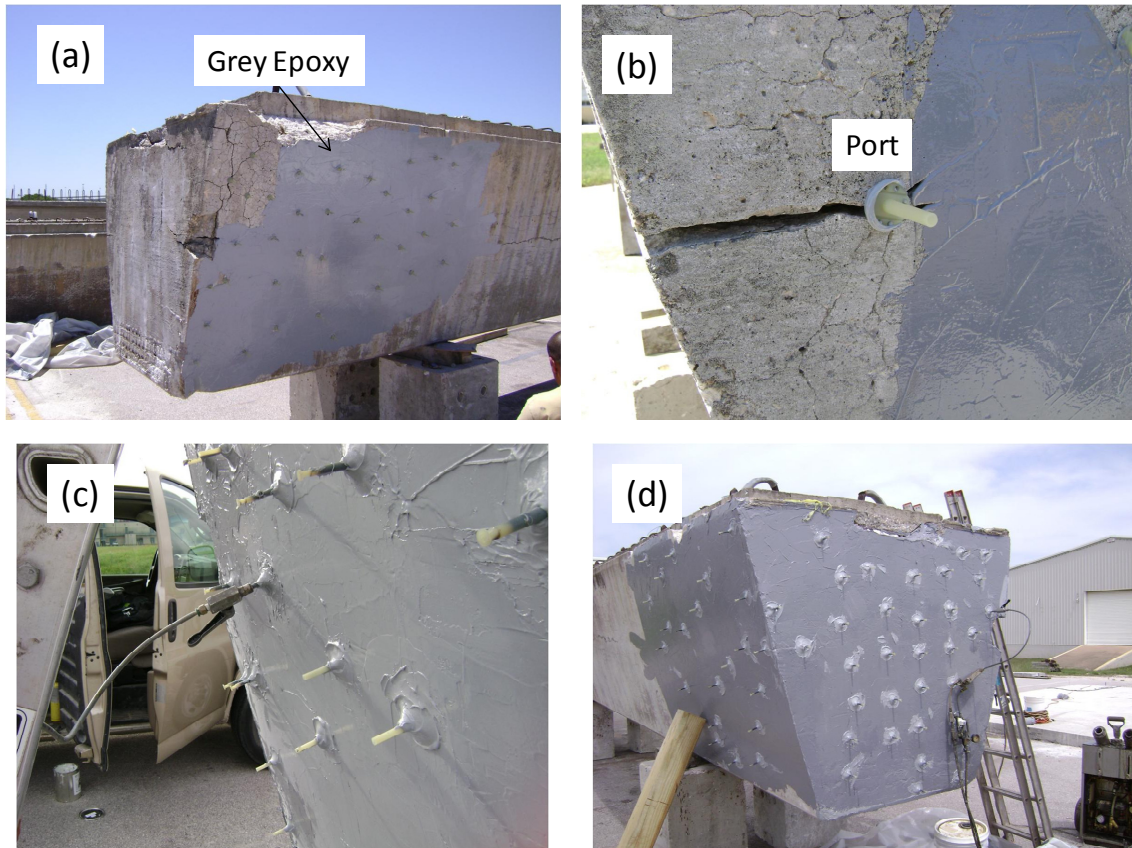


Figure 7.6 (a) Grey epoxy coating (b) Port at the large crack (c) Epoxy injection (d) Finished overview

After injection was completed, the beam was moved into the laboratory. A web shear test was first conducted on a region of the beam where no epoxy was injected. After finishing the shear test, the beam was cut into two pieces in order to move it from the test setup. The injected end region was cut into sections using a diamond wire saw shown in Figure 7.7.



Figure 7.7 Diamond wire saw

7.3.2 Observations

Five sections with thicknesses of 14, 8, 8, 8, and 17 in. were cut sequentially from the end (Figure 7.8). The total length of the solid end block was 42 in.; hence the first four sections were in the solid end block, and 13 in. of the last section was in the hollow section. The sections provided an opportunity to observe the propagation of the cracks caused by ASR and/or DEF in different part of the beam. The same figure also shows that larger cracks were presented in the west side of the beam compared with the east side of the beam.

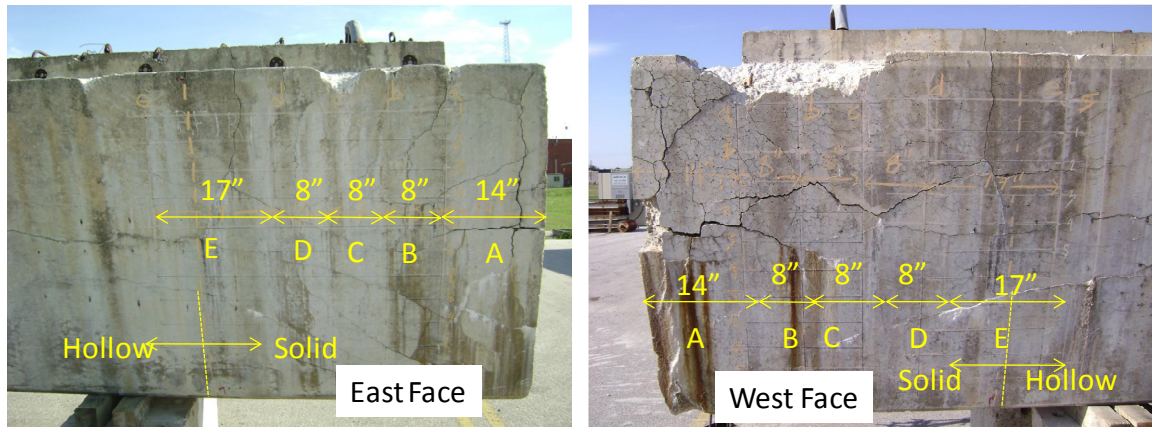


Figure 7.8 Locations of the cut sections

Section A

Section A was 14 in. thick and the first section cut from the end block. In Figure 7.9 an overview and some close-ups of the section are shown. It can be seen that crack was wider on the west side (0.5 in.) than the east side (0.08 in.), corresponding to the observed surface cracking. The crack orientation in both sides was parallel to the concrete surface at about 2 in. away from the surface, a distance equal to the cover over the transverse reinforcement. The cracking parallel to the surface of the web may be due to the lateral restraint provided by transverse reinforcement. Horizontal cracks of about 0.08 in. through the layer of the compression steel and straight steel in the end block shown in Figure 7.10 were also observed in the top of the beam. The crack in the west side deviated away from surface as the crack extended down to the bottom. This change in direction may be due to a transition of the direction of the lateral restraint provided by the transverse reinforcement. It can be seen that the cracks in the top portion are horizontal while the cracks close to the web are parallel to the surface, indicating two different directions of the lateral restraint. Therefore, it is reasonable to infer that the change of the direction of the crack in the west side was a reflection of the transition of the direction of the lateral restraint.

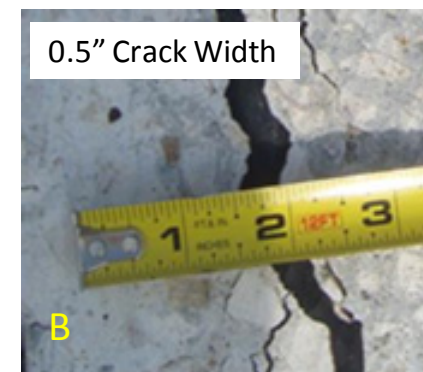
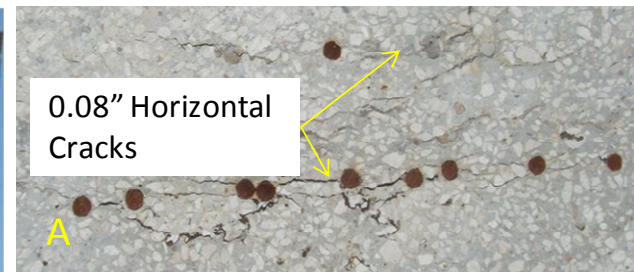
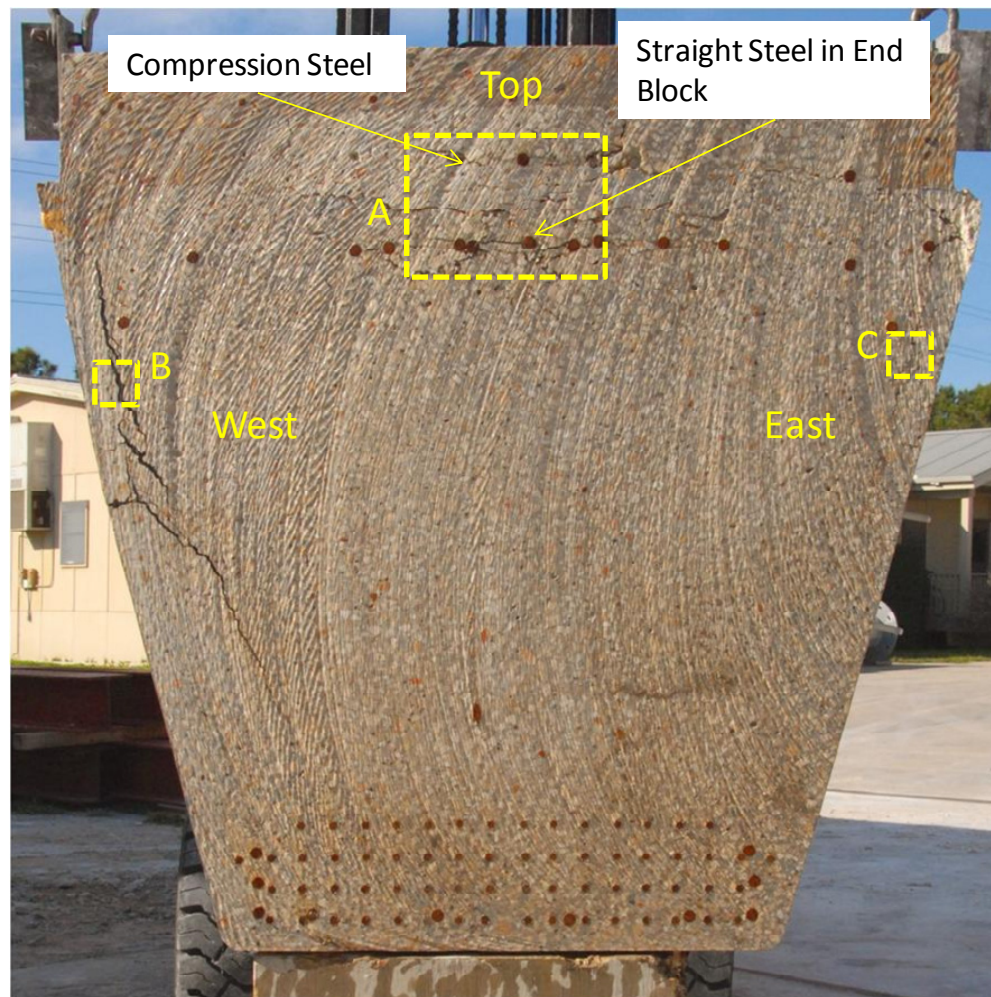


Figure 7.9 Overview and details of Section A

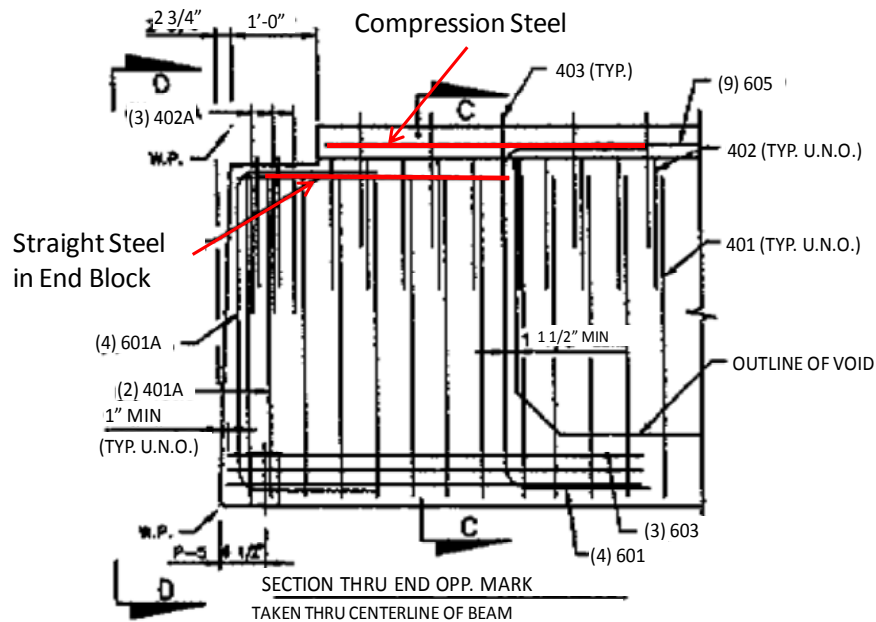


Figure 7.10 Elevation of the end block

Section B

Section B was cut at a distance of 22 in. from the end face, and its thickness was 8 in. thick. Section B was cut through a stirrup (Figure 7.11). This coincidence provided an opportunity to observe the crack pattern around stirrup. It was noted that 0.25 in. gap behind the inner part of the stirrup on the west side was filled with black epoxy, indicating that the reinforcement was pushed outward by concrete expansion due to ASR and/or DEF. Cracks were also found in both west and east sides. The maximum crack width was larger in the west side (0.25 in. near the gap) than the east side (0.02 in.). It should be also noted that the observed crack width was smaller in Section B than in Section A. Similarly, the crack in the west side was parallel to the surface near mid-depth of the section and then angled inward toward the bottom of the section. The crack in the east side narrowed before it reached the bottom of the beam. For the top portion, a crack (0.3 in.) through the compression reinforcement was again observed but not in straight steel in the end block. This difference may be due to the fact that the straight steel in the end block was confined by stirrups whereas the compression steel was located above the

top of stirrup. Therefore horizontal cracks through the layer of the compression steel occurred due to a lack of restraint provided by transverse reinforcement.

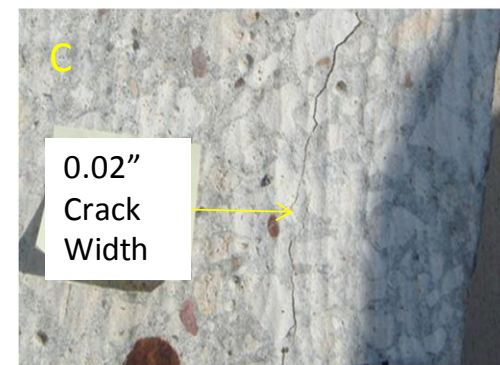
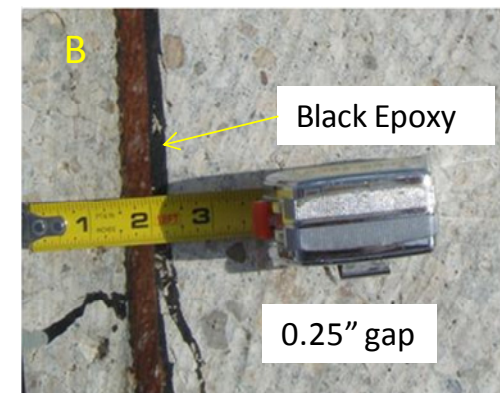
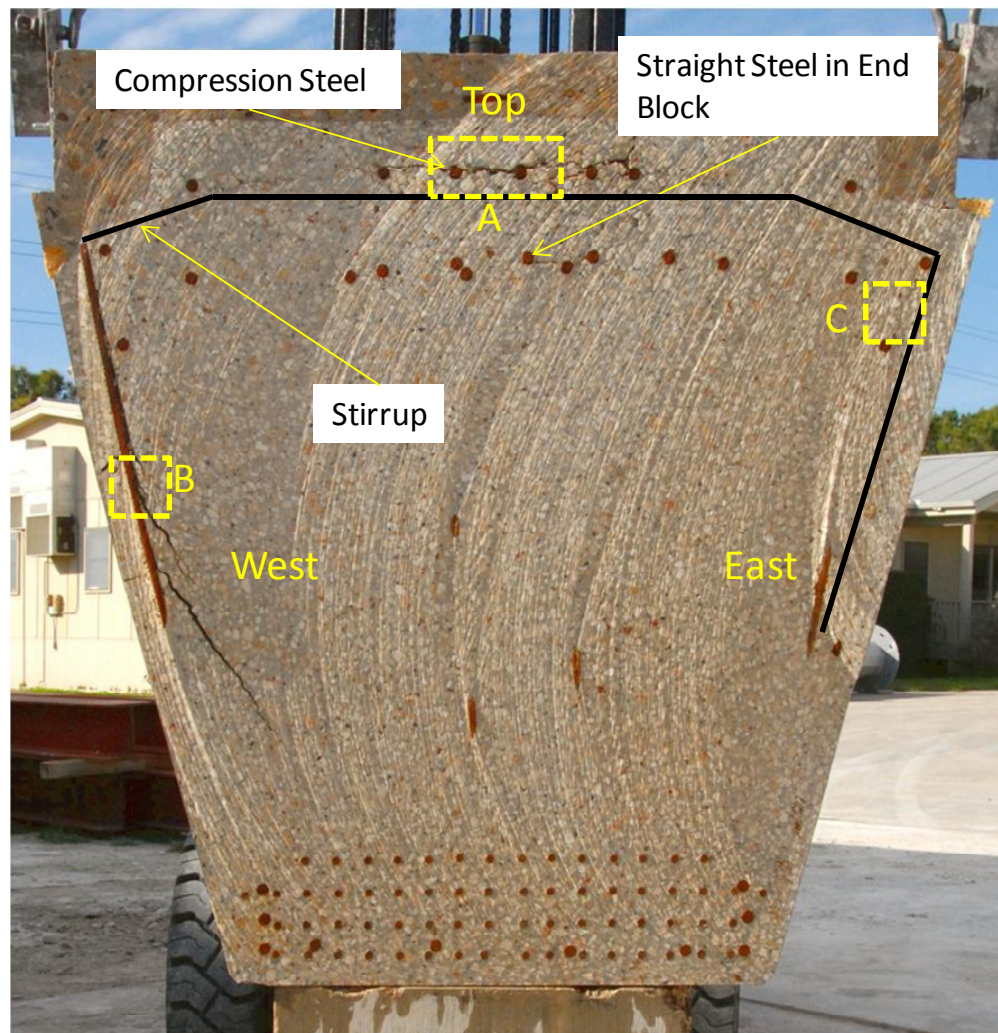


Figure 7.11 Overview and details of Section B

Section C

Section C was cut at a distance of 30 in. from the end face, and its thickness was also 8 in. thick. The crack pattern in this section was similar to that in the previous two sections, but the cracks were narrower and shorter (Figure 7.12). The maximum crack width in the west side decreased to 1/8 in. The crack almost disappeared toward the bottom of the section. Only a hairline crack of about 0.008 in. width around the aggregate was found in the east side. A horizontal crack (0.02 in.) through the layer of the compression reinforcement can still be observed in top portion of the section.

Section D

Section D was cut at a distance of 38 in. away from the end face, and was 8 in. thick. Two cracks were observed in the west side (Figure 7.13) – one crack was at the same location on the west side as was found in the previous sections and had a maximum width of 1/8 in. The other crack was located deeper inside the section and had a maximum width of 0.006 in. This beam was cut through a stirrup like that in Section B. Black epoxy was also observed filling the gap behind the stirrup, indicating the ASR and/or DEF expansion pushed the stirrup outward and caused cracking at the stirrup location. No distinct cracks were found in the east side. A crack (0.02 in.) through the layer of the compression steel was evident.

Section E

Section E was cut at a distance of 56 in. away from the end face, and its thickness was 17 in. thick (Figure 7.14). Section E was the only section involving the hollow section. A crack width of 0.07 in. was observed in the west side but no distinct cracks were observed in the east side. Injected epoxy penetrated through the cracks in the west side into the void and dissolved part of the Styrofoam. A crack through the layer of the compression steel, which was not confined by a stirrup, was evident. Some very fine cracks were found near the prestressing strands. These very fine cracks may have impact on the anchorage of the prestressing strands. Although anchorage did not control the failure in the web shear tests in this study, several cracks in the anchorage zone were observed at failure in the dapped end shear tests (Larson 2010).

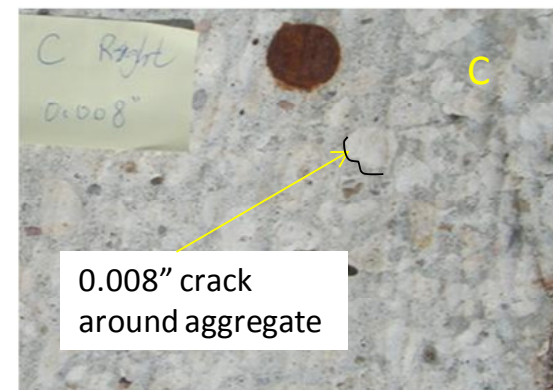
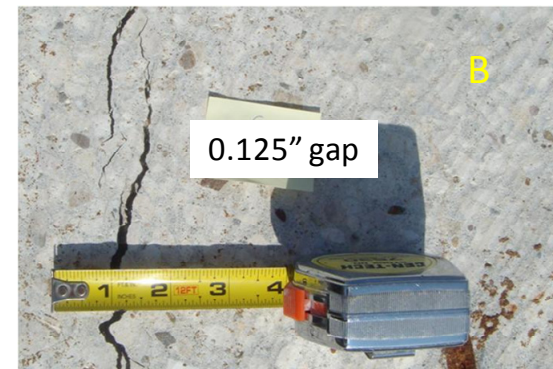
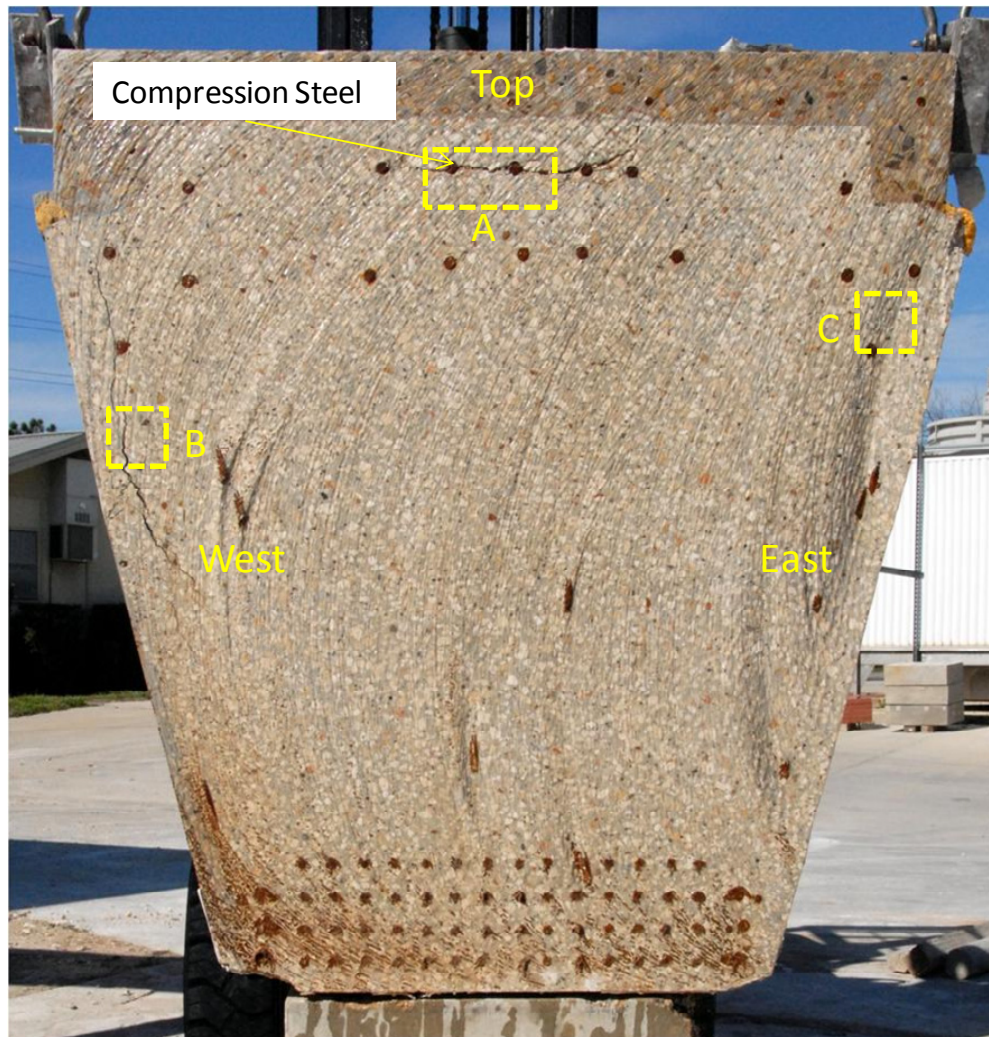


Figure 7.12 Overview and details of Section C

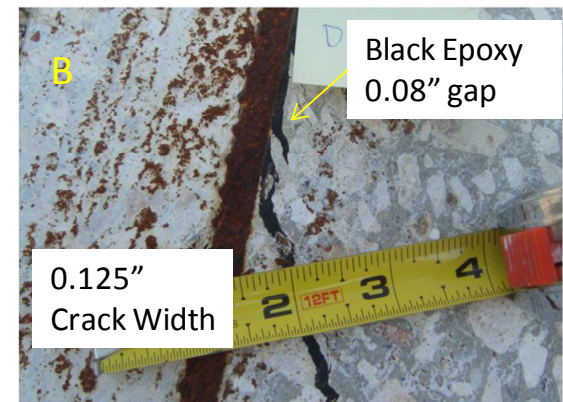
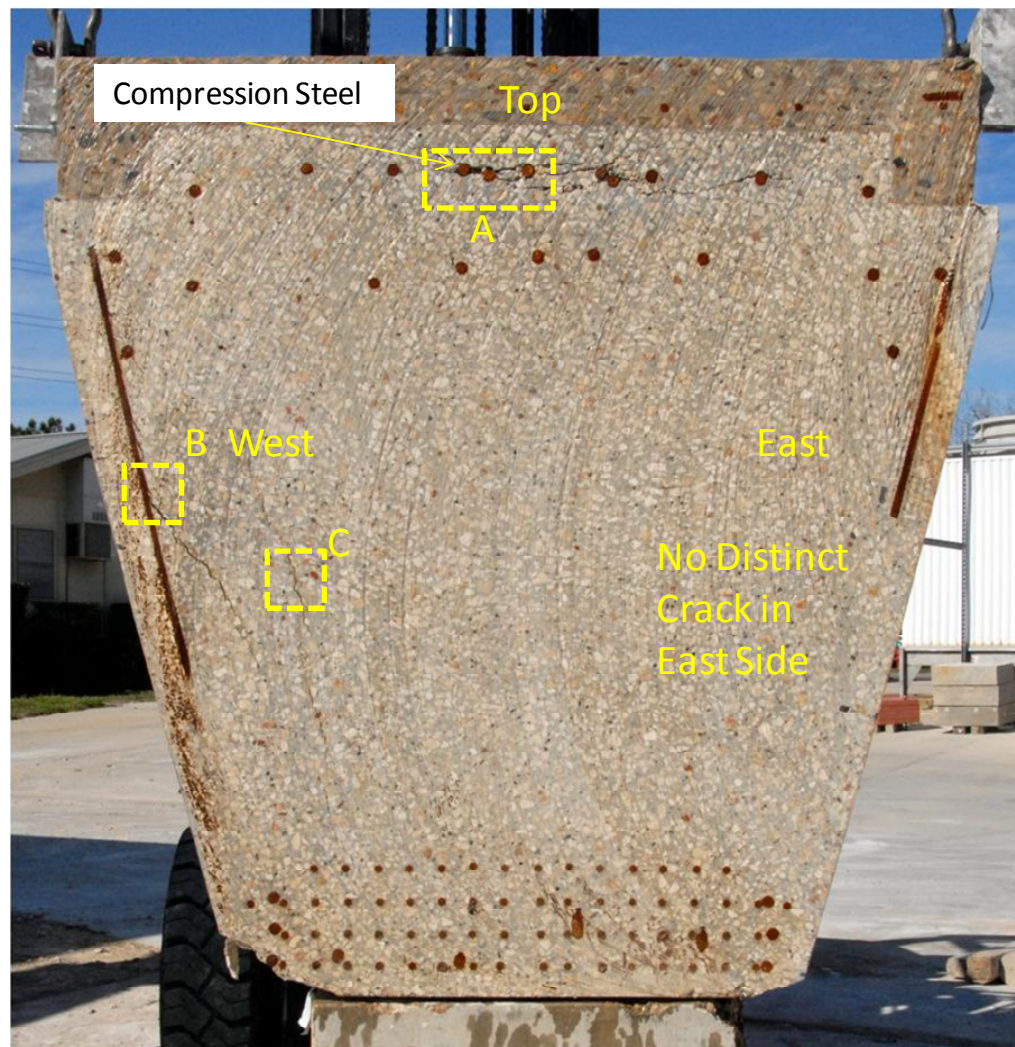


Figure 7.13 Overview and details of Section D

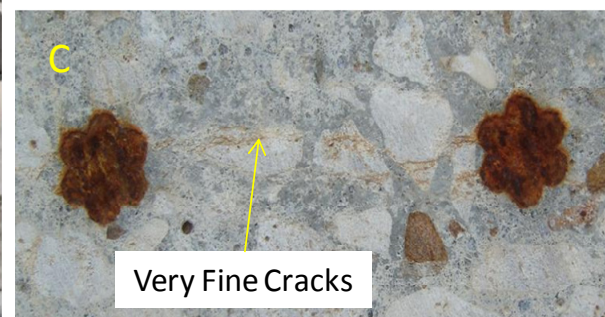
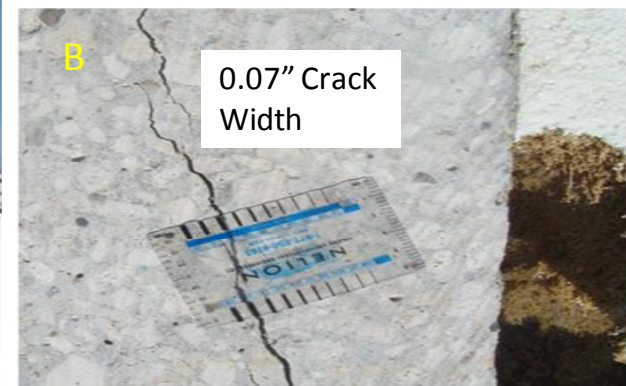
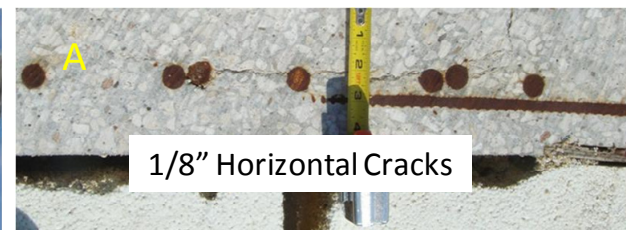
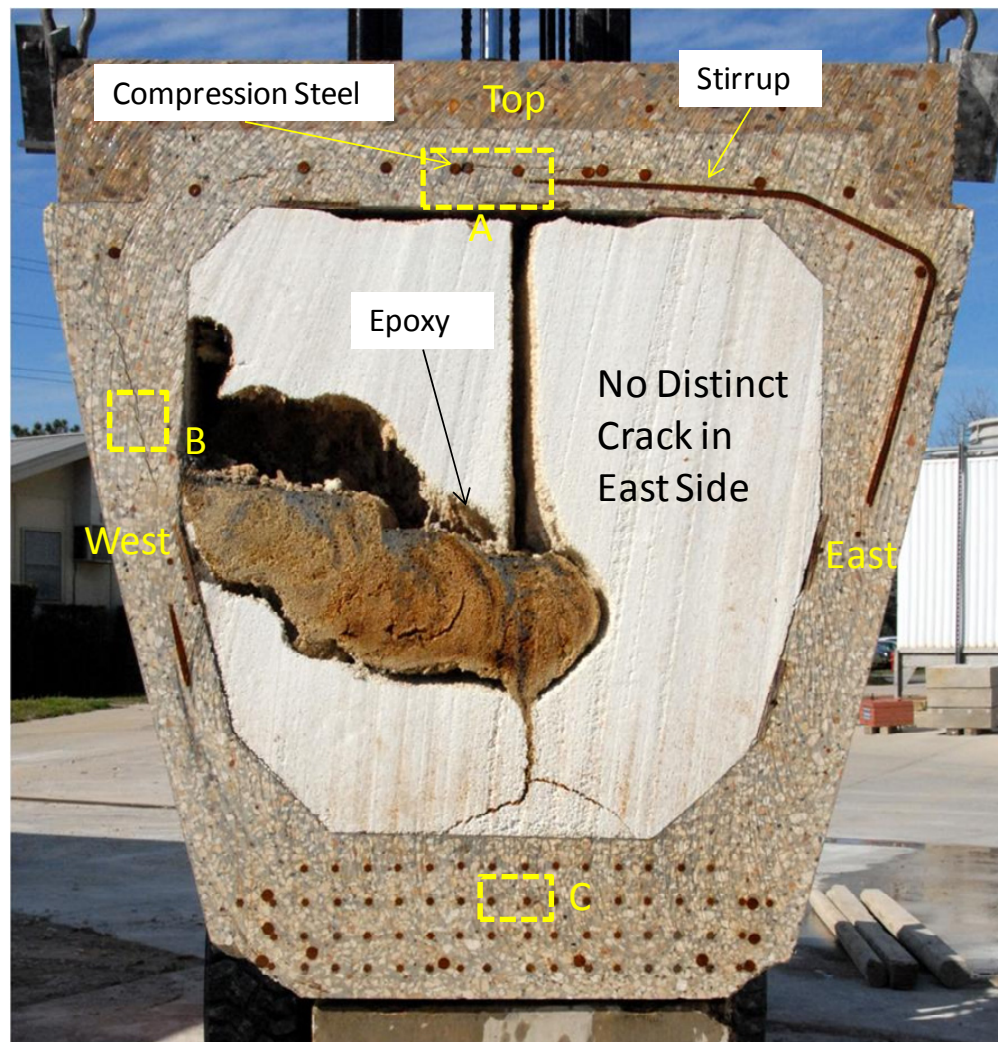


Figure 7.14 Overview and details of Section E

7.3.3 Discussion

From the five cut sections, the general crack patterns can be traced. A crack through the layer of compression steel, which was not confined laterally by stirrups, was observed in the top portion of all sections. Cracks were larger in the west side than in the east side (Figure 7.15). The crack widths were smaller in the sections further from the end face. No distinct cracks were noticed in the east side in section D and E that were farthest from the end. The diminishing crack width is likely due to lower concrete temperatures during curing. The temperature is usually higher in the massive concrete, and the relatively small amount of concrete in the hollow section did not reach temperature high enough to trigger DEF. All the test specimens had more obvious cracking in the end region than in the hollow section (Figure 5.44).

The crack in the west side was parallel to the concrete surface and then turned into the core as the crack extended to the bottom of the section, indicating a transition in the direction of restraint. The formation of a crack parallel to the surface essentially caused delamination of the cover. Such delamination was also reported by Kee (2010). Kee used the impact-echo method to assess the beams with moderate cracking (RF-3R-9-A and C) and heavy cracking (RF-1R-1-C). The impact-echo method can be used to locate a variety of defects within concrete elements such as delaminations, voids, honeycombing, or to measure element thickness (ACI 228). The results showed that delaminations existed in the beam with heavy cracking whereas no delaminations were detected in the beams with moderate cracking. More details related to nondestructive testing on these beams will be published in the future.

Bulging of the end block was evident (Figure 7.16). A level was used to show that the side of the beam was no longer a straight line due to bulging. In addition, bulging in top portion of section A can also be observed. Bulging in top flange of sections B~E was not as apparent as in this section. When expansion creates a tension in excess of the tensile strength of concrete, cover concrete unrestrained laterally by stirrups cracked as

shown in Figure 7.17, but the stirrups prevented cracks from propagating into the structural core.

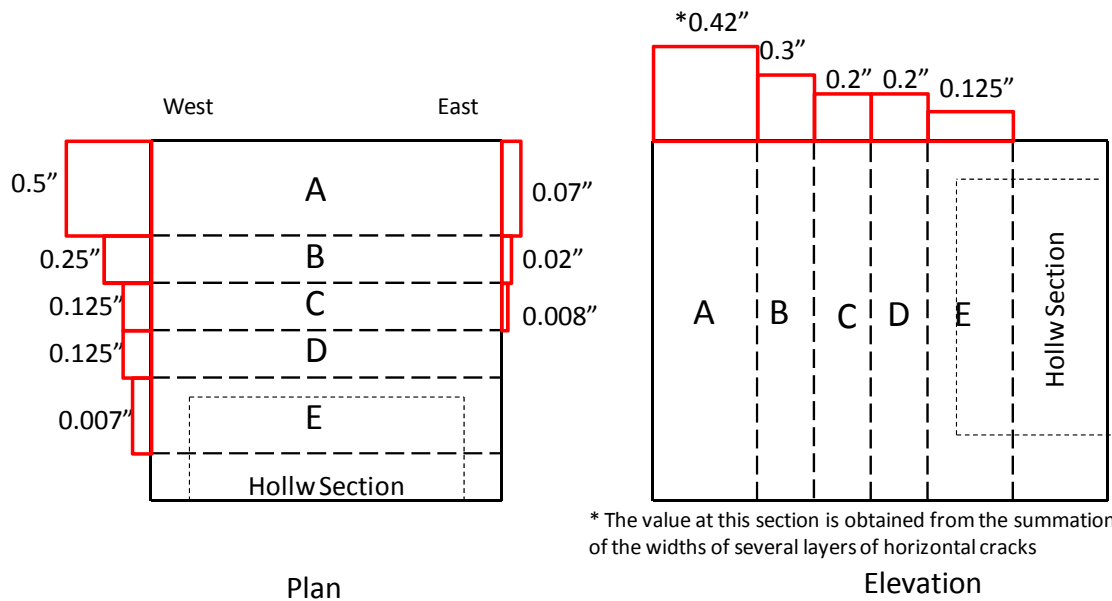


Figure 7.15 Summary of the crack widths

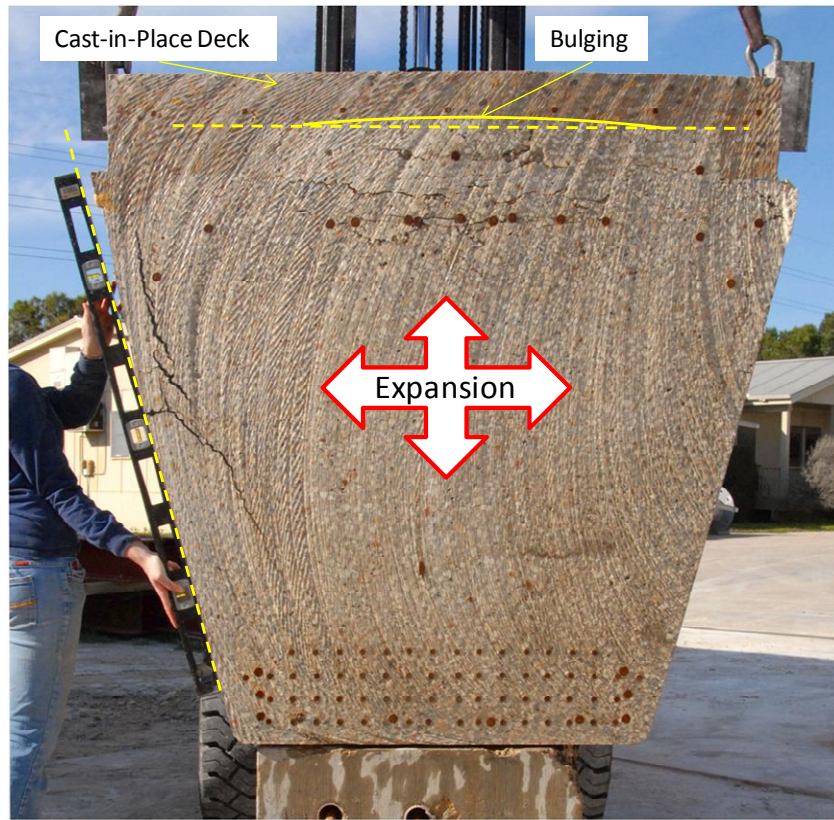


Figure 7.16 Bulging in Section A

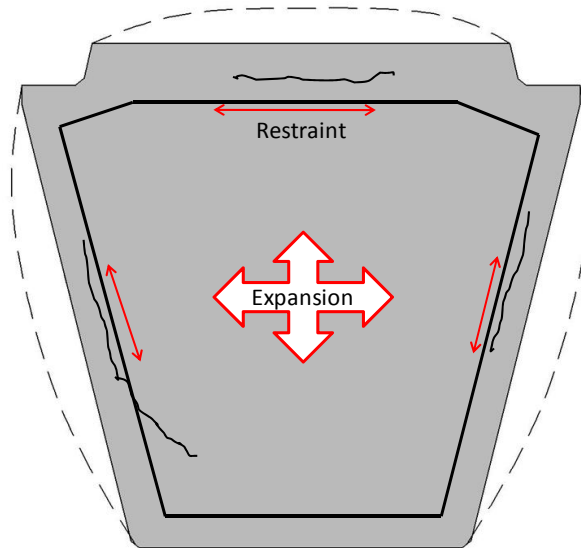


Figure 7.17 Relationship between expansion and restraint

7.4 ELASTIC REBOUND TEST

Theoretically, if perfect bonding exists between reinforcement and ASR and/or DEF affected concrete, the expansive strain in the reinforcement and concrete should be equivalent. The elastic rebound test is based on this concept. *Highly-stressed* transverse reinforcement is exposed and cut, and the rebound strain is measured (Figure 7.18). Assuming that perfect bonding exists, the measured strain can be considered to be caused by ASR and/or DEF expansion. *Highly-stressed* is emphasized because a sufficiently distinguishable strain may not be detected if ASR and/or DEF expansion within concrete is not large. It should be noted that, strains in excess of yielding cannot be correctly detected as shown in Figure 7.19. First assume that perfect bonding exists between reinforcement and concrete. If ASR and/or DEF expansion in the concrete is less than that corresponding to reinforcement yielding, the measured strain from an elastic rebound test should be equal to strain produced by ASR and/or DEF actions. If ASR and/or DEF expansion is greater than yielding but smaller than strain hardening, the measured strain from elastic rebound test should be equal to yielding of reinforcement. If ASR and/or DEF expansion results in the strain hardening of the reinforcement, the measured strain from elastic rebound test should be greater than yielding.

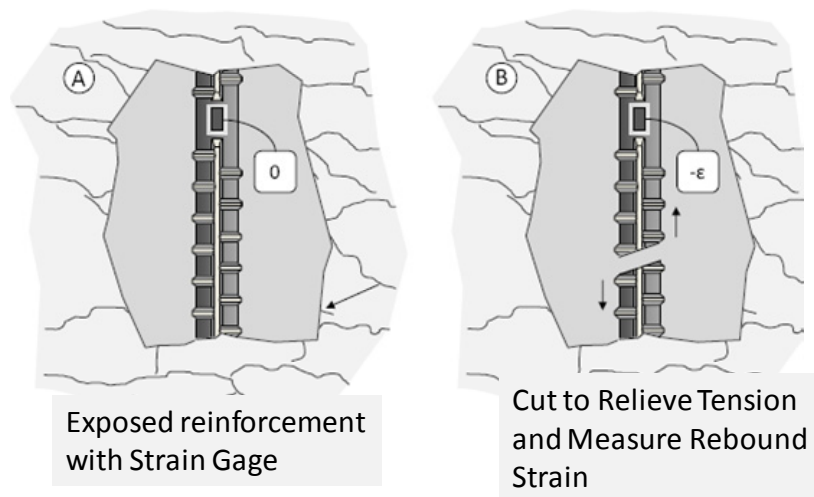


Figure 7.18 Mechanism of elastic rebound test (Deschenes 2009)

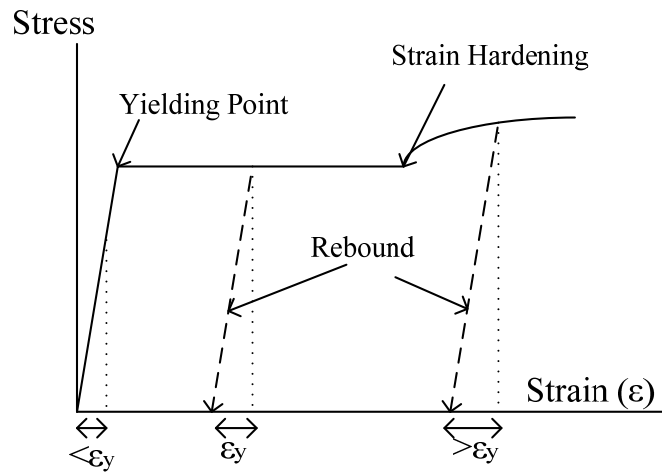


Figure 7.19 Typical stress-strain relationship of steel

Elastic rebound tests were conducted on transverse reinforcement in the end blocks of four beams in this study (Figure 7.20). Two of the beams were not subjected to any loads but the other two were loaded to test the dapped end in shear so locations were carefully chosen in order to avoid the interference from load produced cracks. To expose the transverse reinforcement, an electric jackhammer was used to remove the cover concrete. The reinforcement was smoothed, cleaned, and instrumented with a strain gage. After the preparation work was finished, the exposed reinforcement was cut by a pneumatic saw and the amount of shortening (elastic rebound) was recorded.

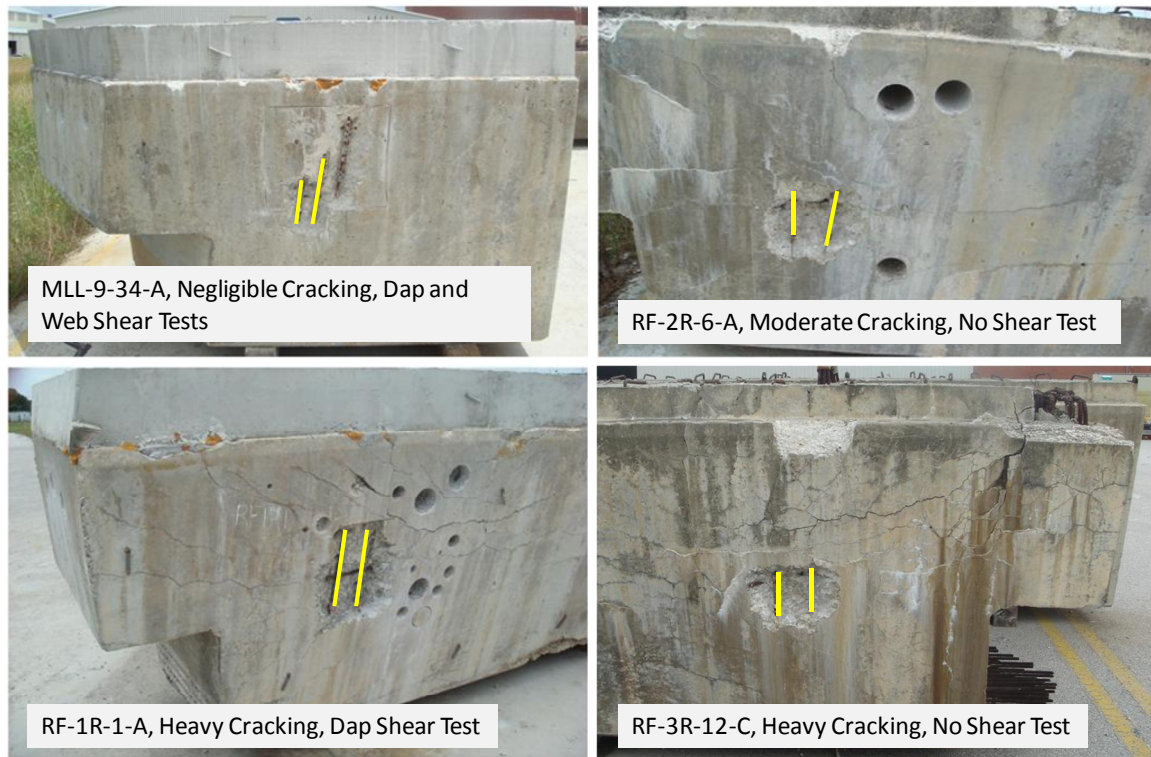


Figure 7.20 Locations of tested steel and cracking condition

In Figure 7.21, the test results are compared for the four beams (two tests each beam). All the strains measured were smaller than the nominal yield of the transverse reinforcement (0.002). This value is also a threshold value proposed by Berube et al. (2004) and described in Fournier et al. (2004) that could result in the reinforcement exceeding its elastic limit, provided that perfect bonding exists between concrete and reinforcement. It is clear that the beam with negligible cracking had the lowest rebound strain as expected. However, the elastic rebound strains did not correspond with the cracking level (moderate or heavy) categorized by visual inspection. The beam with moderate cracking had the highest elastic rebound strain.

Although such results may seem to conflict with the visual inspection, it should be noted that the basic assumption of elastic rebound test is that perfect bonding exists between reinforcement and concrete. However, as described in 7.2 and 7.3, a gap was found behind the reinforcement from both petrographic analysis and beam autopsy. Therefore the results of elastic rebound tests, especially for the beams with heavy

cracking, may not be as accurate as that from the beam with negligible cracking due to loss of bond along the stirrups. Besides, an elastic rebound tests is preferably conducted in an area with the most severe cracking to obtain upper bound estimate. Nevertheless, due to the constraints introduced by the pre-existing core holes and load produced cracks, an ideal area for the test was not readily available. It is also possible that principle direction of ASR and/or DEF expansions did not correspond with the transverse reinforcement; in which case, the testing results cannot truly reflect the level of ASR and/or DEF cracking.

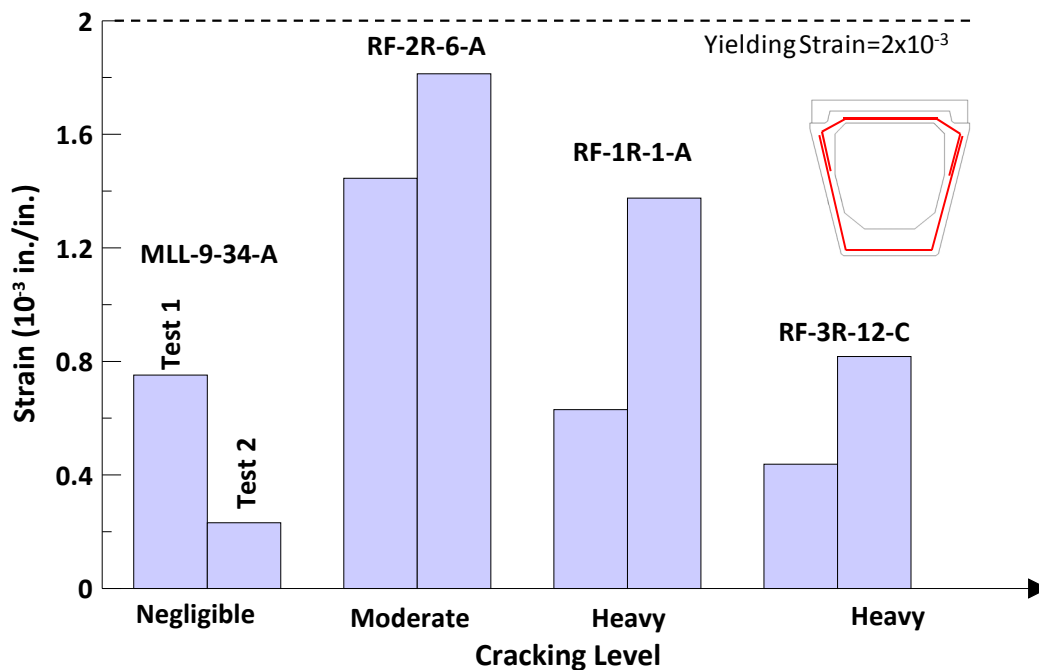


Figure 7.21 Comparison of results from elastic rebound tests

Although all the rebound test strains were smaller than the yielding strain (0.002), yielding of the rebar would not affect the shear capacity of the specimens. In 2.5.2.2, it was shown that beams with shear reinforcement regained shear strength when ASR and/or DEF expansion reached 0.004 (Clayton 1990). Besides, in the shear tests in the current study, the average vertical strains in each beam were all greater than 0.002 before failure (Figure 5.43). These observations indicated that the restraint provided by

transverse reinforcement played an important role in sustaining the shear capacity of the beams subjected to ASR and/or DEF deterioration.

7.5 SUMMARY

In this chapter, three forensic analyses were conducted on the beams with various degrees of cracking due to ASR and/or DEF.

First, cores were extracted from three beams with various degrees of cracking and sent to TxDOT Concrete Laboratory for petrographic analysis. TxDOT personnel concluded that the main distress mechanism was ASR. It was inconclusive whether DEF contributed to the distress because gapping around aggregates due to paste expansion was limited. Micro structural cracks parallel to the concrete surface were observed in the concrete away from the 2 in. cover and beyond the reinforcement. Cores were ranked based on damage severity by counting reactive particles in each core. A relatively small amount of reactive particles was found within the cores extracted from the beam with negligible cracking; however, no distinct relationship between damage severity and reactive particles was found for beams with moderate to heavy cracking.

Second, one beam with heavy cracking was chosen for autopsy. Five cuts were made in the end block of the beam to slice the beam into five pieces. These five slices had generally similar crack patterns but the crack widths varied. Cracks formed gaps behind stirrups and through the layer of compression steel. Cracks parallel to surface were found in the cover concrete and corresponded with the observation of the cores in the petrographic analysis. It can be found that the map cracking was limited to the concrete surface. Very fine cracks were found in between prestressing strands indicating a possible influence of ASR and/or DEF on anchorage performance.

Finally, elastic rebound tests were conducted to investigate the state of strain in transverse reinforcement. The lowest elastic rebound strain was detected within the stirrups of the beam with negligible cracking. However, the measured elastic rebound was higher within the stirrup of the moderately cracked than heavily cracked beams. The results may not truly reflect the degree of ASR and/or DEF expansion in concrete due to

loss of bond, limitation of the testing area, and a discrepancy in the direction of the principle expansions and the transverse reinforcement.

CHAPTER 8

Summary and Conclusions

8.1 SUMMARY

Some concrete bridges in Texas have developed large cracks in bent caps and pretensioned trapezoidal bridge girders. The bridges show premature concrete deterioration due to alkali-silica reaction (ASR) and delayed ettringite formation (DEF). There is concern that ASR and/or DEF-caused cracks may be related to a loss of structural capacity. However, so far there are no quantitative guidelines to evaluate the effect of concrete deterioration due to ASR and/or DEF on structural properties. By developing such guidelines, the urgency of rehabilitating beams with ASR/DEF cracking can be assessed.

The major objective of this research was to assess shear strength of pretensioned trapezoidal box girder specimens suffering from varying degrees of ASR and/or DEF cracking. Tests of the box girders were conducted and the results were used to evaluate the severity of the damage and its impact on structural performance. To achieve this goal, beams that exhibited deterioration due to ASR/DEF over a period of more than ten years were transported to UT for testing and evaluation.

The work reported in this dissertation can be summarized as follows:

1. Five salvaged prestressed trapezoidal box beams about 115 ft. long with varying degrees of ASR and/or DEF cracking were cut into three segments and transported to Ferguson Structural Engineering Laboratory. Visual inspection was conducted on the specimens to determine ASR and/or DEF cracking levels. Different levels of map cracking were generally observed in the end regions. Longitudinal cracks or cold joint were observed in the hollow sections. Various degrees of void floatation were also noticed during the assessment.

2. Tests were conducted on five specimens to determine the impact of ASR and/or DEF cracking on shear capacity. The five specimens had cracking varying from negligible to heavy.
3. Strut-and-tie models were used to compute the shear capacities of the five test specimens. The computed shear capacities were compared with the measured shear capacities. Two types of strut-and-tie models – one-panel models and combination models were utilized to predict the shear capacities of the test specimens. The models were calculated using procedures presented in AASHTO LRFD (2008), ACI 318-08, and TxDOT Project 5253 (Bircher et al. 2008). Shear capacities were calculated using both design concrete strength with nominal steel strength and core strength with tested steel strength.
4. Three different forensic analyses were conducted on the specimens with varying ASR and/or DEF cracking levels. First, nine cores were extracted from three specimens with varying degrees of ASR and/or DEF cracking and were sent to the TxDOT Concrete Laboratory for petrographic analysis. Second, in order to further understand the nature of the ASR and/or DEF cracking, one beam with heavy cracking was autopsied by cutting five sections from the end region of the beam. Through these five sections, internal ASR and/or DEF cracking patterns were observed. Finally, elastic rebound tests were conducted to investigate the state of strain in transverse reinforcement in regions where ASR and/or DEF expansions occurred.

8.2 CONCLUSIONS

The key findings over the course of the experimental program are summarized below:

1. *The main shear failure mode of the test specimens was strut crushing.* Three of the five test specimens failed in strut crushing. One failed in shear tension failure and one exhibited a cold joint failure. The result indicates that the direct strut from load point to the support is the dominant shear transfer mechanism when the shear span-to-depth ratio is 1.85.

2. *No distinct reduction of the shear capacity of the test specimens was shown even in the specimen with heavy ASR and/or DEF cracking.* The lightly cracked beam with an apparent poor construction joint had the lowest shear capacity of the five specimens tested, indicating that the quality of construction may have reduced the shear capacity. The shear capacity of the specimens with negligible cracking and heavy cracking was similar while that of the specimens with moderate cracking was slightly higher.
3. *Specimens with more ASR and/or DEF cracking tended to form new diagonal cracks at higher loads than those with light or negligible cracking.* As reported by Birrcher et al. (2008), service shear for a reinforced concrete bent cap is generally one third of the experimental shear capacity. The specimen with negligible cracking in the current study exhibited new diagonal cracking when the load was about 30% of the measured shear capacity. However, new diagonal cracking did not appear in the specimen with heavy cracking until the load reached 60% of experimental shear capacity. Diagonal cracking provides early warning of poor structural performance. ASR and/or DEF cracking suppress such warning indicators.
4. *Current US design provisions (AASHTO LRFD (2008) and ACI 318-08) and the design provision proposed in TxDOT Project 5253 gave conservative estimates for the shear capacities of the test specimens.* A one-panel strut-and-tie model using core concrete strength and following the procedures of TxDOT Project 5253 gave the most accurate but still quite conservative prediction. However, it should be noted that the proposed provision was based on the reinforced, not prestressed, concrete deep beam tests.
5. *Quantitative forensic analyses did not correlate well with the cracking levels as determined by visual inspection.* Both reactive particle counting in the petrographic analysis and elastic rebound tests failed to provide a good correlation with the visible cracking conditions of the end blocks. However, qualitative (visual) evaluation provides an indication of ASR and/or DEF deterioration.

8.3 FUTURE WORK

1. According to the experimental results, the impact of ASR and/or DEF deteriorations on the measured loss of shear capacity of the prestressed trapezoidal box beams was minimal. However, further deterioration may cause reinforcement fracture and severely impact structural capacity (anchorage or shear capacity) of the trapezoidal box beams. Therefore, future research should focus on potential for and effect of ASR and/or DEF induced reinforcement fracture on the structural capacity.
2. Although TxDOT Project 5253 yielded relatively accurate and conservative results for the computation of shear capacity of prestressed trapezoidal box deep beams in this study, verification of the applicability of the proposed provision for prestressed concrete deep beams still needs further investigation and research.

APPENDIX A

Beam Information

Appendix A includes detailed information of geometry and reinforcement of the prestressed trapezoidal box beams in this study.

A.1 STANDARD DRAWING

The prestressed box beam fabricator shall prepare and submit for approval shop drawings sufficient in detail to enable correct fabrication and inspection without reference to these standard sheets. These beams are designed for HS-20 loading in accordance with AASHTO 1989 Standard Specifications. All reinforcing steel shall be Grade 60. All concrete shall be Class H in strength as shown. Prestressed concrete box beams shall be cast monolithically in two stages. Fabricator shall provide positive verifications to the engineer that the webs, top flange and bottom flange are within the dimensional tolerances specified herein. All prestressing strands will be 0.5" diameter, 270 ksi. Initial pretension is 31.0 kips. Low-relaxation strands must be used. Strands with bond breakage (debonding) shall be encased in plastic tubing along the entire debonded length and ends of tubing sealed with waterproof tape to prohibit grout infiltration. Wrapping of strands with tape to provide debonding will not be permitted. The stressing procedure will be such that no cracks will develop during manufacture of the beam. Cracking is anticipated when the concrete tensile stress exceeds 474 psi. prestressed losses are calculated on a relative humidity of 75%. Cardboard forms are not permitted. Cost of furnishing and installing elastomeric bearing and two-piece threaded bars shall be included in the unit bid price for prestressed concrete beams. Mechanical connector shall develop 125% of bar yield strength. Screed the top surfaces of beams or rough float to bring mortar to the surface and cover all aggregate. The surface shall have a rough wood float or stiff broom finish. Aggregate shall not be loosened when roughening the surface.

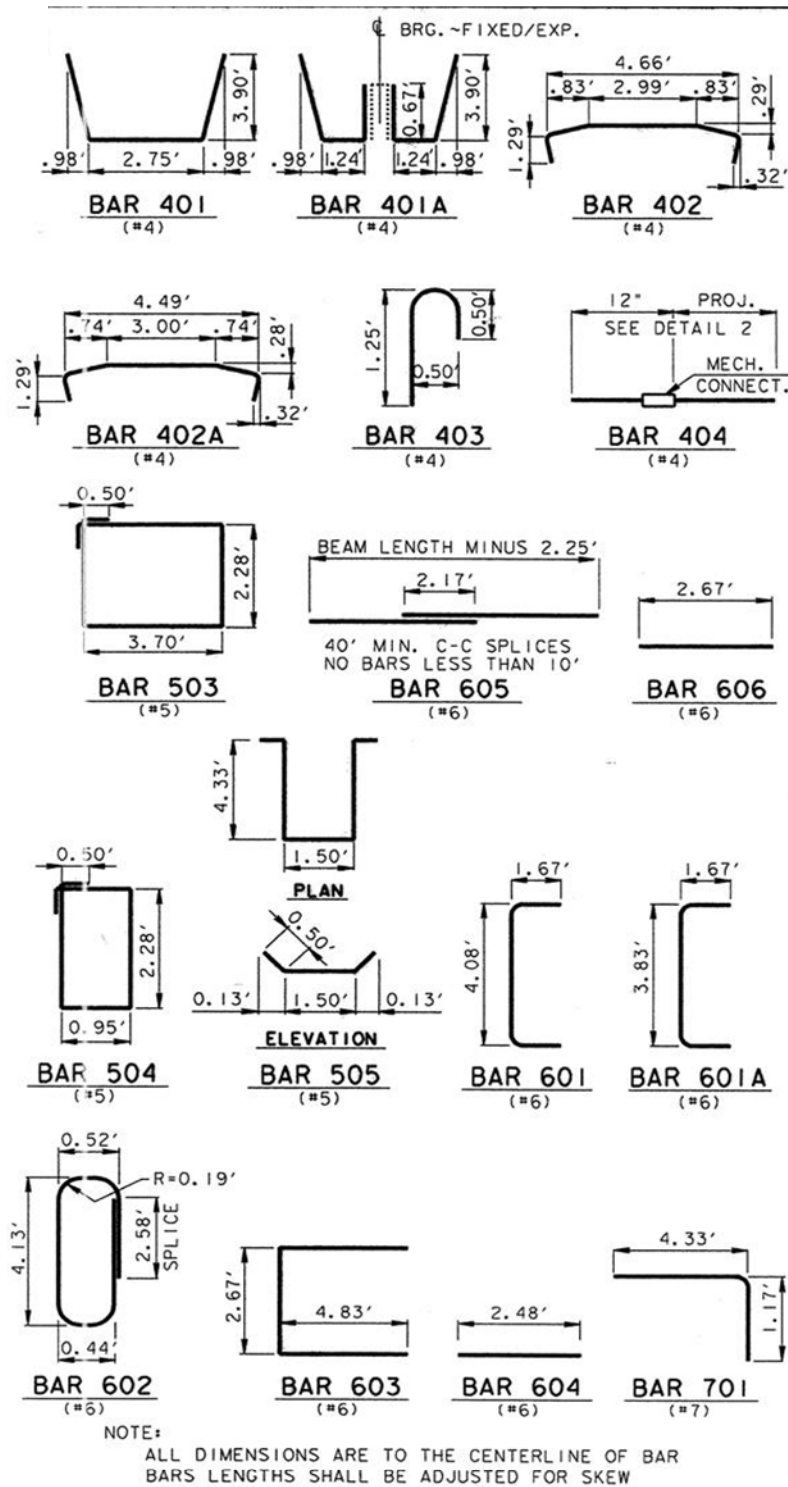
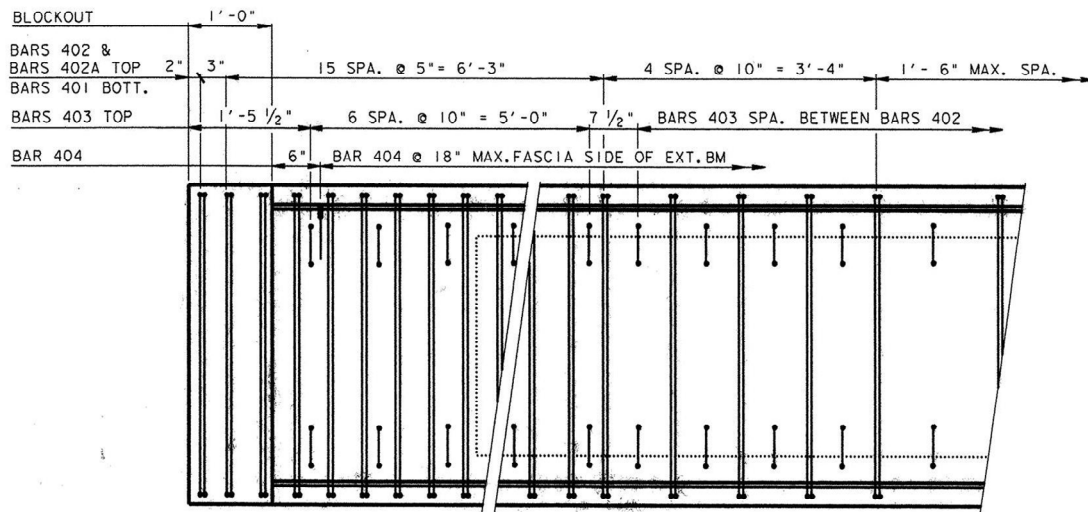
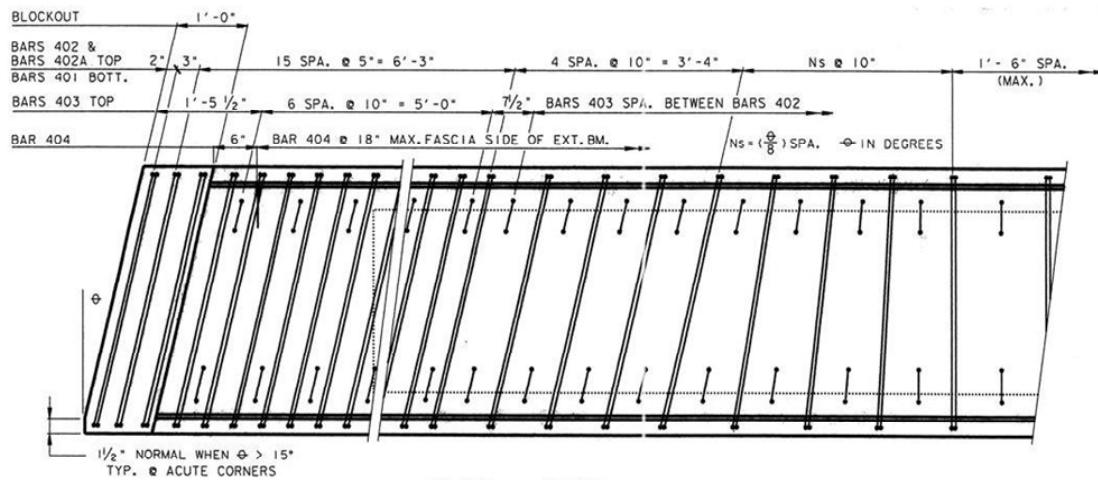


Figure A.1 Standard reinforcement

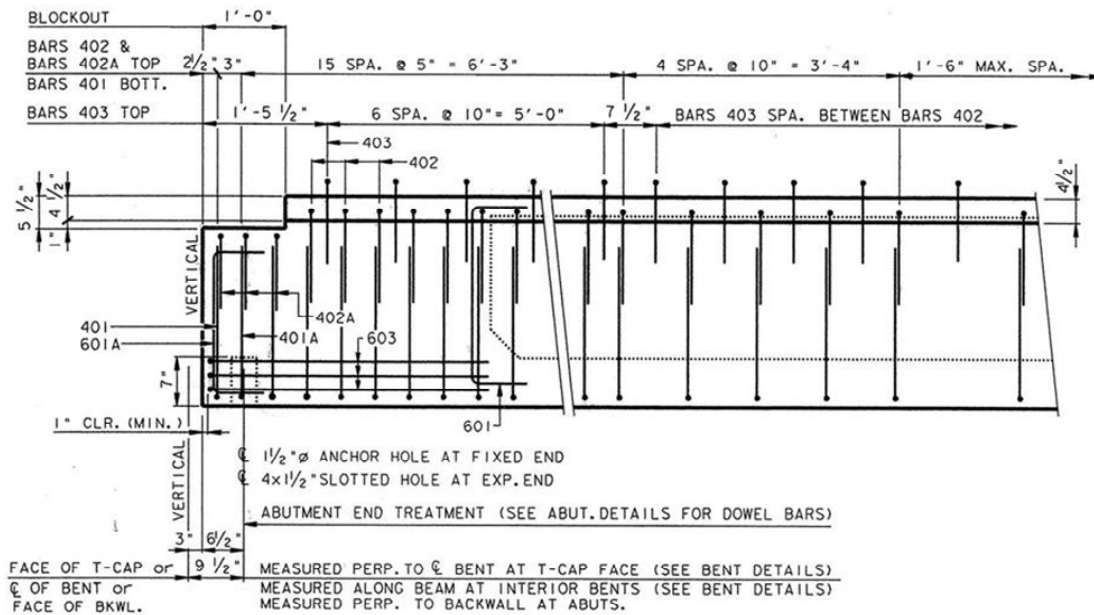


PLAN ~ NORMAL



PLAN ~ SKEW

Figure A.3 Standard plan



ELEVATION ~ STANDARD END DETAIL

Figure A.4 Standard end detail (elevation)

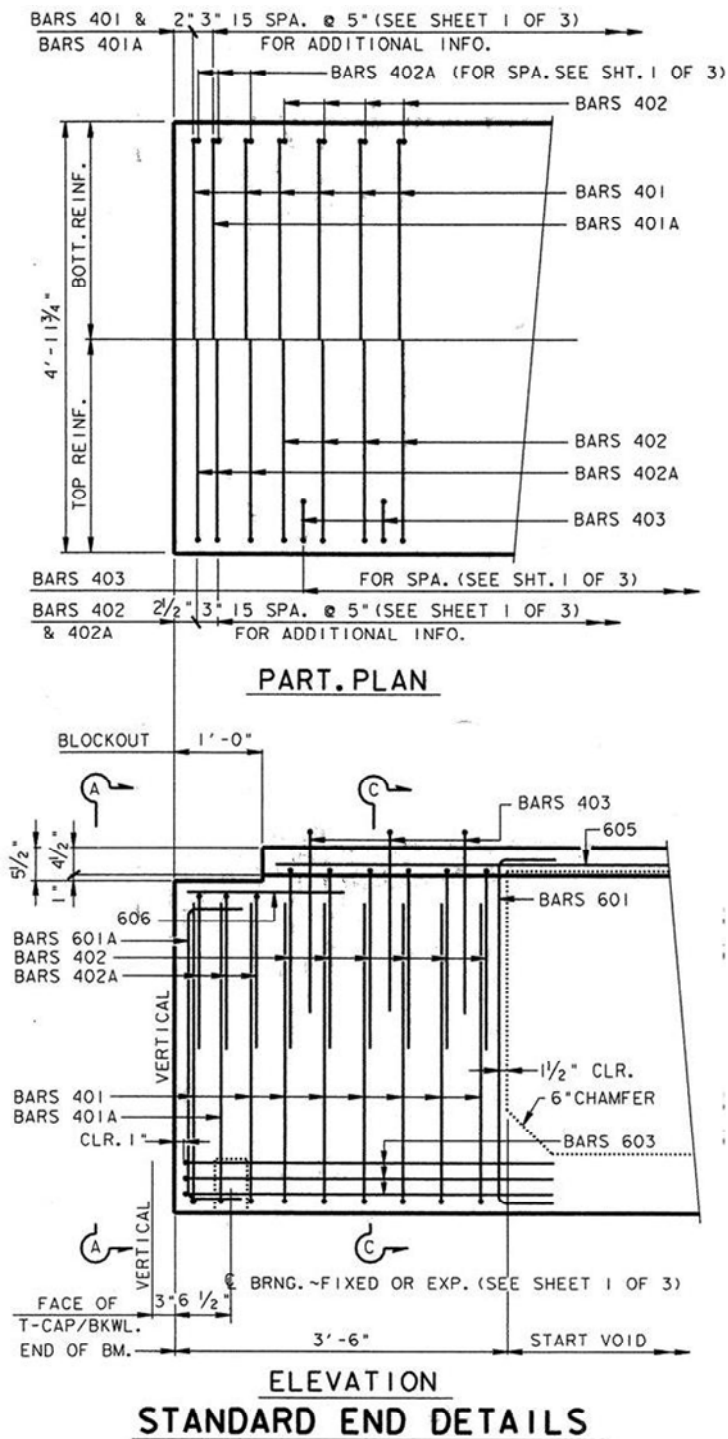


Figure A.5 Standard end detail

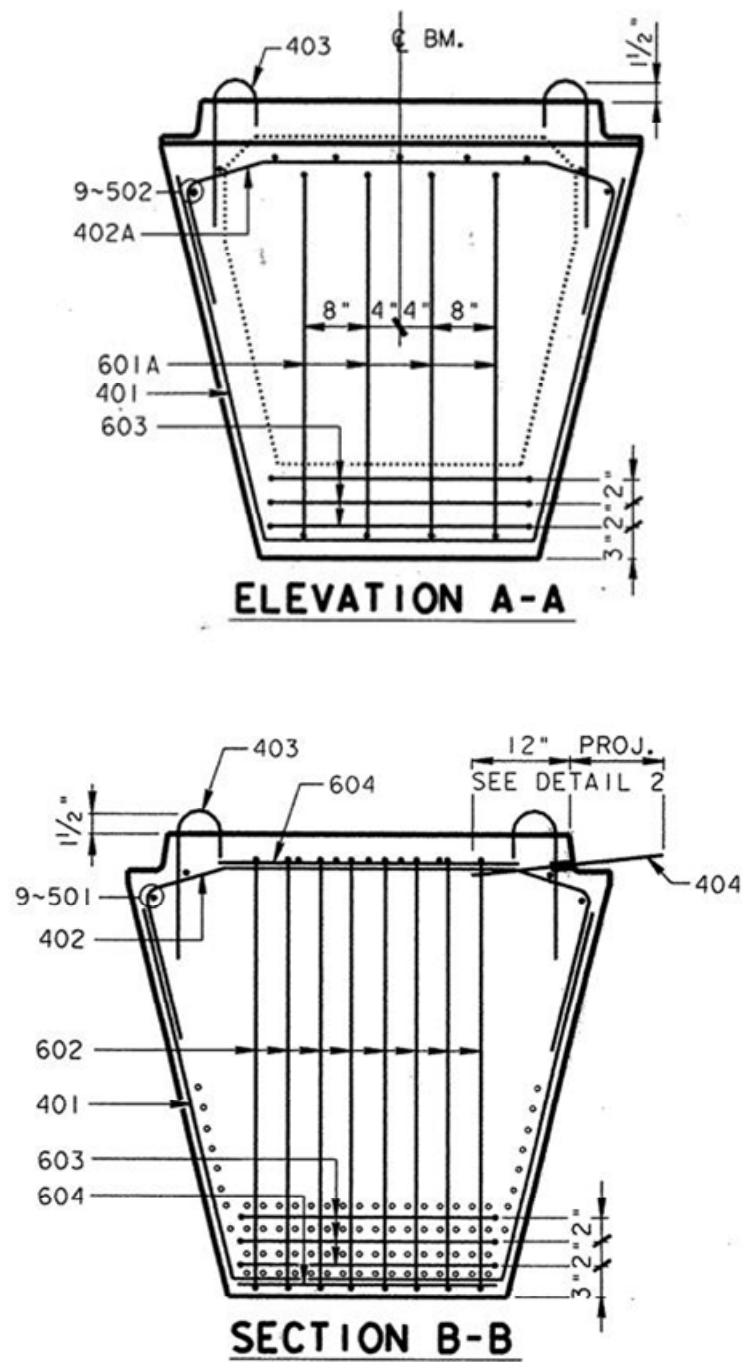


Figure A.7 Standard section profile

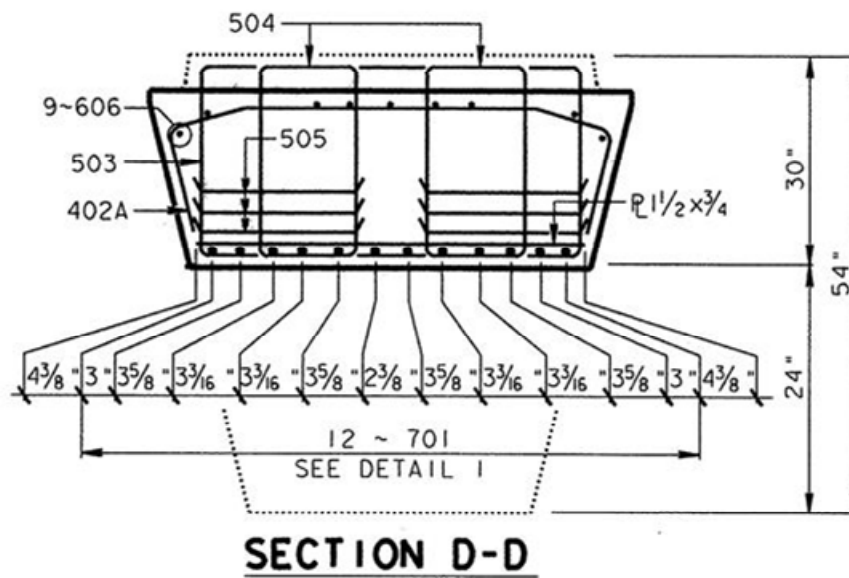
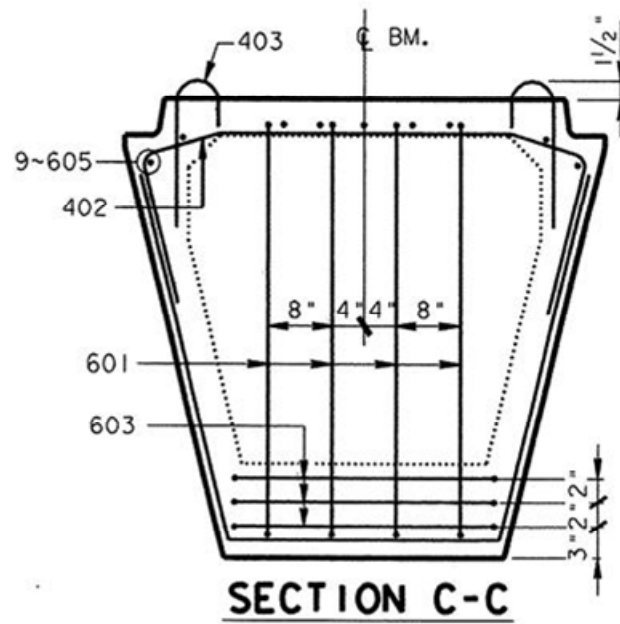


Figure A.8 Standard section profile (continued)

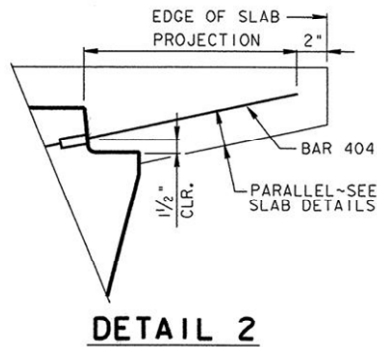
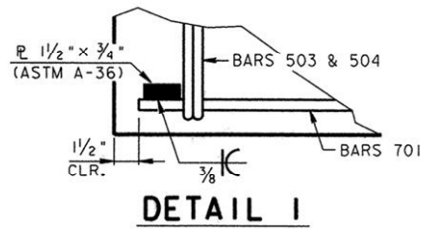
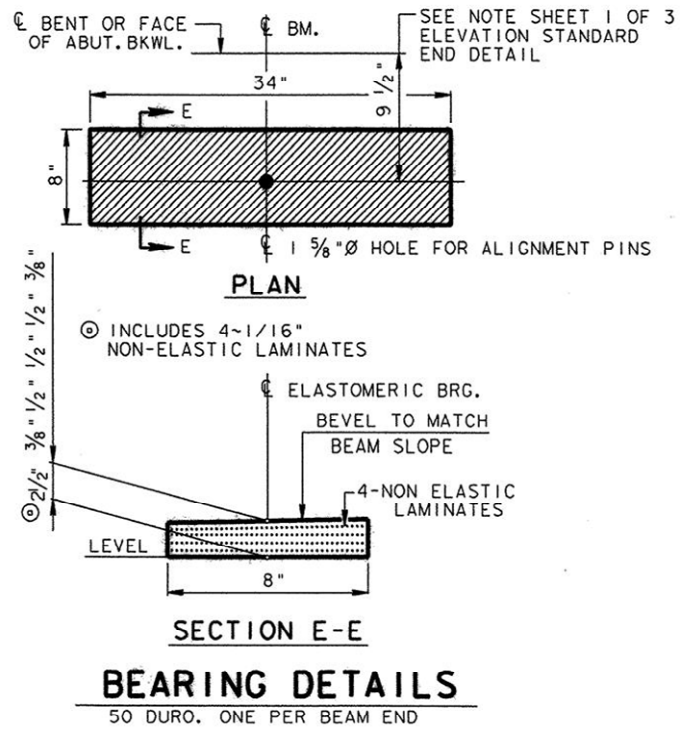


Figure A.9 Bearing and other details

A.2 SHOP DRAWING

A.2.1 RF-1R-1

Table A.1 RF-1R-1 reinforcing bars list

Reinforcing bar list			
Mark	Quan.	Length	Remarks
401	102	10'-10"	See Standard Drawings
401a	2	1'-0"	See Standard Drawings
402	101	7'-5"	See Standard Drawings
402a	6	7'-3"	See Standard Drawings
403	47	7'-3"	See Standard Drawings
404	75	1'-0"	Straight w/ Coupler
503	4	13'-0"	See Standard Drawings
504	6	7'-6"	See Standard Drawings
505	6	11'-2"	See Standard Drawings
601	3	7'-5"	See Standard Drawings
601a	2	7'-2"	See Standard Drawings
603	9	12'-4"	See Standard Drawings
604	16	2'-6"	Straight
605	1	110'-11"	See Standard Drawings
606	16	3'-2"	Straight
L-1	1	3'-8 3/8"	C.L. 1 1/2x3/4" w(12) 701
702	6	12'-0"	See Standard Drawings
P-1	2	10"	3/4" Sleeve
P-2	5	3"	2" C.L. Sleeve
P-3	1	7"	1 1/2" C.L. Sleeve
N.S. denotes near side F.S. denotes far side			

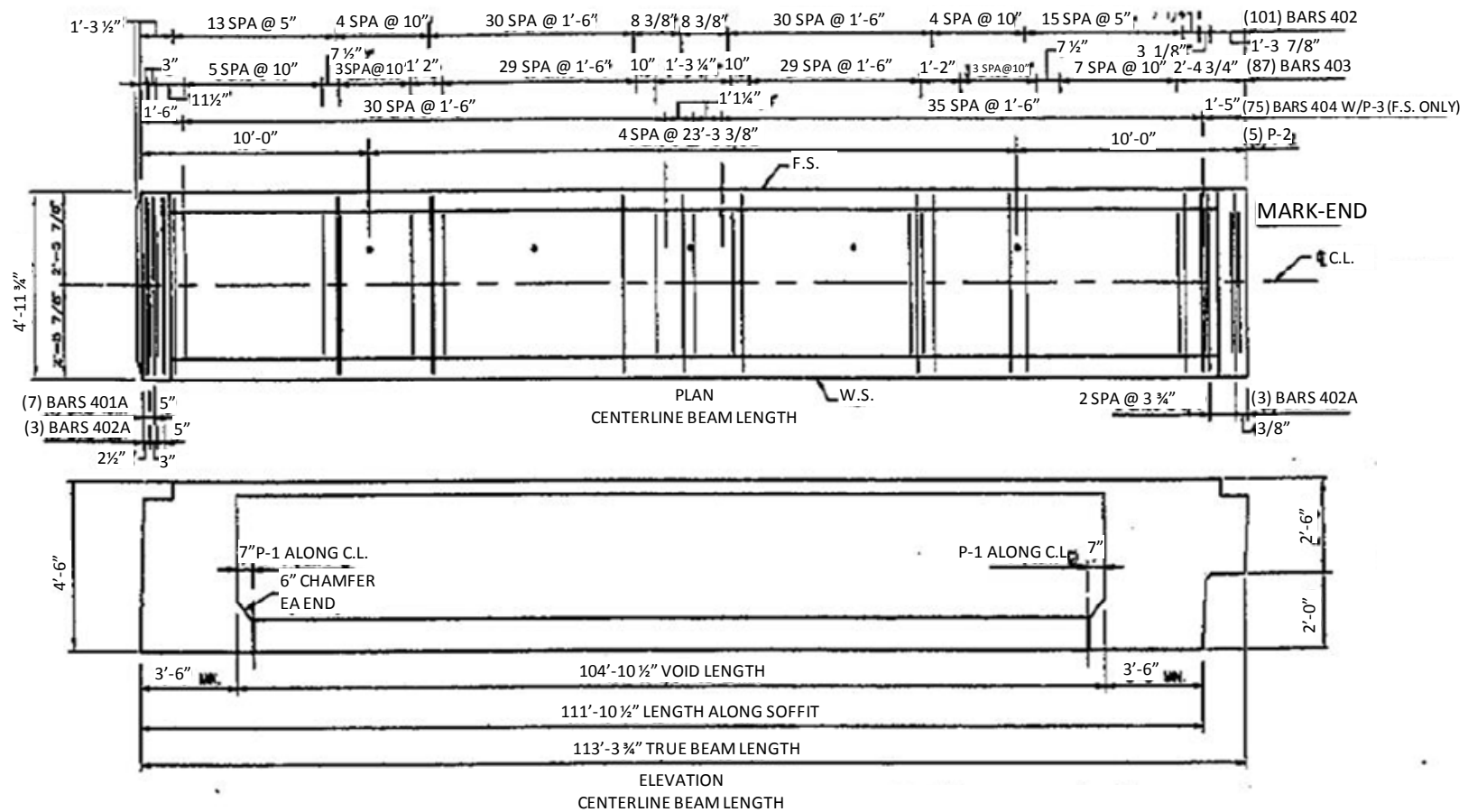


Figure A.10 RF-1R-1 plan

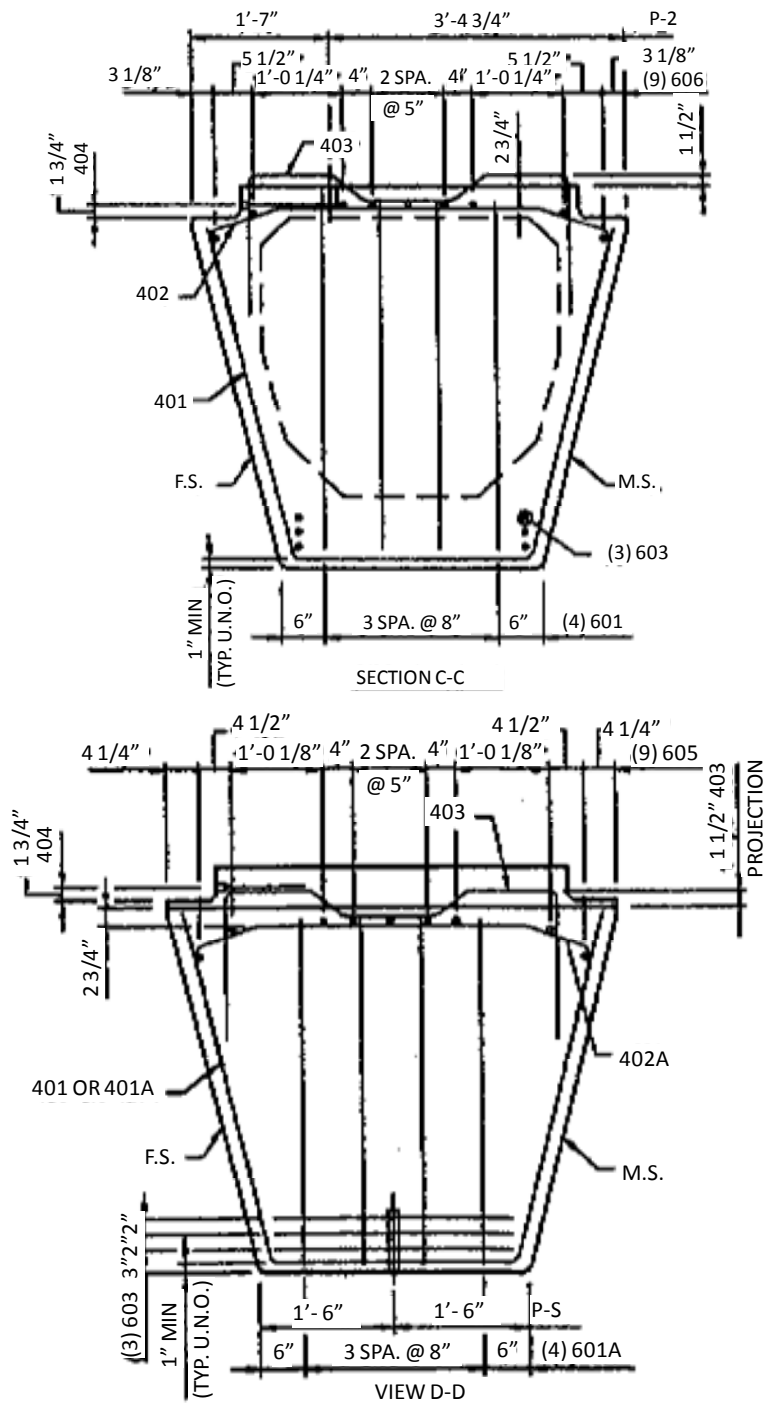


Figure A.13 RF-1R-1 section profile (continued)

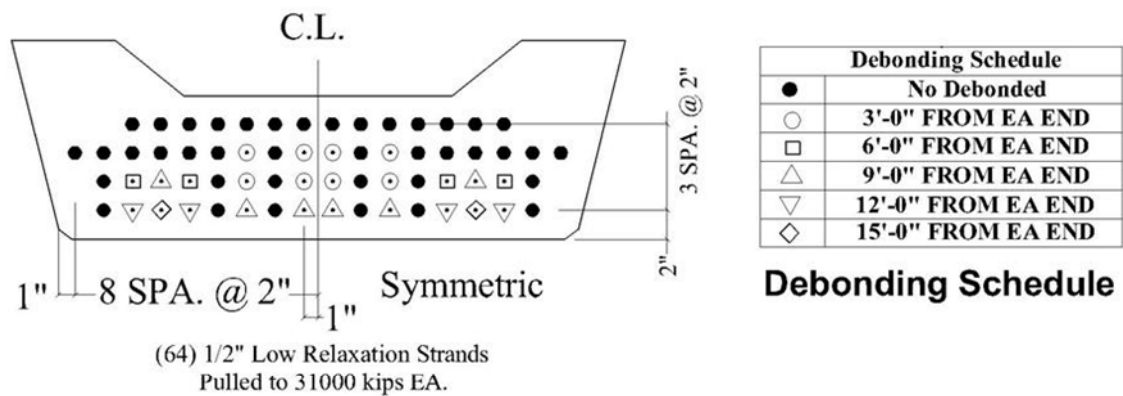


Figure A.14 Strands debonding schedule

A.2.2 RF-2R-6

Table A.2 RF-2R-6 reinforcing bars list

Reinforcing bar list			
Mark	Quan.	Length	Remarks
401	101	10'-10"	See Standard Drawings
402	101	7'-5"	See Standard Drawings
402A	6	7'-3"	See Standard Drawings
403	34	7'-3"	See Standard Drawings
503	8	13'-0"	See Standard Drawings
504	10	7'-6"	See Standard Drawings
505	12	11'-2"	See Standard Drawings
601	6	7'-5"	See Standard Drawings
603	6	12'-4"	See Standard Drawings
604	4	2'-6"	Straight
605	18	108'-2"	See Standard Drawings
606	16	3'-2"	Straight
L-1	2	3'-8 3/8"	C.L. 1 1/2x3/4" w(12) 701
702	16	12'-0"	See Standard Drawings
P-1	2	10"	3/4" Sleeve
P-2	5	3"	2" C.L. Sleeve
N.S. denotes near side F.S. denotes far side			

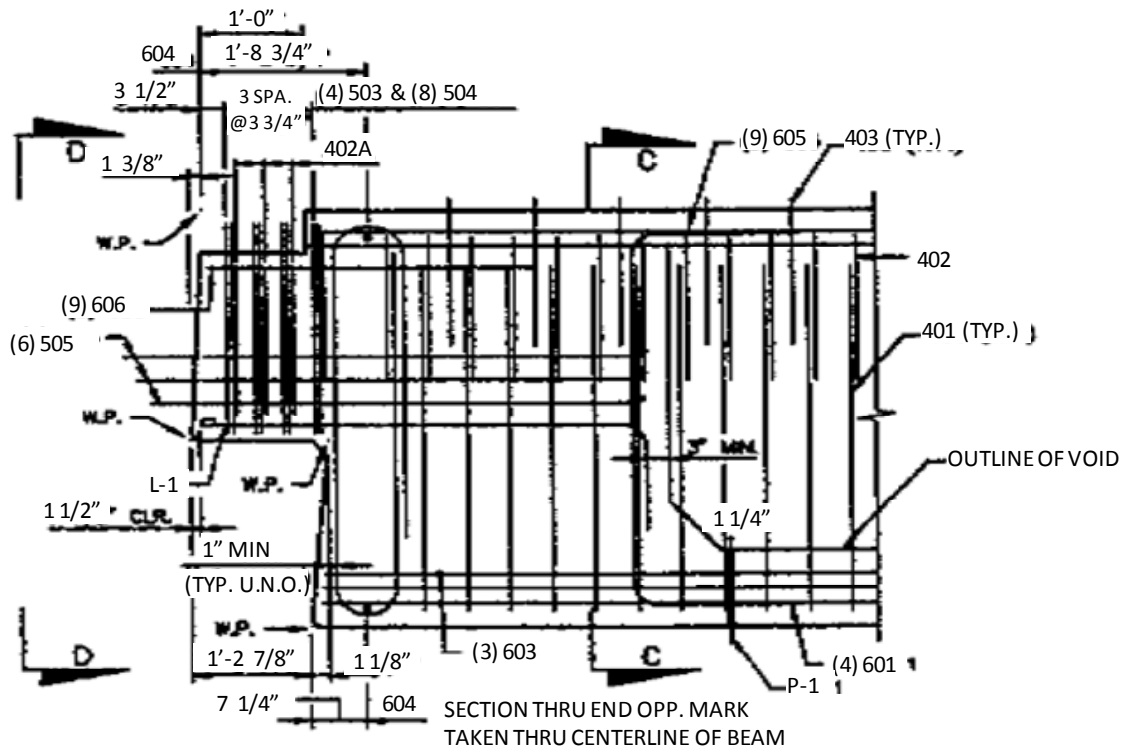
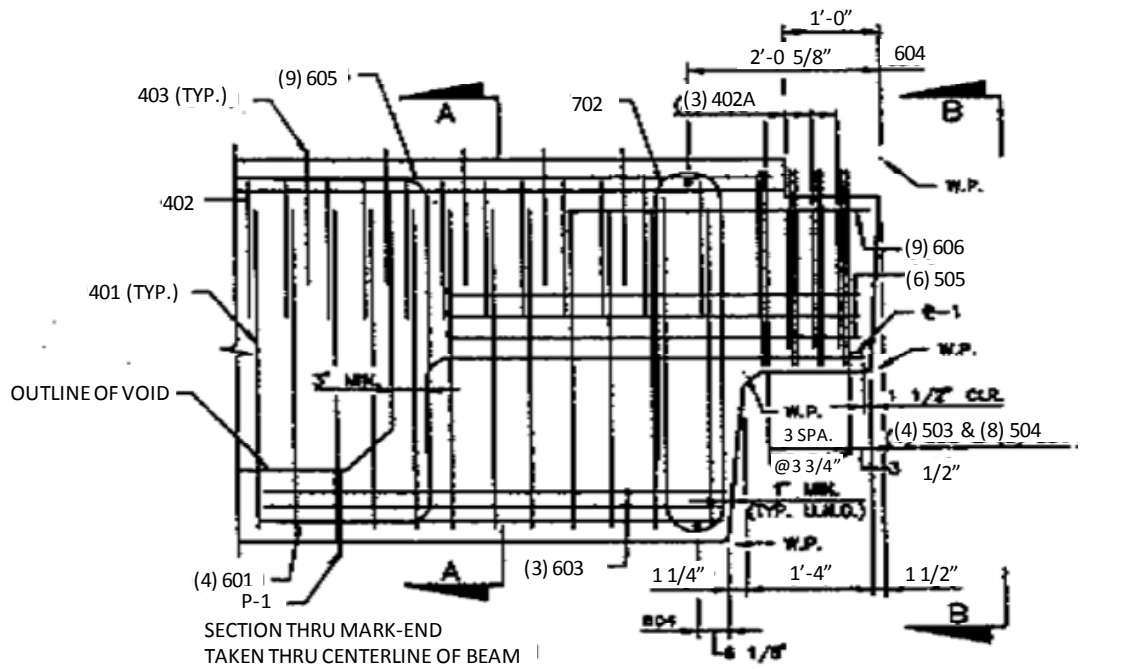


Figure A.16 RF-2R-6 end details

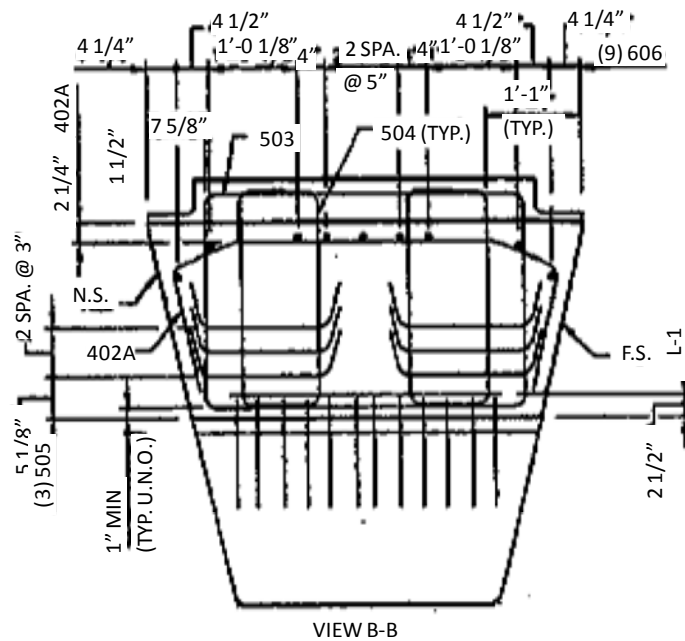
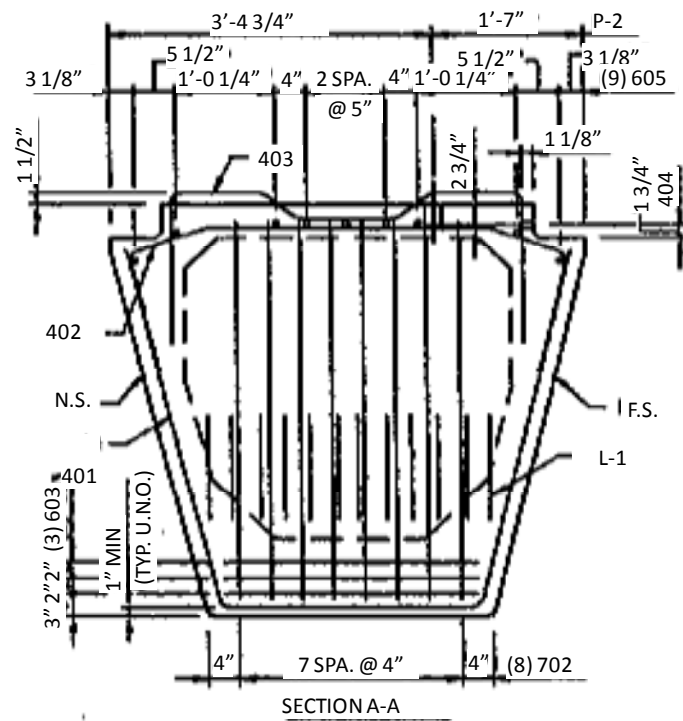


Figure A.17 RF-2R-6 section profile

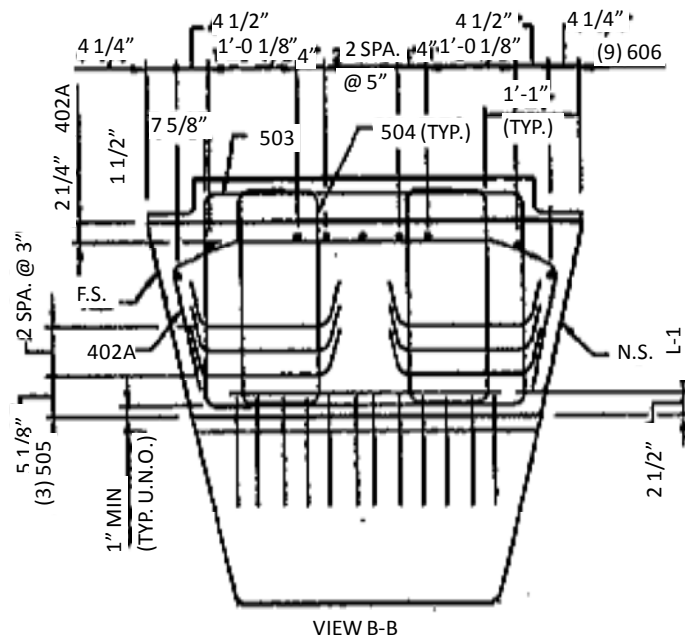
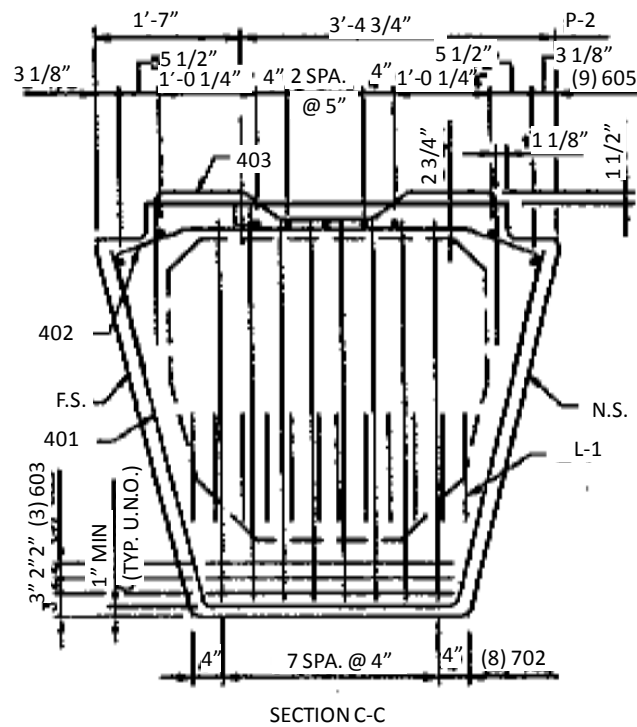


Figure A.18 RF-2R-6 section profile (continued)

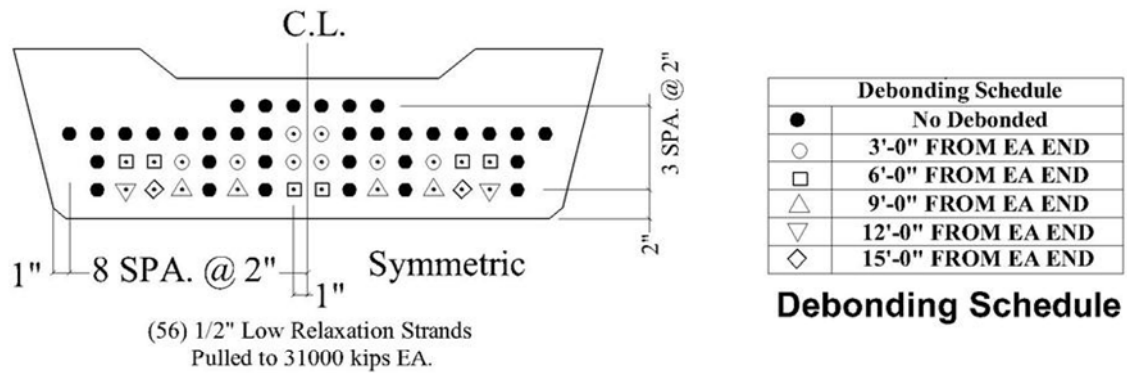


Figure A.19 RF-2R-6 strands debonding schedule

A.2.3 RF-3R-9

Table A.3 RF-3R-9 Reinforcing bars list

Reinforcing bar list			
Mark	Quan.	Length	Remarks
401	101	10'-10"	See Standard Drawings
402	103	7'-5"	See Standard Drawings
402A	6	7'-3"	See Standard Drawings
403	34	7'-3"	See Standard Drawings
404	75	1'-0"	Straight w/ Coupler
503	6	13'-0"	See Standard Drawings
504	16	7'-6"	See Standard Drawings
505	12	11'-2"	See Standard Drawings
601	6	7'-5"	See Standard Drawings
603	6	12'-4"	See Standard Drawings
604	4	2'-6"	Straight
605	9	108'-2"	See Standard Drawings
606	16	3'-2"	Straight
702	16	12'-0"	See Standard Drawings
L-1	2	3'-8 3/8"	C.L. 1 1/2x3/4" w(12) 701
P-1	2	10"	3/4" Sleeve
P-2	5	3"	2" C.L. Sleeve
N.S. denotes near side F.S. denotes far side			

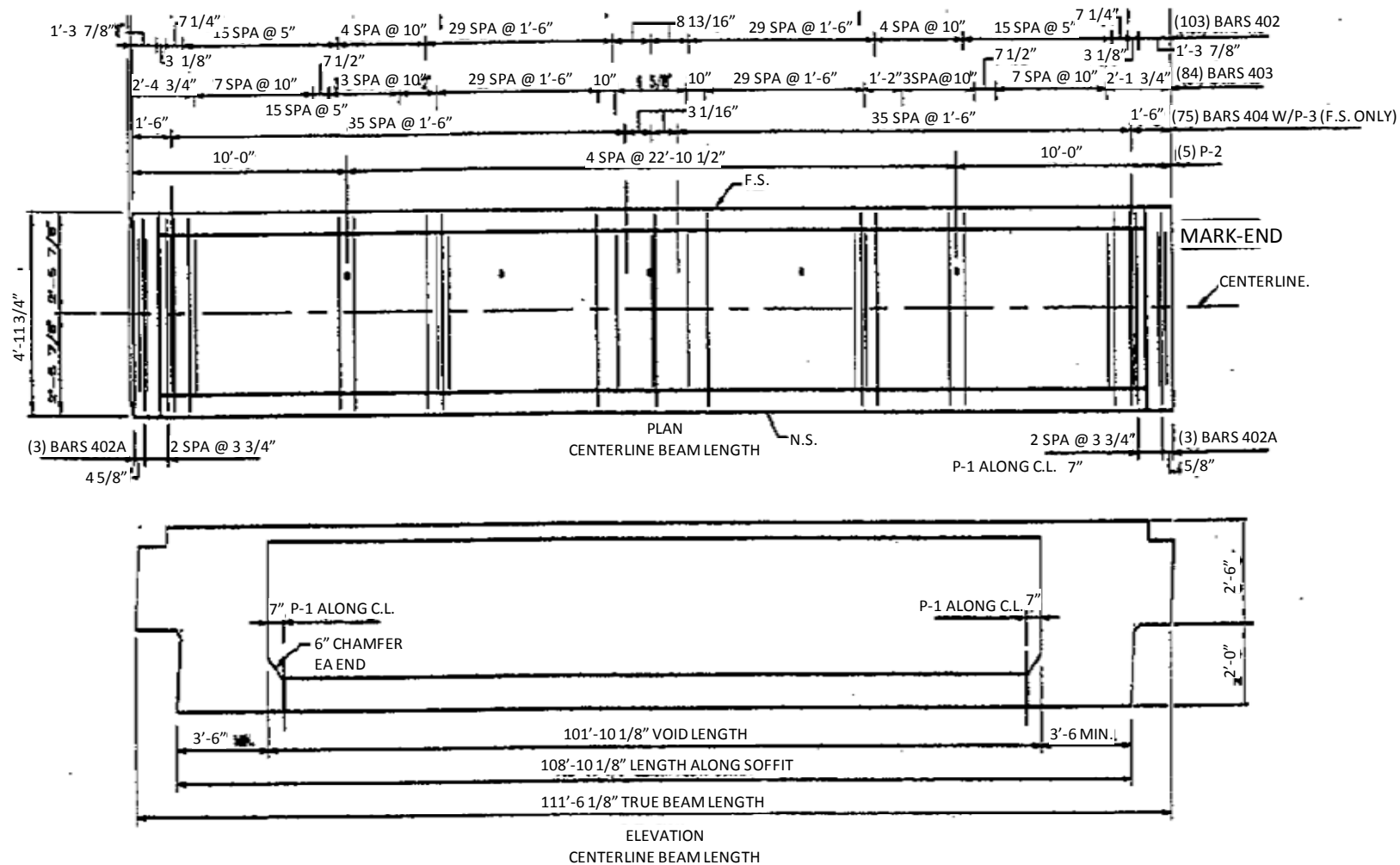


Figure A.20 RF-3R-9 plan

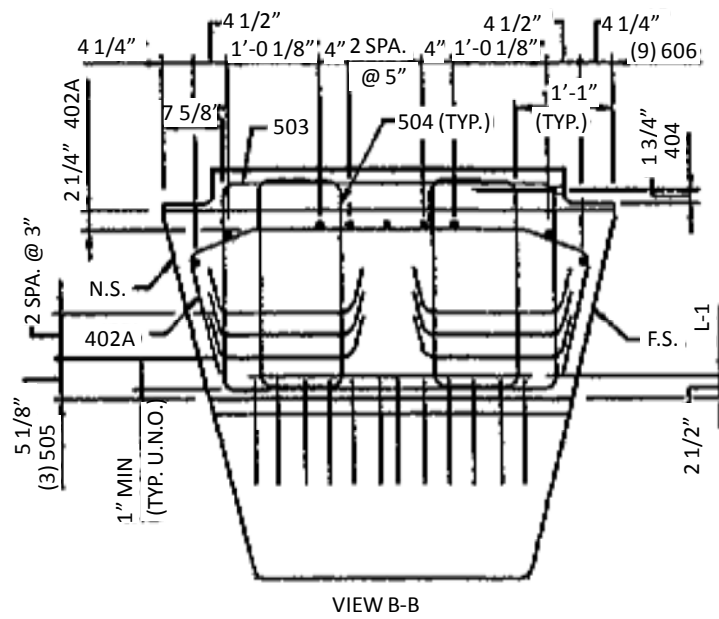
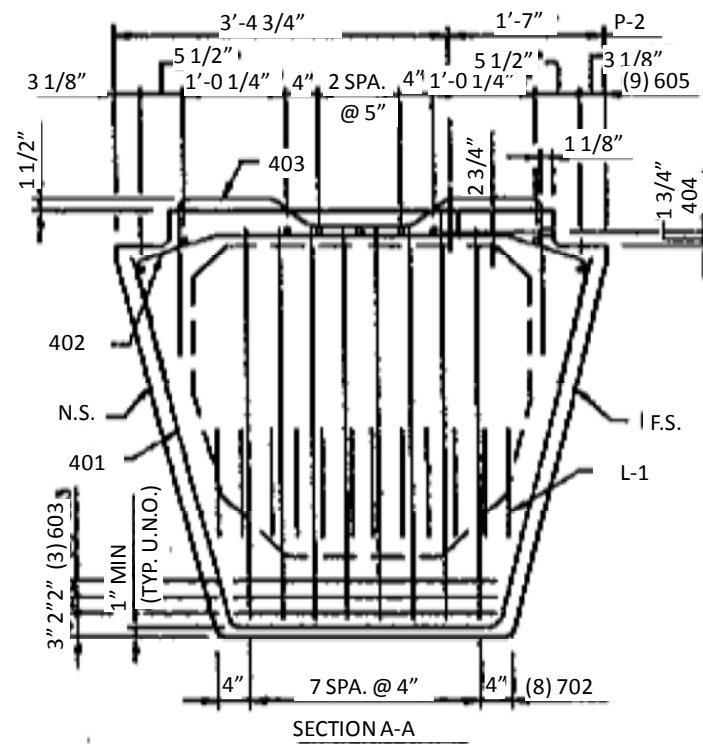
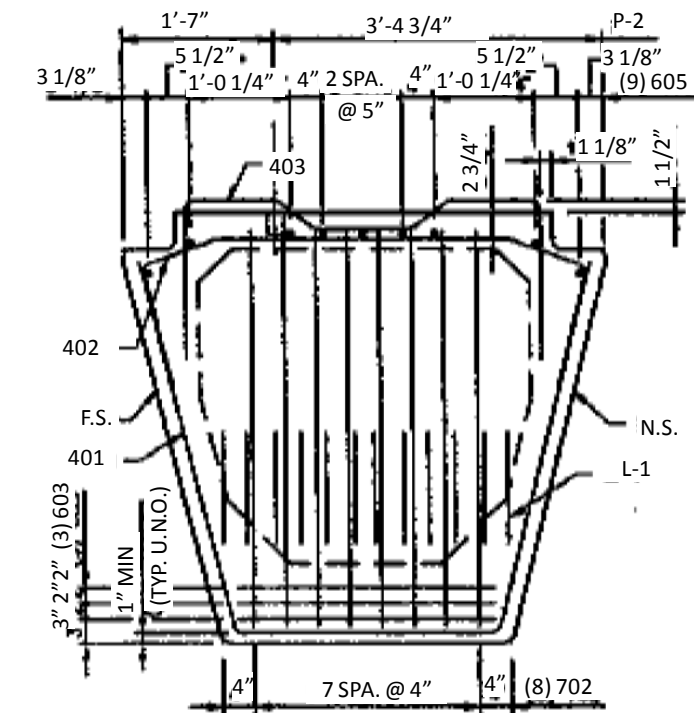
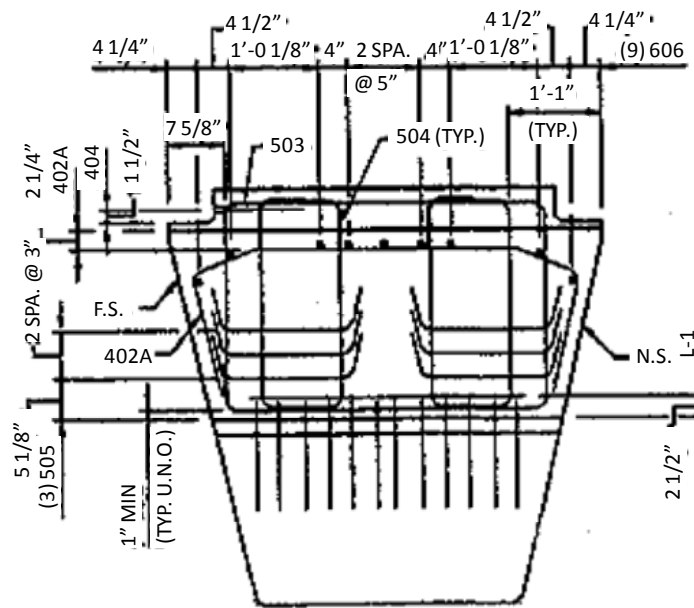


Figure A.22 RF-3R-9 section profile

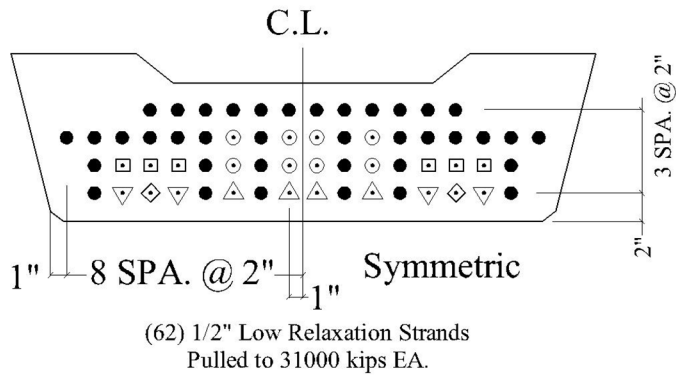


SECTION C-C



VIEW D-D

Figure A.23 RF-3R-9 section profile (continued)



Debonding Schedule	
●	No Debonded
○	3'-0" FROM EA END
□	6'-0" FROM EA END
△	9'-0" FROM EA END
▽	12'-0" FROM EA END
◇	15'-0" FROM EA END

Debonding Schedule

Figure A.24 RF-3R-9 strands debonding schedule

A.2.4 RF-3R-12

Table A.4 RF-3R-12 Reinforcing bars list

Reinforcing bar list			
Mark	Quan.	Length	Remarks
401	101	10'-11"	See Standard Drawings
402	103	7'-5"	
402A	6	7'-3"	
403	34	7'-3"	
404	75	1'-0"	Straight w/ Coupler
503	6	13'-0"	See Standard Drawings
504	16	7'-5"	
505	12	11'-2"	
601	6	7'-5"	
603	6	12'-4"	Straight
604	4	2'-6"	
605	9	106'-11"	See Standard Drawings
606	16	3'-2"	Straight
702	16	12'-0"	See Standard Drawings
L-1	2	3'-8 3/8"	C.L. 1 1/2x3/4" w(12) 701
P-1	2	10"	3/4" Sleeve
P-2	5	3"	2" C.L. Sleeve
N.S. denotes near side F.S. denotes far side			

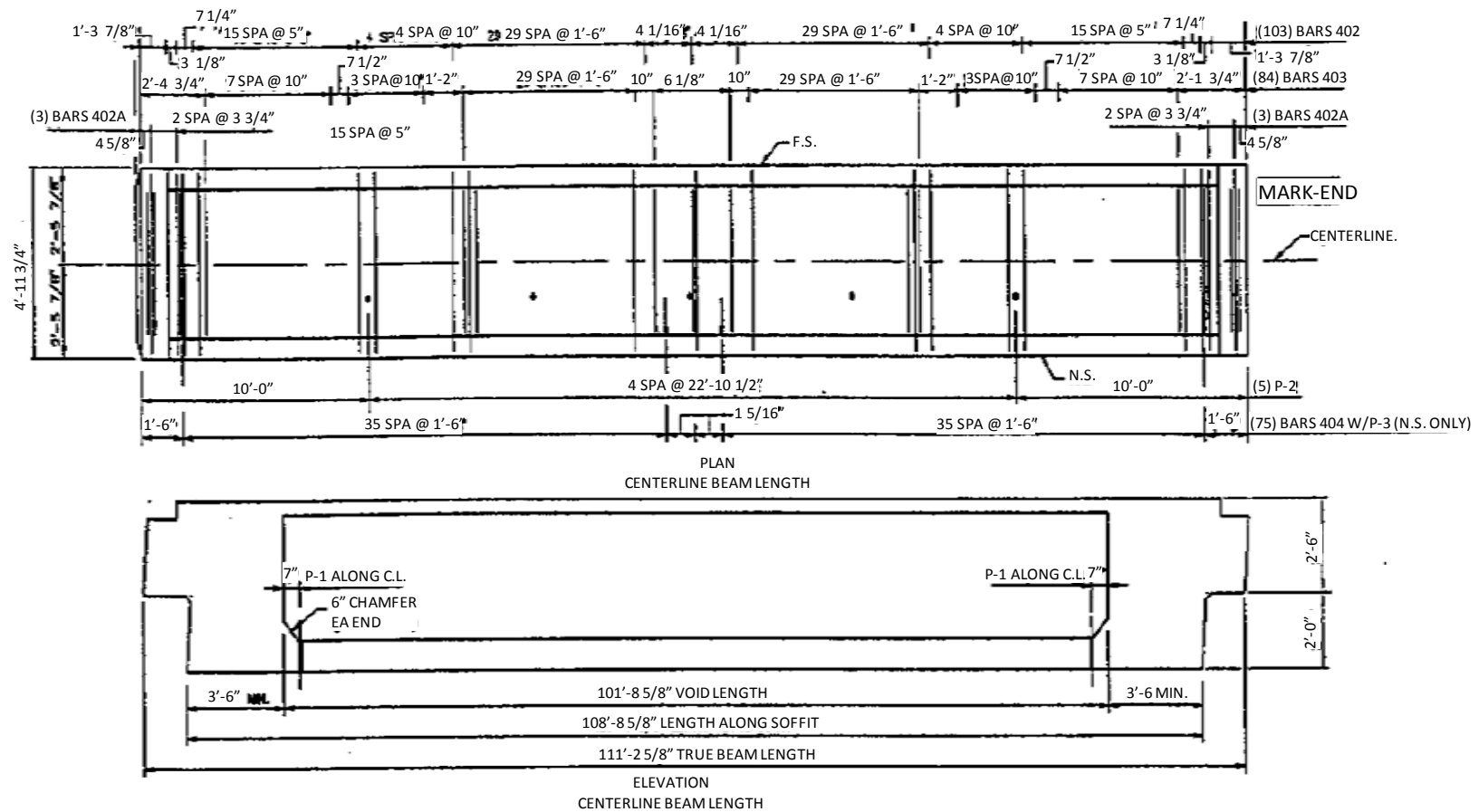


Figure A.25 RF-3R-12 plan

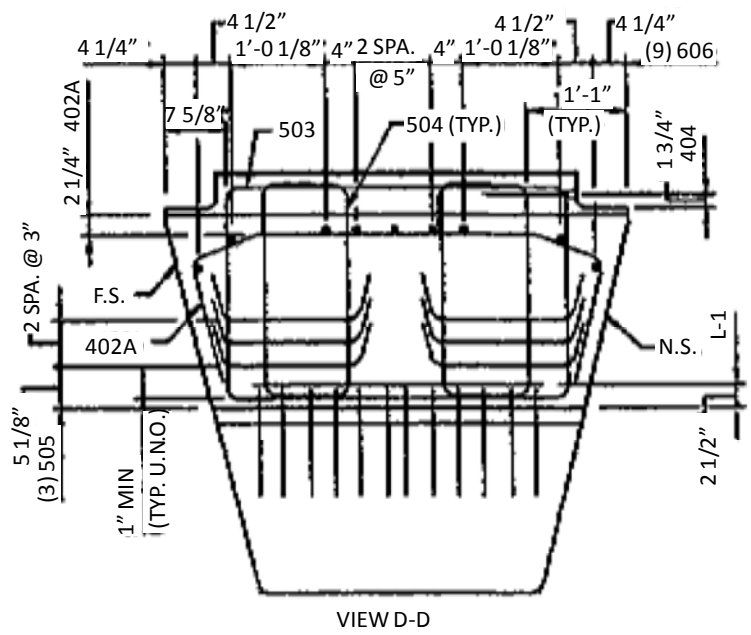
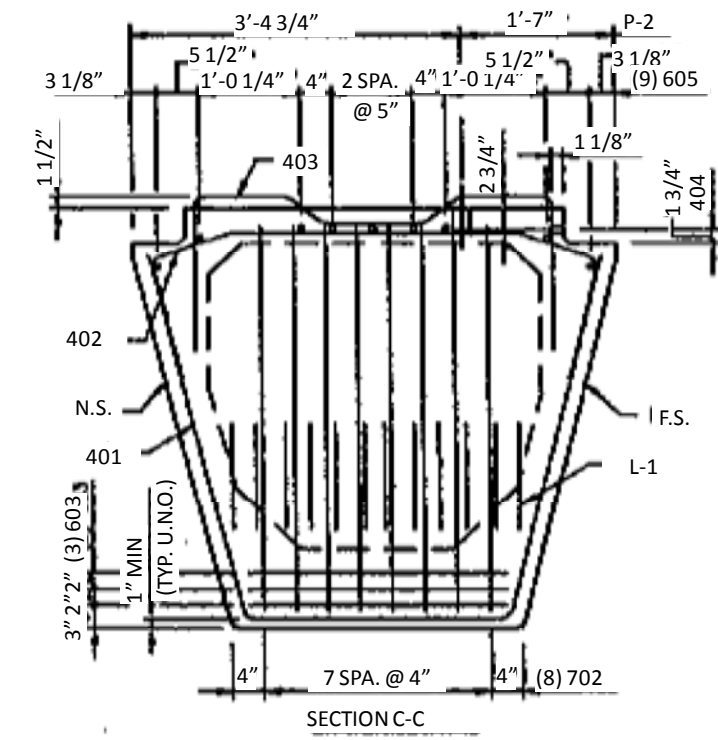


Figure A.28 RF-3R-12 section profile (continued)

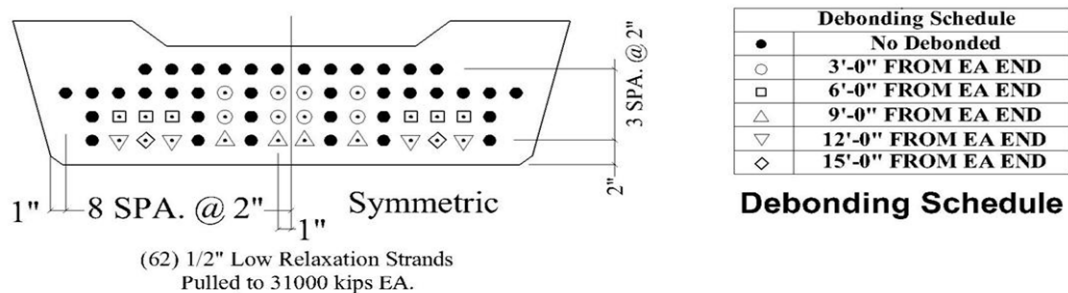


Figure A.29 RF-3R-12 strands debonding schedule

A.2.5 MLL-9-34

Table A.5 MLL-9-34 Reinforcing bars list

Reinforcing bar list					
Mark	Quan.	Remarks	Mark	Quan.	Remarks
401	61	See Standard Drawings	501	9	See Standard Drawings
401B	12		502	18	Straight x 3'-7"
401C	8		503A	4	See Standard Drawings
401D	4		503B	4	
401E	4		504A	8	
401F	6		504B	8	
402	103		505C	6	
402AF	6		505D	6	
402B	12		601	8	
402C	8		603C	3	
402D	4		603D	3	
402E	4		604C	2	
402F	6		604D	2	
403	60		PL-1B	1	1 1/2x3/4" w(12) 701
403B	6		PL-1C	1	1 1/2x3/4" w(12) 701
403C	4		702	16	See Standard Drawings
403D	2		P-1	2	3/4" Sleeve
403E	2		P-2	5	2" Sleeve
403F	2				
N.S. denots near side F.S. denotes far side					

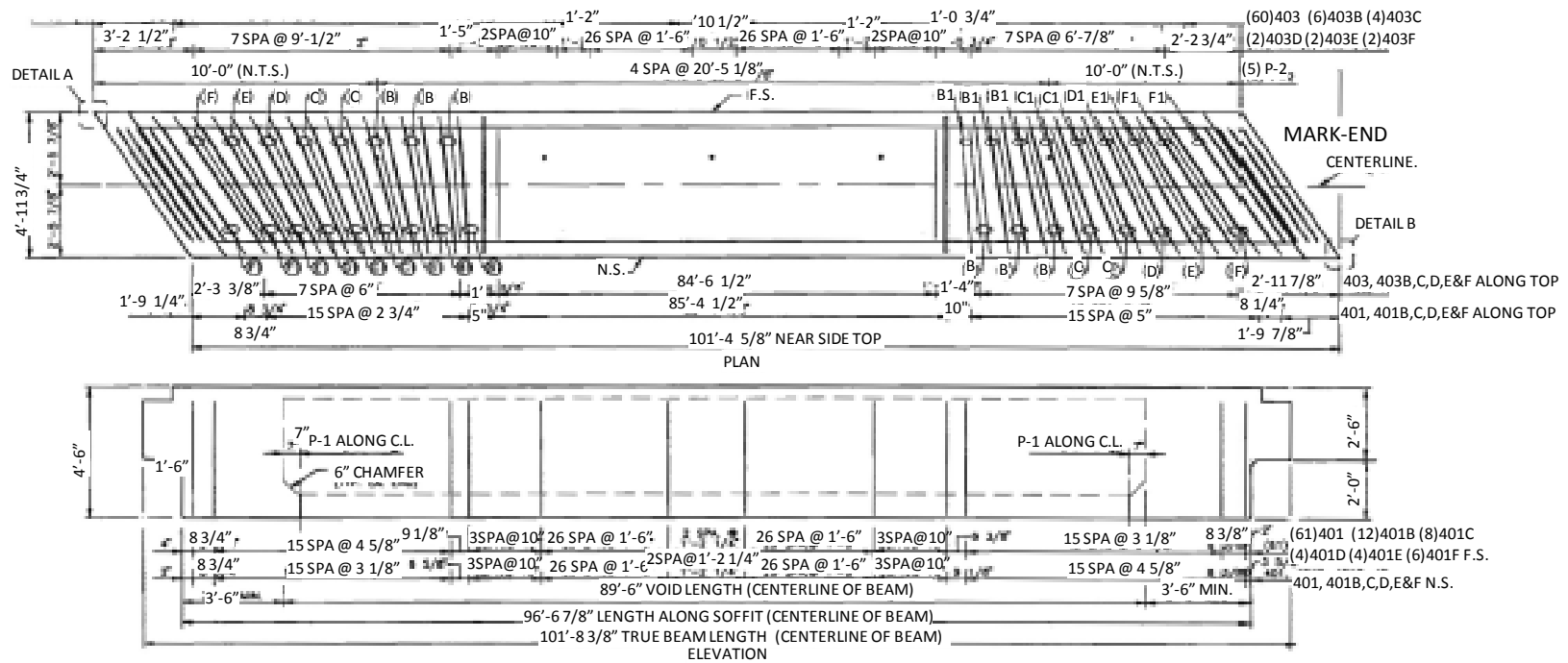


Figure A.30 MLL-9-34 plan

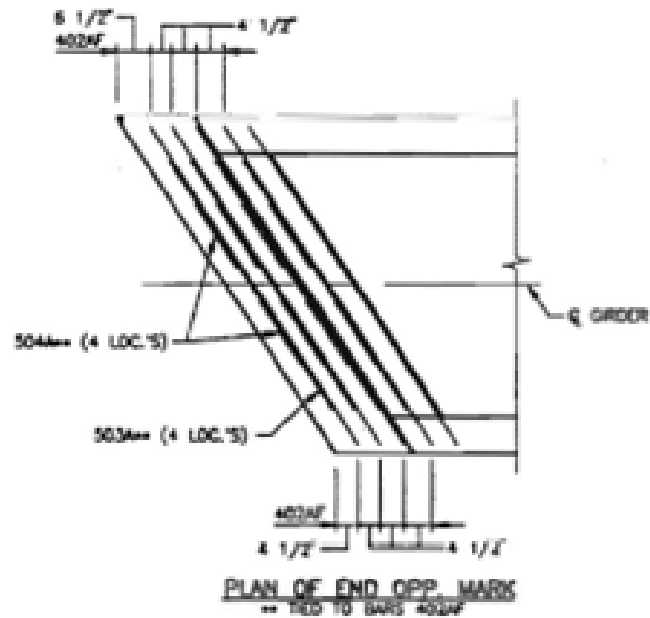
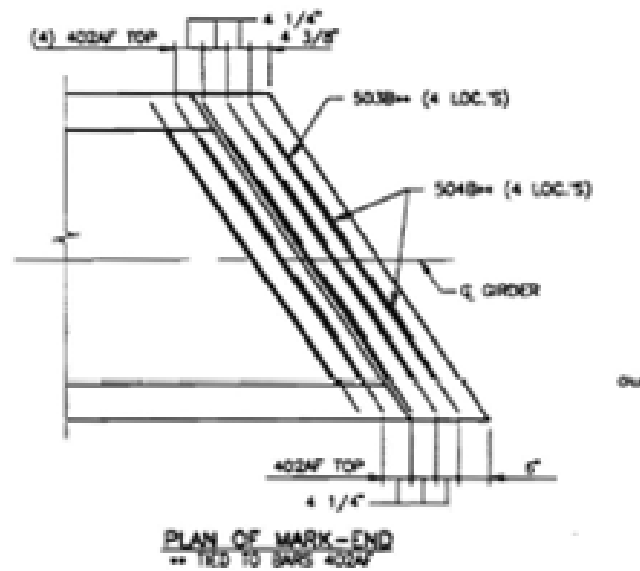


Figure A.32 MLL-9-34 end details (plan)

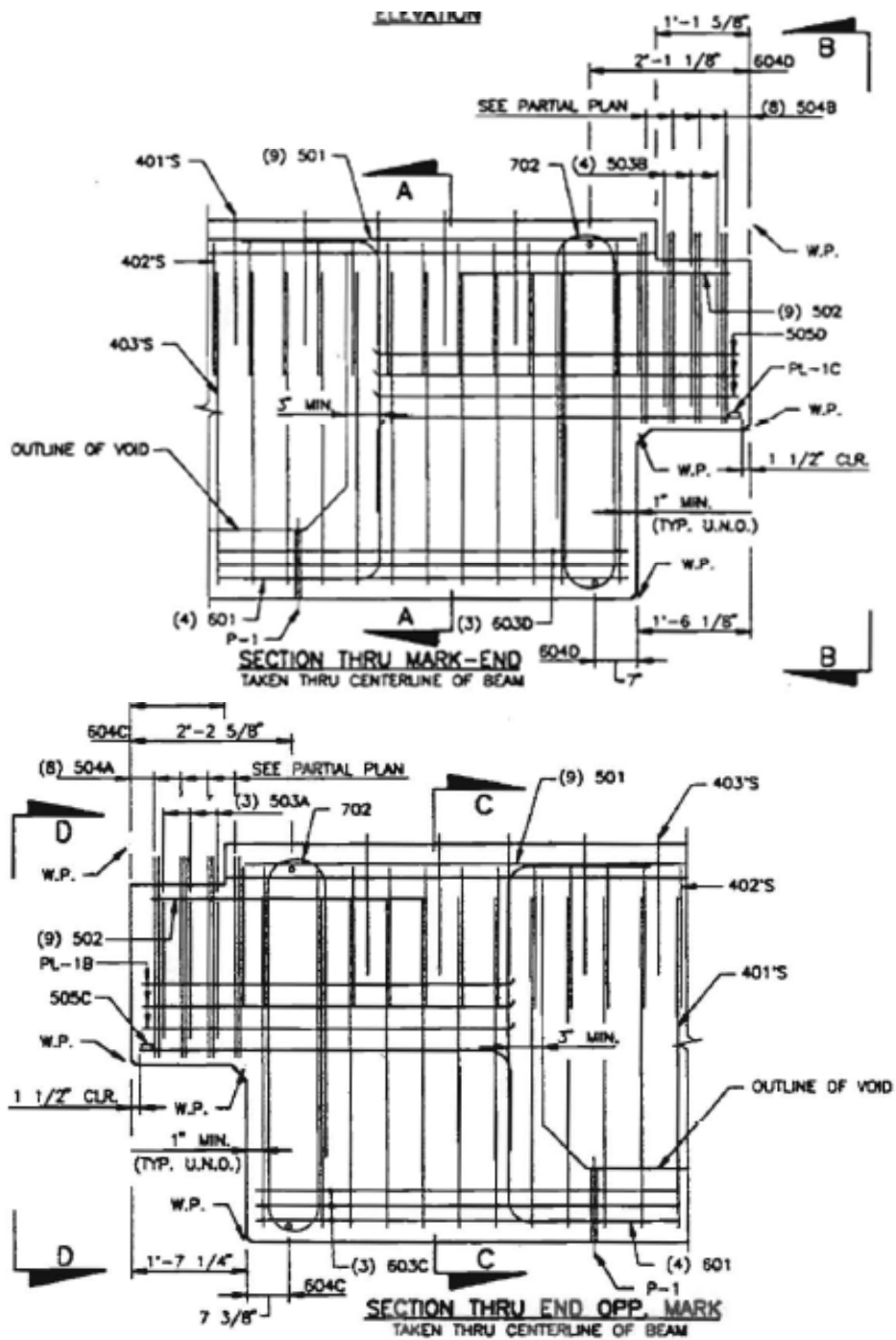


Figure A.33 MLL-9-34 end details (elevation)

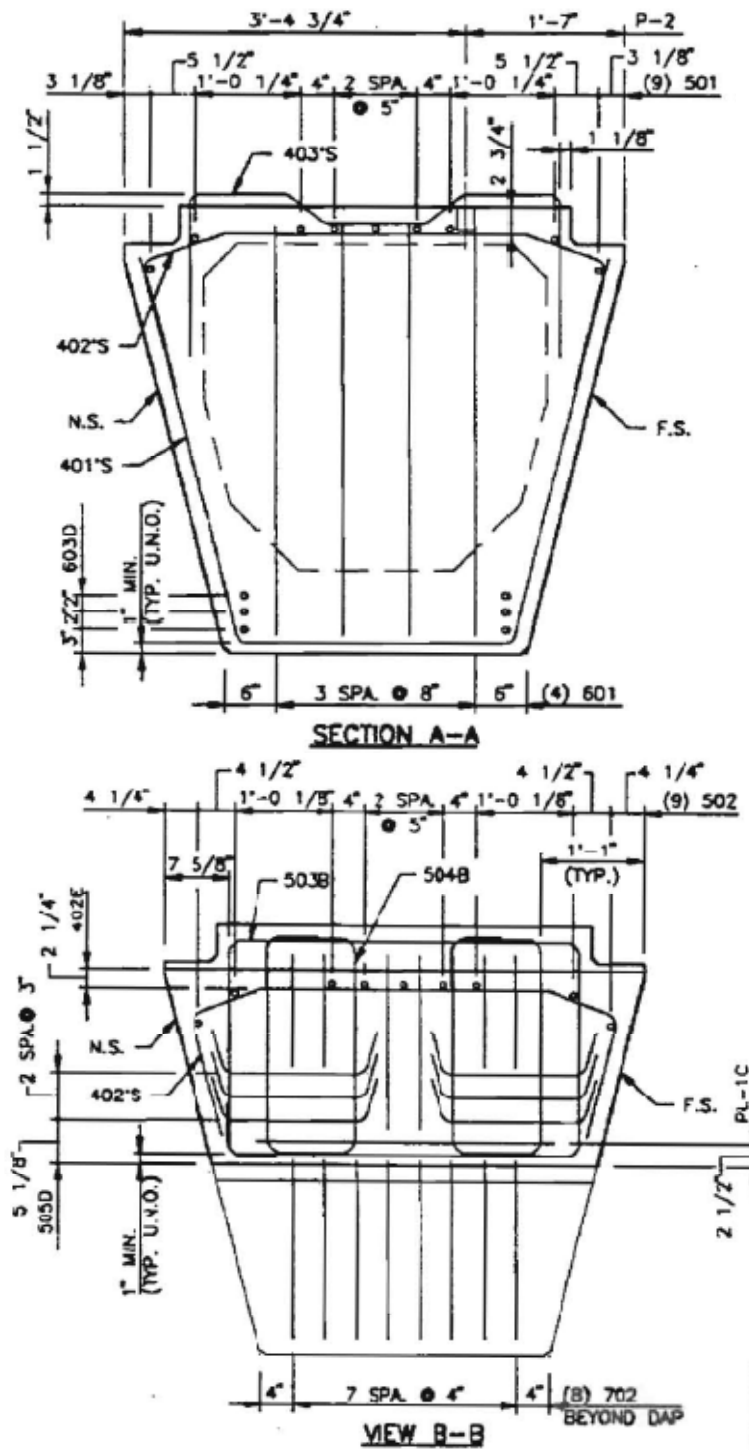


Figure A.34 MLL-9-34 section profile

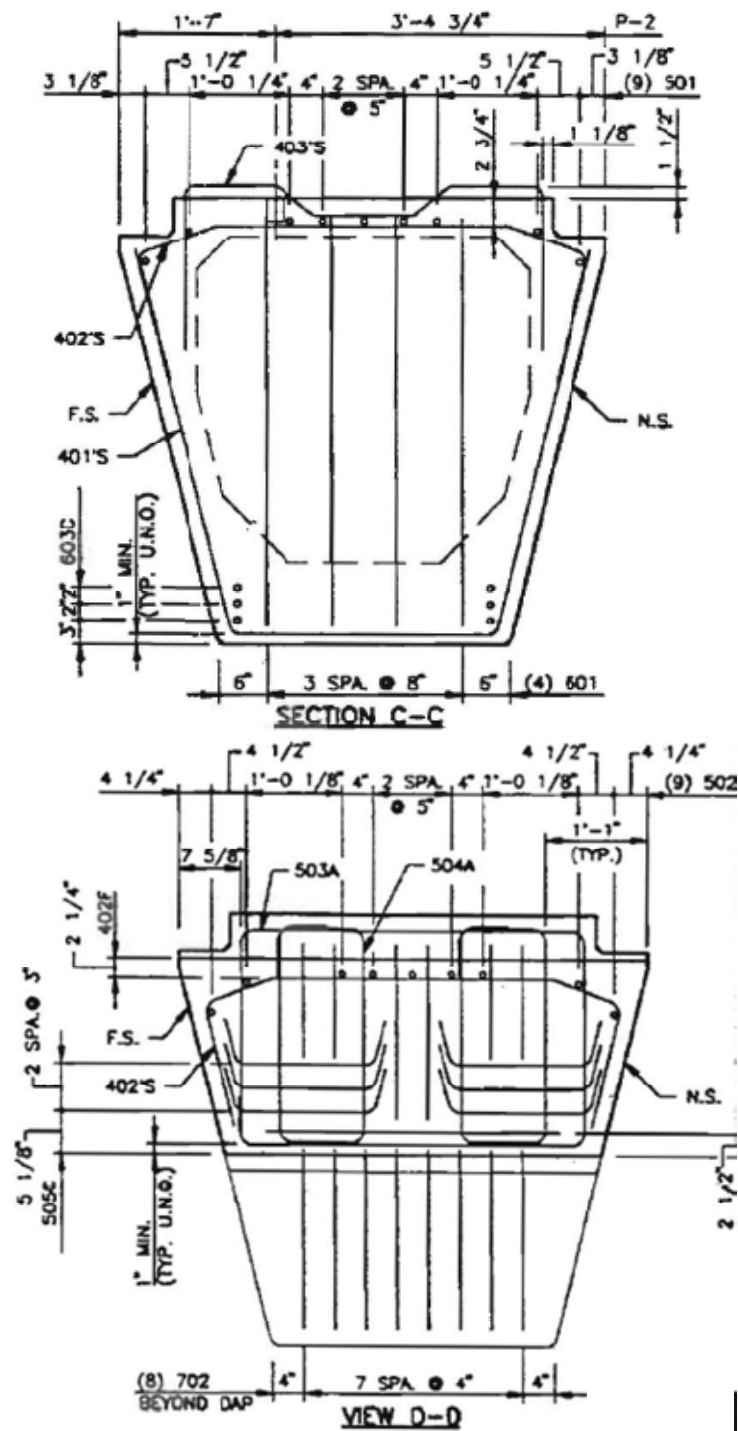
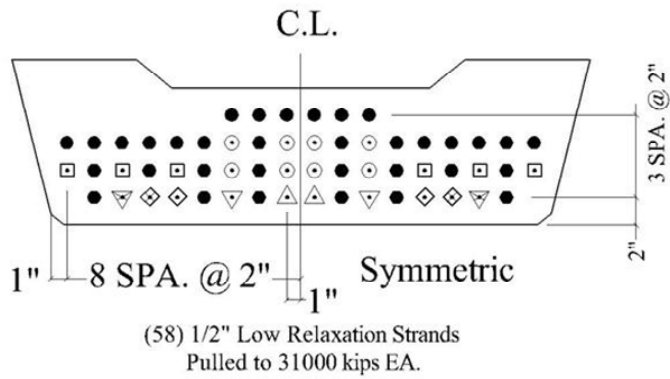


Figure A.35 MLL-9-34 section profile (continued)



Debonding Schedule	
●	No Debonded
○	3'-0" FROM EA END
□	6'-0" FROM EA END
△	9'-0" FROM EA END
▽	12'-0" FROM EA END
◇	15'-0" FROM EA END
▽	21'-0" FROM EA END
◇	24'-0" FROM EA END

Debonding Schedule

Figure A.36 MLL-9-34 strands debonding schedule

APPENDIX B

Concrete Mix Design

B.1 392-03-95-R

PHYSICAL PROPERTIES	Specific Gravity	% Solids	Unit Wt S S D	Sources of Materials
Fine Aggregate (FA)	2.61	0.62	101.4	Hallet
Course Aggregate (CA)	2.42	0.558	84.48	Vulcan
Water	1			Well
Cement	3.1			Capitol Type III

Design Factors			
Cement	(CF)	7.00	Sacks per cubic yard of concrete
Course Aggr.	(CAF)	74.00	Percent of maximum that is CA
Water	(WF)	4.50	Gal. per sack of cement
Air	(AF)	1.00	Percent

ADMIXTURES:

Type F = WRDA – 19
 16 oz. per 100 lbs
 Type D = Daratard 17
 2.0 oz. per 100 lbs

BATCH DESIGN (One-Sack)	VOLUME: 1-SK Batch (CU.FT)	VOL to WT (lb) VOLx62.5xSpGr	1 sk BAT WTS	Batch Factor	Batch Wght for one CY
Yield = $\frac{\text{Cu. Ft.}}{\text{Cu. Yd.}}$ Cement Factor (CF)	$27 / 7 = 3.857$				
Vol CA = Yld x CAF x Solids	$3.857 \times 0.74 \times 0.558 = 1.593$	$\times 62.50 \times 2.42 =$	240.89 x	7.00 =	1686 lbs
Vol Mortar = Yld – Vol CA	$3.857 - 1.593 = 2.264$				
Vol Water = $\frac{\text{Water Factor}}{\text{Gal Water per cu ft}}$	$4.5 / 7.48 = 0.602$	$\times 62.50 \times 1.00 =$	37.60 x	7.00 =	263 lbs
Volume One Sack Cement	$1.00 \times 0.485 = 0.485$	$\times 62.50 \times 3.10 =$	93.97 x	7.00 =	658 lbs
Vol Air = Yld x AirFactor	$3.857 \times 0.010 = 0.039$				
Vol Paste = Volume (Cement + Water + Air)	$0.485 + 0.602 + 0.039 = 1.125$				
Vol FA = Vol Mortar – Vol Paste	$2.264 - 1.125 = 1.139$	$\times 62.50 \times 2.61 =$	185.84x	7.00 =	1301 lbs
	Yield = Sum =	3.857	Total Batch Weight		3908 lbs

$$\text{Fine Aggregate Factor} = \frac{\text{Vol. of FA}}{\text{FA Solids} \times \text{Vol. Mortar}} = \frac{1.139}{0.006 \times 2.264} = 81.15$$

B.2 392-12-95

PHYSICAL PROPERTIES	Specific Gravity	% Solids	Unit Wt S S D	Sources of Materials
Fine Aggregate (FA)	2.61	0.62	101.4	Hallet
Course Aggregate (CA)	2.42	0.558	84.48	Vulcan
Water	1			Well
Cement	3.1			Capitol Type III

Design Factors			
Cement	(CF)	7.00	Sacks per cubic yard of concrete
Course Aggr.	(CAF)	74.00	Percent of maximum that is CA
Water	(WF)	3.25	Gal. per sack of cement
Air	(AF)	1.00	Percent

BATCH DESIGN (One-Sack)	VOLUME: 1-SK Batch (CU.FT)	VOL to WT (lb) VOLx62.5xSpGr	1 sk BAT WTS	Batch Factor	Batch Wght for one CY
Yield = Cu. Ft. / Cu. Yd. Cement Factor (CF)	$27 / 7 = \underline{3.857}$				
Vol CA = Yld x CAF x Solids	$3.857 \times 0.74 \times 0.558 = 1.593$	$\times 62.50 \times 2.42 =$	$240.89 \times$	$7.00 =$	1686 lbs
Vol Mortar = Yld – Vol CA	$3.857 - 1.593 = \underline{2.264}$				
Vol Water = $\frac{\text{Water Factor}}{\text{Gal Water per cu ft}}$	$3.25 / 7.48 = 0.434$	$\times 62.50 \times 1.00 =$	$27.16 \times$	$7.00 =$	190 lbs
Volume One Sack Cement	$1.00 \times 0.485 = 0.485$	$\times 62.50 \times 3.10 =$	$93.97 \times$	$7.00 =$	658 lbs
Vol Air = Yld x AirFactor	$3.857 \times 0.010 = 0.039$				
Vol Paste = Volume (Cement + Water + Air)	$0.485 + 0.434 + 0.039 = \underline{0.958}$				
Vol FA = Vol Mortar – Vol Paste	$2.264 - 0.958 = 1.306$	$\times 62.50 \times 2.61 =$	$213.10 \times$	$7.00 =$	1492 lbs
	Yield = Sum =	3.857	Total Batch Weight		<u>4026 lbs</u>

$$\text{Fine Aggregate Factor} = \frac{\text{Vol. of FA}}{\text{FA Solids} \times \text{Vol. Mortar}} = \frac{1.306}{0.006 \times 2.264} = 83.85$$

APPENDIX C

Prestress Loss and Compression Block

Appendix C includes the calculations for prestress loss and depth of rectangular compression block based on AASHTO LRFD. Software MathCAD was utilized in all the calculations.

C.1 COMMONLY USED PARAMETERS

Prestressing Strand Properties

$f_{pu} := 270 \text{ksi}$	Ultimate strength
$f_{py} := 0.9 \cdot f_{pu} = 243 \cdot \text{ksi}$	Yield Strength
$E_p := 28500 \text{ksi}$	Modulus of Elasticity
$d_b := 0.5 \text{in}$	Strand diameter
$A_{strand} := 0.153 \cdot \text{in}^2$	Area of strand

Concrete Section Properties

$A_g := 1108 \text{in}^2$	Gross cross sectional area
$I_g := 404968 \text{in}^4$	Gross moment of inertia
$y_b := 26.71 \text{in}$	Distance from CG to bottom
$y_t := 27.29 \text{in}$	Distance from CG to top
$w_{sw} := 1.154 \frac{\text{kip}}{\text{ft}}$	Self weight of beam

C.2 PRESTRESS LOSS

C.2.1 RF-3R-9

$$n := 62$$

Number of strands

$$A_{ps} := n \cdot A_{strand} = 9.486 \cdot \text{in}^2$$

Area of prestressing steel

$$P_i := n \cdot 31 \text{ kip} = 1.922 \times 10^3 \cdot \text{kip}$$

Initial pretension

$$f_{pi} := \frac{P_i}{A_{ps}} = 202.614 \cdot \text{ksi}$$

Initial stress in strand

$$f_{ci} := 5.81 \text{ ksi}$$

Concrete Strength at release

$$E_{ci} := 57000 \cdot \sqrt{f_{ci}} = 4.345 \times 10^3 \cdot \text{ksi}$$

Elastic Modulus at release

$$d_p := 52 \text{ in} - \frac{(16.2 + 16.4 + 18.6 + 12.8) \text{ in}}{64} = 47.313 \cdot \text{in}$$

Depth to CG of prestress

$$e_m := d_p - y_t = 20.022 \cdot \text{in}$$

Prestress eccentricity

$$L := 111 \text{ ft} + 6.167 \text{ in}$$

Length of beam

Elastic Shortening (Δf_{pES})

$$M_g := \frac{w_{sw} \cdot L^2}{8} = 1.794 \times 10^3 \cdot \text{kip} \cdot \text{ft}$$

Moment due to self weight

$$\Delta f_{pES} := \frac{A_{ps} \cdot f_{pi} \cdot \left(I_g + e_m^2 \cdot A_g \right) - e_m \cdot M_g \cdot A_g}{A_{ps} \cdot \left(I_g + e_m^2 \cdot A_g \right) + \frac{A_g \cdot I_g \cdot E_{ci}}{E_p}} = 15.1 \cdot \text{ksi} \quad (\text{C5.9.5.2.3a-1})$$

Time dependent losses (Δf_{pLT})

$$H := 75$$

75% relative humidity

$$\gamma_h := 1.7 - 0.01H = 0.95$$

(5.9.5.3-2)

$$\gamma_{st} := \frac{5}{\left(1 + \frac{f_{ci}}{\text{ksi}} \right)} = 0.734$$

(5.9.5.3-3)

$$\Delta f_{pR} := 2.4 \text{ ksi}$$

Low relaxation strand

$$\Delta f_{pLT} := 10.0 \cdot \frac{f_{pi} \cdot A_{ps}}{A_g} \cdot \gamma_h \cdot \gamma_{st} + 12.0 \text{ksi} \cdot \gamma_h \cdot \gamma_{st} + \Delta f_{pR} = 22.869 \cdot \text{ksi} \quad (5.9.5.3-1)$$

$$\Delta f_{pT} := \Delta f_{pES} + \Delta f_{pLT} = 37.97 \cdot \text{ksi}$$

Total prestress loss

$$f_{pe} := f_{pi} - \Delta f_{pT} = 164.645 \cdot \text{ksi}$$

Effective stress in RF-3R-9

C.2.2 RF-3R-12

$$n := 62$$

Number of strands

$$A_{ps} := n \cdot A_{strand} = 9.486 \cdot \text{in}^2$$

Area of prestressing steel

$$P_i := n \cdot 31 \text{ kip} = 1.922 \times 10^3 \cdot \text{kip}$$

Initial pretension

$$f_{pi} := \frac{P_i}{A_{ps}} = 202.614 \cdot \text{ksi}$$

Initial stress in strand

$$f_{ci} := 5.81 \text{ ksi}$$

Concrete Strength at release

$$E_{ci} := 57000 \cdot \sqrt{f_{ci} \cdot \text{psi}} = 4.345 \times 10^3 \cdot \text{ksi}$$

Elastic Modulus at release

$$d_p := 52 \text{ in} - \frac{(16.2 + 16.4 + 18.6 + 12.8) \text{ in}}{64} = 47.313 \cdot \text{in}$$

Depth to CG of prestress

$$e_m := d_p - y_t = 20.022 \cdot \text{in}$$

Prestress eccentricity

$$L := 111 \text{ ft} + 2.64 \text{ in}$$

Length of beam

Elastic Shortening (Δf_{pES})

$$M_g := \frac{w_{sw} \cdot L^2}{8} = 1.784 \times 10^3 \cdot \text{kip} \cdot \text{ft}$$

Moment due to self weight

$$\Delta f_{pES} := \frac{A_{ps} \cdot f_{pi} \cdot \left(I_g + e_m^2 \cdot A_g \right) - e_m \cdot M_g \cdot A_g}{A_{ps} \cdot \left(I_g + e_m^2 \cdot A_g \right) + \frac{A_g \cdot I_g \cdot E_{ci}}{E_p}} = 15.133 \cdot \text{ksi} \quad (\text{C5.9.5.2.3a-1})$$

Time dependent losses (Δf_{pLT})

$$H := 75$$

75% relative humidity

$$\gamma_h := 1.7 - 0.01H = 0.95$$

(5.9.5.3-2)

$$\gamma_{st} := \frac{5}{\left(1 + \frac{f_{ci}}{\text{ksi}} \right)} = 0.734$$

(5.9.5.3-3)

$$\Delta f_{pR} := 2.4 \text{ ksi}$$

Low relaxation strand

$$\Delta f_{pLT} := 10.0 \cdot \frac{f_{pi} \cdot A_{ps}}{A_g} \cdot \gamma_h \cdot \gamma_{st} + 12.0 \text{ksi} \cdot \gamma_h \cdot \gamma_{st} + \Delta f_{pR} = 22.869 \cdot \text{ksi} \quad (5.9.5.3-1)$$

$$\Delta f_{pT} := \Delta f_{pES} + \Delta f_{pLT} = 38.003 \cdot \text{ksi} \quad \text{Total prestress loss}$$

$$f_{pe} := f_{pi} - \Delta f_{pT} = 164.612 \cdot \text{ksi} \quad \text{Effective stress in RF-3R-12}$$

C.2.3 MLL-9-34

$$n := 58$$

Number of strands

$$A_{ps} := n \cdot A_{strand} = 8.874 \cdot \text{in}^2$$

Area of prestressing steel

$$P_i := n \cdot 31 \text{ kip} = 1.798 \times 10^3 \cdot \text{kip}$$

Initial pretension

$$f_{pi} := \frac{P_i}{A_{ps}} = 202.614 \cdot \text{ksi}$$

Initial stress in strand

$$f_{ci} := 5.012 \text{ ksi}$$

Concrete Strength at release

$$E_{ci} := 57000 \cdot \sqrt{f_{ci} \cdot \text{psi}} = 4.035 \times 10^3 \cdot \text{ksi}$$

Elastic Modulus at release

$$d_p := 52 \text{ in} - \frac{(16.2 + 18.4 + 18.6 + 6.8) \text{ in}}{64} = 47.938 \cdot \text{in}$$

Depth to CG of prestress

$$e_m := d_p - y_t = 20.648 \cdot \text{in}$$

Prestress eccentricity

$$L := 98 \text{ ft} + 6.36 \text{ in}$$

Length of beam

Elastic Shortening (Δf_{pES})

$$M_g := \frac{w_{sw} \cdot L^2}{8} = 1.4 \times 10^3 \cdot \text{kip} \cdot \text{ft}$$

Moment due to self weight

$$\Delta f_{pES} := \frac{A_{ps} \cdot f_{pi} \cdot \left(I_g + e_m^2 \cdot A_g \right) - e_m \cdot M_g \cdot A_g}{A_{ps} \cdot \left(I_g + e_m^2 \cdot A_g \right) + \frac{A_g \cdot I_g \cdot E_{ci}}{E_p}} = 16.728 \cdot \text{ksi}$$

Time dependent losses (Δf_{pLT})

$$H := 75$$

75% relative humidity

$$\gamma_h := 1.7 - 0.01H = 0.95$$

(5.9.5.3-2)

$$\gamma_{st} := \frac{5}{\left(1 + \frac{f_{ci}}{\text{ksi}} \right)} = 0.832$$

(5.9.5.3-3)

$$\Delta f_{pR} := 2.4 \text{ ksi}$$

Low relaxation strand

$$\Delta f_{pLT} := 10.0 \cdot \frac{f_{pi} \cdot A_{ps}}{A_g} \cdot \gamma_h \cdot \gamma_{st} + 12.0 \text{ksi} \cdot \gamma_h \cdot \gamma_{st} + \Delta f_{pR} = 24.702 \cdot \text{ksi} \quad (5.9.5.3-1)$$

$$\Delta f_{pT} := \Delta f_{pES} + \Delta f_{pLT} = 41.43 \cdot \text{ksi} \quad \text{Total prestress loss}$$

$$f_{pe} := f_{pi} - \Delta f_{pT} = 161.185 \cdot \text{ksi} \quad \text{Effective stress in MLL-9-34}$$

C.2.4 RF-1R-1

$$n := 64$$

Number of strands

$$A_{ps} := n \cdot A_{strand} = 9.792 \cdot \text{in}^2$$

Area of prestressing steel

$$P_i := n \cdot 31 \text{ kip} = 1.984 \times 10^3 \cdot \text{kip}$$

Initial pretension

$$f_{pi} := \frac{P_i}{A_{ps}} = 202.614 \cdot \text{ksi}$$

Initial stress in strand

$$f_c := 5.989 \text{ ksi}$$

Design Strength

$$f_{ci} := 5.989 \text{ ksi}$$

Concrete Strength at release

$$E_{ci} := 57000 \cdot \sqrt{f_{ci}} = 4.411 \times 10^3 \cdot \text{ksi}$$

Elastic Modulus at release

$$d_p := 52 \text{ in} - \frac{(16.2 + 16.4 + 18.6 + 12.8) \text{ in}}{64} = 47.313 \cdot \text{in}$$

Depth to CG of prestress

$$e_m := d_p - y_t = 20.022 \cdot \text{in}$$

Prestress eccentricity

$$L := 111 \text{ ft} + 10.44 \text{ in}$$

Length of beam

Elastic Shortening (Δf_{pES})

$$M_g := \frac{w_{sw} \cdot L^2}{8} = 1.805 \times 10^3 \cdot \text{kip} \cdot \text{ft}$$

Moment due to self weight

$$\Delta f_{pES} := \frac{A_{ps} \cdot f_{pi} \cdot \left(I_g + e_m^2 \cdot A_g \right) - e_m \cdot M_g \cdot A_g}{A_{ps} \cdot \left(I_g + e_m^2 \cdot A_g \right) + \frac{A_g \cdot I_g \cdot E_{ci}}{E_p}} = 15.485 \cdot \text{ksi}$$

Time dependent losses (Δf_{pLT})

$$H := 75$$

75% relative humidity

$$\gamma_h := 1.7 - 0.01H = 0.95$$

(5.9.5.3-2)

$$\gamma_{st} := \frac{5}{\left(\frac{f_{ci}}{1 + \frac{f_{ci}}{\text{ksi}}} \right)} = 0.715$$

(5.9.5.3-3)

$$\Delta f_{pR} := 2.4 \text{ ksi}$$

Low relaxation strand

$$\Delta f_{pLT} := 10.0 \cdot \frac{f_{pi} \cdot A_{ps}}{A_g} \cdot \gamma_h \cdot \gamma_{st} + 12.0 \text{ksi} \cdot \gamma_h \cdot \gamma_{st} + \Delta f_{pR} = 22.725 \cdot \text{ksi} \quad (5.9.5.3-1)$$

$$\Delta f_{pT} := \Delta f_{pES} + \Delta f_{pLT} = 38.21 \cdot \text{ksi} \quad \text{Total prestress loss}$$

$$f_{pe} := f_{pi} - \Delta f_{pT} = 164.404 \cdot \text{ksi} \quad \text{Effective stress in RF-1R-1}$$

C.3 DEPTH OF RECTANGULAR STRESS BLOCK

C.3.1 Design Strength

C.3.1.1 RF-3R-9-A

Concrete Properties

$f_c := 5.81 \text{ ksi}$ Design concrete strength

$\beta_1 := 0.76$ (5.7.2.2)

$n := 46$ Number of bonding prestressed strands at load point

$A_{ps} := 0.153 \text{ in}^2 \cdot n = 7.038 \cdot \text{in}^2$ Area of the prestressed strands

$c_{gs} := 5.565 \text{ in}$ Center of gravity of the prestressed strands

$b := 58.25 \text{ in}$ Width of the beam

$h := 58 \text{ in}$ Height of composite beam

$d_p := h - c_{gs} = 52.435 \cdot \text{in}$

$$k := 2 \cdot \left(1.04 - \frac{f_{py}}{f_{pu}} \right) = 0.28 \quad (5.7.3.1.1-2)$$

$$c := \frac{A_{ps} \cdot f_{pu}}{\left(0.85 \cdot f_c \cdot \beta_1 \cdot b + k \cdot A_{ps} \cdot \frac{f_{pu}}{d_p} \right)} = 8.306 \cdot \text{in} \quad (5.7.3.1.1-4)$$

$$f_{ps} := f_{pu} \cdot \left(1 - k \cdot \frac{c}{d_p} \right) = 258.024 \cdot \text{ksi} \quad (5.7.3.1.1-1)$$

$a := \beta_1 \cdot c = 6.313 \cdot \text{in}$ Depth of the rectangular stress block

C.3.1.2 RF-3R-9-C

$f_c := 5.81 \text{ ksi}$ Design concrete strength

$\beta_1 := 0.76$ (5.7.2.2)

$n := 56$ Number of bonding prestressed strands at load point

$A_{ps} := 0.153 \text{ in}^2 \cdot n = 8.568 \cdot \text{in}^2$ Area of the prestressed strands

$c_{gs} := 5.143 \text{ in}$ Center of gravity of the prestressed strands

$b := 58.25 \text{ in}$ Width of the beam

$h := 58 \text{ in}$ Height of composite beam

$d_p := h - c_{gs} = 52.857 \cdot \text{in}$

$k := 2 \cdot \left(1.04 - \frac{f_{py}}{f_{pu}} \right) = 0.28$ (5.7.3.1.1-2)

$c := \frac{A_{ps} \cdot f_{pu}}{\left(0.85 \cdot f_c \cdot \beta_1 \cdot b + k \cdot A_{ps} \cdot \frac{f_{pu}}{d_p} \right)} = 10.02 \cdot \text{in}$ (5.7.3.1.1-4)

$f_{ps} := f_{pu} \cdot \left(1 - k \cdot \frac{c}{d_p} \right) = 255.669 \cdot \text{ksi}$ (5.7.3.1.1-1)

$a := \beta_1 \cdot c = 7.615 \cdot \text{in}$ Depth of the rectangular stress block

C.3.1.3 RF-3R-12-A

$f_c := 5.81 \text{ ksi}$ Design concrete strength

$\beta_1 := 0.76$ (5.7.2.2)

$n := 52$ Number of bonding prestressed strands at load point

$A_{ps} := 0.153 \text{ in}^2 \cdot n = 7.956 \cdot \text{in}^2$ Area of the prestressed strands

$c_{gs} := 5.385 \text{ in}$ Center of gravity of the prestressed strands

$b := 58.25 \text{ in}$ Width of the beam

$h := 58 \text{ in}$ Height of composite beam

$d_p := h - c_{gs} = 52.615 \cdot \text{in}$

$k := 2 \cdot \left(1.04 - \frac{f_{py}}{f_{pu}} \right) = 0.28$ (5.7.3.1.1-2)

$c := \frac{A_{ps} \cdot f_{pu}}{\left(0.85 \cdot f_c \cdot \beta_1 \cdot b + k \cdot A_{ps} \cdot \frac{f_{pu}}{d_p} \right)} = 9.337 \cdot \text{in}$ (5.7.3.1.1-4)

$f_{ps} := f_{pu} \cdot \left(1 - k \cdot \frac{c}{d_p} \right) = 256.584 \cdot \text{ksi}$ (5.7.3.1.1-1)

$a := \beta_1 \cdot c = 7.096 \cdot \text{in}$ Depth of the rectangular stress block

C.3.1.4 MLL-9-34-A

$$f_c := 5.419 \text{ ksi} \quad \text{Design concrete strength}$$

$$\beta_1 := 0.78 \quad (5.7.2.2)$$

$$n := 48 \quad \text{Number of bonding prestressed strands at load point}$$

$$A_{ps} := 0.153 \text{ in}^2 \cdot n = 7.344 \cdot \text{in}^2 \quad \text{Area of the prestressed strands}$$

$$c_{gs} := 5 \text{ in} \quad \text{Center of gravity of the prestressed strands}$$

$$b := 58.25 \text{ in} \quad \text{Width of the beam}$$

$$h := 58 \text{ in} \quad \text{Height of composite beam}$$

$$d_p := h - c_{gs} = 53 \cdot \text{in}$$

$$k := 2 \cdot \left(1.04 - \frac{f_{py}}{f_{pu}} \right) = 0.28 \quad (5.7.3.1.1-2)$$

$$c := \frac{A_{ps} \cdot f_{pu}}{\left(0.85 \cdot f_c \cdot \beta_1 \cdot b + k \cdot A_{ps} \cdot \frac{f_{pu}}{d_p} \right)} = 9.023 \cdot \text{in} \quad (5.7.3.1.1-4)$$

$$f_{ps} := f_{pu} \cdot \left(1 - k \cdot \frac{c}{d_p} \right) = 257.129 \cdot \text{ksi} \quad (5.7.3.1.1-1)$$

$$a := \beta_1 \cdot c = 7.038 \cdot \text{in} \quad \text{Depth of the rectangular stress block}$$

C.3.1.5 RF-IR-1-C

$f_c := 5.989 \text{ ksi}$	Design concrete strength
$\beta_1 := 0.75$	(5.7.2.2)
$n := 52$	Number of bonding prestressed strands at load point
$A_{ps} := 0.153 \text{ in}^2 \cdot n = 7.956 \cdot \text{in}^2$	Area of the prestressed strands
$c_{gs} := 5.538 \text{ in}$	Center of gravity of the prestressed strands
$b := 58.25 \text{ in}$	Width of the beam
$h := 58 \text{ in}$	Height of composite beam
$d_p := h - c_{gs} = 52.462 \cdot \text{in}$	
$k := 2 \cdot \left(1.04 - \frac{f_{py}}{f_{pu}} \right) = 0.28$	(5.7.3.1.1-2)
$c := \frac{A_{ps} \cdot f_{pu}}{\left(0.85 \cdot f_c \cdot \beta_1 \cdot b + k \cdot A_{ps} \cdot \frac{f_{pu}}{d_p} \right)} = 9.185 \cdot \text{in}$	(5.7.3.1.1-4)
$f_{ps} := f_{pu} \cdot \left(1 - k \cdot \frac{c}{d_p} \right) = 256.763 \cdot \text{ksi}$	(5.7.3.1.1-1)
$a := \beta_1 \cdot c = 6.889 \cdot \text{in}$	Depth of the rectangular stress block

C.3.2 Core Strength

C.3.2.1 RF-3R-9-A

Concrete Properties

$$f_{c_core} := 8.56 \text{ ksi} \quad \text{Cored concrete strength}$$

$$f_c := \frac{f_{c_core}}{0.85} = 10.071 \cdot \text{ksi} \quad \text{Core tests having average of 85 percent of the specified strength are realistic}$$

$$\beta_1 := 0.65 \quad (5.7.2.2)$$

Steel Properties

$$f_{pu} := 270 \text{ ksi} \quad f_{py} := 0.9 \cdot f_{pu} = 243 \cdot \text{ksi}$$

Section Properties

$$n := 46 \quad \text{Number of bonding prestressed strands at load point}$$

$$A_{ps} := 0.153 \text{ in}^2 \cdot n = 7.038 \cdot \text{in}^2 \quad \text{Area of the prestressed strands}$$

$$c_{gs} := 5.565 \text{ in} \quad \text{Center of gravity of the prestressed strands}$$

$$b := 58.25 \text{ in} \quad \text{Width of the beam}$$

$$h := 58 \text{ in} \quad \text{Height of composite beam}$$

$$d_p := h - c_{gs} = 52.435 \cdot \text{in}$$

$$k := 2 \cdot \left(1.04 - \frac{f_{py}}{f_{pu}} \right) = 0.28 \quad (5.7.3.1.1-2)$$

$$\bar{c} := \frac{A_{ps} \cdot f_{pu}}{\left(0.85 \cdot f_c \cdot \beta_1 \cdot b + k \cdot A_{ps} \cdot \frac{f_{pu}}{d_p} \right)} = 5.685 \cdot \text{in} \quad (5.7.3.1.1-4)$$

$$f_{ps} := f_{pu} \cdot \left(1 - k \cdot \frac{c}{d_p} \right) = 261.803 \cdot \text{ksi} \quad (5.7.3.1.1-1)$$

$$a := \beta_1 \cdot \bar{c} = 3.695 \cdot \text{in} \quad \text{Depth of the rectangular stress block}$$

C.3.2.2 RF-3R-9-C

Concrete Properties

$$f_{c_core} := 8.56 \text{ ksi}$$

$$f_c := \frac{f_{c_core}}{0.85} = 10.071 \cdot \text{ksi}$$

Core tests having average of 85 percent of the specified strength are realistic (ACI 318-08 5.6.5)

$$\beta_1 := 0.65$$

Steel Properties

$$f_{pu} := 270 \text{ ksi} \quad f_{py} := 0.9 \cdot f_{pu} = 243 \cdot \text{ksi}$$

Section Properties

$$n := 56$$

Number of bonding prestressed strands at load point

$$A_{ps} := 0.153 \text{ in}^2 \cdot n = 8.568 \cdot \text{in}^2$$

Area of the prestressed strands

$$c_{gs} := 5.143 \text{ in}$$

Center of gravity of the prestressed strands

$$b := 58.25 \text{ in}$$

Width of the beam

$$h := 58 \text{ in}$$

Height of composite beam

$$d_p := h - c_{gs} = 52.857 \cdot \text{in}$$

$$k := 2 \cdot \left(1.04 - \frac{f_{py}}{f_{pu}} \right) = 0.28 \quad (5.7.3.1.1-2)$$

$$c := \frac{A_{ps} \cdot f_{pu}}{\left(0.85 \cdot f_c \cdot \beta_1 \cdot b + k \cdot A_{ps} \cdot \frac{f_{pu}}{d_p} \right)} = 6.878 \cdot \text{in} \quad (5.7.3.1.1-4)$$

$$f_{ps} := f_{pu} \cdot \left(1 - k \cdot \frac{c}{d_p} \right) = 260.163 \cdot \text{ksi} \quad (5.7.3.1.1-1)$$

$$a := \beta_1 \cdot c = 4.47 \cdot \text{in}$$

Depth of the rectangular stress block

C.3.2.3 RF-3R-12-A

Concrete Properties

$$f_{c_core} := 8.93 \text{ ksi} \quad \text{Cored concrete strength}$$

$$f_c := \frac{f_{c_core}}{0.85} = 10.506 \cdot \text{ksi} \quad \text{Core tests having average of 85 percent of the specified strength are realistic}$$

$$\beta_1 := 0.65 \quad (5.7.2.2)$$

Steel Properties

$$f_{pu} := 270 \text{ ksi}$$

$$f_{py} := 0.9 \cdot f_{pu} = 243 \cdot \text{ksi}$$

Section Properties

$$n := 52 \quad \text{Number of bonding prestressed strands at load point}$$

$$A_{ps} := 0.153 \text{ in}^2 \cdot n = 7.956 \cdot \text{in}^2 \quad \text{Area of the prestressed strands}$$

$$c_{gs} := 5.385 \text{ in} \quad \text{Center of gravity of the prestressed strands}$$

$$b := 58.25 \text{ in} \quad \text{Width of the beam}$$

$$h := 58 \text{ in} \quad \text{Height of composite beam}$$

$$d_p := h - c_{gs} = 52.615 \cdot \text{in}$$

$$k := 2 \cdot \left(1.04 - \frac{f_{py}}{f_{pu}} \right) = 0.28 \quad (5.7.3.1.1-2)$$

$$c := \frac{A_{ps} \cdot f_{pu}}{\left(0.85 \cdot f_c \cdot \beta_1 \cdot b + k \cdot A_{ps} \cdot \frac{f_{pu}}{d_p} \right)} = 6.145 \cdot \text{in} \quad (5.7.3.1.1-4)$$

$$f_{ps} := f_{pu} \cdot \left(1 - k \cdot \frac{c}{d_p} \right) = 261.17 \cdot \text{ksi} \quad (5.7.3.1.1-1)$$

$$a := \beta_1 \cdot c = 3.995 \cdot \text{in} \quad \text{Depth of the rectangular stress block}$$

C.3.2.4 MLL-9-34-A

Concrete Properties

$$f_{c_core} := 6.43 \text{ ksi} \quad \text{Cored concrete strength}$$

$$f_c := \frac{f_{c_core}}{0.85} = 7.565 \cdot \text{ksi} \quad \text{Core tests having average of 85 percent of the specified strength are realistic}$$

$$\beta_1 := 0.67 \quad (5.7.2.2)$$

Steel Properties

$$f_{pu} := 270 \text{ ksi}$$

$$f_{py} := 0.9 \cdot f_{pu} = 243 \cdot \text{ksi}$$

Section Properties

$$n := 48 \quad \text{Number of bonding prestressed strands at load point}$$

$$A_{ps} := 0.153 \text{ in}^2 \cdot n = 7.344 \cdot \text{in}^2 \quad \text{Area of the prestressed strands}$$

$$c_{gs} := 5 \text{ in} \quad \text{Center of gravity of the prestressed strands}$$

$$b := 58.25 \text{ in} \quad \text{Width of the beam}$$

$$h := 58 \text{ in} \quad \text{Height of composite beam}$$

$$d_p := h - c_{gs} = 53 \cdot \text{in}$$

$$k := 2 \cdot \left(1.04 - \frac{f_{py}}{f_{pu}} \right) = 0.28 \quad (5.7.3.1.1-2)$$

$$c := \frac{A_{ps} \cdot f_{pu}}{\left(0.85 \cdot f_c \cdot \beta_1 \cdot b + k \cdot A_{ps} \cdot \frac{f_{pu}}{d_p} \right)} = 7.585 \cdot \text{in} \quad (5.7.3.1.1-4)$$

$$f_{ps} := f_{pu} \cdot \left(1 - k \cdot \frac{c}{d_p} \right) = 259.181 \cdot \text{ksi} \quad (5.7.3.1.1-1)$$

$$a := \beta_1 \cdot c = 5.082 \cdot \text{in} \quad \text{Depth of the rectangular stress block}$$

C.3.2.5 RF-1R-1-C

Concrete Properties

$$f_{c_core} := 6.24 \text{ ksi} \quad \text{Cored concrete strength}$$

$$f_c := \frac{f_{c_core}}{0.85} = 7.341 \cdot \text{ksi} \quad \text{Core tests having average of 85 percent of the specified strength are realistic (ACI 318-08 5.6.5)}$$

$$\beta_1 := 0.68 \quad (5.7.2.2)$$

Steel Properties

$$f_{pu} := 270 \text{ ksi}$$

$$f_{py} := 0.9 \cdot f_{pu} = 243 \cdot \text{ksi}$$

Section Properties

$$n := 52 \quad \text{Number of bonding prestressed strands at load point}$$

$$A_{ps} := 0.153 \text{ in}^2 \cdot n = 7.956 \cdot \text{in}^2 \quad \text{Area of the prestressed strands}$$

$$c_{gs} := 5.538 \text{ in} \quad \text{Center of gravity of the prestressed strands}$$

$$b := 58.25 \text{ in} \quad \text{Width of the beam}$$

$$h := 58 \text{ in} \quad \text{Height of composite beam}$$

$$d_p := h - c_{gs} = 52.462 \cdot \text{in}$$

$$k := 2 \cdot \left(1.04 - \frac{f_{py}}{f_{pu}} \right) = 0.28 \quad (5.7.3.1.1-2)$$

$$c := \frac{A_{ps} \cdot f_{pu}}{\left(0.85 \cdot f_c \cdot \beta_1 \cdot b + k \cdot A_{ps} \cdot \frac{f_{pu}}{d_p} \right)} = 8.306 \cdot \text{in} \quad (5.7.3.1.1-4)$$

$$f_{ps} := f_{pu} \cdot \left(1 - k \cdot \frac{c}{d_p} \right) = 258.031 \cdot \text{ksi} \quad (5.7.3.1.1-1)$$

$$a := \beta_1 \cdot c = 5.648 \cdot \text{in} \quad \text{Depth of the rectangular stress block}$$

APPENDIX D

Calculations for Strut-and-Tie Models

Appendix D includes the calculations of five beams for one-panel model and combination model (one-panel and two-panel model) based on AASHTO LRFD 2008, ACI 318-08, and TxDOT Project 5253. Besides, each beam is calculated based on design and core strength divided by 0.85. Therefore, there are $5 \times 3 \times 2 \times 2 = 60$ strut-and-tie models. For sake of brevity, complete six calculations for strut-and-tie models of RF-3R-9-A in design strength will be presented first. All the other strut-and-tie models have the same critical elements, and hence can be presented in table. Check for other non-critical elements is neglected here. Software MathCAD was utilized in all the calculations.

D.1 RF-3R-9-A

D.1.1 Design Strength

Concrete Properties

$f'_c := 5.81 \text{ksi}$ Design Concrete Strength

Steel Properties

$f_{pu} := 270 \text{ksi}$ Specified tensile strength of prestressing steel

$f_{py} := 0.9 \cdot f_{pu} = 243 \cdot \text{ksi}$ Specified yield Strength of prestressing steel

$f_{pe} := 164.6 \text{ksi}$ Effective prestress

$f_{ps} := 258 \text{ksi}$ Stress in prestressing steel at nominal flexural strength

$f_y := 60 \text{ksi}$ Specified tensile strength of reinforcement

$E_p := 28500 \text{ksi}$ Modulus of elasticity of prestressing steel

$d_{bs} := 0.5 \text{in}$ Nominal diameter of prestressing strand

$A_{strand} := 0.153 \text{in}^2$ Nominal area of prestressing strand

$A_{4b} := 0.2 \text{in}^2$ Nominal area of #4 standard reinforcing bar

Testing parameters

Span := 349in Total Span

a := 99in Shear Span

Number of bonded prestressing strands (Figure D.1)

$n_0 := 38$ Bonding starts at the end face

$n_3 := 8$	Bonding starts at 3 ft from the end face
$n_6 := 6$	Bonding starts at 6 ft from the end face
$n_9 := 4$	Bonding starts at 9 ft from the end face
$n_{12} := 4$	Bonding starts at 12 ft from the end face
$n_{15} := 2$	Bonding starts at 15 ft from the end face
$n := 46$	Number of bonded strands at the critical point
$A_{ps} := n \cdot A_{strand} = 7.038 \cdot \text{in}^2$	Area of prestressing steel at the critical point

Testing Result

$V_{dead} := 26.88 \text{ kip}$	Calculated self weight
$V_{exp} := 668 \text{ kip}$	Experimental shear capacity

RF-3R-9-A Elevation (No Skew Dapped End)

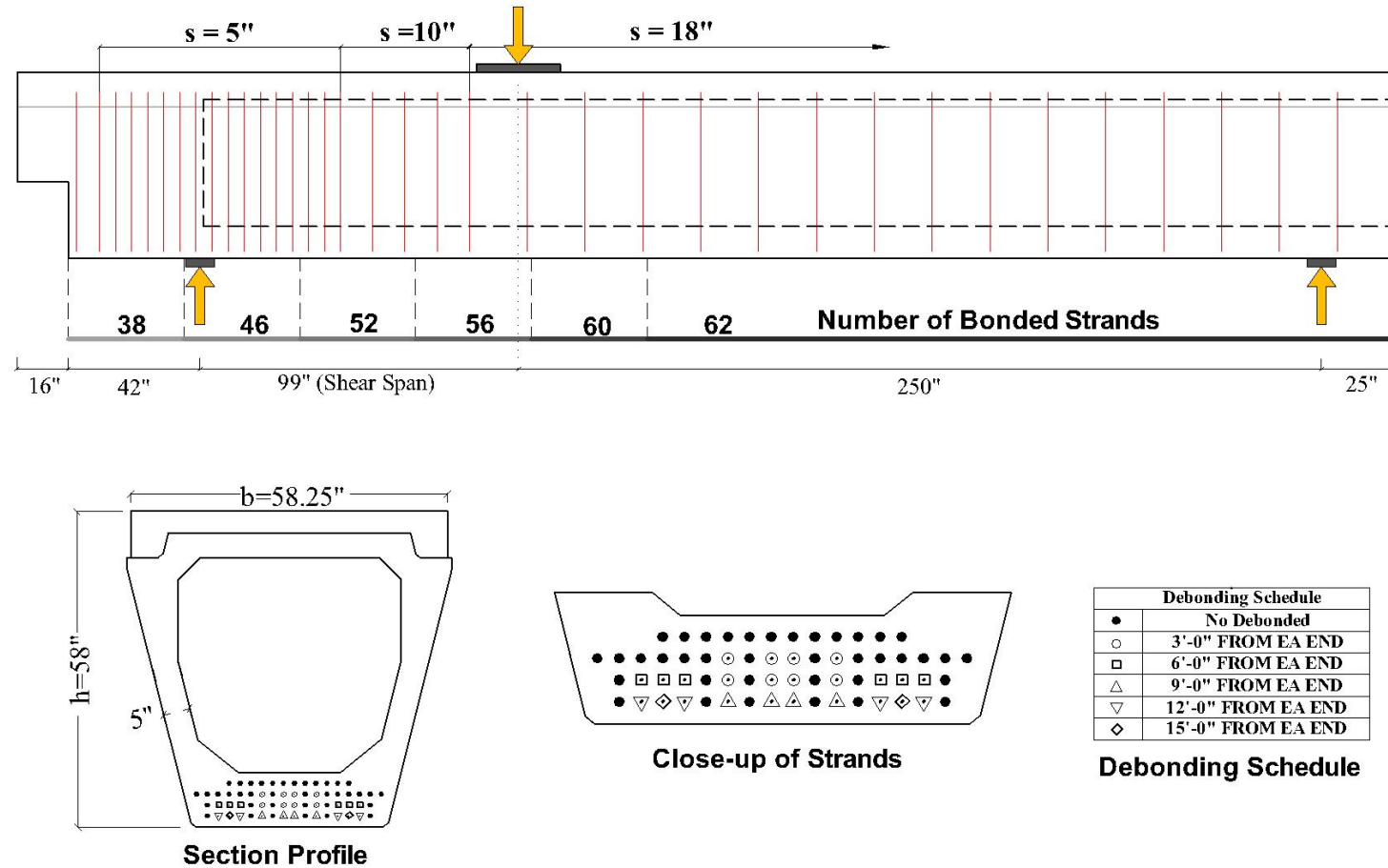
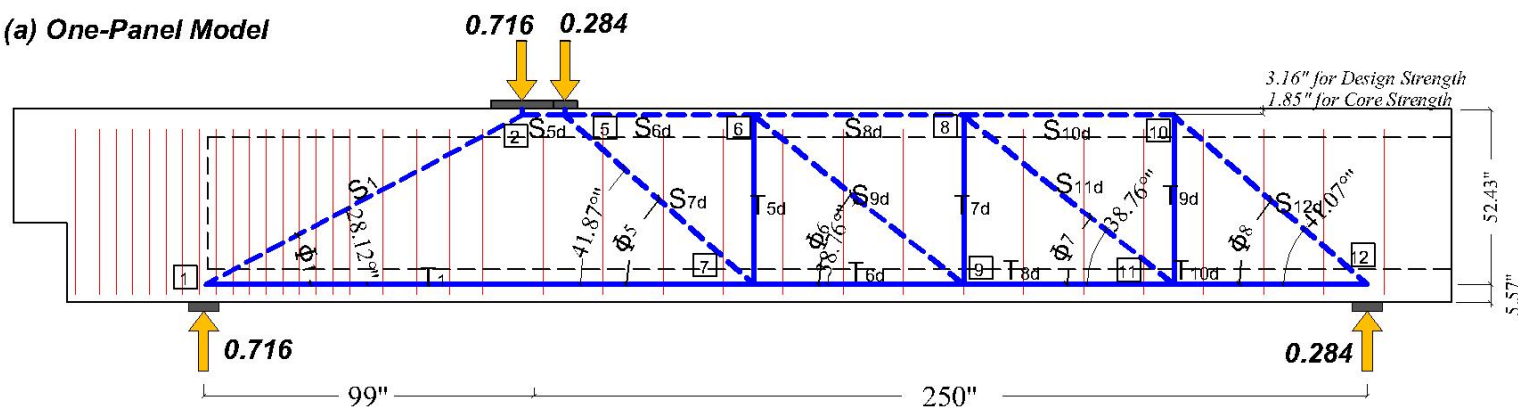


Figure D.1 RF-3R-9-A Elevation, section, and debonding schedule

(a) One-Panel Model



(b) Two-Panel Model

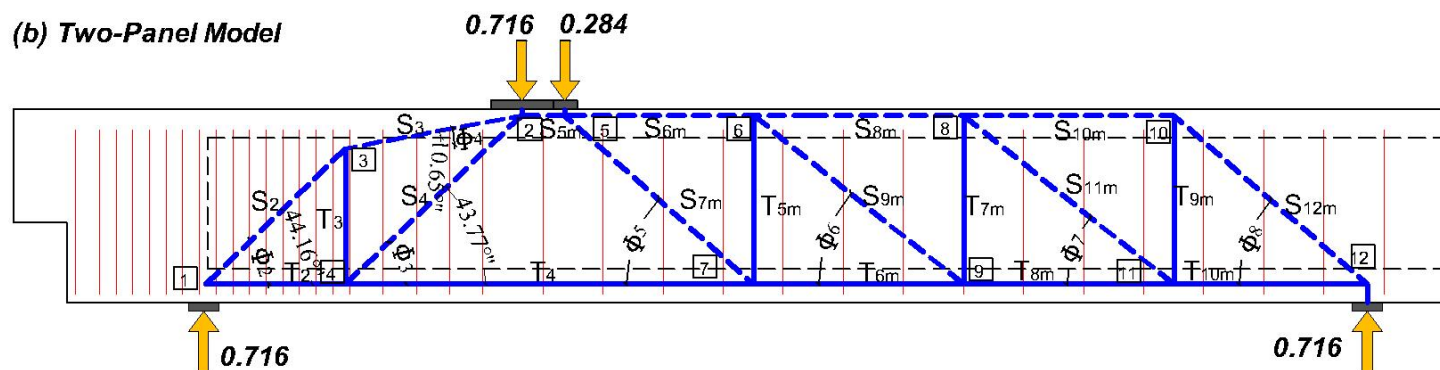


Figure D.2 RF-3R-9-A strut-and-tie model (a) One-panel (b) Two-panel

Geometry of the strut-and-tie model (Figure D.2)

$$\phi_1 := 27.50\text{deg} \quad \phi_2 := 44.16\text{deg} \quad \phi_3 := 43.02\text{deg}$$

$$\phi_4 := 9.28\text{deg} \quad \phi_5 := 36.98\text{deg} \quad \phi_6 := 42.38\text{deg}$$

$$\phi_7 := 42.38\text{deg} \quad \phi_8 := 36.31\text{deg}$$

Forces in the one-panel model when unit load is applied

$$V_1 := 1\text{kip} \cdot \frac{(\text{Span} - a)}{\text{Span}} = 0.716 \cdot \text{kip} \quad \text{The larger reaction when unit load is applied}$$

$$S_1 := \frac{V_1}{\sin(\phi_1)} = 1.551 \cdot \text{kip}$$

$$T_1 := S_1 \cdot \cos(\phi_1) = 1.376 \cdot \text{kip}$$

$$S_{5d} := S_1 \cdot \cos(\phi_1) = 1.376 \cdot \text{kip} \quad \text{d in the subscript means direct-strut model}$$

$$S_{7d} := \frac{(1\text{kip} - V_1)}{\sin(\phi_5)} = 0.472 \cdot \text{kip}$$

$$S_{6d} := S_{5d} - S_{7d} \cdot \cos(\phi_5) = 0.999 \cdot \text{kip}$$

$$T_{5d} := S_{7d} \cdot \sin(\phi_5) = 0.284 \cdot \text{kip}$$

$$T_{6d} := T_1 - S_{7d} \cdot \cos(\phi_5) = 0.999 \cdot \text{kip}$$

$$S_{9d} := \frac{T_{5d}}{\sin(\phi_6)} = 0.421 \cdot \text{kip}$$

$$S_{8d} := S_{6d} - S_{9d} \cdot \cos(\phi_6) = 0.688 \cdot \text{kip}$$

$$T_{7d} := S_{9d} \cdot \sin(\phi_6) = 0.284 \cdot \text{kip}$$

$$T_{8d} := T_{6d} - S_{9d} \cdot \cos(\phi_6) = 0.688 \cdot \text{kip}$$

$$S_{11d} := \frac{T_{7d}}{\sin(\phi_7)} = 0.421 \cdot \text{kip}$$

$$S_{10d} := S_{8d} - S_{11d} \cdot \cos(\phi_7) = 0.378 \cdot \text{kip}$$

$$T_{9d} := S_{11d} \cdot \sin(\phi_7) = 0.284 \cdot \text{kip}$$

$$T_{10d} := T_{8d} - S_{11d} \cdot \cos(\phi_7) = 0.378 \cdot \text{kip}$$

$$S_{12d} := \frac{T_{10d}}{\cos(\phi_8)} = 0.469 \cdot \text{kip}$$

$$S_{12d} \cdot \sin(\phi_8) = 0.277 \cdot \text{kip}$$

The reaction is supposed to be 0.284 kip. The location of the stirrups causes this discrepancy.

$$\text{atan} \left(\frac{1 \text{ kip} - V_1}{T_{10d}} \right) = 36.915 \cdot \text{deg}$$

Compare to ϕ_8 , 0.6 degree does not make much difference and therefore discrepancy is negligible.

D.1.1.1 One-Panel Model

AASHTO LRFD 2008

Assumed applied load

$$P_d := 165 \text{ kip} \quad \text{Load applied to the direct-strut model}$$

After scaling...

$$T1 := P_d \cdot \frac{T_1}{1 \text{ kip}} = 227.05 \cdot \text{kip}$$

$$S1 := P_d \cdot \frac{S_1}{1 \text{ kip}} = 255.972 \cdot \text{kip}$$

Start to check the strut-and-tie model

Tie 1

Development length of the prestressing strands

$$\kappa := 1.6$$

$$l_d := \kappa \cdot \frac{\left(f_{ps} - \frac{2}{3} \cdot f_{pe}\right) \cdot d_{bs}}{\text{ksi}} = 118.613 \cdot \text{in} \quad \text{AASHTO LRFD 5.11.4.2-1}$$

$$f(x) := \begin{cases} \frac{x}{60 \cdot d_{bs}} \cdot f_{pe} & \text{if } x < 60d_{bs} \\ f_{pe} + \frac{(x - 60d_{bs})}{(l_d - 60d_{bs})} \cdot (f_{ps} - f_{pe}) & \text{if } 60d_{bs} < x < l_d \\ f_{ps} & \text{otherwise} \end{cases}$$

Available Length

Stress in the strands

$$l_{a0} := 56 \text{ in}$$

$$f(l_{a0}) = 192.004 \cdot \text{ksi}$$

$$l_{a3} := l_{a0} - 36 \text{ in} = 20 \cdot \text{in}$$

$$f(l_{a3}) = 109.733 \cdot \text{ksi}$$

$$T_{n1} := A_{\text{strand}} \cdot (n_0 \cdot f(l_{a0}) + n_3 \cdot f(l_{a3})) = 1.251 \times 10^3 \cdot \text{kip}$$

Tie capacity

$$T1 = 227.05 \cdot \text{kip}$$

$$\text{Check} := \begin{cases} \text{"OK"} & \text{if } T_{n1} > T1 \\ \text{"NG"} & \text{otherwise} \end{cases}$$

Check = "OK"

Node 1 CCT Node (Figure D.3)

$$\beta_{n1} := 0.75$$

Concrete efficiency factor per AASHTO LRFD 5.6.3.5

Bearing Plate

$$A_1 := 32\text{in} \cdot 9\text{in} = 288 \cdot \text{in}^2$$

Area of bottom bearing plate

$$f_{cebl} := \beta_{n1} \cdot f_c = 4.357 \cdot \text{ksi}$$

Effective concrete stress

$$F_{nn1_bear} := f_{cebl} \cdot A_1 = 1.255 \times 10^3 \cdot \text{kip}$$

Capacity

$$V1 := (P_d) \cdot \frac{(\text{Span} - a)}{\text{Span}} = 118.195 \cdot \text{kip}$$

Load (V1d)

$$\text{Check} := \begin{cases} \text{"OK"} & \text{if } F_{nn1_bear} \geq V1 \\ \text{"NG"} & \text{otherwise} \end{cases}$$

Check = "OK"

Back Face

$$h_{n1} := 10\text{in}$$

Height of node 1

$$l_{b1} := 9\text{in}$$

Width of node 1 bearing plate

$$F_{nn1_back} := f_{cebl} \cdot h_{n1} \cdot l_{b1} = 392.175 \cdot \text{kip}$$

Capacity

$$T1 = 227.05 \cdot \text{kip}$$

Load

$$\text{Check} := \begin{cases} \text{"OK"} & \text{if } F_{nn1_back} \geq T1 \\ \text{"NG"} & \text{otherwise} \end{cases}$$

Check = "OK"

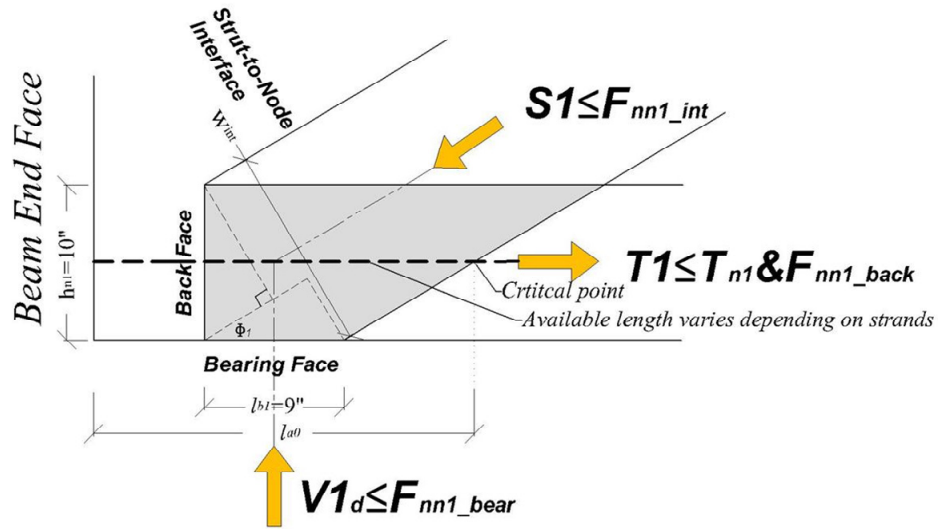


Figure D.3 Close-up of Node 1

Strut-to-Node Interface

$$l_{b1} = 9 \cdot \text{in}$$

$$w_{\text{int}1} := l_{b1} \cdot \sin(\phi_1) + h_{n1} \cdot \cos(\phi_1) = 13.026 \cdot \text{in} \quad \text{Width of interface}$$

$$t_{s1} := 10 \text{in} \quad \text{Minimum thickness}$$

Iterate the following four equations to get the efficiency factor

$$F_{\text{nint}1_try} := 256 \text{kip}$$

$$\epsilon_s := \frac{F_{\text{nint}1_try} \cdot \cos(\phi_1)}{A_{ps} \cdot E_p} = 1.132 \times 10^{-3}$$

$$\epsilon_1 := \epsilon_s + (\epsilon_s + 0.002) \cdot (\cot(\phi_1))^2 = 0.013 \quad \text{AASHTO LRFD 5.6.3.3.3-2}$$

$$v_{s1} := \min\left(0.85, \frac{1}{0.8 + 170 \cdot \epsilon_1}\right) = 0.338 \quad \text{AASHTO LRFD 5.6.3.3.3-1}$$

$$f_{ce1} := v_{s1} \cdot f'_c = 1.965 \cdot \text{ksi}$$

$$F_{nn1_int} := f_{ce1} \cdot t_{s1} \cdot w_{\text{int}1} = 255.91 \cdot \text{kip} \quad \text{Capacity}$$

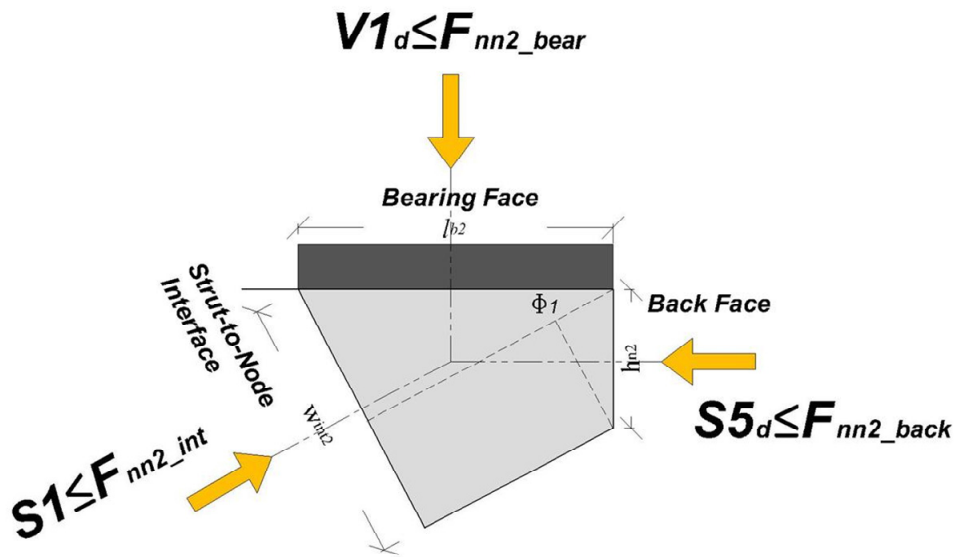


Figure D.4 Close-up of Node 2

Strut-to-Node Interface

$$w_{int2} := l_{b2} \cdot \sin(\phi_1) + h_{n2} \cdot \cos(\phi_1) = 14.197 \cdot \text{in} \quad \text{Width of interface}$$

$$F_{nn2_int} := f_{cen2} \cdot w_{int2} \cdot 2.24 \text{in} = 3.365 \times 10^3 \cdot \text{kip} \quad \text{Capacity}$$

$$S1 = 255.972 \cdot \text{kip} \quad \text{Load}$$

$$\text{Check} := \begin{cases} \text{"OK"} & \text{if } F_{nn2_int} \geq S1 \\ \text{"NG"} & \text{otherwise} \end{cases}$$

Check = "OK"

$$V1 = 118.195 \cdot \text{kip} \quad \text{Calculated shear}$$

$$V_{exp} = 668 \cdot \text{kip}$$

$$\frac{V_{exp}}{V1} = 5.652$$

The failure mode is strut failure (S1)

ACI 318-08

Assumed applied load

$P_d := 249\text{kip}$ Load applied to the direct-strut model

After scaling...

$$T_1 := P_d \cdot \frac{T_1}{1\text{kip}} = 342.639 \cdot \text{kip}$$

$$S_1 := P_d \cdot \frac{S_1}{1\text{kip}} = 386.285 \cdot \text{kip}$$

Start to check the strut-and-tie model

Check the ACI 318-08 A.3.3.1 requirement for an adequate reinforced strut

$$A_{4b} = 0.2 \cdot \text{in}^2$$

$b_s := 10\text{in}$ Width of strut perpendicular to the plane of reinforcement

$s := 10\text{in}$ Spacing of stirrup

$$\rho_v := \frac{2 \cdot A_{4b} \sin(\phi_1)}{b_s \cdot s} = 1.847 \times 10^{-3}$$
 Minimum reinforcement requirement per A-4

$$\beta_s := \begin{cases} 0.75 & \text{if } \rho_v > 0.003 \\ 0.60 & \text{otherwise} \end{cases}$$
 ACI A.3.2.2

$\beta_s = 0.6$ Non-reinforced strut

Strut 1

$t_{s1} := 10\text{in}$ The smallest thickness of the web

$h_{n1} := 10\text{in}$ Height of node 1

$l_{b1} := 9\text{in}$ Length of node 1
(bearing plate width)

$$w_{int1} := l_{b1} \cdot \sin(\phi_1) + h_{n1} \cdot \cos(\phi_1) = 13.026 \cdot \text{in}$$

Minimum width of strut

$$F_{ns1} := 0.85 \cdot \beta_s \cdot f_c \cdot w_{int1} \cdot t_{s1} = 385.969 \cdot \text{kip}$$

Capacity of strut 1

$$S1 = 386.285 \cdot \text{kip}$$

Load

$$\text{Check} := \begin{cases} \text{"OK"} & \text{if } F_{ns1} \geq S1 \\ \text{"NG"} & \text{otherwise} \end{cases}$$

Check = "NG"

Tie 1

Development Length of the strands

$$l_{ds} := \left(\frac{f_{pe}}{3000 \text{ psi}} \right) \cdot d_{bs} + \left(\frac{f_{ps} - f_{pe}}{1000 \cdot \text{psi}} \right) \cdot d_{bs} = 74.133 \cdot \text{in}$$

$$f(x) := \begin{cases} \frac{x}{\left(\frac{f_{pe}}{3000 \text{ psi}} \right) \cdot d_{bs}} \cdot f_{pe} & \text{if } x < \frac{f_{pe}}{3000 \text{ psi}} \cdot d_{bs} \\ f_{pe} + \frac{\left[x - \left(\frac{f_{pe}}{3000 \text{ psi}} \right) \cdot d_{bs} \right]}{\left[\left(\frac{f_{ps} - f_{pe}}{1000 \cdot \text{psi}} \right) \cdot d_{bs} \right]} \cdot (f_{ps} - f_{pe}) & \text{if } \frac{f_{pe}}{3000 \text{ psi}} \cdot d_{bs} < x < l_{ds} \\ f_{ps} & \text{otherwise} \end{cases}$$

Available Length

Stress in the strands

$$l_{a0} := 56 \text{ in} \quad (\text{Figure D.3})$$

$$f(l_{a0}) = 221.733 \cdot \text{ksi}$$

$$l_{a3} := l_{a0} - 36 \text{ in} = 20 \cdot \text{in}$$

$$f(l_{a3}) = 120 \cdot \text{ksi}$$

$$T_{n1} := A_{strand} \cdot (n_0 \cdot f(l_{a0}) + n_3 \cdot f(l_{a3})) = 1.436 \times 10^3 \cdot \text{kip}$$

Tie Capacity

$$T1 = 342.639 \cdot \text{kip}$$

Load

$$\text{Check} := \begin{cases} \text{"OK"} & \text{if } T_{n1} > T1 \\ \text{"NG"} & \text{otherwise} \end{cases}$$

Check = "OK"

Node 1 CCT Node (Figure D.3)

$$\beta_{n1} := 0.80$$

Concrete efficiency factor per ACI A.5.2

Bearing Plate

$$A_1 := 32\text{in} \cdot 9\text{in} = 288 \cdot \text{in}^2$$

Area of bottom bearing plate

$$f_{cen1} := 0.85 \cdot \beta_{n1} \cdot f_c = 3.951 \cdot \text{ksi}$$

Effective concrete stress

$$F_{nn1_bear} := f_{cen1} \cdot A_1 = 1.138 \times 10^3 \cdot \text{kip}$$

Capacity

$$V1 := (P_d) \cdot \frac{(\text{Span} - a)}{\text{Span}} = 178.367 \cdot \text{kip}$$

Load (V1d)

$$\text{Check} := \begin{cases} \text{"OK"} & \text{if } F_{nn1_bear} \geq V1 \\ \text{"NG"} & \text{otherwise} \end{cases}$$

Check = "OK"

Back Face

$$h_{n1} = 10 \cdot \text{in}$$

Height of node 1

$$w_{b1} := 32\text{in}$$

Width of node 1 (length of bearing plate)

$$F_{nn1_back} := f_{cen1} \cdot h_{n1} \cdot w_{b1} = 1.264 \times 10^3 \cdot \text{kip}$$

Capacity

$$T1 = 342.639 \cdot \text{kip}$$

Load

$$\text{Check} := \begin{cases} \text{"OK"} & \text{if } F_{nn1_back} \geq T1 \\ \text{"NG"} & \text{otherwise} \end{cases}$$

Check = "OK"

Strut-to-Node Interface

$t_{s1} := 10\text{in}$ Minimum web thickness

$w_{int1} = 13.026\cdot\text{in}$ Width of interface

$F_{nn1_int} := f_{cen1} \cdot w_{int1} \cdot h_{n1} = 514.625\cdot\text{kip}$ Capacity

$S1 = 386.285\cdot\text{kip}$ Load

Check := $\begin{cases} \text{"OK"} & \text{if } F_{nn1_int} \geq S1 \\ \text{"NG"} & \text{otherwise} \end{cases}$

Check = "OK"

Notice: F_{nn_int1} in Figure D.3 is F_{ns1} because F_{ns1} is smaller than F_{nn1_int} calculated above.

Node 2 CCC Node (Figure D.4)

$\beta_{n2} := 1.0$ Concrete efficiency factor per ACI A.5.2

$f_{cen2} := 0.85 \cdot \beta_{n2} \cdot f_c = 4.938\cdot\text{ksi}$ Effective concrete strength

Top Bearing Plate

$l_{b2} := 18.62\text{in}$ Length of node 2 (part of length of bearing plate based on the proportion of load)

$F_{nn2_bear} := f_{cen2} \cdot l_{b2} \cdot 2 \cdot 24\text{in} = 4.414 \times 10^3\cdot\text{kip}$ Capacity

$V1 = 178.367\cdot\text{kip}$ Load ($V1_d$)

Check := $\begin{cases} \text{"OK"} & \text{if } F_{nn2_bear} > V1 \\ \text{"NG"} & \text{otherwise} \end{cases}$

Check = "OK"

Back Face

$$h_{n2} := 6.313 \text{ in}$$

Height of node 2

$$F_{nn2_back} := f_{cen2} \cdot h_{n2} \cdot 2.24 \text{ in} = 1.496 \times 10^3 \cdot \text{kip}$$

Capacity

$$S5_d := \frac{P_d \cdot S5_d}{1 \text{ kip}} = 342.639 \cdot \text{kip}$$

Load

$$\text{Check} := \begin{cases} \text{"OK"} & \text{if } F_{nn2_back} \geq S5_d \\ \text{"NG"} & \text{otherwise} \end{cases}$$

Check = "OK"

Strut-to-Node Interface

$$w_{int2} := l_{b2} \cdot \sin(\phi_1) + h_{n2} \cdot \cos(\phi_1) = 14.197 \cdot \text{in}$$

Width of interface

$$F_{nn2_int} := f_{cen2} \cdot w_{int2} \cdot 2.24 \text{ in} = 3.365 \times 10^3 \cdot \text{kip}$$

Capacity

$$S1 = 386.285 \cdot \text{kip}$$

Load

$$\text{Check} := \begin{cases} \text{"OK"} & \text{if } F_{nn2_int} \geq S1 \\ \text{"NG"} & \text{otherwise} \end{cases}$$

Check = "OK"

$$V1 = 178.367 \cdot \text{kip}$$

Calculated shear (V1d)

$$V_{exp} = 668 \cdot \text{kip}$$

$$\frac{V_{exp}}{V1} = 3.745$$

The failure mode is strut failure (S1)

TxDOT Project 5253

Assumed applied load

$$P_d := 289.4 \text{ kip} \quad \text{Load applied to the direct-strut model}$$

After scaling...

$$T_1 := P_d \cdot \frac{T_1}{1 \text{ kip}} = 398.232 \cdot \text{kip}$$

$$S_1 := P_d \cdot \frac{S_1}{1 \text{ kip}} = 448.96 \cdot \text{kip}$$

Start to check the strut-and-tie model

Tie 1

Development length

$$\kappa := 1.6 \quad f_{pe} = 164.6 \cdot \text{ksi}$$

$$l_d := \kappa \cdot \frac{\left(f_{ps} - \frac{2}{3} \cdot f_{pe}\right) \cdot d_{bs}}{\text{ksi}} = 118.613 \cdot \text{in} \quad \text{AASHTO LRFD 5.11.4.2-1}$$

$$f(x) := \begin{cases} \frac{x}{60 \cdot d_{bs}} \cdot f_{pe} & \text{if } x < 60d_{bs} \\ f_{pe} + \frac{(x - 60d_{bs})}{(l_d - 60d_{bs})} \cdot (f_{ps} - f_{pe}) & \text{if } 60d_{bs} < x < l_d \\ f_{ps} & \text{otherwise} \end{cases}$$

Available Length

Stress in the strands

$$l_{a0} := 56 \text{ in} \quad (\text{Figure D.3})$$

$$f(l_{a0}) = 192.004 \cdot \text{ksi}$$

$$l_{a3} := l_{a0} - 36 \text{ in} = 20 \cdot \text{in}$$

$$f(l_{a3}) = 109.733 \cdot \text{ksi}$$

Tie capacity at the critical point

$$T_{n1} := A_{\text{strand}} \cdot (n_0 \cdot f(l_{a0}) + n_3 \cdot f(l_{a3})) = 1.251 \times 10^3 \cdot \text{kip}$$

$$T1 = 398.232 \cdot \text{kip}$$

Load

$$\text{Check} := \begin{cases} \text{"OK"} & \text{if } T_{n1} > T1 \\ \text{"NG"} & \text{otherwise} \end{cases}$$

Check = "OK"

Node 1 CCT Node (Figure D.3)

Bearing Plate

$$A_1 := 32\text{in} \cdot 9\text{in} = 288 \cdot \text{in}^2$$

Area of bottom bearing plate

$$A_2 := 13.63\text{in} \cdot 36.63\text{in} = 499.267 \cdot \text{in}^2$$

Projection of A_1 (Figure D.5)

$$v_1 := 0.70$$

Efficiency factor defined by Appendix A of
TxDOT Project 5253 (5.6.3.3.3)

$$m := \sqrt{\frac{A_2}{A_1}} = 1.317$$

Triaxial confinement factor

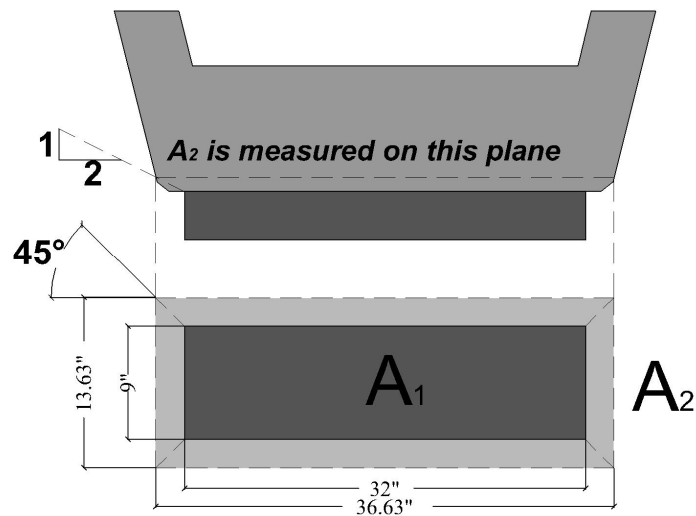


Figure D.5 Determination of tri-axial confinement factor of Node 1

$$f_{cebl} := m \cdot v_1 \cdot f'_c = 5.355 \cdot \text{ksi} \quad \text{Effective concrete stress}$$

$$F_{nn1_bear} := f_{cebl} \cdot A_1 = 1.542 \times 10^3 \cdot \text{kip} \quad \text{Capacity}$$

$$V1 := (P_d) \cdot \frac{(\text{Span} - a)}{\text{Span}} = 207.307 \cdot \text{kip} \quad \text{Load (V1d)}$$

$$\text{Check} := \begin{cases} \text{"OK"} & \text{if } F_{nn1_bear} \geq V1 \\ \text{"NG"} & \text{otherwise} \end{cases}$$

Check = "OK"

Back Face

$$h_{n1} := 10 \text{in} \quad \text{Height of node 1}$$

$$l_{b1} := 9 \text{in} \quad \text{Width of node 1 (width of bearing plate)}$$

$$F_{nn1_back} := f_{cebl} \cdot h_{n1} \cdot l_{b1} = 481.933 \cdot \text{kip} \quad \text{Capacity}$$

$$T1 = 398.232 \cdot \text{kip} \quad \text{Load}$$

$$\text{Check} := \begin{cases} \text{"OK"} & \text{if } F_{nn1_back} \geq T1 \\ \text{"NG"} & \text{otherwise} \end{cases}$$

Check = "OK"

Strut-to-Node Interface

$$l_{b1} = 9 \cdot \text{in} \quad \text{Width of node 1 bearing plate}$$

$$w_{intl} := l_{b1} \cdot \sin(\phi_1) + h_{n1} \cdot \cos(\phi_1) = 13.026 \cdot \text{in} \quad \text{Width of interface}$$

$$t_{s1} := 10 \text{in} \quad \text{Minimum thickness}$$

$$s := 10 \text{in} \quad \text{Spacing of stirrup}$$

$$\rho_h := 0 \quad \text{Steel ratio in the horizontal direction}$$

$$v_1 := \begin{cases} 0.45 & \text{if } 2 \cdot \left(\frac{A_{4b}}{t_{s1} \cdot s} \right) < 0.003 \\ \left(0.85 - \frac{f'_c}{20 \text{ksi}} \right) & \text{otherwise} \end{cases} \vee \rho_h < 0.003$$

$$v_1 = 0.45$$

Without crack control reinforcement

$$f_{ce1} := m \cdot v_1 \cdot f_c = 3.442 \cdot \text{ksi}$$

Effective concrete stress

$$F_{nn1_int} := f_{ce1} \cdot t_{s1} \cdot w_{int1} = 448.399 \cdot \text{kip}$$

Capacity

$$S1 = 448.96 \cdot \text{kip}$$

Load

$$\text{Check} := \begin{cases} \text{"OK"} & \text{if } F_{nn1_int} \geq S1 \\ \text{"NG"} & \text{otherwise} \end{cases}$$

Check = "NG"

Node 2 CCC Node (Figure D.4)

Top Bearing Plate

$$A_1 := 26\text{in} \cdot 24\text{in} = 624 \cdot \text{in}^2$$

Area of top bearing plate

$$A_2 := 26\text{in} \cdot 28\text{in} = 728 \cdot \text{in}^2$$

Projection of A_1 (Figure D.6)

$$m := \sqrt{\frac{A_2}{A_1}} = 1.08$$

Triaxial confinement factor

$$v_2 := 0.85$$

Concrete efficiency factor

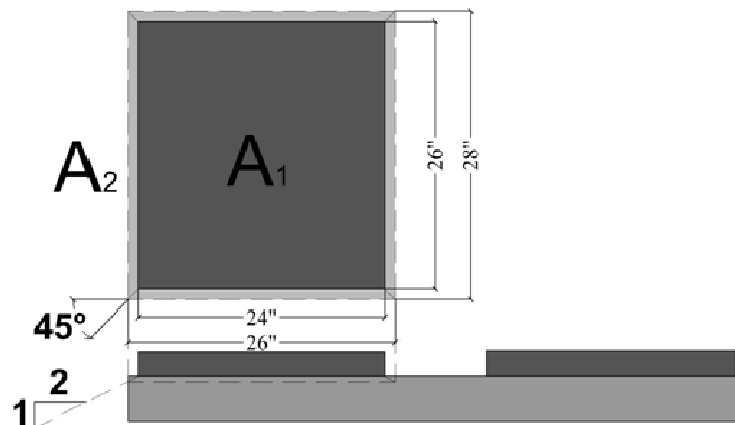


Figure D.6 Determination of tri-axial confinement factor of Node 2

$$l_{b2} := 18.62 \text{ in}$$

Length of bearing plate according to the proportion of the applied load resisted by near support

$$f_{\text{cen2}} := m \cdot v_2 \cdot f'_c = 5.334 \cdot \text{ksi}$$

Effective concrete stress

$$F_{\text{nn2_bear}} := m \cdot f_{\text{cen2}} \cdot l_{b2} \cdot 2 \cdot 24 \text{ in} = 5.149 \times 10^3 \cdot \text{kip} \quad \text{Capacity}$$

$$V1 = 207.307 \cdot \text{kip}$$

Load ($V1_d$)

$$\text{Check} := \begin{cases} \text{"OK"} & \text{if } F_{\text{nn2_bear}} > V1 \\ \text{"NG"} & \text{otherwise} \end{cases}$$

Check = "OK"

Back Face

$$h_{n2} := 6.313 \text{ in}$$

Height of node 2

$$F_{\text{nn2_back}} := f_{\text{cen2}} \cdot h_{n2} \cdot 2 \cdot 24 \text{ in} = 1.616 \times 10^3 \cdot \text{kip} \quad \text{Capacity}$$

$$S5 := \frac{P_d \cdot S_{5d}}{1 \text{ kip}} = 398.232 \cdot \text{kip}$$

Load

$$\text{Check} := \begin{cases} \text{"OK"} & \text{if } F_{\text{nn2_back}} \geq S5 \\ \text{"NG"} & \text{otherwise} \end{cases}$$

Check = "OK"

Strut-to-Node Interface

$$w_{\text{int2}} := l_{b2} \cdot \sin(\phi_1) + h_{n2} \cdot \cos(\phi_1) = 14.197 \cdot \text{in}$$

Width of interface

$$v_2 := 0.45$$

Without crack control reinforcement

$$f_{\text{cen2}} := m \cdot v_2 \cdot f'_c = 2.824 \cdot \text{ksi}$$

$$F_{nn2_int} := f_{cen2} \cdot w_{int2} \cdot 2 \cdot 24in = 1.924 \times 10^3 \cdot kip \quad \text{Capacity}$$

$$S1 = 448.96 \cdot kip \quad \text{Load}$$

$$\text{Check} := \begin{cases} \text{"OK"} & \text{if } F_{nn2_int} \geq S1 \\ \text{"NG"} & \text{otherwise} \end{cases}$$

$$\text{Check} = \text{"OK"}$$

$$V1 = 207.307 \cdot kip \quad \text{Calculated shear}$$

$$V_{exp} = 668 \cdot kip$$

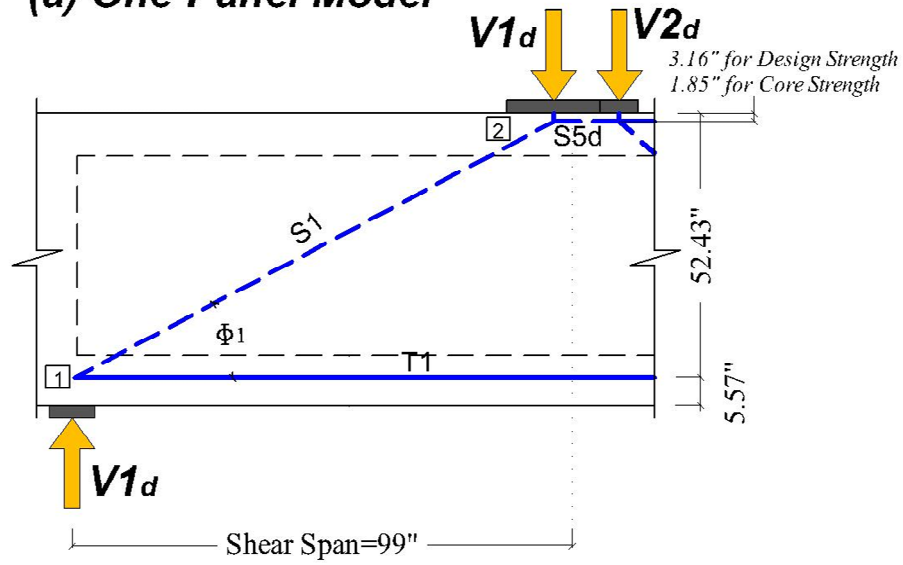
$$\frac{V_{exp}}{V1} = 3.222$$

The failure mode is strut failure (S1)

D.1.1.2 Combination Model

The combination model is superposition of a one-panel model and a two-panel model. Since members in the long span are not critical, a close-up of shear span of the beam is presented in **Figure D.7** for sake of brevity. This simplified presentation will be also utilized for the other four beams.

(a) One-Panel Model



(b) Two-Panel Model

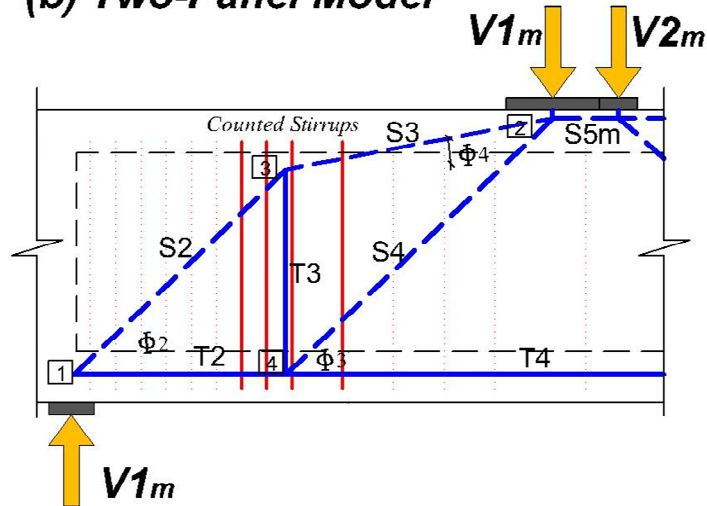


Figure D.7 Strut-and-tie model in the shear span (a) One-panel (b) Two-panel

AASHTO LRFD 2008

Assumed applied load

$$P_d := 150.1 \text{ kip} \quad \text{Load applied to the direct-strut model}$$

$$P_m := \frac{P_d}{2} = 75.05 \cdot \text{kip} \quad \text{Load applied to the multi-panel model}$$

$$P_d + P_m = 225.15 \cdot \text{kip} \quad \text{Total applied load}$$

After scaling...

$$T1 := P_d \cdot \frac{T_1}{1 \text{ kip}} = 206.547 \cdot \text{kip}$$

$$S1 := P_d \cdot \frac{S_1}{1 \text{ kip}} = 232.857 \cdot \text{kip}$$

$$S2 := P_m \cdot \frac{S_2}{1 \text{ kip}} = 77.169 \cdot \text{kip}$$

$$S3 := P_m \cdot \frac{S_3}{1 \text{ kip}} = 56.095 \cdot \text{kip}$$

$$S4 := P_m \cdot \frac{S_4}{1 \text{ kip}} = 65.54 \cdot \text{kip}$$

$$T2 := P_m \cdot \frac{T_2}{1 \text{ kip}} = 55.361 \cdot \text{kip}$$

$$T4 := P_m \cdot \frac{T_4}{\text{kip}} = 103.278 \cdot \text{kip}$$

$$S5 := \frac{P_d \cdot S_{5d} + P_m \cdot S_{5m}}{1 \text{ kip}} = 309.825 \text{ kip}$$

$$T3 := P_m \cdot \frac{T_3}{1 \text{ kip}} = 44.715 \cdot \text{kip}$$

Calculate the resultant of S1 and S2

$$S1_x := S1 \cdot \cos(\phi_1) = 206.547 \cdot \text{kip} \quad S1_y := S1 \cdot \sin(\phi_1) = 107.521 \cdot \text{kip}$$

$$S2_x := S2 \cdot \cos(\phi_2) = 55.361 \cdot \text{kip} \quad S2_y := S2 \cdot \sin(\phi_2) = 53.761 \cdot \text{kip}$$

$$S_{1_2} := \sqrt{(S1_x + S2_x)^2 + (S1_y + S2_y)^2} = 307.583 \cdot \text{kip}$$

$$\phi_{1_2} := \text{atan} \left(\frac{\lceil (S1_y + S2_y) \rceil}{\lfloor (S1_x + S2_x) \rfloor} \right) = 31.625 \cdot \text{deg}$$

Calculate the resultant of S1, S3, and S4

$$S3_x := S3 \cdot \cos(\phi_4) = 55.361 \cdot \text{kip} \quad S3_y := S3 \cdot \sin(\phi_4) = 9.046 \cdot \text{kip}$$

$$S4_x := S4 \cdot \cos(\phi_3) = 47.917 \cdot \text{kip} \quad S4_y := S4 \cdot \sin(\phi_3) = 44.715 \cdot \text{kip}$$

$$S_{1_3_4} := \sqrt{(S1_x + S3_x + S4_x)^2 + (S1_y + S3_y + S4_y)^2} = 349.29 \cdot \text{kip}$$

$$\phi_{1_3_4} := \text{atan} \left(\frac{\lceil (S1_y + S3_y + S4_y) \rceil}{\lfloor (S1_x + S3_x + S4_x) \rfloor} \right) = 27.5 \cdot \text{deg}$$

Start to check the strut-and-tie model

Tie 1 + Tie 2

Development length

$$\kappa := 1.6 \quad f_{pe} = 164.6 \cdot \text{ksi}$$

$$l_d := \kappa \cdot \frac{\left(f_{ps} - \frac{2}{3} \cdot f_{pe} \right) \cdot d_{bs}}{\text{ksi}} = 118.613 \cdot \text{in} \quad \text{AASHTO LRFD 5.11.4.2-1}$$

$$f(x) := \begin{cases} \frac{x}{60 \cdot d_{bs}} \cdot f_{pe} & \text{if } x < 60d_{bs} \\ f_{pe} + \frac{(x - 60d_{bs})}{(l_d - 60d_{bs})} \cdot (f_{ps} - f_{pe}) & \text{if } 60d_{bs} < x < l_d \\ f_{ps} & \text{otherwise} \end{cases}$$

Available Length

Stress in the strands

$$l_{a0} := 55 \cdot \text{in} \quad (\text{Figure D.8}) \quad f(l_{a0}) = 190.95 \cdot \text{ksi}$$

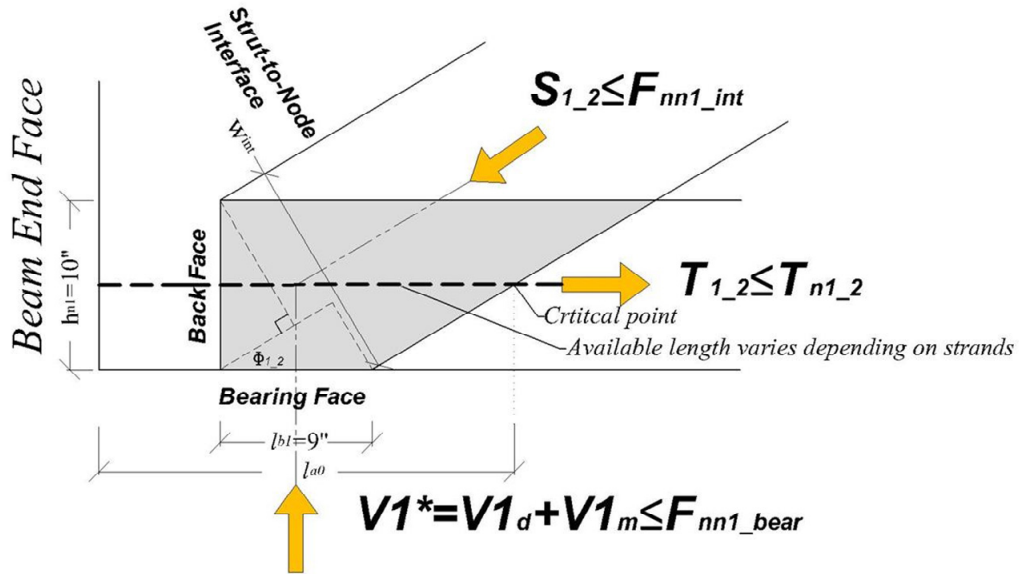


Figure D.8 Close-up of Node 1 of the combination model

$$l_{a3} := l_{a0} - 36\text{in} = 19\text{in} \quad f(l_{a3}) = 104.247\text{ksi}$$

$$T_{n1_2} := A_{\text{strand}} \cdot (n_0 \cdot f(l_{a0}) + n_3 \cdot f(l_{a3})) = 1.238 \times 10^3 \cdot \text{kip} \quad \text{Tie capacity}$$

$$T_{1_2} := \frac{P_d \cdot T_1 + P_m \cdot T_2}{1\text{kip}} = 261.908 \cdot \text{kip}$$

$$\text{Check} := \begin{cases} \text{"OK"} & \text{if } T_{n1_2} > T_{1_2} \\ \text{"NG"} & \text{otherwise} \end{cases}$$

Check = "OK"

Tie 1 + Tie 4

$$T_{1_4} := \frac{P_d \cdot T_1 + P_m \cdot T_4}{1\text{kip}} = 309.825 \cdot \text{kip} \quad \text{Load}$$

$$\text{Check} := \begin{cases} \text{"OK"} & \text{if } T_{n1_2} > T_{1_4} \\ \text{"NG"} & \text{otherwise} \end{cases}$$

Check = "OK"

$$S1 = 255.972 \cdot \text{kip}$$

Load

$$\text{Check} := \begin{cases} \text{"OK"} & \text{if } F_{mn1_int} \geq S1 \\ \text{"NG"} & \text{otherwise} \end{cases}$$

Check = "NG"

Node 2 CCC Node (Figure D.4)

$$\beta_{n2} := 0.85$$

Concrete efficiency factor per AASHTO LRFD 5.6.3.5

Top Bearing Plate

$$l_{b2} := 18.62 \text{ in}$$

Length of node 2 (part of length of bearing plate based on the proportion of load)

$$f_{cen2} := \beta_{n2} \cdot f_c = 4.938 \cdot \text{ksi}$$

Effective concrete stress

$$F_{nn2_bear} := f_{cen2} \cdot l_{b2} \cdot 24 \text{ in} \cdot 2 = 4.414 \times 10^3 \cdot \text{kip}$$

Capacity

$$V1 = 118.195 \cdot \text{kip}$$

Load

$$\text{Check} := \begin{cases} \text{"OK"} & \text{if } F_{nn2_bear} > V1 \\ \text{"NG"} & \text{otherwise} \end{cases}$$

Check = "OK"

Back Face

$$h_{n2} := 6.313 \text{ in}$$

Height of node 2

$$F_{nn2_back} := f_{cen2} \cdot h_{n2} \cdot 2 \cdot 24 \text{ in} = 1.496 \times 10^3 \cdot \text{kip}$$

Capacity

$$S5_d := \frac{P_d \cdot S5_d}{1 \text{ kip}} = 227.05 \cdot \text{kip}$$

Load

$$\text{Check} := \begin{cases} \text{"OK"} & \text{if } F_{nn2_back} \geq S5_d \\ \text{"NG"} & \text{otherwise} \end{cases}$$

Check = "OK"

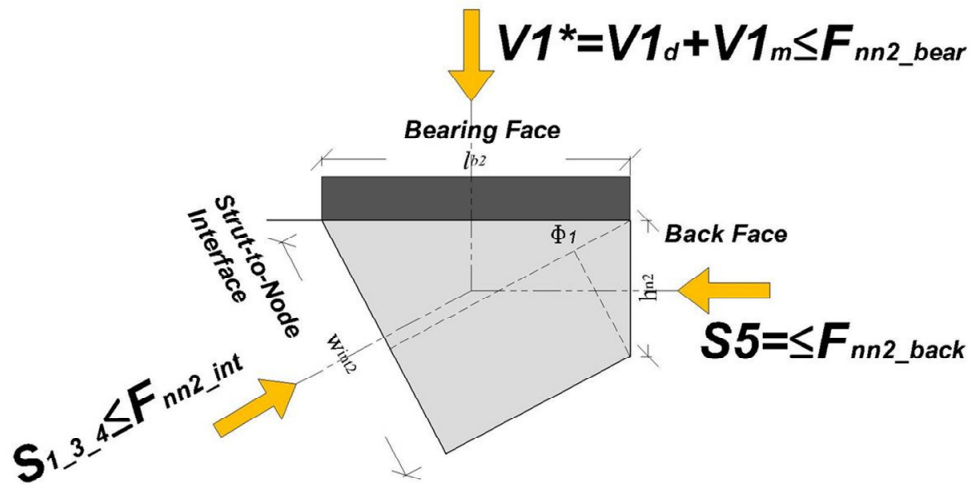


Figure D.9 Close-up of Node 2 of the combination model

$$S_{1_3_4} = 349.29 \cdot \text{kip}$$

Load

$$\text{Check} := \begin{cases} \text{"OK"} & \text{if } F_{nn2_int} \geq S_{1_3_4} \\ \text{"NG"} & \text{otherwise} \end{cases}$$

Check = "OK"

$$V1 = 161.282 \cdot \text{kip}$$

Calculated shear

$$V_{\text{exp}} = 668 \cdot \text{kip}$$

$$\frac{V_{\text{exp}}}{V1} = 4.142$$

The failure mode is strut failure

ACI 318-08**Assumed applied load**

$$P_d := 191.4 \text{ kip}$$

Load applied to the direct-strut model

$$P_m := \frac{P_d}{2} = 95.7 \text{ kip}$$

Load applied to the multi-panel model

$$P_d + P_m = 287.1 \text{ kip}$$

Total applied load

After scaling...

$$T1 := P_d \cdot \frac{T_1}{1 \text{ kip}} = 263.378 \cdot \text{kip}$$

$$S1 := P_d \cdot \frac{S_1}{1 \text{ kip}} = 296.928 \cdot \text{kip}$$

$$S2 := P_m \cdot \frac{S_2}{1 \text{ kip}} = 98.402 \cdot \text{kip}$$

$$S3 := P_m \cdot \frac{S_3}{1 \text{ kip}} = 71.529 \cdot \text{kip}$$

$$S4 := P_m \cdot \frac{S_4}{1 \text{ kip}} = 83.573 \cdot \text{kip}$$

$$T2 := P_m \cdot \frac{T_2}{1 \text{ kip}} = 70.593 \cdot \text{kip}$$

$$T4 := P_m \cdot \frac{T_4}{\text{kip}} = 131.695 \cdot \text{kip}$$

$$S5 := \frac{P_d \cdot S_{5d} + P_m \cdot S_{5m}}{1 \text{ kip}} = 395.073 \cdot \text{kip}$$

$$T3 := P_m \cdot \frac{T_3}{1 \text{ kip}} = 57.018 \cdot \text{kip}$$

Calculate the resultant of S1 and S2

$$S1_x := S1 \cdot \cos(\phi_1) = 263.378 \cdot \text{kip}$$

$$S1_y := S1 \cdot \sin(\phi_1) = 137.106 \cdot \text{kip}$$

$$S2_x := S2 \cdot \cos(\phi_2) = 70.593 \cdot \text{kip}$$

$$S2_y := S2 \cdot \sin(\phi_2) = 68.553 \cdot \text{kip}$$

Strut 1+Strut 2 (Figure D.8)

$$t_{s1} := 10\text{in}$$

The smallest thickness of the web

$$h_{n1} := 10\text{in}$$

Height of node 1

$$l_{b1} := 9\text{in}$$

Length of node 1
(bearing plate width)

$$w_{int1} := l_{b1} \cdot \sin(\phi_{1_2}) + h_{n1} \cdot \cos(\phi_{1_2}) = 13.234 \cdot \text{in}$$

Width of strut

$$F_{ns1_2} := 0.85 \cdot \beta_s \cdot f_c \cdot w_{int1} \cdot t_{s1} = 392.142 \cdot \text{kip}$$

Capacity of strut 1

$$S_{1_2} = 392.215 \cdot \text{kip}$$

Load

$$\text{Check} := \begin{cases} \text{"OK"} & \text{if } F_{ns1_2} \geq S_{1_2} \\ \text{"NG"} & \text{otherwise} \end{cases}$$

Check = "NG"

Strut 1 + Strut 3 + Strut 4 (Figure D.9)

$$h_{n2} := 6.313\text{in}$$

Height of node 2

$$l_{b2} := 18.62\text{in}$$

Length of bearing plate according to the
proportion of the applied load resisted by
near support

$$w_{int2} := l_{b2} \cdot \sin(\phi_{1_3_4}) + h_{n2} \cdot \cos(\phi_{1_3_4}) = 14.197 \cdot \text{in}$$

Width of strut

$$F_{ns1_3_4} := 0.85 \cdot \beta_s \cdot f_c \cdot w_{int2} \cdot 2 \cdot 24\text{in} = 2.019 \times 10^3 \cdot \text{kip}$$

Capacity of strut 1+3+4

$$S_{1_3_4} = 445.397 \cdot \text{kip}$$

Load

$$\text{Check} := \begin{cases} \text{"OK"} & \text{if } F_{ns1_3_4} \geq S_{1_3_4} \\ \text{"NG"} & \text{otherwise} \end{cases}$$

Check = "OK"

Tie 1 + Tie 2

Development Length of the strands

$$l_{ds} := \left(\frac{f_{pe}}{3000 \text{ psi}} \right) \cdot d_{bs} + \left(\frac{f_{ps} - f_{pe}}{1000 \cdot \text{psi}} \right) \cdot d_{bs} = 74.133 \cdot \text{in}$$

$$f(x) := \begin{cases} \frac{x}{\left(\frac{f_{pe}}{3000 \text{ psi}} \right) \cdot d_{bs}} \cdot f_{pe} & \text{if } x < \frac{f_{pe}}{3000 \text{ psi}} \cdot d_{bs} \\ f_{pe} + \frac{\left[x - \left(\frac{f_{pe}}{3000 \text{ psi}} \right) \cdot d_{bs} \right]}{\left[\left(\frac{f_{ps} - f_{pe}}{1000 \cdot \text{psi}} \right) \cdot d_{bs} \right]} \cdot (f_{ps} - f_{pe}) & \text{if } \frac{f_{pe}}{3000 \text{ psi}} \cdot d_{bs} < x < l_{ds} \\ f_{ps} & \text{otherwise} \end{cases}$$

Available Length

Stress in the strands

$$l_{a0} := 55 \text{ in} \quad (\text{Figure D.8})$$

$$f(l_{a0}) = 219.733 \cdot \text{ksi}$$

$$l_{a3} := l_{a0} - 36 \text{ in} = 19 \cdot \text{in}$$

$$f(l_{a3}) = 114 \cdot \text{ksi}$$

$$T_{n1_2} := A_{\text{strand}} \cdot (n_0 \cdot f(l_{a0}) + n_3 \cdot f(l_{a3})) = 1.417 \times 10^3 \cdot \text{kip}$$

Tie Capacity

$$T_{1_2} := \frac{P_d \cdot T_1 + P_m \cdot T_2}{1 \text{ kip}} = 333.971 \cdot \text{kip}$$

Load

$$\text{Check} := \begin{cases} \text{"OK"} & \text{if } T_{n1_2} > T_{1_2} \\ \text{"NG"} & \text{otherwise} \end{cases}$$

Check = "OK"

Tie 1 + Tie 4

$$T_{1_4} := \frac{P_d \cdot T_1 + P_m \cdot T_4}{1 \text{ kip}} = 395.073 \cdot \text{kip} \quad \text{Load}$$

$$\text{Check} := \begin{cases} \text{"OK"} & \text{if } T_{n1_2} > T_{1_4} \\ \text{"NG"} & \text{otherwise} \end{cases}$$

Check = "OK"

Tie 3

$$T_{n3} := 2 \cdot A_{4b} \cdot f_y = 96 \cdot \text{kip} \quad \text{Capacity}$$

$$T_3 = 57.018 \cdot \text{kip} \quad \text{Load}$$

$$\text{Check} := \begin{cases} \text{"OK"} & \text{if } T_{n3} > T_3 \\ \text{"NG"} & \text{otherwise} \end{cases}$$

Check = "OK"

Node 1 CCT Node (Figure D.8)

$$\beta_{n1} := 0.80 \quad \text{Concrete efficiency factor per ACI A.5.2}$$

Bearing Plate

$$A_1 := 32 \text{ in} \cdot 9 \text{ in} = 288 \cdot \text{in}^2 \quad \text{Area of bottom bearing plate}$$

$$f_{cen1} := 0.85 \cdot \beta_{n1} \cdot f_c = 3.951 \cdot \text{ksi} \quad \text{Effective concrete stress}$$

$$F_{nn1_bear} := f_{cen1} \cdot A_1 = 1.138 \times 10^3 \cdot \text{kip} \quad \text{Capacity}$$

$$V_1 := (P_d + P_m) \cdot \frac{(\text{Span} - a)}{\text{Span}} = 205.659 \cdot \text{kip} \quad \text{Load (V1*)}$$

$$\text{Check} := \begin{cases} \text{"OK"} & \text{if } F_{nn1_bear} \geq V_1 \\ \text{"NG"} & \text{otherwise} \end{cases}$$

Check = "OK"

Back Face

$h_{n1} = 10 \cdot \text{in}$	Height of node 1
$w_{b1} := 32 \text{in}$	Width of node 1 (bearing plate)
$F_{nn1_back} := f_{cen1} \cdot h_{n1} \cdot w_{b1} = 1.264 \times 10^3 \cdot \text{kip}$	Capacity
$T_{1_2} = 333.971 \cdot \text{kip}$	Load
Check := $\begin{cases} \text{"OK"} & \text{if } F_{nn1_back} \geq T_{1_2} \\ \text{"NG"} & \text{otherwise} \end{cases}$	

Check = "OK"

Strut-to-Node Interface

$l_{b1} = 9 \cdot \text{in}$	Width of node 1
$h_{n1} = 10 \cdot \text{in}$	Height of node 1
$t_{s1} = 10 \cdot \text{in}$	Minimum web thickness
$w_{int1} = 13.234 \text{ in}$	Width of interface
$F_{nn1_int} := f_{cen1} \cdot w_{int1} \cdot t_{s1} = 522.856 \cdot \text{kip}$	Capacity
$S_{1_2} = 392.215 \cdot \text{kip}$	Load
Check := $\begin{cases} \text{"OK"} & \text{if } F_{nn1_int} \geq S_{1_2} \\ \text{"NG"} & \text{otherwise} \end{cases}$	

Check = "OK"

Notice: F_{nn_int1} in Figure D.8 is F_{ns1_2} because F_{ns1_2} is smaller than F_{nn1_int} calculated above.

Node 2 CCC Node (Figure D.9)

$\beta_{n2} := 1.0$	Concrete efficiency factor per ACI A.5.2
---------------------	--

$$f_{\text{cen2}} := 0.85 \cdot \beta_{\text{n2}} \cdot f_c = 4.938 \cdot \text{ksi} \quad \text{Effective concrete strength}$$

Top Bearing Plate

$$F_{\text{nn2_bear}} := f_{\text{cen2}} \cdot 2l_{\text{b2}} \cdot 24\text{in} = 4.414 \times 10^3 \cdot \text{kip} \quad \text{Capacity}$$

$$V1 = 205.659 \cdot \text{kip} \quad \text{Load}$$

$$\text{Check} := \begin{cases} \text{"OK"} & \text{if } F_{\text{nn2_bear}} > V1 \\ \text{"NG"} & \text{otherwise} \end{cases}$$

Check = "OK"

Back Face

$$h_{\text{n2}} = 6.313 \cdot \text{in} \quad \text{Height of node 2}$$

$$F_{\text{nn2_back}} := f_{\text{cen2}} \cdot h_{\text{n2}} \cdot 2 \cdot 24\text{in} = 1.496 \times 10^3 \cdot \text{kip} \quad \text{Capacity}$$

$$S5 = 395.073 \cdot \text{kip} \quad \text{Load}$$

$$\text{Check} := \begin{cases} \text{"OK"} & \text{if } F_{\text{nn2_back}} \geq S5 \\ \text{"NG"} & \text{otherwise} \end{cases}$$

Check = "OK"

Strut-to-Node Interface

$$w_{\text{int2}} := l_{\text{b2}} \cdot \sin(\phi_{1_3_4}) + h_{\text{n2}} \cdot \cos(\phi_{1_3_4}) = 1 \cdot \text{in} \quad \text{Width of interface}$$

$$F_{\text{nn2_int}} := f_{\text{cen2}} \cdot w_{\text{int2}} \cdot 2 \cdot 24\text{in} = 3.365 \times 10^3 \cdot \text{kip} \quad \text{Capacity}$$

$$S_{1_3_4} = 445.397 \cdot \text{kip} \quad \text{Load}$$

$$\text{Check} := \begin{cases} \text{"OK"} & \text{if } F_{\text{nn2_int}} \geq S_{1_3_4} \\ \text{"NG"} & \text{otherwise} \end{cases}$$

Check = "OK"

Notice: F_{nn2_int} in Figure D.8 is $F_{ns1_3_4}$ because $F_{ns1_3_4}$ is smaller than F_{nn2_int} calculated above.

$$V1 = 205.659 \cdot \text{kip}$$

Calculated shear ($V1^*$)

$$V_{\text{exp}} = 668 \cdot \text{kip}$$

$$\frac{V_{\text{exp}}}{V1} = 3.248$$

The failure mode is strut failure

TxDOT Project 5253*Assumed applied load*

$$P_d := 222.4 \text{ kip} \quad \text{Load applied to the direct-strut model}$$

$$P_m := \frac{P_d}{2} = 111.2 \cdot \text{kip} \quad \text{Load applied to the multi-panel model}$$

$$P_d + P_m = 333.6 \cdot \text{kip} \quad \text{Total applied load}$$

After scaling... (Figure D,7)

$$T1 := P_d \cdot \frac{T_1}{1 \text{ kip}} = 306.036 \cdot \text{kip}$$

$$S1 := P_d \cdot \frac{S_1}{1 \text{ kip}} = 345.02 \cdot \text{kip}$$

$$S2 := P_m \cdot \frac{S_2}{1 \text{ kip}} = 114.339 \cdot \text{kip}$$

$$S3 := P_m \cdot \frac{S_3}{1 \text{ kip}} = 83.115 \cdot \text{kip}$$

$$S4 := P_m \cdot \frac{S_4}{1 \text{ kip}} = 97.109 \cdot \text{kip}$$

$$T2 := P_m \cdot \frac{T_2}{1 \text{ kip}} = 82.027 \cdot \text{kip}$$

$$T4 := P_m \cdot \frac{T_4}{\text{kip}} = 153.025 \cdot \text{kip}$$

$$S5 := \frac{P_d \cdot S_{5d} + P_m \cdot S_{5m}}{1 \text{ kip}} = 459.061 \cdot \text{kip}$$

$$T3 := P_m \cdot \frac{T_3}{1 \text{ kip}} = 66.253 \cdot \text{kip}$$

Calculate the resultant of S1 and S2 (Figure D.8)

$$S1_x := S1 \cdot \cos(\phi_1) = 306.036 \cdot \text{kip} \quad S1_y := S1 \cdot \sin(\phi_1) = 159.312 \cdot \text{kip}$$

$$S2_x := S2 \cdot \cos(\phi_2) = 82.027 \cdot \text{kip} \quad S2_y := S2 \cdot \sin(\phi_2) = 79.656 \cdot \text{kip}$$

$$S_{1_2} := \sqrt{(S1_x + S2_x)^2 + (S1_y + S2_y)^2} = 455.74 \cdot \text{kip}$$

$$\phi_{1_2} := \text{atan} \left(\frac{\lceil (S1_y + S2_y) \rceil}{\lfloor (S1_x + S2_x) \rfloor} \right) = 31.625 \cdot \text{deg}$$

Calculate the resultant of S1, S3, and S4 (Figure D.9)

$$S3_x := S3 \cdot \cos(\phi_4) = 82.027 \cdot \text{kip} \quad S3_y := S3 \cdot \sin(\phi_4) = 13.403 \cdot \text{kip}$$

$$S4_x := S4 \cdot \cos(\phi_3) = 70.998 \cdot \text{kip} \quad S4_y := S4 \cdot \sin(\phi_3) = 66.253 \cdot \text{kip}$$

$$S_{1_3_4} := \sqrt{(S1_x + S3_x + S4_x)^2 + (S1_y + S3_y + S4_y)^2} = 517.535 \cdot \text{kip}$$

$$\phi_{1_3_4} := \text{atan} \left(\frac{\lceil (S1_y + S3_y + S4_y) \rceil}{\lfloor (S1_x + S3_x + S4_x) \rfloor} \right) = 27.5 \cdot \text{deg}$$

Start to check the strut-and-tie model

Tie 1 + Tie 2

Development length

$$\kappa := 1.6 \quad f_{pe} = 164.6 \cdot \text{ksi}$$

$$l_d := \kappa \cdot \frac{\left(f_{ps} - \frac{2}{3} \cdot f_{pe} \right) \cdot d_{bs}}{\text{ksi}} = 118.613 \cdot \text{in} \quad \text{AASHTO LRFD 5.11.4.2-1}$$

$$f(x) := \begin{cases} \frac{x}{60 \cdot d_{bs}} \cdot f_{pe} & \text{if } x < 60d_{bs} \\ f_{pe} + \frac{(x - 60d_{bs})}{(l_d - 60d_{bs})} \cdot (f_{ps} - f_{pe}) & \text{if } 60d_{bs} < x < l_d \\ f_{ps} & \text{otherwise} \end{cases}$$

Available Length

Stress in the strands

$$l_{a0} := 55\text{in} \quad (\text{Figure D.8})$$

$$f(l_{a0}) = 190.95 \cdot \text{ksi}$$

$$l_{a3} := l_{a0} - 36\text{in} = 19\text{in}$$

$$f(l_{a3}) = 104.247 \cdot \text{ksi}$$

Tie capacity at the critical point

$$T_{n1_2} := A_{\text{strand}} \cdot (n_0 \cdot f(l_{a0}) + n_3 \cdot f(l_{a3})) = 1.238 \times 10^3 \cdot \text{kip}$$

$$T_{1_2} := \frac{P_d \cdot T_1 + P_m \cdot T_2}{1 \text{ kip}} = 388.063 \cdot \text{kip}$$

$$\text{Check} := \begin{cases} \text{"OK"} & \text{if } T_{n1_2} > T_{1_2} \\ \text{"NG"} & \text{otherwise} \end{cases}$$

Check = "OK"

Tie 1 + Tie 4

$$T_{1_4} := \frac{P_d \cdot T_1 + P_m \cdot T_4}{1 \text{ kip}} = 459.061 \cdot \text{kip} \quad \text{Load}$$

$$\text{Check} := \begin{cases} \text{"OK"} & \text{if } T_{n1_2} > T_{1_4} \\ \text{"NG"} & \text{otherwise} \end{cases}$$

Check = "OK"

Tie 3

$$T_{n3} := 2 \cdot 4 \cdot A_{4b} \cdot f_y = 96 \cdot \text{kip} \quad \text{Capacity}$$

$$T_3 = 66.253 \cdot \text{kip} \quad \text{Load}$$

$$\text{Check} := \begin{cases} \text{"OK"} & \text{if } T_{n3} > T_3 \\ \text{"NG"} & \text{otherwise} \end{cases}$$

Check = "OK"

Tie 3

$$T_{n3} := 2 \cdot 4 \cdot A_{4b} \cdot f_y = 96 \cdot \text{kip}$$

Capacity

$$T_3 = 66.253 \cdot \text{kip}$$

Load

$$\text{Check} := \begin{cases} \text{"OK"} & \text{if } T_{n3} > T_3 \\ \text{"NG"} & \text{otherwise} \end{cases}$$

Check = "OK"

Node 1 CCT Node (Figure D.8)

Bearing Plate

$$A_1 := 32 \text{ in} \cdot 9 \text{ in} = 288 \cdot \text{in}^2$$

Area of bottom bearing plate

$$A_2 := 13.63 \text{ in} \cdot 36.63 \text{ in} = 499.267 \cdot \text{in}^2$$

Projection of A_1 (Figure D.5)

$$v_1 := 0.70$$

Efficiency factor defined by Appendix A of
TxDOT Project 5253 (5.6.3.3.3)

$$m := \sqrt{\frac{A_2}{A_1}} = 1.317$$

Triaxial confinement factor

$$f_{cebl} := m \cdot v_1 \cdot f'_c = 5.355 \cdot \text{ksi}$$

Effective concrete stress

$$F_{nn1_bear} := f_{cebl} \cdot A_1 = 1.542 \times 10^3 \cdot \text{kip}$$

Capacity

$$V1 := (P_d + P_m) \cdot \frac{(\text{Span} - a)}{\text{Span}} = 238.968 \cdot \text{kip}$$

Load (V1*)

$$\text{Check} := \begin{cases} \text{"OK"} & \text{if } F_{nn1_bear} \geq V1 \\ \text{"NG"} & \text{otherwise} \end{cases}$$

Check = "OK"

Back Face

Back face is not necessary to be checked because of the bonding condition.

Strut-to-Node Interface

$l_{b1} := 9\text{in}$ Width of node 1 bearing plate

$h_{n1} := 10\text{in}$ Minimum web thickness

$w_{int2} := l_{b1} \cdot \sin(\phi_{1_2}) + h_{n1} \cdot \cos(\phi_{1_2}) = 13.234 \cdot \text{in}$ Width of interface

$t_{s1_2} := 10\text{in}$ Minimum thickness

$s := 10\text{in}$ Spacing of stirrup

$\rho_h := 0$ Steel ratio in the horizontal direction

$$v_1 := \begin{cases} 0.45 & \text{if } 2 \cdot \frac{A_{4b}}{h_{n1} \cdot s} < 0.003 \\ \left(0.85 - \frac{f_c}{20\text{ksi}} \right) & \text{otherwise} \end{cases} \vee \rho_h < 0.003$$

$v_1 = 0.45$ Without crack control reinforcement

$f_{ce1_2} := m \cdot v_1 \cdot f_c = 3.442 \cdot \text{ksi}$

$F_{nint1_2} := f_{ce1_2} \cdot t_{s1_2} \cdot w_{int2} = 455.571 \cdot \text{kip}$ Capacity

$S_{1_2} = 455.74 \cdot \text{kip}$ Load

Check := $\begin{cases} \text{"OK"} & \text{if } F_{nint1_2} \geq S_{1_2} \\ \text{"NG"} & \text{otherwise} \end{cases}$

Check = "NG"

Node 2 CCC Node (Figure D.9)

Top Bearing Plate

$$A_1 := 26\text{in} \cdot 24\text{in} = 624 \cdot \text{in}^2$$

Area of top bearing plate

$$A_2 := 26\text{in} \cdot 28\text{in} = 728 \cdot \text{in}^2$$

Projection of A_1 (Figure D.6)

$$m := \sqrt{\frac{A_2}{A_1}} = 1.08$$

Triaxial confinement factor

$$v_2 := 0.85$$

Concrete efficiency factor

$$l_{b2} := 18.62\text{in}$$

Length of bearing plate according to the proportion of the applied load resisted by near support

$$f_{\text{cen2}} := m \cdot v_2 \cdot f_c = 5.334 \cdot \text{ksi}$$

Effective concrete stress

$$F_{\text{nn2_bear}} := m \cdot f_{\text{cen2}} \cdot l_{b2} \cdot 24\text{in} \cdot 2 = 5.149 \times 10^3 \cdot \text{kip}$$

Capacity

$$V1 = 238.968 \cdot \text{kip}$$

Load

$$\text{Check} := \begin{cases} \text{"OK"} & \text{if } F_{\text{nn2_bear}} > V1 \\ \text{"NG"} & \text{otherwise} \end{cases}$$

Check = "OK"

Back Face

$$h_{n2} := 6.313\text{in}$$

Height of node 2

$$F_{\text{nn2_back}} := f_{\text{cen2}} \cdot h_{n2} \cdot 2 \cdot 24\text{in} = 1.616 \times 10^3 \cdot \text{kip}$$

Capacity

$$S5 = 459.061 \cdot \text{kip}$$

Load

$$\text{Check} := \begin{cases} \text{"OK"} & \text{if } F_{\text{nn2_back}} \geq S5 \\ \text{"NG"} & \text{otherwise} \end{cases}$$

Check = "OK"

Strut-to-Node Interface

$$w_{int2} := l_{b2} \cdot \sin(\phi_{1_3_4}) + h_{n2} \cdot \cos(\phi_{1_3_4}) = 14.197 \cdot \text{in}$$

Width of interface

$$v_2 := 0.45$$

Without crack control reinforcement

$$f_{cen2} := m \cdot v_2 \cdot f'_c = 2.824 \cdot \text{ksi}$$

$$F_{nn2_int} := f_{cen2} \cdot w_{int2} \cdot 2824 \text{ in} = 1.132 \times 10^5 \cdot \text{kip}$$

Capacity

$$S_{1_3_4} = 517.535 \cdot \text{kip}$$

Load

$$\text{Check} := \begin{cases} \text{"OK"} & \text{if } F_{nn2_int} \geq S_{1_3_4} \\ \text{"NG"} & \text{otherwise} \end{cases}$$

Check = "OK"

$$V_1 = 238.968 \cdot \text{kip}$$

Calculated shear (V1*)

$$V_{exp} = 668 \cdot \text{kip}$$

$$\frac{V_{exp}}{V_1} = 2.795$$

The failure mode is strut failure

D.1.2 Core Strength

The critical element in these strut-and-tie models is either the strut-to-node interface of Node 1 or the vertical tie (T3). Therefore, for sake of brevity, only checking for these two parts is tabulated in Table for both design and core strength. Other non-critical elements are omitted in the following sections.

D.1.2.1 One-Panel Model

Table D.1 Member forces in the one panel model (RF-3R-9-A)

RF-3R-9-A One-Panel Model (Figure D.7(a))						
	Design Strength = 5.81 ksi			Core Strength/0.85 = 10.07 ksi		
	AASHTO	ACI 318	5253	AASHTO	ACI 318	5253
$\Phi 1$ (deg.)	27.5	27.5	27.5	28.1	28.1	28.1
V_{1d} (kips)	118	178	207	187	316	368
V_{2d} (kips)	47	71	82	74	126	146
S_1 (kips)	256	386	449	397	671	780
T_1 (kips)	227	343	398	350	592	688
S_{5d} (kips)	227	343	398	350	592	688

Table D.2 Node 1 check (RF-3R-9-A)

RF-3R-9-A Node 1 in One-Panel Model (Figure D.3)						
	Design Strength = 5.81 ksi			Core Strength/0.85 = 10.07 ksi		
	AASHTO	ACI 318	5253	AASHTO	ACI 318	5253
$\Phi 1$ (deg)	27.5	27.5	27.5	28.1	28.1	28.1
w_{int1} (in.)	13.03	13.03	13.03	13.06	13.06	13.06
l_{a0} (in.)	56	56	56	56	56	56
V_{1d} (kips)	118	178	207	187	316	368
F_{nn1_bear} (kips)	1255	1138	1542	2175	1972	2673
S_1 (kips)	256	386	449	396	671	780
F_{nn1_int} (kips)	256	386	449	396	671	780
T_1 (kips)	227	343	398	350	592	807
T_{n1} (kips)	1251	1436	1251	1252	1436	1252

D.1.2.2 Combination Model

Table D.3 Member forces in the combination model (RF-3R-9-A)

RF-3R-9-A Combination Model						
	Design Strength = 5.81 ksi			Core Strength/0.85 = 10.07 ksi $f_y=69$ ksi		
	AASHTO	ACI 318	5253	AASHTO	ACI 318	5253
One-Panel Model (Figure D.7(a))						
$\Phi 1$ (deg)	27.5	27.5	27.5	28.1	28.1	28.1
V_{1d} (kips)	107	137	159	167	242	275
V_{2d} (kips)	43	54	63	66	96	109
S_1 (kips)	233	297	345	353	513	584
T_1 (kips)	207	263	306	312	452	515
S_{5d} (kips)	207	263	306	312	452	515
Two-Panel Model (Figure D.7(b))						
$\Phi 2$ (deg)	44.2	44.2	44.2	44.2	44.2	44.2
$\Phi 3$ (deg)	43	43	43	43.8	43.8	43.8
$\Phi 4$ (deg)	9.3	9.3	9.3	10.7	10.7	10.7
V_{1m} (kips)	54	69	80	83	121	138
V_{2m} (kips)	21	27	31	33	48	54
S_2 (kips)	77	98	114	120	174	197
S_3 (kips)	56	72	83	87	127	144
S_4 (kips)	66	84	97	97	141	160
S_{5m} (kips)	103	132	153	156	226	257
T_2 (kips)	55	71	82	86	124	141
T_3 (kips)	45	57	66	67	97	111
T_4 (kips)	103	132	153	156	226	257

Table D.4 Node 1 and T3 check (RF-3R-9-A)

RF-3R-9-A Node 1 in Combination Model (Figure D.8)						
	Design Strength = 5.81 ksi			Core Strength/0.85 = 10.07 ksi $f_y = 69$ ksi		
	AASHTO	ACI 318	5253	AASHTO	ACI 318	5253
Φ_{1_2} (deg)	31.6	31.6	31.6	32.2	32.2	32.2
l_{a0} (in.)	55	55	55	55	55	55
w_{int1} (in.)	13.23	13.23	13.23	13.26	13.26	13.26
$V1^*$ (kips)	161	206	239	250	363	413
F_{nn1_bear} (kips)	1255	1138	1542	2175	1972	2673
S_{1_2} (kips)	307	392	456	469	681	775
F_{nn1_int} (kips)	307	392	456	469	681	791
T_{1_2} (kips)	262	334	388	397	577	656
T_{n1_2} (kips)	1238	1417	1238	1239	1417	1239
RF-3R-9-A Vertical Tie (T3) in Two-Panel Model						
T3 (kips)	45	57	66	67	97	110
T_{n3} (kips)	96	96	96	110	110	110
Failure	S_{1+2}	S_{1+2}	S_{1+2}	S_{1+2}	S_{1+2}	T3

D.2 RF-3R-9-C

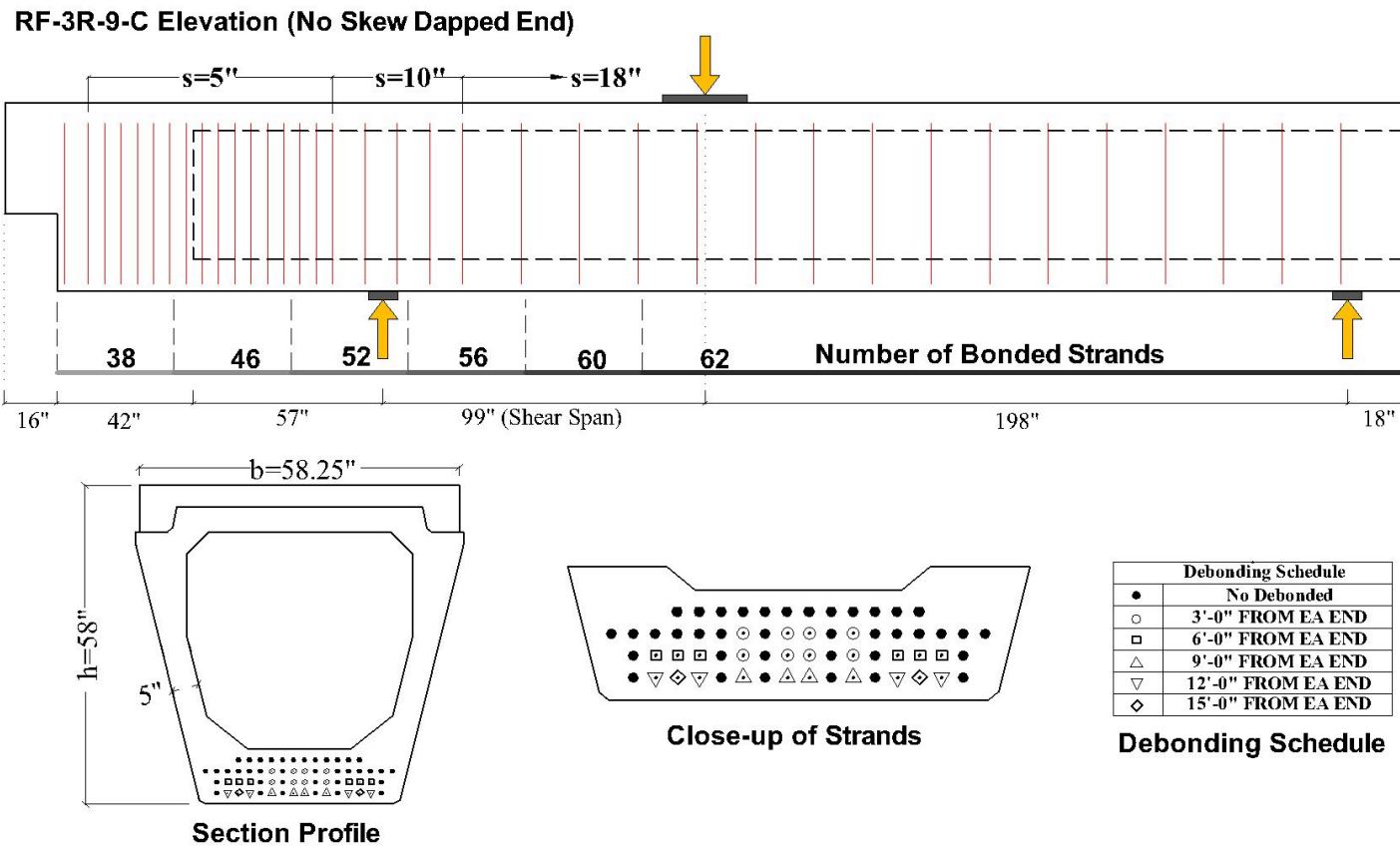
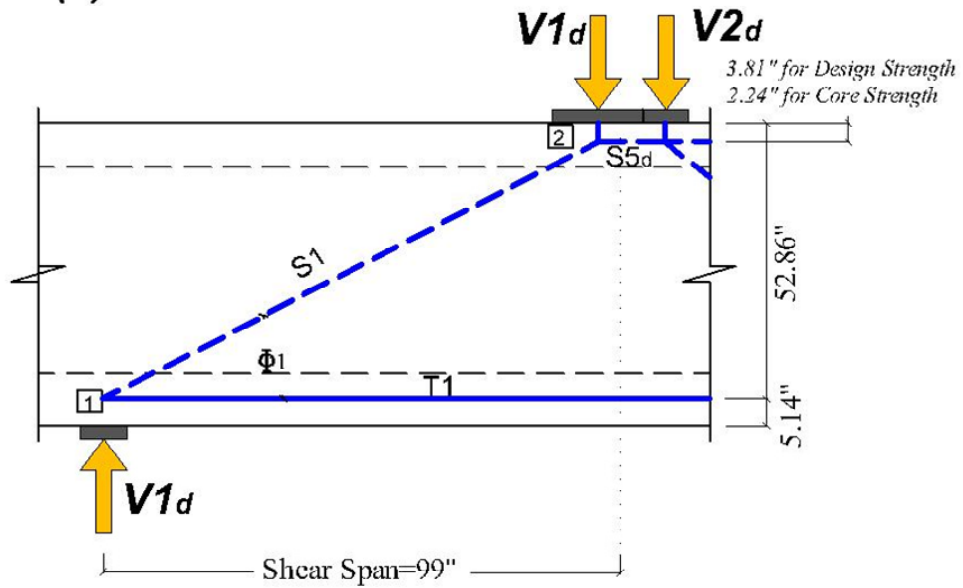


Figure D.10 RF-3R-9-C Elevation, section, and debonding schedule

(a) One-Panel Model



(b) Two-Panel Model

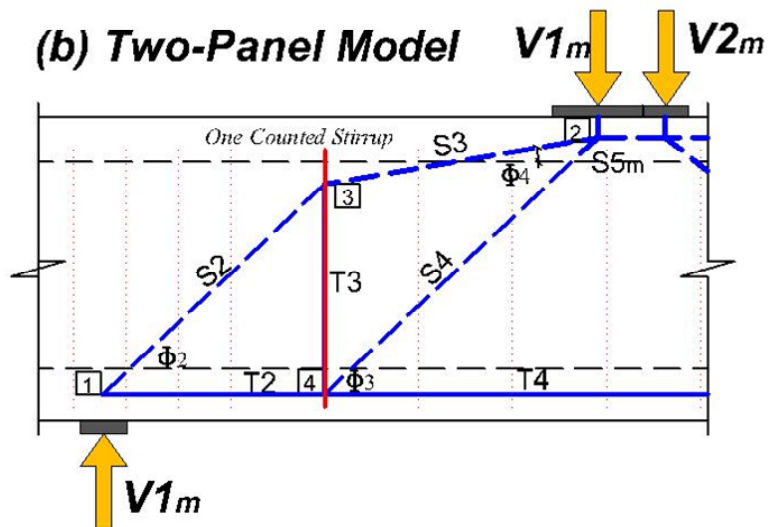


Figure D.11 RF-3R-9-C Strut-and-tie model in the shear span (a) One-panel (b) Two-panel

D.2.1 One-Panel Model

Table D.5 Member forces in the one panel model (RF-3R-9-C)

RF-3R-9-C One-Panel Model (Figure D.11(a))						
	Design Strength = 5.81 ksi			Core Strength/0.85 = 10.07 ksi		
	AASHTO	ACI 318	5253	AASHTO	ACI 318	5253
$\Phi 1$ (deg.)	27.4	27.4	27.4	28.1	28.1	28.1
V_{1d} (kips)	123	178	207	197	316	368
V_{2d} (kips)	61	89	103	99	159	183
S_1 (kips)	267	386	449	419	671	779
T_1 (kips)	237	343	398	369	592	687
S_{5d} (kips)	237	343	398	369	592	687

Table D.6 Node 1 check (RF-3R-9-C)

RF-3R-9-C Node 1 in One-Panel Model (Figure D.3)						
	Design Strength = 5.81 ksi			Core Strength/0.85 = 10.07 ksi		
	AASHTO	ACI 318	5253	AASHTO	ACI 318	5253
$\Phi 1$ (deg)	27.4	27.4	27.4	28.1	28.1	28.1
w_{int1} (in.)	13.02	13.02	13.02	13.06	13.06	13.06
l_{a0} (in.)	113	113	113	113	113	113
V_{1d} (kips)	123	178	207	197	316	368
F_{nn1_bear} (kips)	1255	1138	1542	2175	1972	2673
S_1 (kips)	267	386	449	419	671	779
F_{nn1_int} (kips)	267	386	449	419	671	779
T_1 (kips)	237	343	398	369	592	687
T_{n1} (kips)	1904	1996	1904	1908	2024	1906

D.2.2 Combination Model

Table D.7 Member forces in the combination model (RF-3R-9-C)

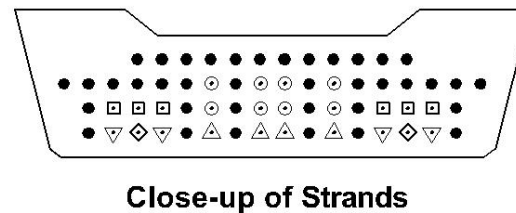
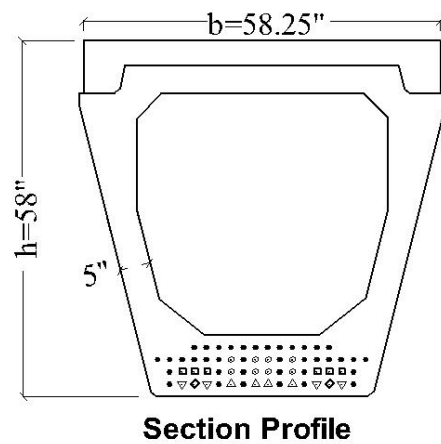
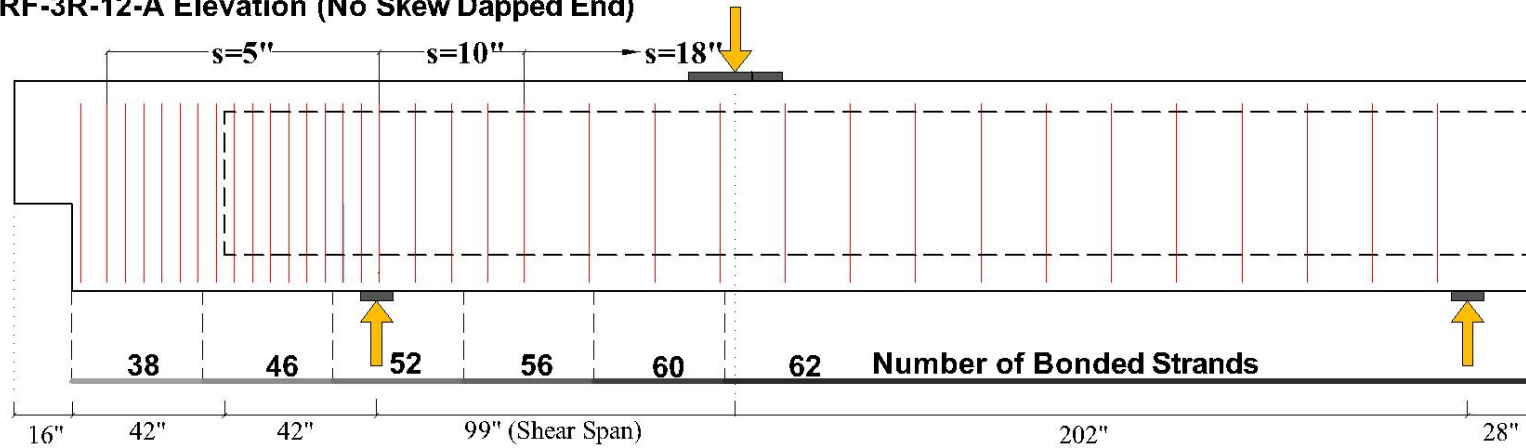
RF-3R-9-C Combination Model						
	Design Strength = 5.81 ksi			Core Strength/0.85 =10.07 ksi $f_y=69$ ksi		
	AASHTO	ACI 318	5253	AASHTO	ACI 318	5253
One-Panel Model (Figure D.11(a))						
$\Phi 1$ (deg)	27.4	27.4	27.4	28.1	28.1	28.1
$V1_d$ (kips)	59	59	59	70	70	70
$V2_d$ (kips)	29	29	29	36	36	36
$S1$ (kips)	127	127	127	149	149	149
$T1$ (kips)	113	113	113	132	132	132
$S5d$ (kips)	113	113	113	132	132	132
Two-Panel Model (Figure D.11(b))						
$\Phi 2$ (deg)	43.5	43.5	43.5	43.5	43.5	43.5
$\Phi 3$ (deg)	43.2	43.2	43.2	44.1	44.1	44.1
$\Phi 4$ (deg)	9.8	9.8	9.8	11.4	11.4	11.4
$V1_m$ (kips)	29	29	29	36	36	36
$V2_m$ (kips)	15	15	15	18	18	18
$S2$ (kips)	43	43	43	51	51	51
$S3$ (kips)	31	31	31	38	38	38
$S4$ (kips)	35	35	35	40	40	40
$S5m$ (kips)	57	57	57	66	66	66
$T2$ (kips)	31	31	31	37	37	37
$T3$ (kips)	24	24	24	28	28	28
$T4$ (kips)	57	57	57	66	66	66

Table D.8 Node 1 and T3 check (RF-3R-9-C)

RF-3R-9-C Node 1 in Combination Model (Figure D.8)						
	Design Strength = 5.81 ksi			Core Strength/0.85 =10.07 ksi $f_y=69$ ksi		
	AASHTO	ACI 318	5253	AASHTO	ACI 318	5253
Φ_{1_2} (deg)	31.4	31.4	31.4	32.0	32.0	32.0
l_{a0} (in.)	113	113	113	113	113	113
w_{int1} (in.)	13.23	13.23	13.23	13.25	13.25	13.25
$V1^*$ (kips)	88	88	88	106	106	106
F_{nn1_bear} (kips)	1255	1138	1542	2175	1972	2673
S_{1_2} (kips)	169	169	169	199	199	199
F_{nn1_int} (kips)	319	392	455	493	681	791
T_{1_2} (kips)	144	144	144	169	169	169
T_{n1_2} (kips)	1904	1996	1904	1908	2024	1908
RF-3R-9-C Vertical Tie (T3) in Two-Panel Model						
T3 (kips)	24	24	24	28	28	28
T_{n3} (kips)	24	24	24	28	28	28
Failure	T3	T3	T3	T3	T3	T3

D.3 RF-3R-12-A

RF-3R-12-A Elevation (No Skew Dapped End)



Debonding Schedule	
●	No Debonded
○	3'-0" FROM EA END
□	6'-0" FROM EA END
△	9'-0" FROM EA END
▽	12'-0" FROM EA END
◇	15'-0" FROM EA END

Debonding Schedule

Figure D.12 RF-3R-12-A Elevation, section, and debonding schedule

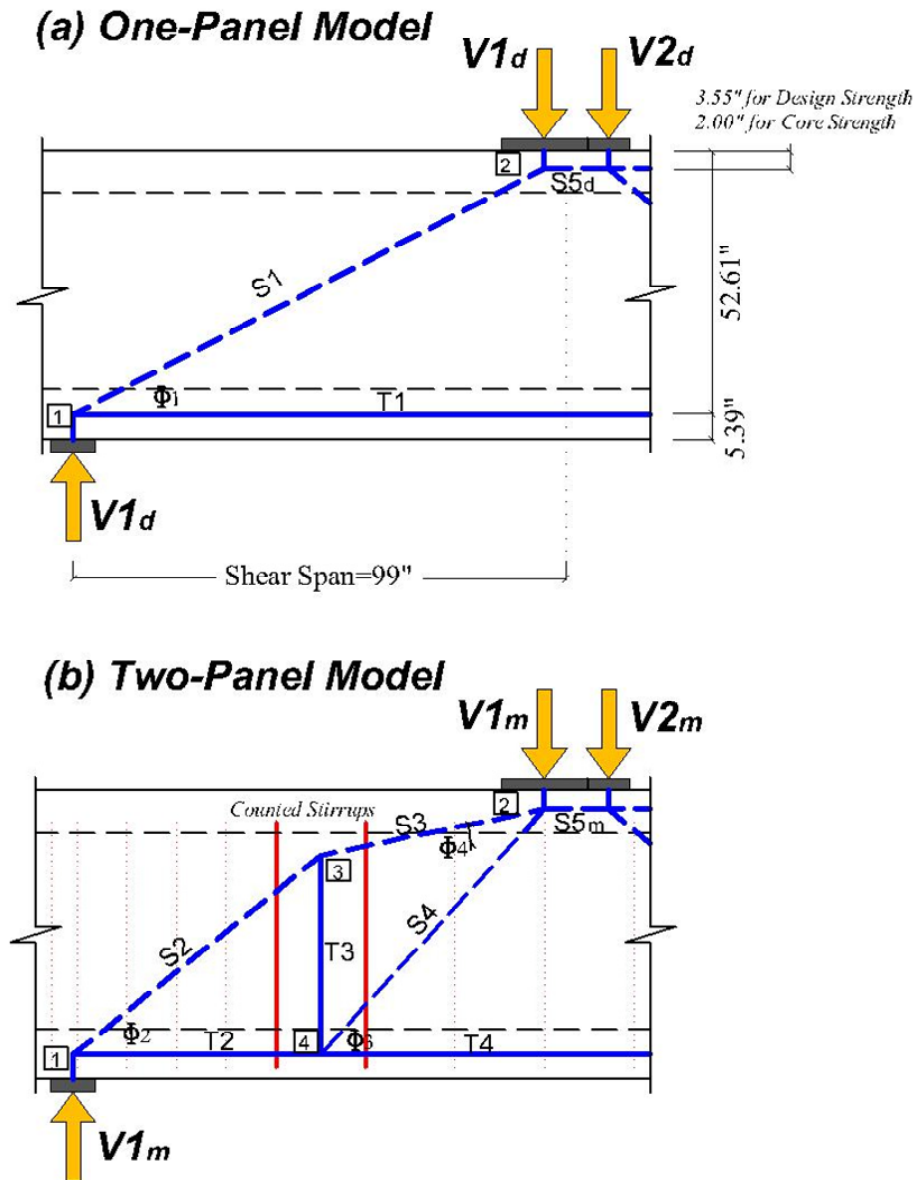


Figure D.13 RF-3R-12-A Strut-and-tie model in the shear span (a) One-panel (b) Two-panel

D.3.1 One-Panel Model

Table D.9 Member forces in the one panel model (RF-3R-12-A)

RF-3R-12-A One-Panel Model (Figure D.13(a))						
	Design Strength = 5.81 ksi			Core Strength/0.85 = 10.51 ksi		
	AASHTO	ACI 318	5253	AASHTO	ACI 318	5253
$\Phi 1$ (deg.)	27.6	27.6	27.6	28.3	28.3	28.3
V_{1d} (kips)	122	179	208	202	332	386
V_{2d} (kips)	60	87	101	99	163	189
S_1 (kips)	264	386	449	426	700	814
T_1 (kips)	234	342	398	375	617	717
S_{5d} (kips)	234	342	398	375	617	717

Table D.10 Node 1 check (RF-3R-12-A)

RF-3R-12-A Node 1 in One-Panel Model (Figure D.3)						
	Design Strength = 5.81 ksi			Core Strength/0.85 = 10.51 ksi		
	AASHTO	ACI 318	5253	AASHTO	ACI 318	5253
$\Phi 1$ (deg)	27.6	27.6	27.6	28.3	28.3	28.3
w_{int1} (in.)	13.03	13.03	13.03	13.07	13.07	13.07
l_{a0} (in.)	98	98	98	98	98	98
V_{1d} (kips)	122	179	208	202	332	386
F_{nn1_bear} (kips)	1255	1138	1542	2269	2057	2789
S_1 (kips)	264	386	449	426	700	814
F_{nn1_int} (kips)	264	386	449	426	700	814
T_1 (kips)	234	342	398	375	617	717
T_{n1} (kips)	1747	1923	1747	1747	1923	1744

D.3.2 Combination Model

Table D.11 Member forces in the combination model (RF-3R-12-A)

RF-3R-12-A Combination Model						
	Design Strength = 5.81 ksi			Core Strength/0.85 = 10.51 ksi $f_y=69$ ksi		
	AASHTO	ACI 318	5253	AASHTO	ACI 318	5253
One-Panel Model (Figure D.13(a))						
$\Phi 1$ (deg)	27.6	27.6	27.6	28.3	28.3	28.3
$V1_d$ (kips)	103	129	129	158	158	158
$V2_d$ (kips)	49	64	64	77	77	77
$S1$ (kips)	223	280	280	333	333	333
$T1$ (kips)	198	248	248	293	293	293
$S5d$ (kips)	198	248	248	293	293	293
Two-Panel Model (Figure D.13(b))						
$\Phi 2$ (deg)	38.9	38.9	38.9	38.9	38.9	38.9
$\Phi 3$ (deg)	47.7	47.7	47.7	48.6	48.6	48.6
$\Phi 4$ (deg)	11.7	11.7	11.7	13.6	13.6	13.6
$V1_m$ (kips)	52	65	65	79	79	79
$V2_m$ (kips)	25	31	31	39	39	39
$S2$ (kips)	82	103	103	126	126	126
$S3$ (kips)	66	82	82	101	101	101
$S4$ (kips)	52	65	65	74	74	74
$S5m$ (kips)	99	124	124	147	147	147
$T2$ (kips)	64	80	80	98	98	98
$T3$ (kips)	38	48	48	55	55	55
$T4$ (kips)	99	124	124	147	147	147

Table D.12 Node 1 and T3 check (RF-3R-12-A)

RF-3R-12-A Node 1 in Combination Model (Figure D.13(a)&(b))						
	Design Strength = 5.81 ksi			Core Strength/0.85 = 10.51 ksi $f_y=69$ ksi		
	AASHTO	ACI 318	5253	AASHTO	ACI 318	5253
Φ_{1_2} (deg)	30.6	30.6	30.6	31.2	31.2	31.2
l_{a0} (in.)	97	97	97	96	96	96
w_{int1} (in.)	13.19	13.19	13.19	13.22	13.22	13.22
$V1^*$ (kips)	155	194	194	237	237	237
F_{nn1_bear} (kips)	1255	1138	1542	2269	2057	2789
S_{1_2} (kips)	304	381	381	457	457	457
F_{nn1_int} (kips)	304	391	454	482	708	823
T_{1_2} (kips)	262	328	328	391	391	391
T_{n1_2} (kips)	1734	1916	1734	1725	1931	1725
RF-3R-12-A Vertical Tie (T3) in Two-Panel Model						
T3 (kips)	38	48	48	55	55	55
T_{n3} (kips)	48	48	48	55	55	55
Failure	S_{1+2}	T3	T3	T3	T3	T3

D.4 MLL-9-34-A

MLL-9-34-A Elevation (Skew Dapped End)

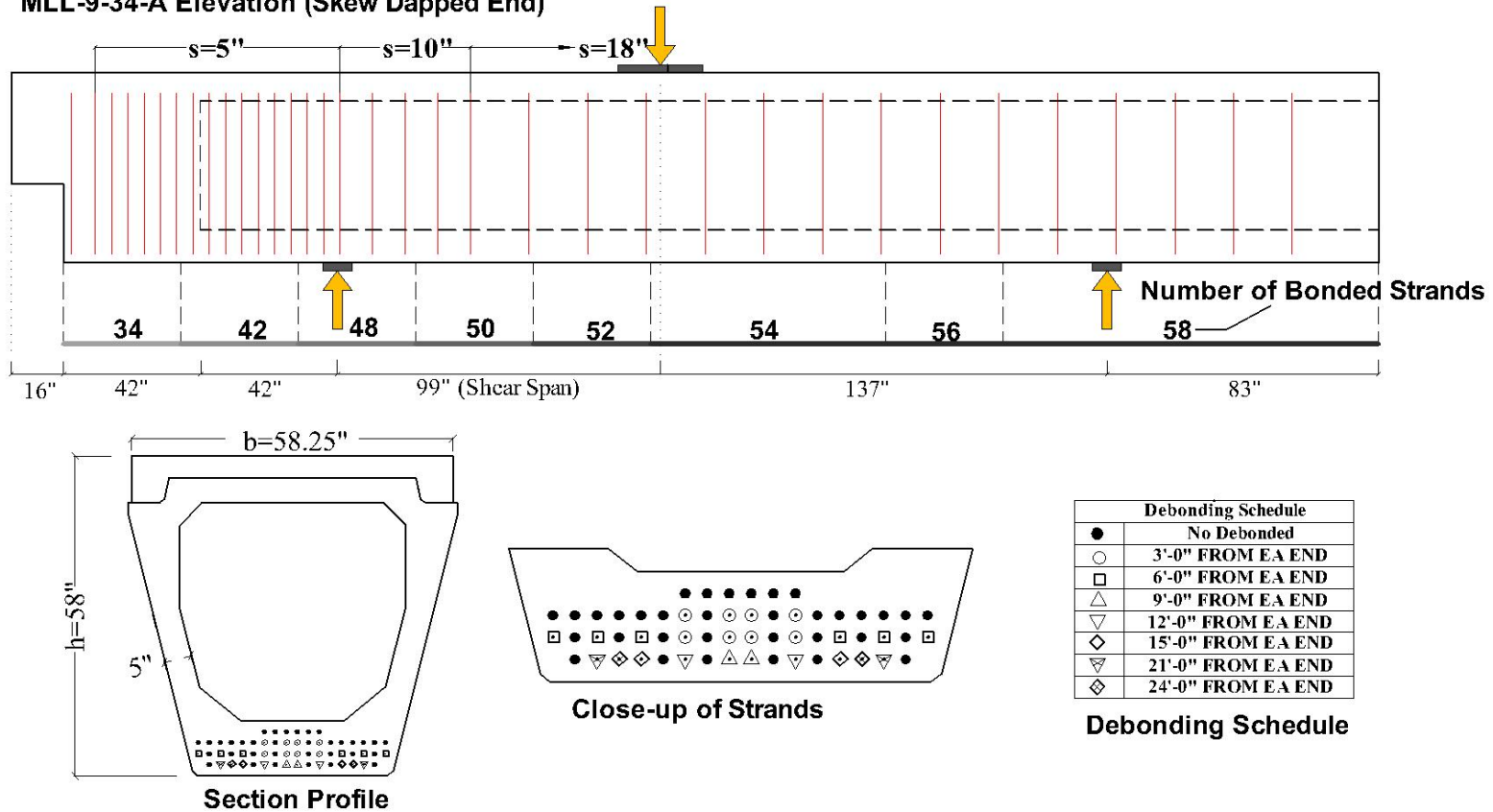


Figure D.14 MLL-9-34-A Elevation, section, and debonding schedule

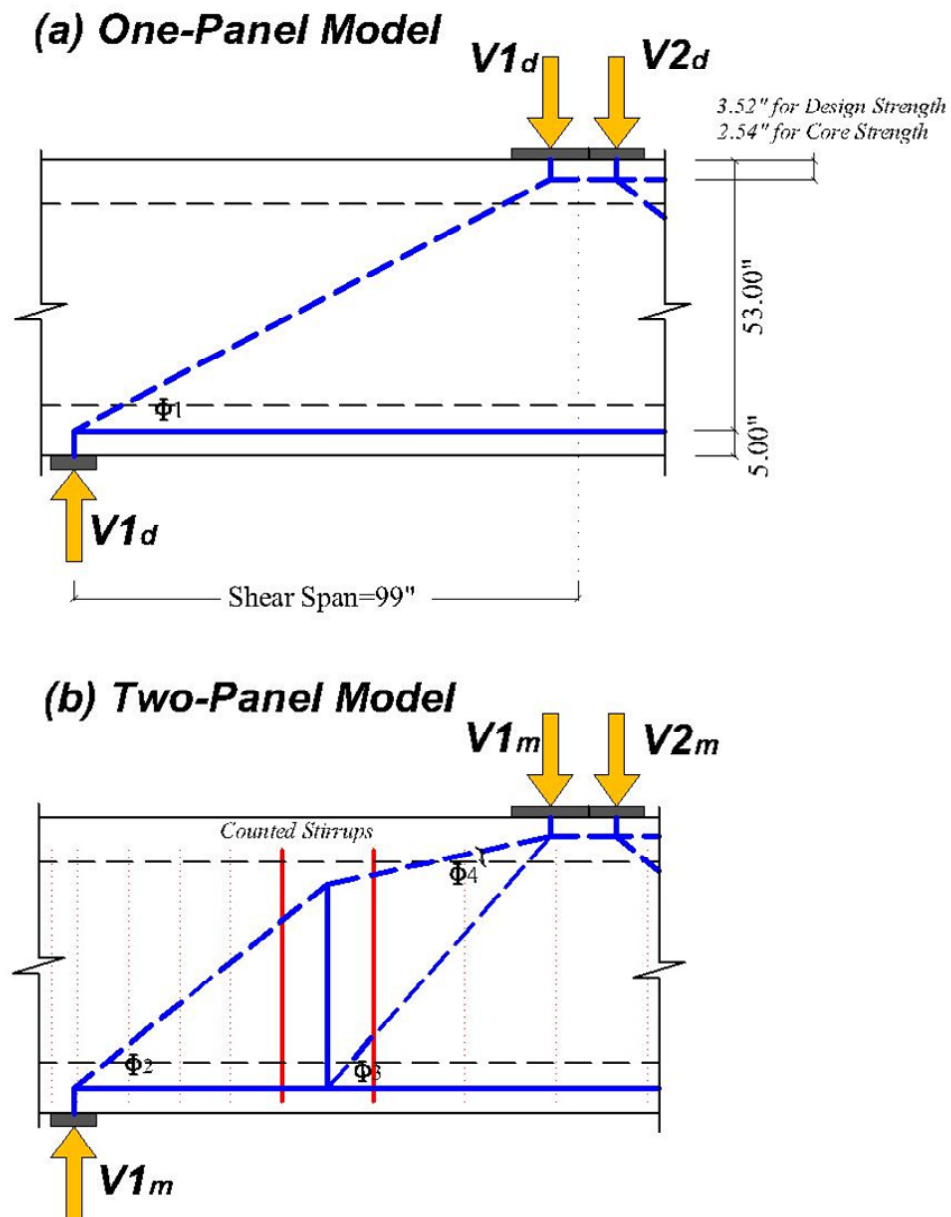


Figure D.15 RF-3R-12-A Strut-and-tie model in the shear span (a) One-panel (b) Two-panel

D.4.1 One-Panel Model

Table D.13 Member forces in the one panel model (MLL-9-34-A)

MLL-9-34-A One-Panel Model (Figure D.15(a))						
	Design Strength = 5.42 ksi			Core Strength/0.85 = 7.57 ksi		
	AASHTO	ACI 318	5253	AASHTO	ACI 318	5253
$\Phi 1$ (deg.)	27.9	27.9	27.9	28.3	28.3	28.3
V_{1d} (kips)	117	169	196	156	239	278
V_{2d} (kips)	84	122	145	113	174	201
S_1 (kips)	250	361	419	329	504	586
T_1 (kips)	221	319	371	289	444	516
S_{5d} (kips)	221	319	371	289	444	516

Table D.14 Node 1 check (MLL-9-34-A)

MLL-9-34-A Node 1 in One-Panel Model (Figure D.3)						
	Design Strength = 5.42 ksi			Core Strength/0.85 = 7.57 ksi		
	AASHTO	ACI 318	5253	AASHTO	ACI 318	5253
$\Phi 1$ (deg)	27.9	27.9	27.9	28.3	28.3	28.3
w_{int1} (in.)	13.05	13.05	13.05	13.07	13.07	13.07
l_{a0} (in.)	98	98	98	98	98	98
V_{1d} (kips)	117	169	196	156	239	278
F_{nn1_bear} (kips)	1171	1061	1438	1634	1481	2008
S_1 (kips)	250	361	419	329	504	586
F_{nn1_int} (kips)	250	361	419	329	504	586
T_1 (kips)	221	319	371	289	444	516
T_{n1} (kips)	1584	1763	1584	1585	1774	1585

D.4.2 Combination Model

Table D.15 Member forces in the combination model (MLL-9-34-A)

MLL-9-34-A Combination Model						
	Design Strength = 5.42 ksi			Core Strength/0.85 = 7.57 ksi $f_y=69$ ksi		
	AASHTO	ACI 318	5253	AASHTO	ACI 318	5253
One-Panel Model (Figure D.15(a))						
$\Phi 1$ (deg)	27.9	27.9	27.9	28.3	28.3	28.3
$V1_d$ (kips)	98	125	131	129	157	157
$V2_d$ (kips)	70	90	94	93	114	114
$S1$ (kips)	209	267	280	271	335	330
$T1$ (kips)	184	236	247	239	296	290
$S5d$ (kips)	184	236	247	239	296	290
Two-Panel Model (Figure D.15(b))						
$\Phi 2$ (deg)	38.9	38.9	38.9	38.9	38.9	38.9
$\Phi 3$ (deg)	48.5	48.5	48.5	49.0	49.0	49.0
$\Phi 4$ (deg)	12.1	12.1	12.1	13.3	13.3	13.3
$V1_m$ (kips)	48	62	65	64	78	78
$V2_m$ (kips)	36	46	47	47	57	57
$S2$ (kips)	78	99	104	103	125	125
$S3$ (kips)	62	79	83	82	100	100
$S4$ (kips)	48	61	64	60	73	73
$S5m$ (kips)	92	118	124	119	145	145
$T2$ (kips)	60	77	81	80	97	97
$T3$ (kips)	36	46	48	46	55	55
$T4$ (kips)	92	118	124	119	145	145

Table D.16 Node 1 and T3 check (MLL-9-34-A)

MLL-9-34-A Node 1 in Combination Model (Figure D.8)						
	Design Strength = 5.42 ksi			Core Strength/0.85 = 7.57 ksi $f_y=69$ ksi		
	AASHTO	ACI 318	5253	AASHTO	ACI 318	5253
Φ_{1_2} (deg)	30.9	30.9	30.9	31.2	30.9	31.2
l_{a0} (in.)	96	96	96	96	96	96
w_{int1} (in.)	13.20	13.20	13.20	13.22	13.2	13.22
$V1^*$ (kips)	146	187	196	193	235	235
F_{nn1_bear} (kips)	1171	1061	1438	1634	1481	2008
S_{1_2} (kips)	285	365	382	373	453	453
F_{nn1_int} (kips)	285	365	424	373	509	592
T_{1_2} (kips)	245	313	328	319	393	387
T_{n1_2} (kips)	1560	1748	1560	1562	1748	1562
MLL-9-34-A Vertical Tie (T3) in Two-Panel Model						
T3 (kips)	36	46	48	46	55	55
T_{n3} (kips)	48	48	48	55	55	55
Failure	S_{1+2}	S_{1+2}	T3	S_{1+2}	T3	T3

D.5 RF-1R-C

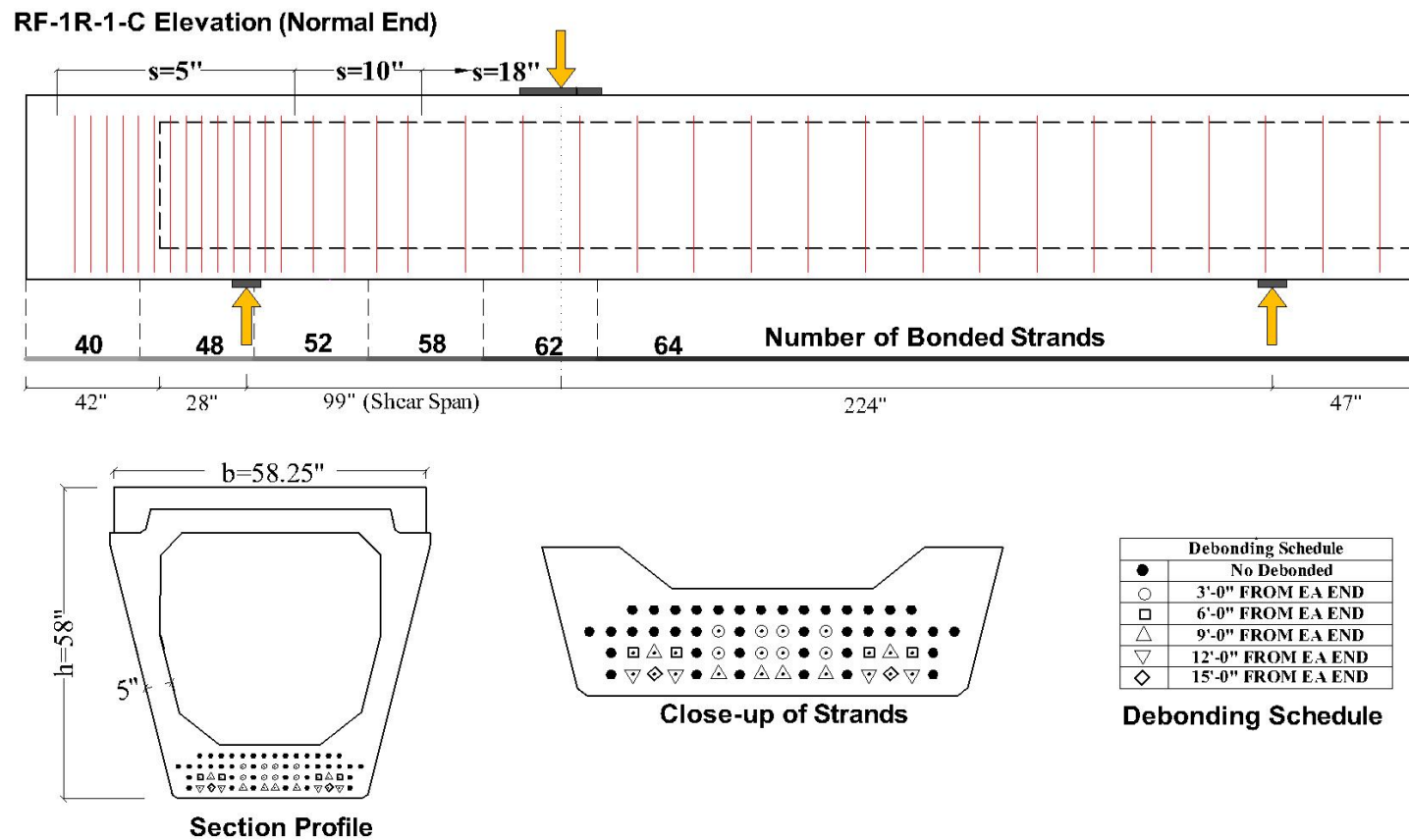


Figure D.16 RF-1R-1-C Elevation, section, and debonding schedule

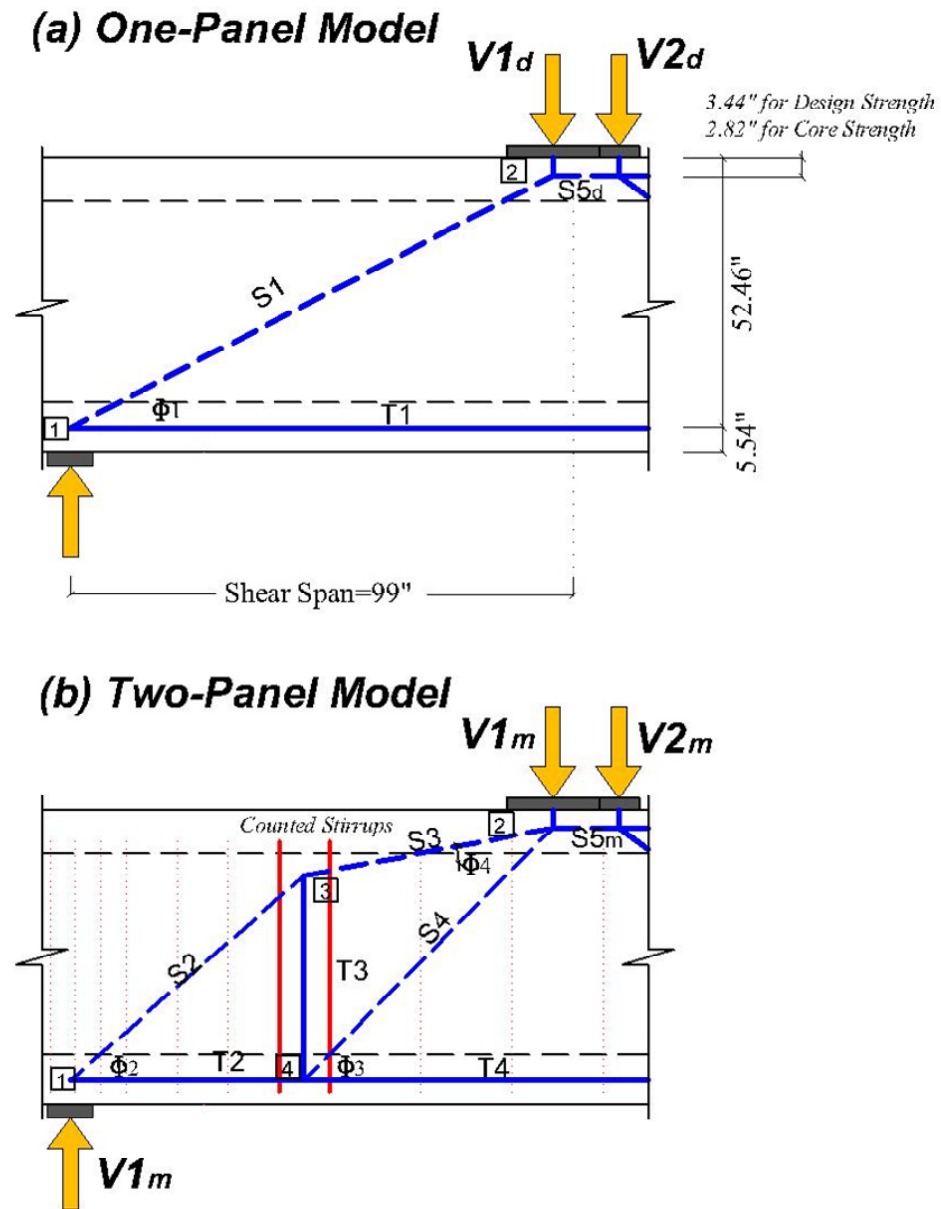


Figure D.17 RF-3R-12-A Strut-and-tie model in the shear span (a) One-panel (b) Two-panel

D.5.1 One-Panel Model

Table D.17 Member forces in the one panel model (RF-1R-1-C)

RF-1R-1-C One-Panel Model (Figure D.17(a))						
	Design Strength = 5.99 ksi			Core Strength/0.85 = 7.34 ksi		
	AASHTO	ACI 318	5253	AASHTO	ACI 318	5253
$\Phi 1$ (deg)	27.6	27.6	27.6	27.8	27.8	27.8
V_{1d} (kips)	125	184	214	150	228	265
V_{2d} (kips)	56	82	95	66	101	117
S_1 (kips)	271	398	463	320	489	568
T_1 (kips)	240	353	410	283	432	502
S_{5d} (kips)	240	353	410	283	432	502

Table D.18 Node 1 check (RF-1R-1-C)

RF-1R-1-C Node 1 in One-Panel Model (Figure D.3)						
	Design Strength = 5.99 ksi			Core Strength/0.85 = 7.34 ksi		
	AASHTO	ACI 318	5253	AASHTO	ACI 318	5253
$\Phi 1$ (deg)	27.6	27.6	27.6	27.8	27.8	27.8
w_{int1} (in.)	13.03	13.03	13.03	13.05	13.05	13.05
l_{a0} (in.)	84	84	84	84	84	84
V_{1d} (kips)	125	184	214	150	228	265
F_{nn1_bear} (kips)	1294	1173	1590	1586	1438	1949
S_1 (kips)	270	398	463	320	489	568
F_{nn1_int} (kips)	270	398	463	320	489	568
T_1 (kips)	240	353	410	283	432	502
T_{n1} (kips)	1619	1862	1619	1620	1862	1620

D.5.2 Combination Model

Table D.19 Member forces in the combination model (RF-1R-1-C)

RF-1R-1-C Combination Model						
	Design Strength = 5.99 ksi			Core Strength/0.85 = 7.34 ksi $f_y=69$ ksi		
	AASHTO	ACI 318	5253	AASHTO	ACI 318	5253
One-Panel Model (Figure D.17(a))						
$\Phi 1$ (deg)	27.6	27.6	27.6	27.8	27.8	27.8
$V1_d$ (kips)	109	123	123	129	145	145
$V2_d$ (kips)	48	55	55	57	64	64
$S1$ (kips)	235	267	267	277	310	310
$T1$ (kips)	209	236	236	245	274	274
$S5d$ (kips)	209	236	236	245	274	274
Two-Panel Model (Figure D.17(b))						
$\Phi 2$ (deg)	41.1	41.1	41.1	41.1	41.1	41.1
$\Phi 3$ (deg)	45.3	45.3	45.3	45.7	45.7	45.7
$\Phi 4$ (deg)	10.9	10.9	10.9	11.6	11.6	11.6
$V1_m$ (kips)	54	62	62	65	72	72
$V2_m$ (kips)	25	27	27	28	32	32
$S2$ (kips)	83	94	94	98	110	110
$S3$ (kips)	64	72	72	76	85	85
$S4$ (kips)	60	68	68	69	77	77
$S5m$ (kips)	104	118	118	122	137	137
$T2$ (kips)	62	71	71	74	83	83
$T3$ (kips)	42	48	48	49	55	55
$T4$ (kips)	104	118	118	122	137	137

Table D.20 Node 1 and T3 check (RF-1R-1-C)

RF-1R-1-C Node 1 in Combination Model (Figure D.8)						
	Design Strength = 5.99 ksi			Core Strength/0.85 = 7.34 ksi $f_y=69$ ksi		
	AASHTO	ACI 318	5253	AASHTO	ACI 318	5253
Φ_{1_2} (deg)	31.1	31.1	31.1	31.3	31.3	31.3
l_{a0} (in.)	82	82	82	82	82	82
w_{int1} (in.)	13.21	13.21	13.21	13.22	13.22	13.22
$V1^*$ (kips)	163	185	185	194	217	217
F_{nn1_bear} (kips)	1294	1173	1590	1586	1438	1949
S_{1_2} (kips)	317	359	359	373	417	417
F_{nn1_int} (kips)	317	403	469	373	495	575
T_{1_2} (kips)	271	307	307	319	356	310
T_{n1_2} (kips)	1597	1856	1597	1597	1862	1597
RF-1R-1-C Vertical Tie (T3) in Two-Panel Model						
T3 (kips)	42	48	48	49	55	55
T_{n3} (kips)	48	48	48	55	55	55
Failure	S_{1+2}	T3	T3	T3	T3	T3

APPENDIX E

Petrographic Analysis

03/30/2010

Report:	UT ASR DEF
Date Received:	03/3/2010
Structure Type:	Unknown
Sample Type:	Core
Location:	Unknown
Coarse Aggregate Producer:	NA
Coarse Aggregate Type:	Crushed Limestone
Fine Aggregate Producer:	NA
Fine Aggregate Type:	Siliceous Sand
Cement Producer:	NA
Cement Type:	NA
Comments:	

This petrographic analysis was performed in response to a request from Caroline Herrera, P.E., (CST/Soils and Aggregates Branch Director) to assist the University of Texas in an ASR/DEF investigation of nine submitted cores. The following objectives were specified by UT:

- General observations on concrete quality. (Comments on placement, mixture proportions, water-cement ratio).
- Visual documentation of ASR and/or DEF micro structural damage. (Images depicting gel/ettringite locations, cracking and gapping of paste/aggregate interfaces).
- Qualitative study of damage severity in each sample. (Comparison of micro structural damage between all samples).
- Qualitative study of damage progression through the length of the sample. (Comparison of micro structural damage in surface and core concretes of each sample).

General observations on concrete quality (comments on placement, mixture proportions, water-cement ratio)

General Appearance: Nine cores were submitted for analysis and were designated as: P1, P2, P3, P4, P5, P6, P7, P8 and P9. The submitted cores were 3-3/4 inch in diameter and ranged from 7.5 to 13 inches in length. Cores P1, P2, P5, P7, P8 and P9 had obvious distress cracks on the surface of the core.

Water/Cement Ratio: None of the cores had abnormal or elevated w-c ratio. Cores P1, P2 and P3 had a slightly lower w-c ratio than the remaining cores. In order to estimate w-c ratio, a mix design plus a standard job site cylinder would have been required.

Proportioning and types of aggregate: Without a batch design we could not determine if excesses or deficiencies exist between the point count data and the theoretical values from the batch design. Based on point count data the paste volume indicate a high sack mix. Coarse aggregate consist of crushed limestone and a small percentage of chert. Fine aggregate consist of quartz, agate, feldspar, carbonates, sandstone and chert. The following table summarizes the point count data:

Core ID	Paste Volume	FA Volume	CA Volume	% Entrapped Air	% Entrained Air
P1	26.61	27.01	42.29	3.03	0.92
P2	28.59	27.14	40.45	2.24	1.58
P3	28.07	34.82	34.68	1.10	1.21
P4	29.42	31.71	36.3	1.21	0.81
P5	26.28	22.1	49.73	0.81	0.81
P6	30.09	31.31	34.82	2.16	1.08
P7	33.42	29.92	35.44	0.67	0.40
P8	28.3	32.27	38.28	0.38	0.51
P9	29.69	31.98	36.57	0.27	1.21

Paste content and appearance: Paste content is indicative of a high sack mix and appearance is normal except for the numerous fine micro cracking observed in the cores. No fly ash or other mineral admixtures were present in the mix.

Air Content: Non-Air Entrained.

Degree of Hydration: Normal.

Carbonation: Carbonation was noted at the exterior surface of all the cores. The following chart represents the depth of carbonation for each core:

Core ID	Carbonation Depth From Exterior Surface of Core	Carbonation Depth Observed Along Surface Crack
P1	1/16"	1/8"
P2	3/32"	NA
P3	3/32	5/8"
P4	3/16	7/16"
P5	1/32"	3/4"
P6	1/8"	NA
P7	3/16"	3/8"
P8	1/8"	3/16"
P9	3/16"	NA

Deleterious Reaction Mechanism: All cores have suffered significant distress from ASR. The primary ASR aggregate type is a microcrystalline chert fine aggregate. Ettringite was observed filling most of the micro crack generated by ASR distress. Ettringite was also noted in many of the air voids and in some discrete nests within the paste. The occurrence of gapping around aggregates due to paste expansion (DEF) was limited. Complete gapping of the aggregates was only observed in a minor amount of the particles. It is inconclusive whether DEF has contributed to the distress based on the limited amount of true gapping due to paste expansion.

Microscopic documentation of ASR and/or DEF micro structural damage.

(Images depicting ASR gel/ettringite formation, cracking and gapping at paste/aggregate interfaces)

ASR Related Evidence

Image of Core P5 illustrating ASR distress cracking from eactive fine aggregate.

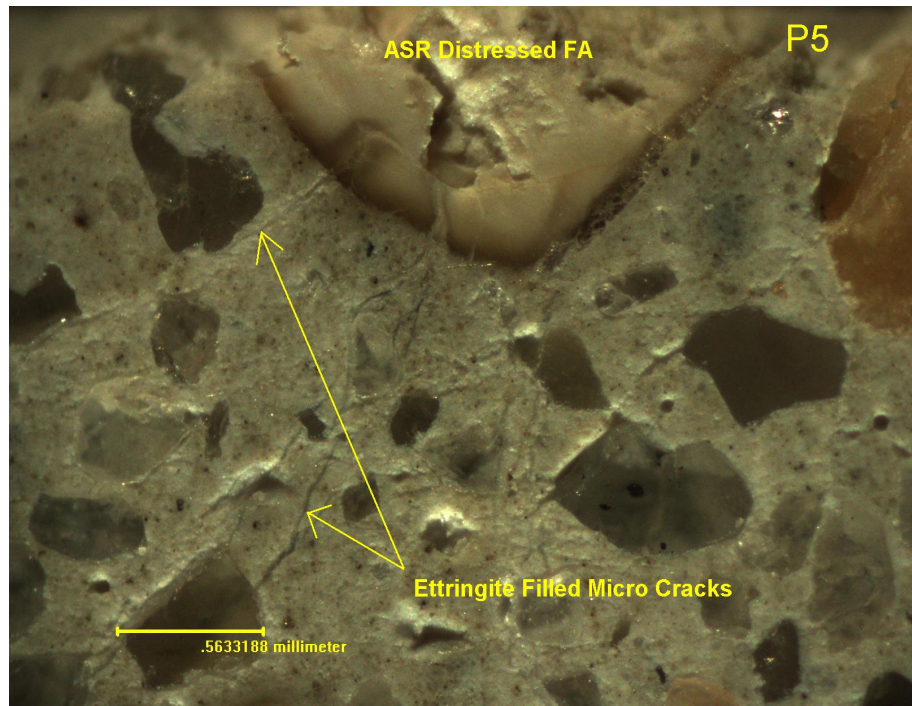


image illustrating ettringite filled gap surrounding fine aggregate

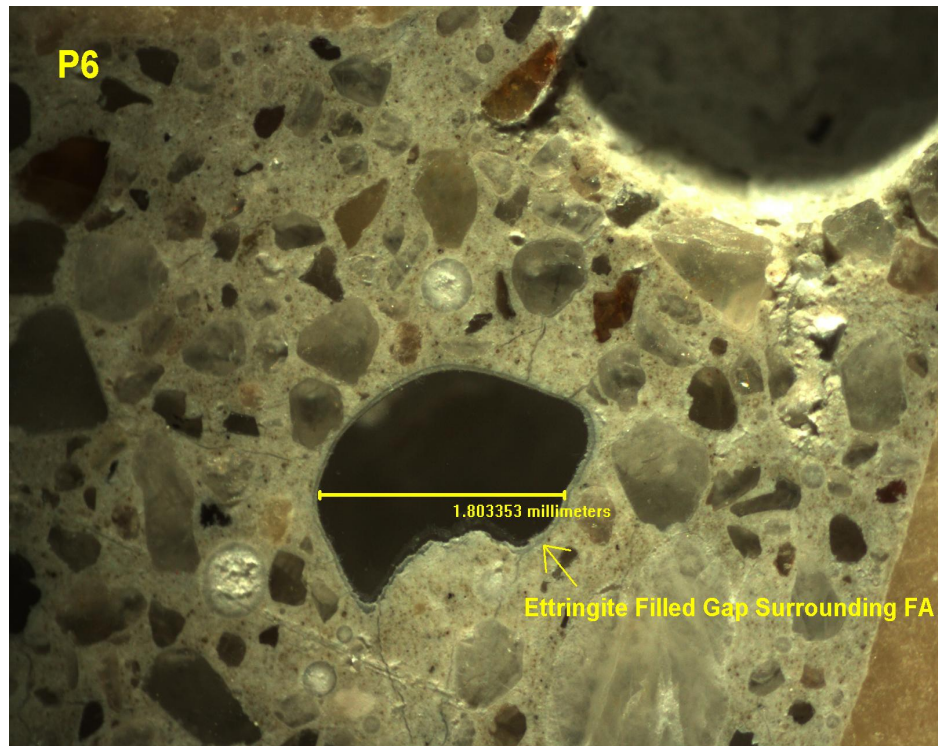


Image illustrating highly distress fine aggregate

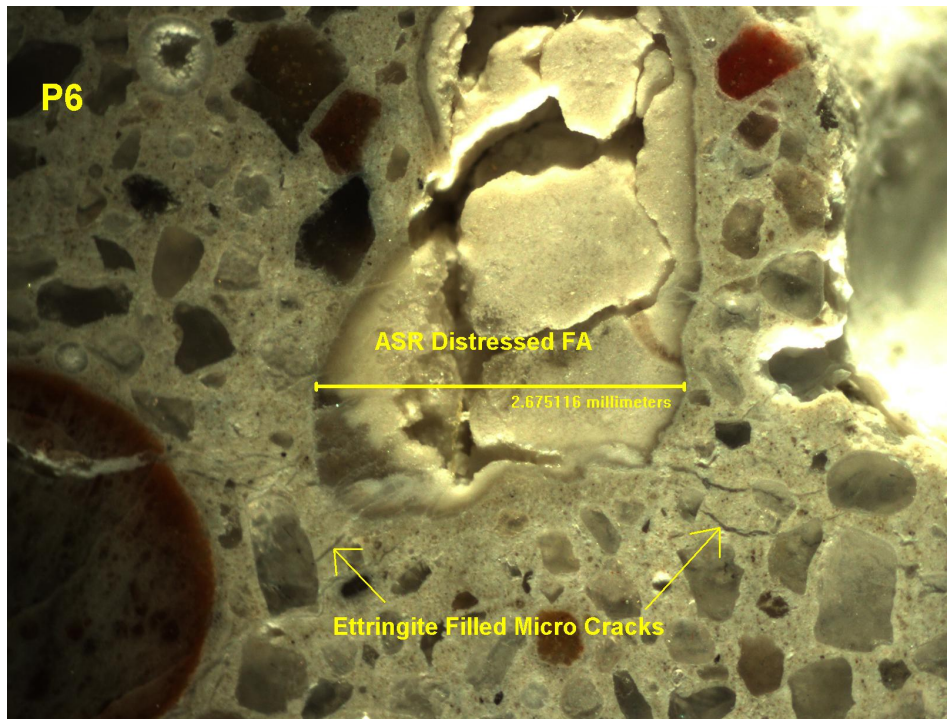


Image illustrating fine network of ettringite filled micro cracks and ASR distressed fine aggregate

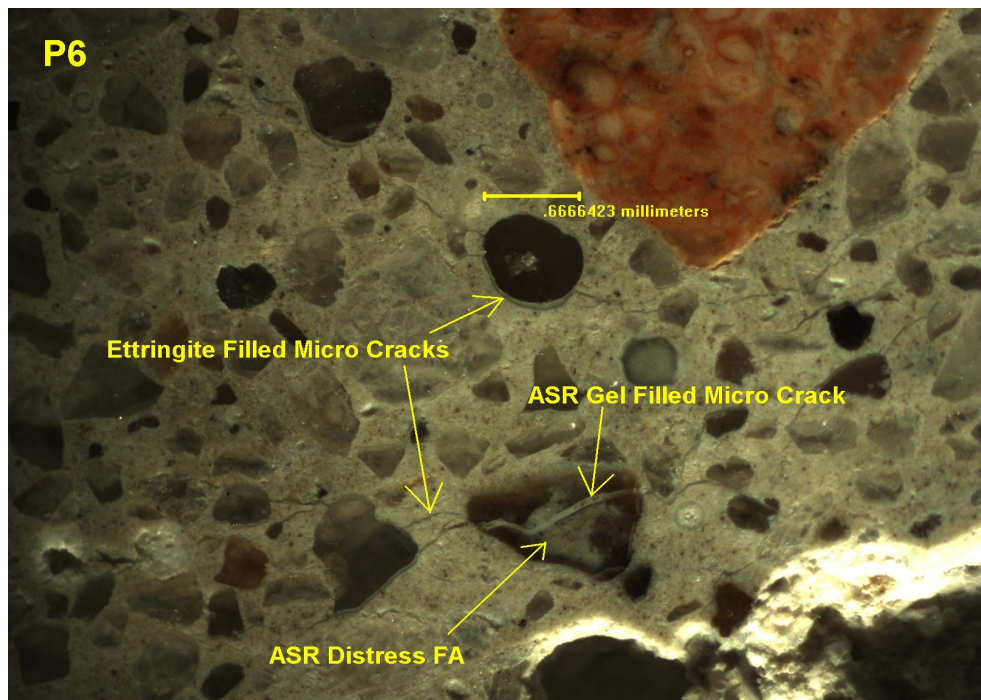
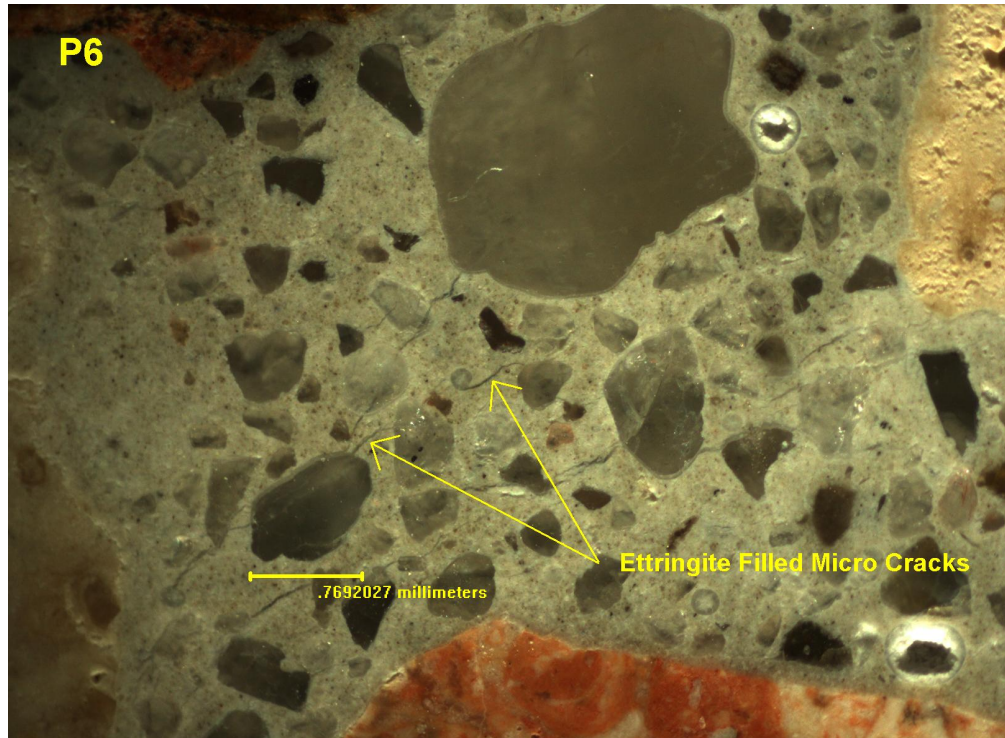


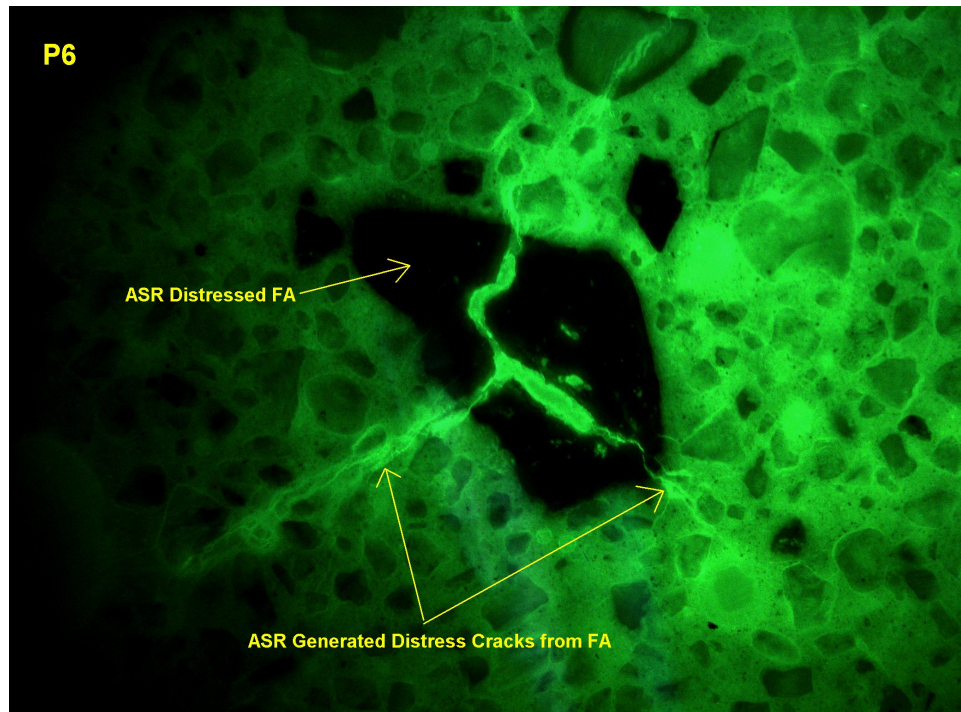
Image illustrating ettringite filled micro cracks



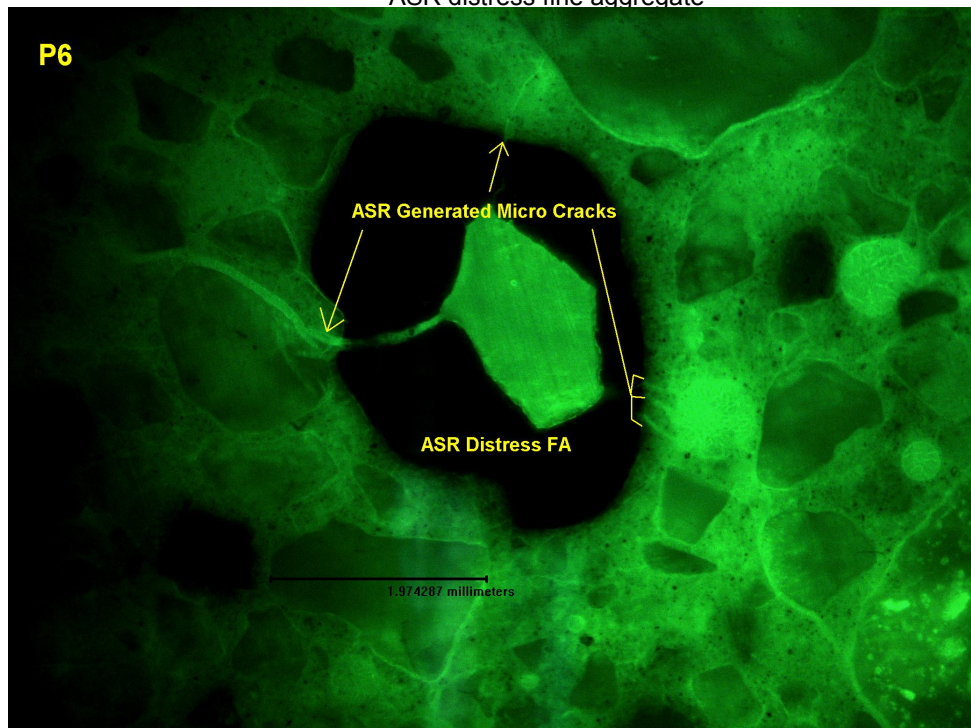
Fluorescence Microscopy Documentation

Fluorescent imaging is very useful tool in highlighting the fine micro cracking associated with PCD mechanism. The following images illustrate the level of distress associated with the reaction:

Fluorescent image illustrating ASR distressed fine aggregate and associated distress cracking



ASR distress fine aggregate



Highly distressed fine aggregate illustrating radial distress cracking

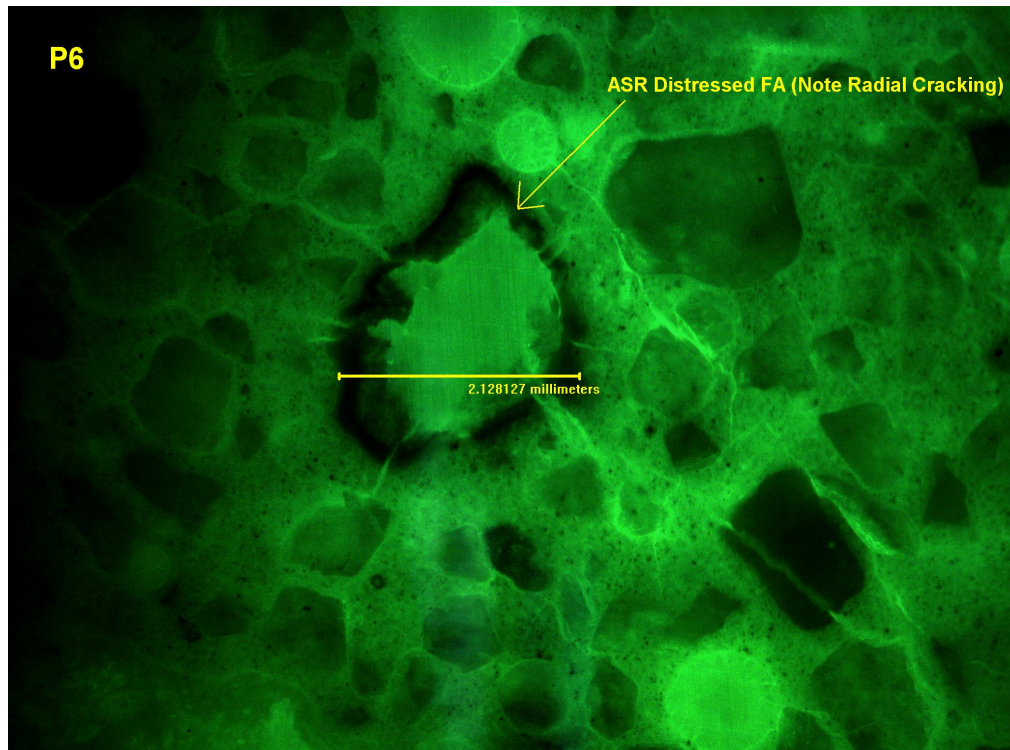


Image illustrating ettringite filled gap surrounding aggregate

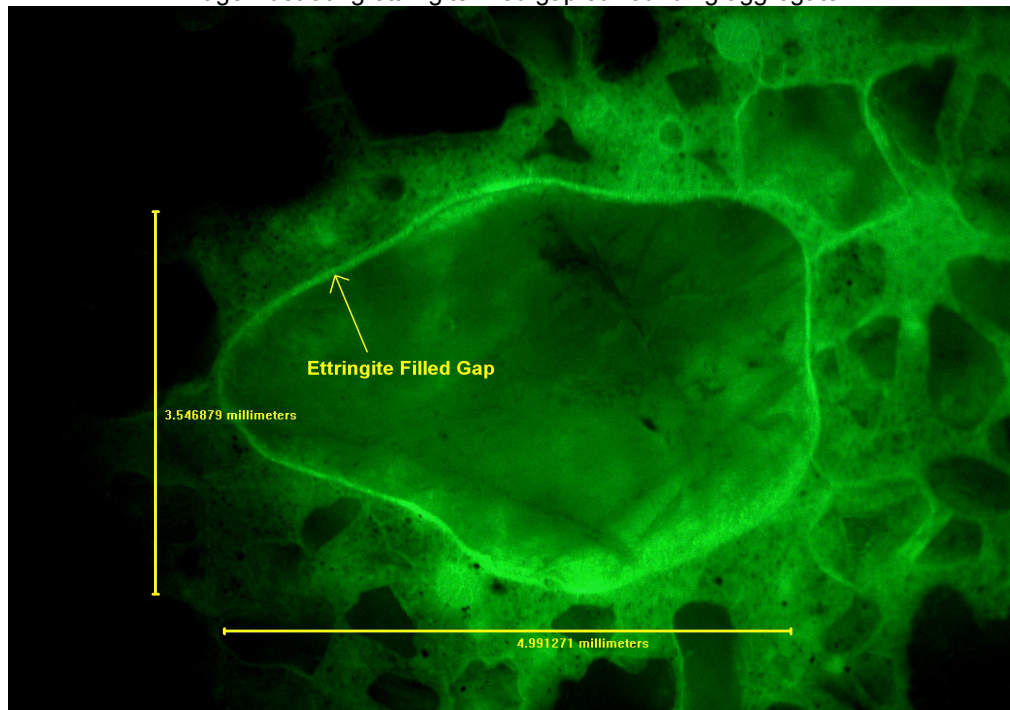


Image illustrating ettringite filled gap around FA

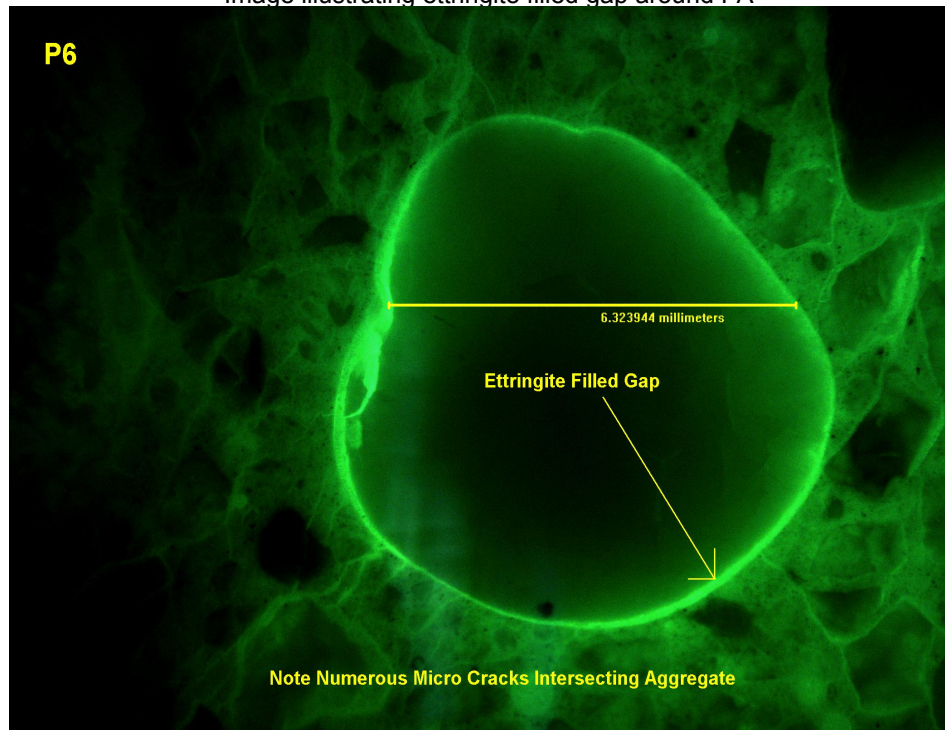
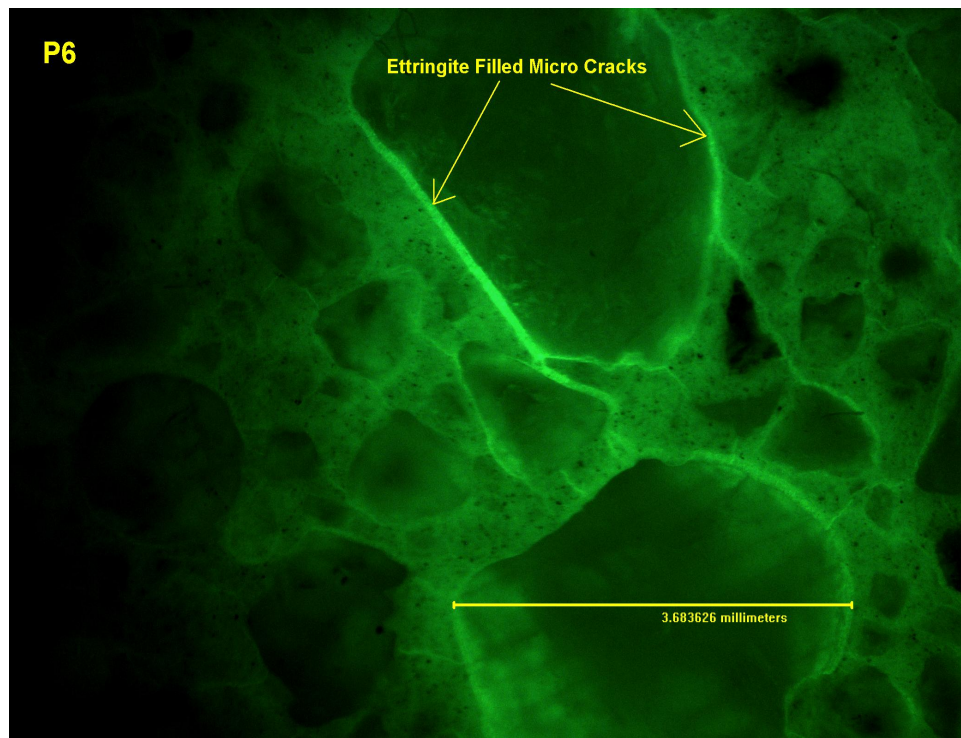
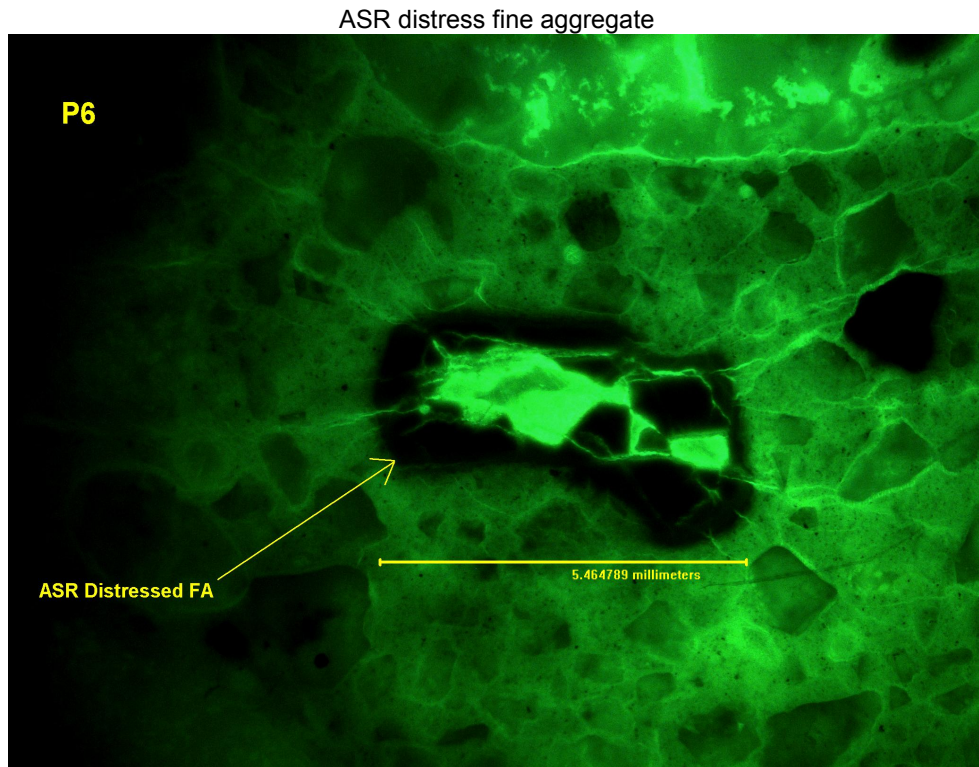


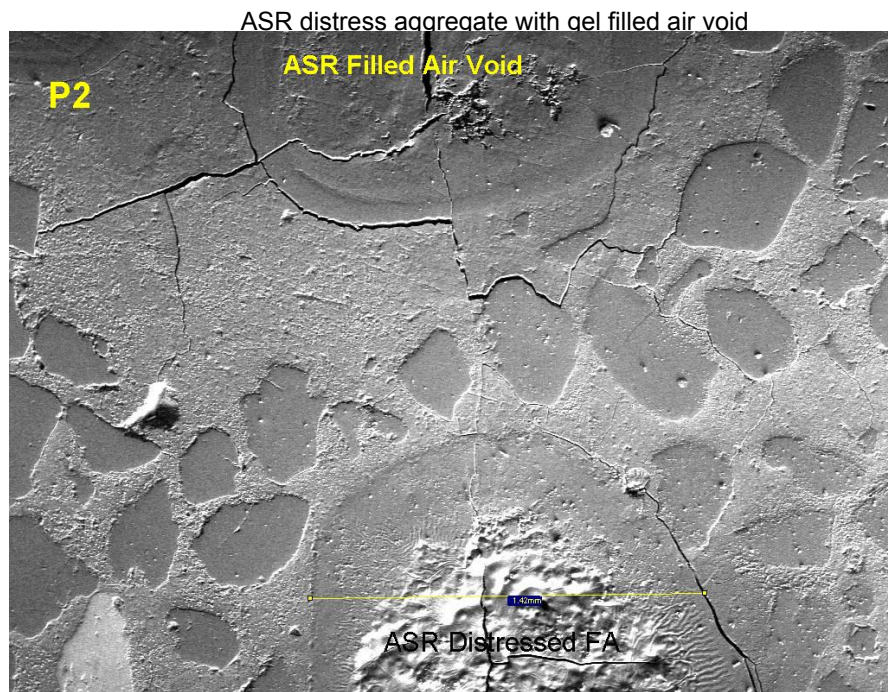
Image illustrating intersection of ettringite filled micro cracks



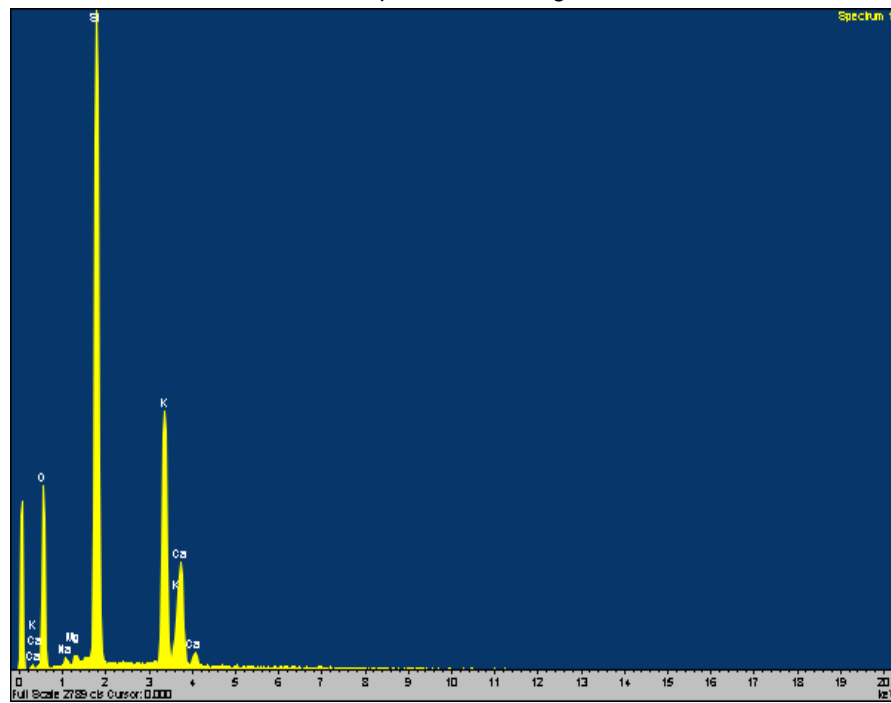


Scanning Electron Microscope (SEM) Documentation

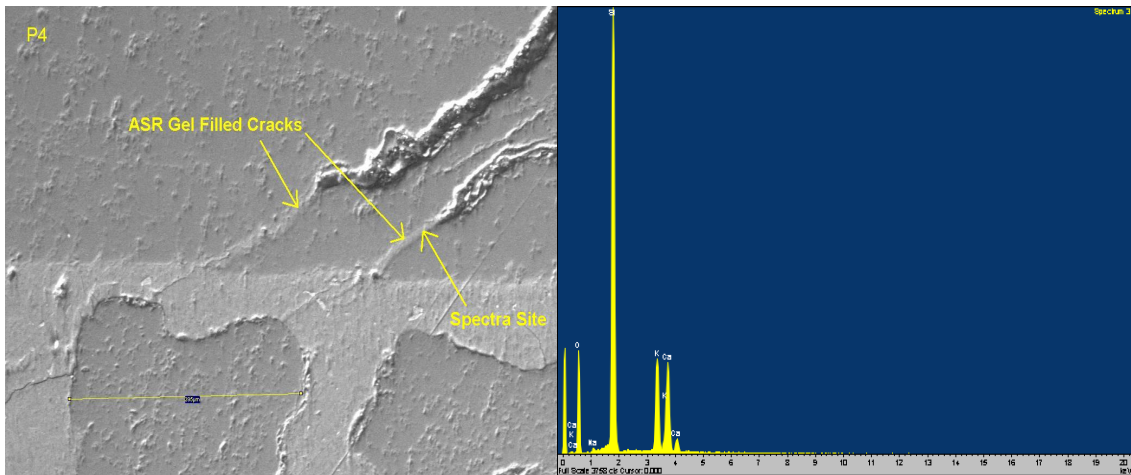
The SEM analysis was performed on a Hitachi brand 3200N variable pressure microscope with a Oxford EDS system. This tool was used to document and confirm the type of PCD responsible for the distressed concrete. EDS spectral analysis was used to verify reaction site chemistry and relationship to other phases in the mix (paste, aggregate). EDS elemental dot mapping was performed to document the location of reaction product within the mix. The following images document numerous ASR distressed aggregates and ettringite formation sites:



SEM/EDS spectra taken in gel filled air void



SEM image and EDS spectra illustrating ASR distress with associated reaction products



ASR distress aggregate

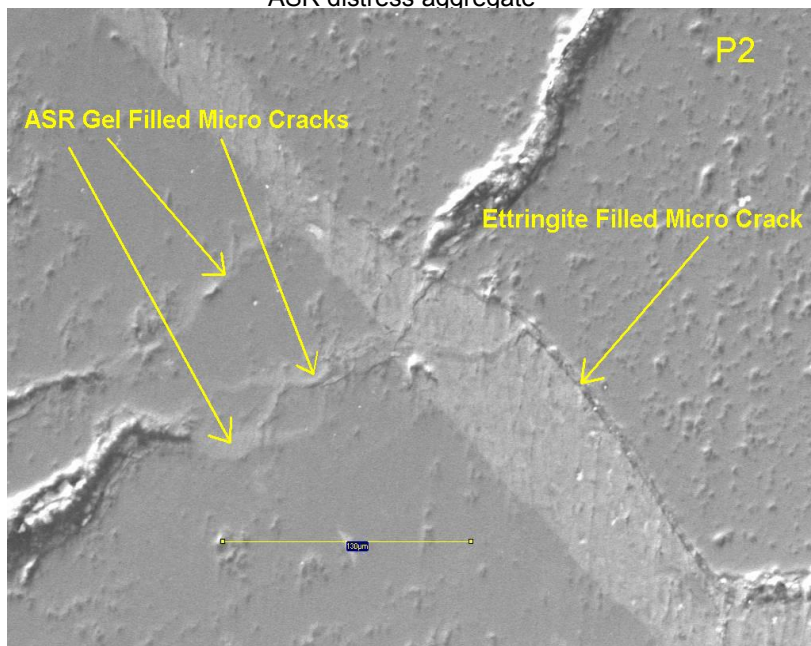
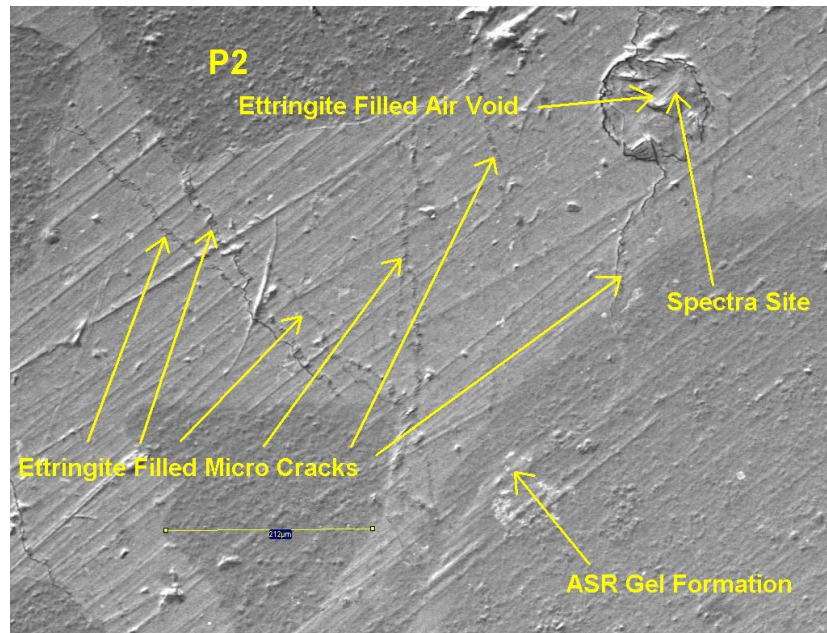
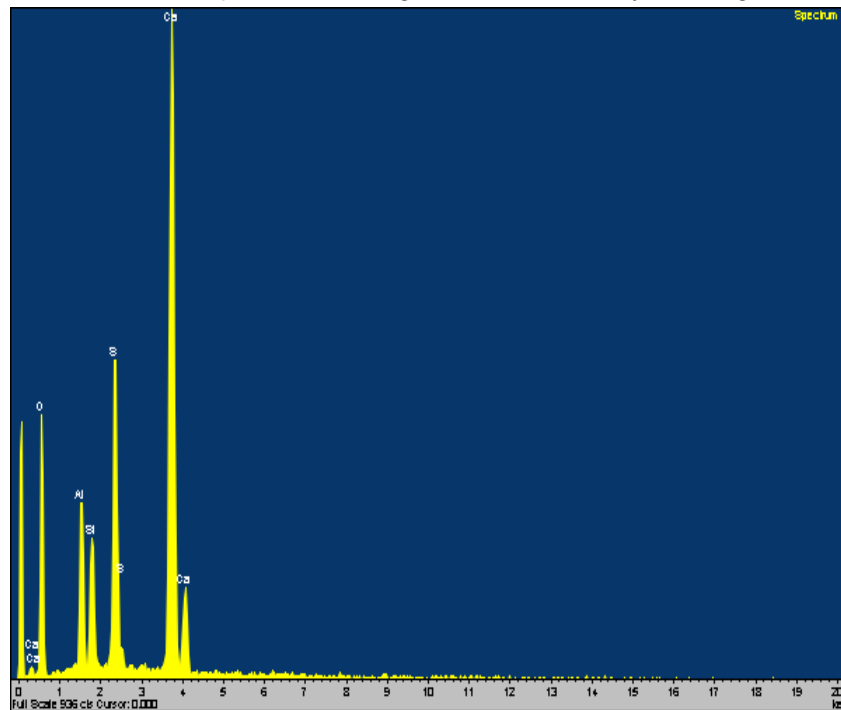


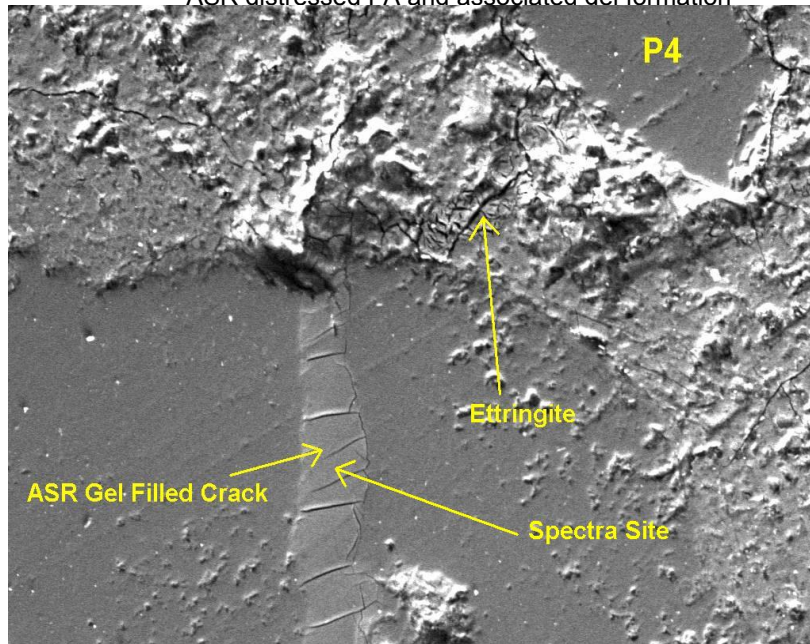
Image illustrating numerous fine ettringite filled micro cracks



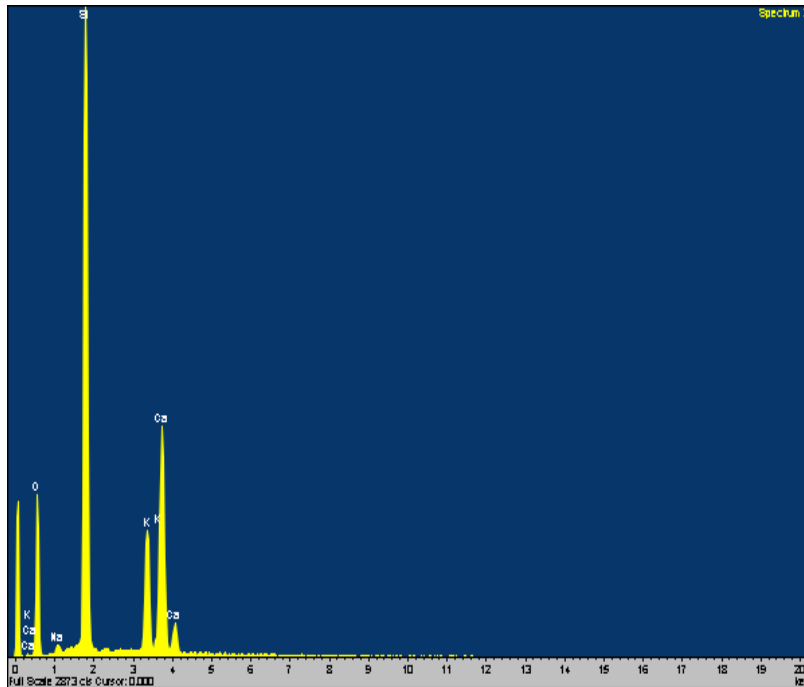
SEM/EDS spectra illustrating elemental chemistry of ettringite



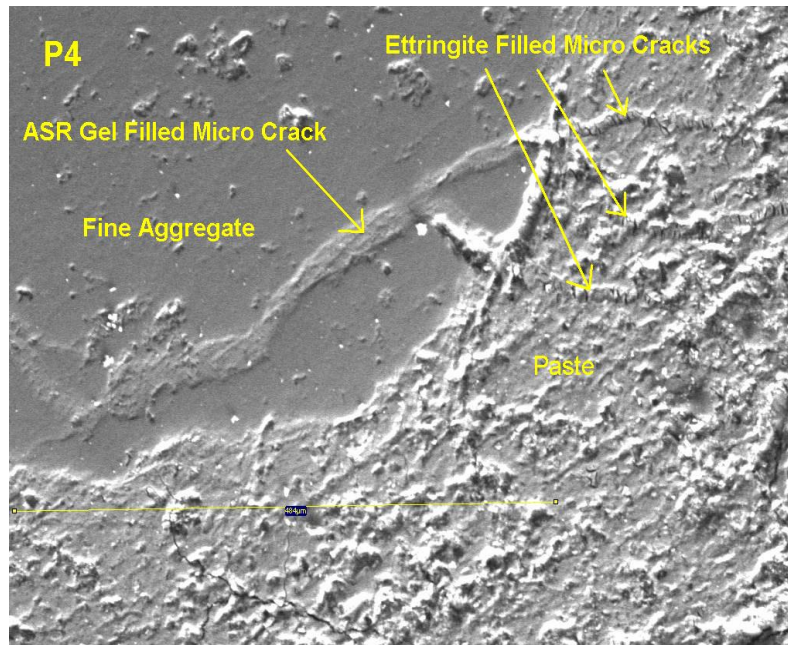
ASR distressed FA and associated gel formation



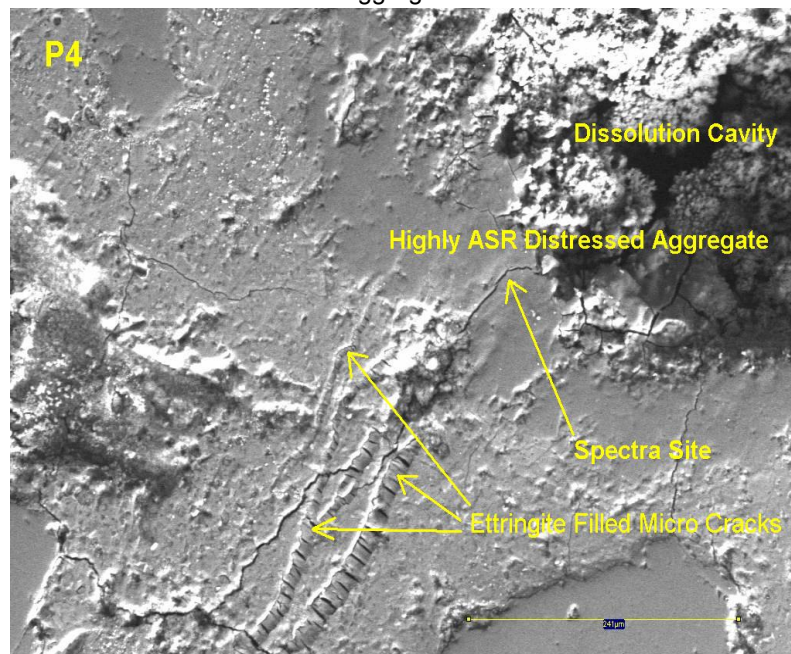
SEM/EDS spectra confirming ASR gel chemistry



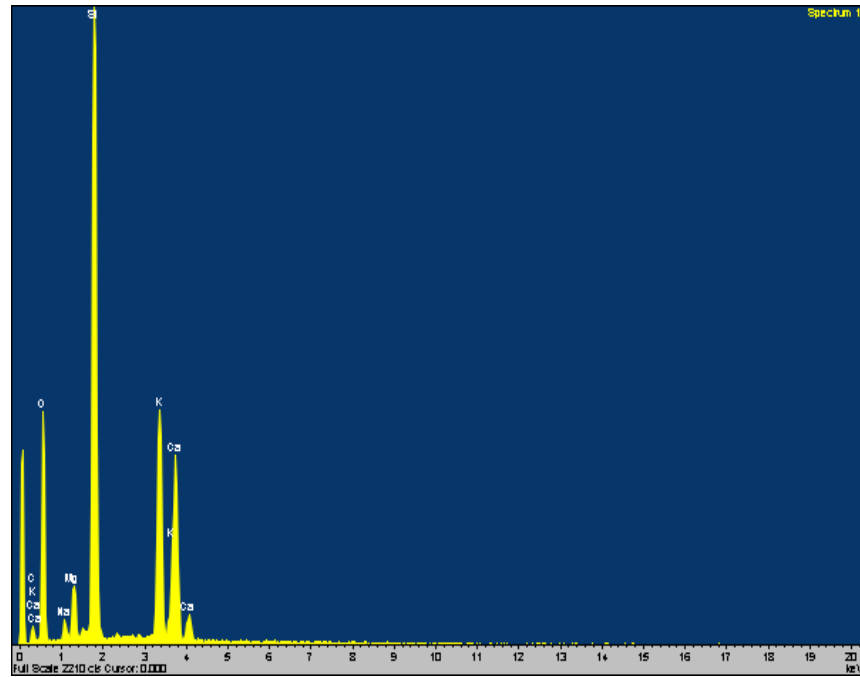
ASR distress FA



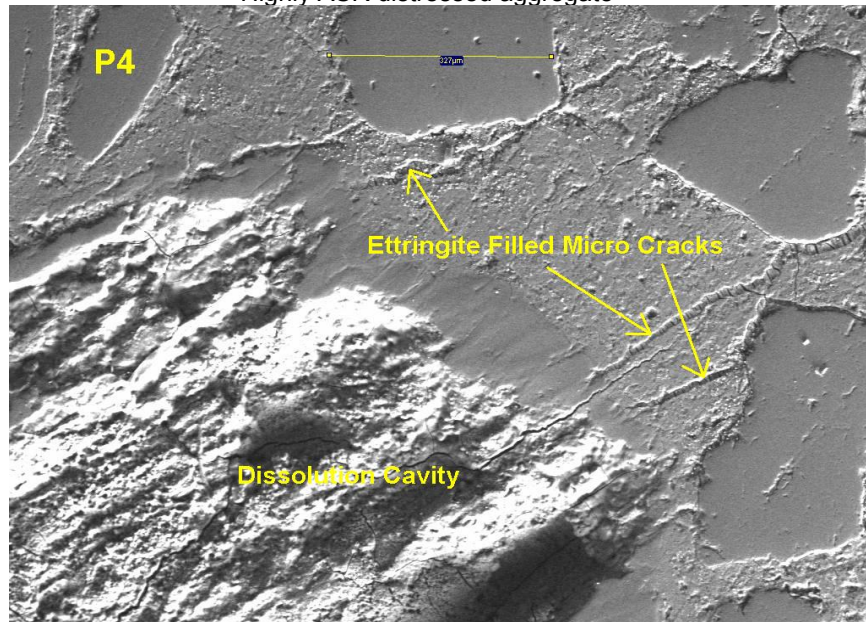
ASR distress FA illustrating gel formation and significant dissolution of the reactive aggregate.



SEM/EDS spectra confirming gel chemistry



Highly ASR distressed aggregate



SEM/EDS spectra confirming ASR gel chemistry

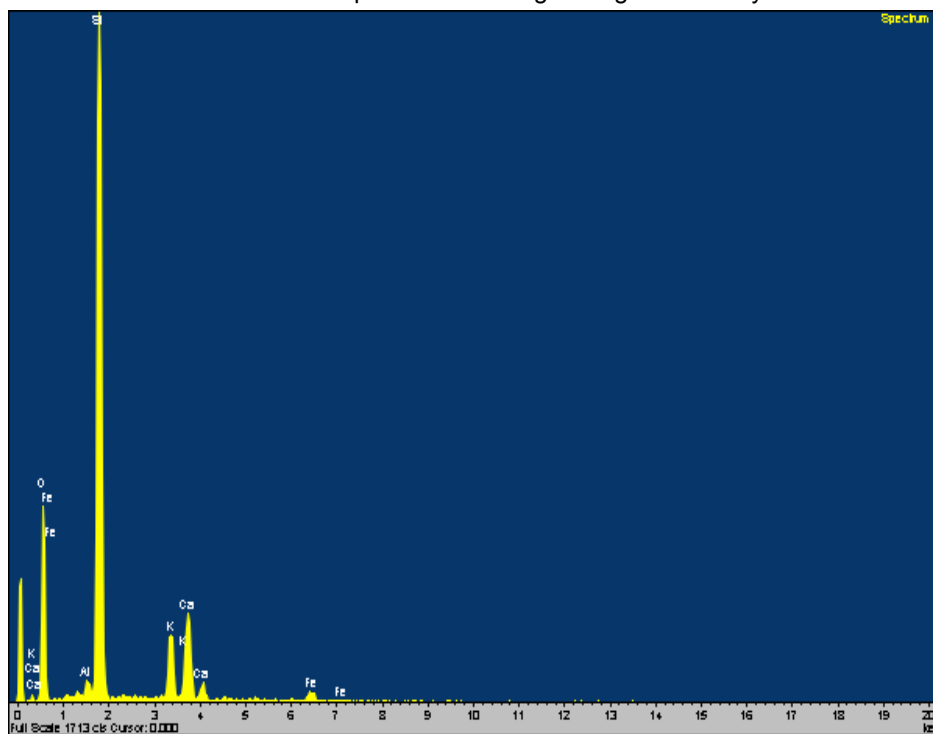
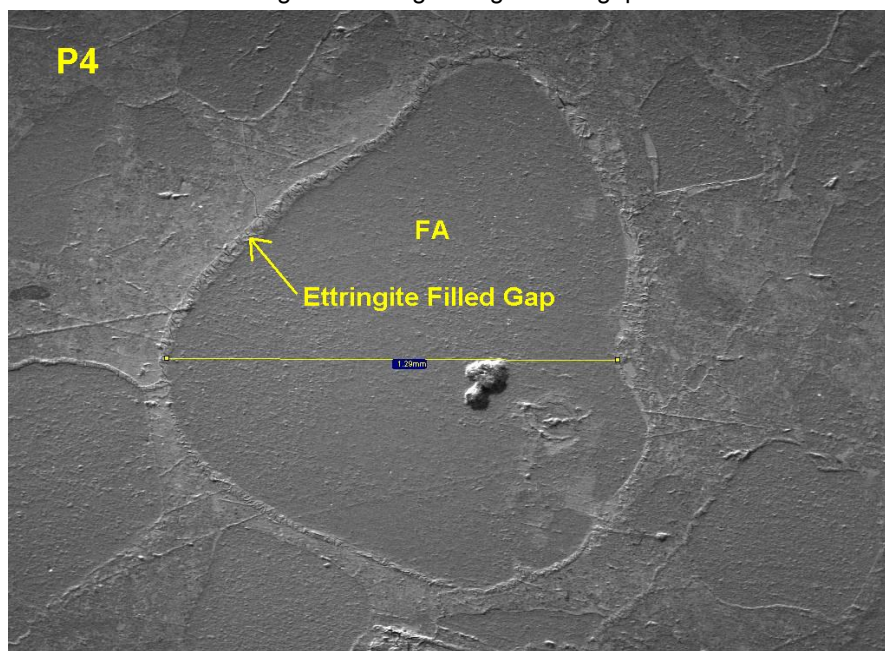


Image illustrating ettringite filled gap around FA



SEM/EDS Dot map illustrating sulfur rich ettringite filled gap and silica rich FA

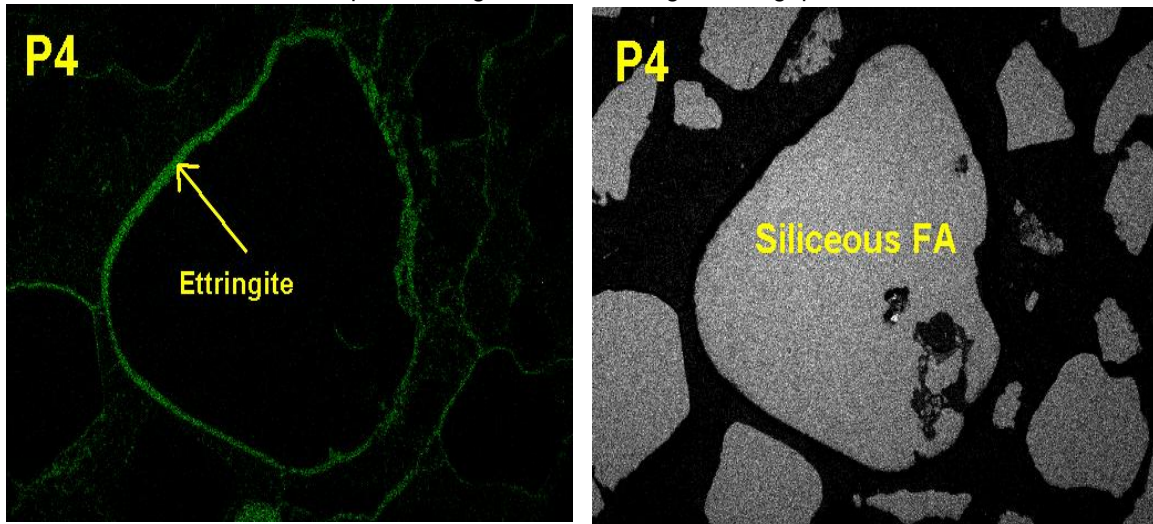
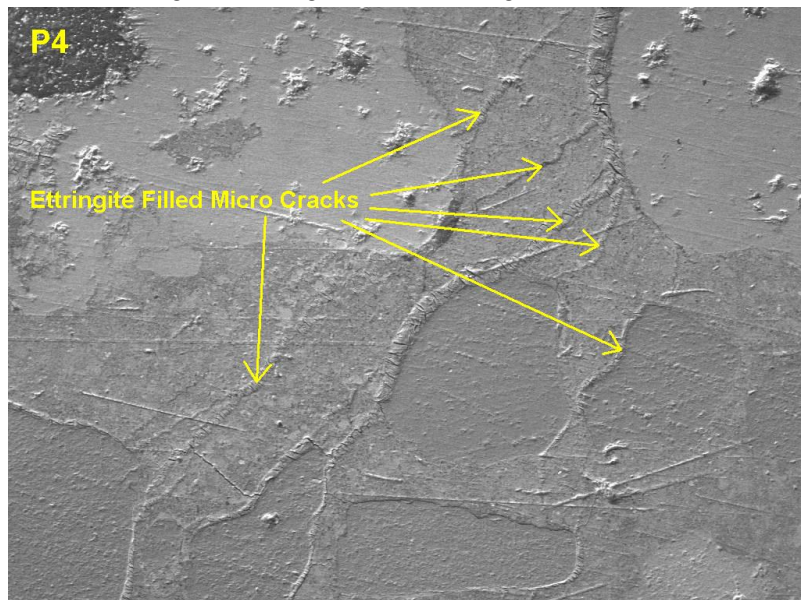


Image illustrating numerous ettringite filled micro cracks



Sulfur Dot map illustrating ettringite filled micro cracks

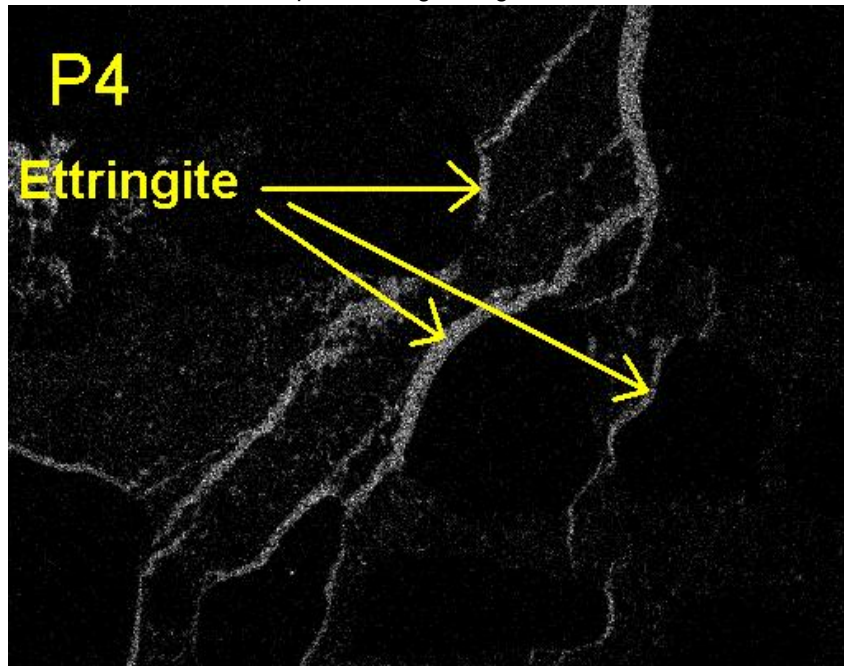


Image illustrating ettringite filled micro cracks

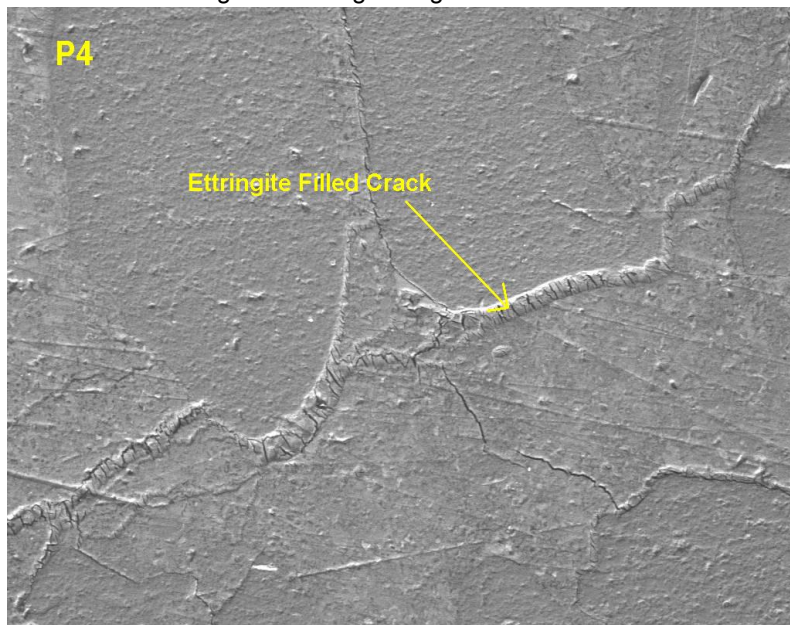
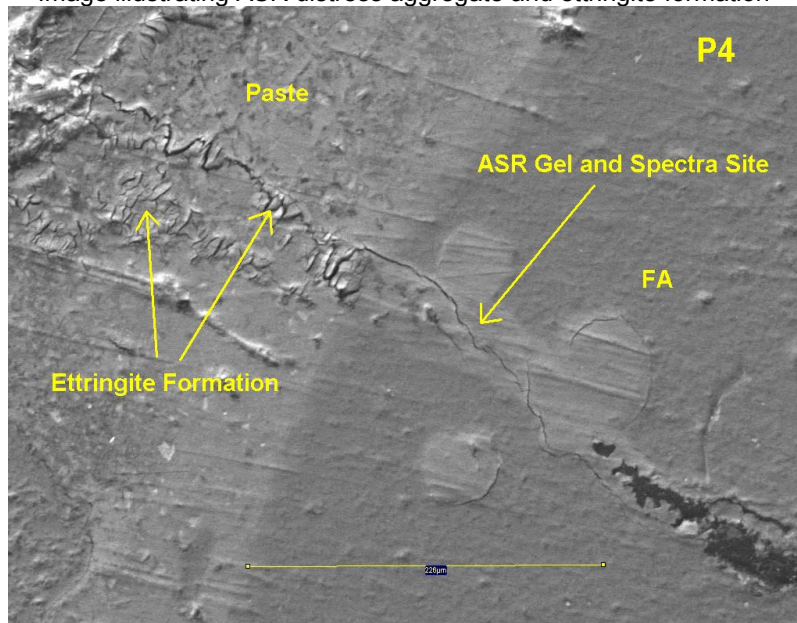


Image illustrating ASR distress aggregate and ettringite formation



SEM/EDS spectra confirming ASR gel chemistry

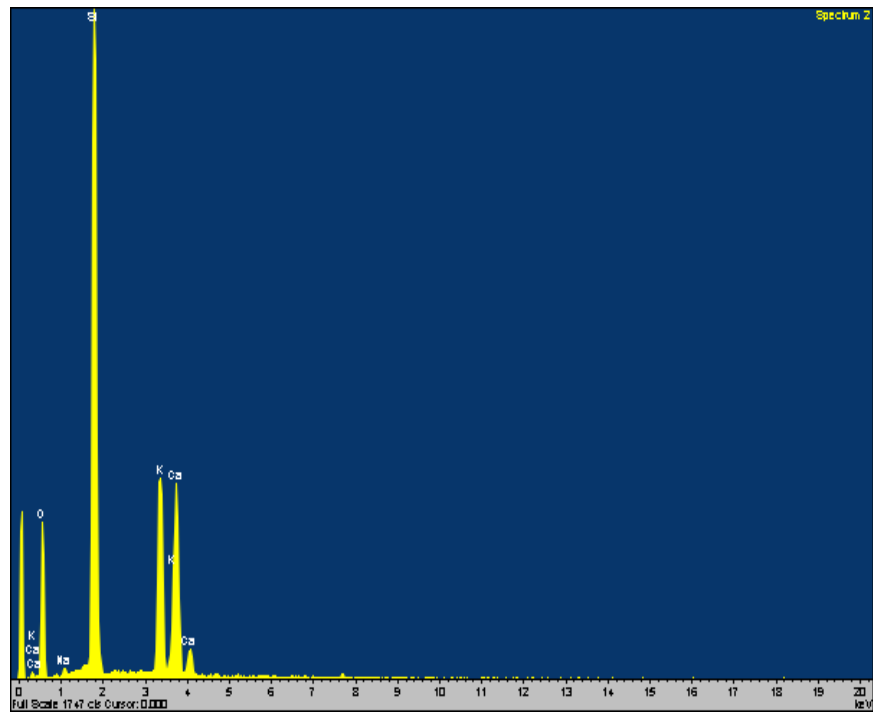
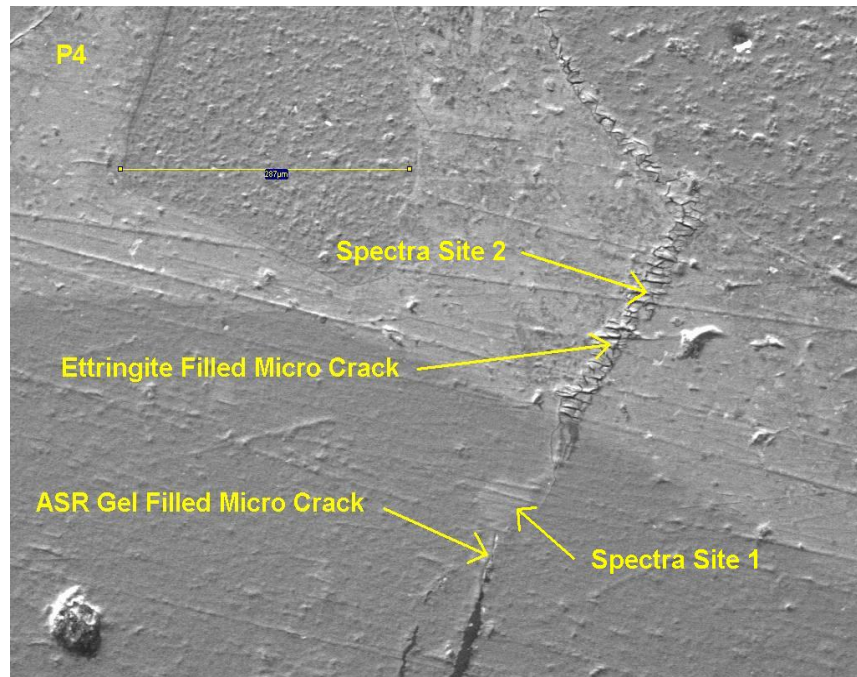


Image illustrating ASR site and ettringite filled crack



SEM/EDS spectra sites confirming ASR gel and ettringite chemistry

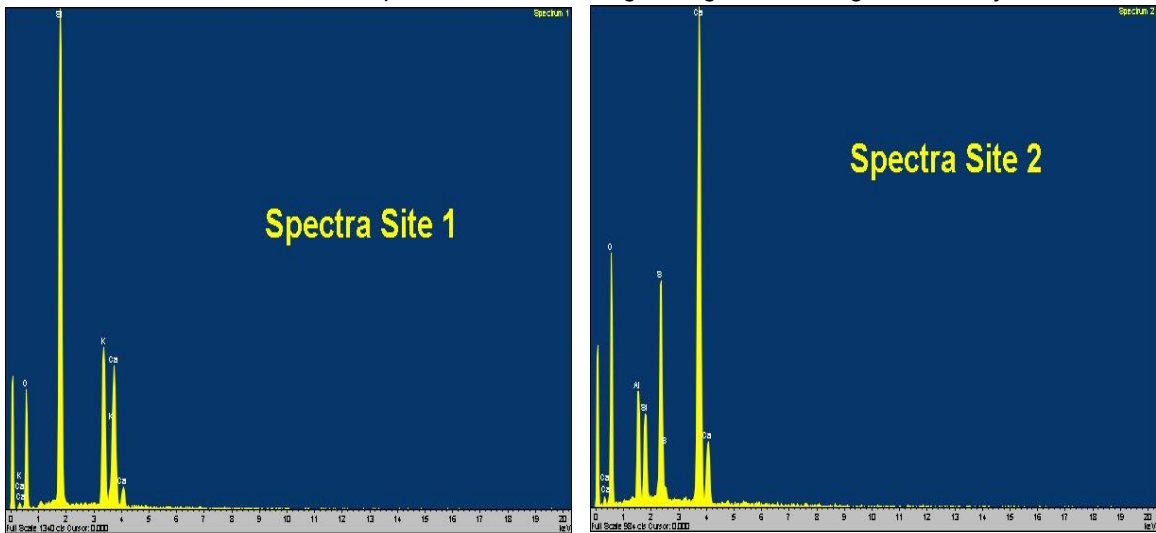
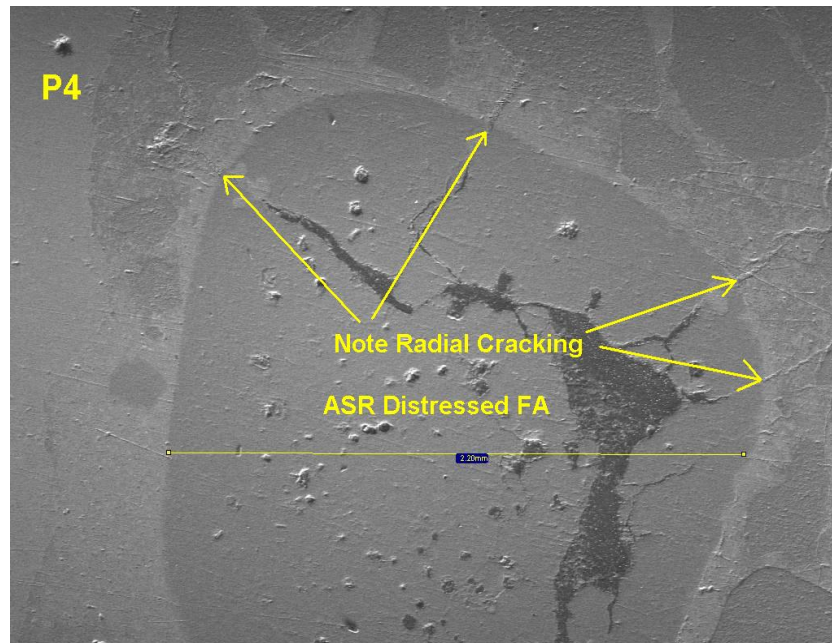


Image illustrating ASR distress intermediate size aggregate



Qualitative study of damage severity in each sample and damage progression through the length of the sample. (Comparison of micro structural damage between all samples).

Core #	Total Length	Micro Structural Damage and # Reactive Particles Counted on Cross-Sectional Polished Slab			
		Top 4 Inches	4-8 Inches	4-12 Inches or Remainder	Remainder
P1	10 "	3 reactive particles. Primary Macro vertical crack propagated full length of section and pierced numerous CA. Fine ettringite filled cracks associated with FA reactivity	6 reactive particles. Primary crack continues another 1-1/2 in this section. Ettringite filled fine micro cracks associated with FA ASR. Distress level is moderate.	9 reactive particles in remaining 2". Fine ettringite filled cracks associated with ASR. Similar distress level as 4-8 section.	

		oriented more vertical become sub-parallel to surface with depth. Overall level of distress is low to moderate.			
P2	8-3/4 "	7 reactive particles. Two surface cracks one 3/4 "deep and the other 3/8 inch deep. Fine ettringite filled crack oriented more vertical becoming sub-parallel to surface with depth. Level of distress slightly higher than P1.	12 Reactive particles. Ettringite filled fine micro cracks associated with FA ASR. Distress level slightly higher than P1.	15 reactive particles in remaining 2-3/4 ". Ettringite filled fine micro cracks associated with FA ASR. Distress level slightly higher than P1.	
P3	10-1/2 "	4 reactive particles. Three shallow surface cracks ranging from 7/8 to 2/8 in depth. Some fine ettringite filled cracks. Level of distress is less than P1 and P2.	16 reactive particles. Fine ettringite filled cracking and level of distress is similar to P1.	4 reactive particles in remaining 2-1/2 ". Level of distress is less than P1 and P2.	
P4	8-1/2 "	13 reactive particles.	16 reactive particles.	3 reactive particles in	

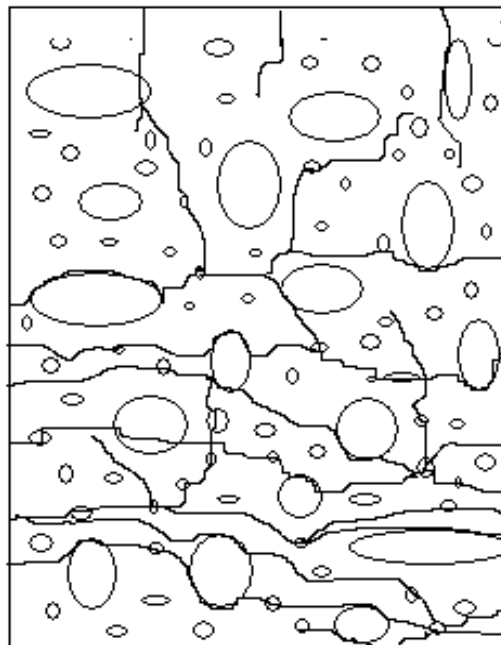
		Several shallow ¼ to 1/8 “surface cracks. Distress level similar to P2.	Numerous fine ettringite filled micro cracks oriented sub-parallel to surface. Slightly higher level of distress than P2.	remaining 2-1/2 “. Lower # ASR particles than P1, P2 and P3. Abundant ettringite filled cracks. Level of distress similar to P2.	
P5	11”	9 reactive particle. Surface cracks to 1-1/2 inch deep. Fine ettringite filled micro cracks increase in lower section. Level of distress is higher than P2.	23 reactive particles. Abundant fine ettringite filled cracks and larger crack in lower section pierced limestone CA. Level of distress is higher than P2.	12 reactive particles in remaining 3 inches. Abundant fine ettringite filled micro cracks. Larger cracks piercing limestone CA oriented sub-parallel to the surface. Level of distress similar to 4-8 section.	
P6	13-1/2”	12 reactive particles. Fine ettringite filled micro crack increasing with deep to abundant level. Level of distress is similar to P5.	23 reactive particles. Abundant ettringite filled micro cracks oriented both vertical and sub-parallel to surface. Level of distress is higher than P5.	18 reactive particles. Abundant ettringite filled micro cracks. Larger cracks oriented sub-parallel to surface piercing numerous limestone CA. Level of distress is	3 reactive particles in remaining 1-1/2 “. Ettringite filled micro cracks abundant. Larger cracks oriented parallel to surface were observed. Level of distress is

				higher than P5.	higher than P5.
P7	10-3/4"	14 reactive particles. Surface crack to 1/2 inch and larger cracks oriented near vertical to sub-parallel to the surface. Abundant fine ettringite filled micro cracks increase with deep of section. Level of distress is similar to P6.	19 reactive particles. Abundant ettringite filled micro cracks. Some larger cracks in top section running sub-parallel to surface. Level of distress is similar to P6.	18 Reactive particles in remaining 2-3/4 ". Abundant ettringite filled micro cracks. Level of distress is similar to P6.	
P8	12-3/4"	13 reactive particles. Surface crack to 3/8 inch deep. Fine ettringite filled micro cracks oriented more vertical in top section and sub parallel with depth. Larger cracks oriented sub-parallel to surface in lower section. Level of distress is similar to P6	22 reactive particle. Abundant ettringite filled micro cracks. Level of distress is similar to P6 and P7.	24 reactive particles. Micro cracking similar to 4-8 section. Level of distress is similar to P6 and P7.	3 reactive particles in remaining 3/4 "section. Level of distress similar to 8-12 section.

		and P7.			
P9	7-1/2"	9 reactive particles. Surface crack to 3/8 deep. Level of distress is similar to P3.	18 reactive particles in remaining 3-1/2". Level of distress is similar to 4-8 section in P3.		

The following schematic is a representation of the cracking and orientation observed in these specimens.

Representation of Micro Structural Damage



Conclusion: Based on this analysis ASR is the primary PCD mechanism responsible for the distressed concrete in all 9 cores. A microcrystalline chert fine aggregates is the principle lithologic mineral associated with the reaction. Micro structural damage from the ASR resulted in an extensive network of fine micro cracks (see above images) observed throughout these cores. The expansive reactions resulting in development of larger vertical surface crack seen in most of the cores.

It is inconclusive whether DEF has played a role in the distressed concrete. Due to the limited occurrence of true gapping (resulting from bulk expansion of the paste) DEF does not appear to have played a significant role in the distress. Most of the site that appear to be gapping were created as a result of ASR generated micro cracks intersecting the aggregate and then partially wrapping around them (fluorescent and SEM demonstrates this occurrence). Bifurcation of the intersecting cracks can sometime make it look like gapping has occurred. It is unclear whether the ettringite precipitation and potential imbibing of moisture could generate enough stress to potentially widen these cracks at the paste aggregate interfaces. Ettringite was noted as small discrete nests within the paste and in air voids. A coating of ettringite was also noted where the rebar had dislodged (on imprint of rebar) during the polishing process in Core P4. This indicates that either a separation occurred (debonding) between the rebar and paste forming a gap large enough for ettringite precipitation or possibly settlement gaps or thermal cracks had occurred.

REFERENCES

1. *AASHTO LRFD Bridge Design Specifications, 4th Edition, 2008 Interim Revisions*. Washington, D.C.: American Association of State Highway and Transportation Officials, 2007.
2. ACI Committee 209. *Prediction of Creep, Shrinkage, and Temperature Effects in Concrete Structures*. Farmington Hills: American Concrete Institute, 1997.
3. ACI Committee 228. *Nondestructive Test Methods for Evaluation of Concrete in Structures (ACI 228.2R-98)*. Farmington Hills: American Concrete Institute, 2004.
4. ACI Committee 318-2008. *Building Code Requirements for Reinforced Concrete (ACI 318-08)*. Farmington Hills: American Concrete Institute, 2008.
5. Ahmed, T.; Burley, E. and Rigden, S. "The Static and Fatigue Strength of Reinforced Concrete Beams Affected by Akali-Silica Reaction." *ACI Materials Journal* Vol. 95 No. 4 (1998): 376-388.
6. Ahmed, T; Burley, E.; Rigden, S. and Abu-Tair, A.I. "The Effect of Alkali Reactivity on the Mechanical Properties of Concrete." *Construction and Building Materials* Vol. 14 (2003): 123-144.
7. *ASTM C 39/C 39M Standard Test Method for Compressive Strength of Cylindrical Concrete Specimens*. West Conshohocken: American Society for Testing and Materials, 2005.
8. *ASTM C 42/C 42M Standard Test Method for Obtaining and Testing Drilled Cores and Sawed Beams of Concrete*. West Conshohocken: American Society for Testing and Materials, 2004.
9. *ASTM C 856-04 Standard Practice for Petrographic Examination of Hardened Concrete*. West Conshohocken: American Society for Testing and Materials, 2004.
10. Bach, F.; Thorsen, T.S. and Nielsen, M.P. "Load-Carrying Capacity of Structural Members Subjected to Alkali-Silica Reactions." *Construction and Building Materials* Vol. 7 No. 2 (1993): 109-115.
11. Bae, S.; Bayrak, O.; Jirsa J.O. and Klingner, R.E. *Anchor Bolt Behavior in ASR/DEF-Damaged Drilled Shafts*. Austin: Ferguson Structural Engineering Laboratory, University of Texas at Austin, 2007. TxDOT IAC 88-5DDIA004.
12. Bauer, S.; Cornell, B.; Figurski, D.; Ley, T.; Miralles, J. and Folliard, K.J. *Alkali-Silica Reaction and Delayed Ettringite Formation in Concrete: A Literature Review*.

Austin: Center for Transportation Research, University of Texas at Austin, 2001. TxDOT Report 0-4085-1.

13. Berube, M.A.; Smaoui, N.; Fournier, B.; Bissonnette, B. and Durand, B. "Evaluation of the Expansion Attained to Date by Concrete Affected by Alkali-Silica Reaction. Part III: Application to Existing Structures." *Canadian Journal of Civil Engineering* Vol. 32 No. 3 (2005): 463-479.
14. Bindrich, B.V. "The Effects of Alkali-Silica Reaction and Delayed-Ettringite Formation on the Structural Performance of the Dapped End Region of Prestressed Concrete Trapezoidal Box Beams." MS Thesis. University of Texas at Austin, 2009.
15. Birrcher, D.; Tuchscherer, R.; Huizinga, M.; Bayrak, O.; Wood, S. and Jirsa, J.O. *Strength and Serviceability Design of Reinforced Concrete Deep Beams*. Austin: Center for Transportation Research, University of Texas at Austin, 2008. TxDOT Report 0-5253-1.
16. Boenig, A. "Bridges with Premature Concrete Deterioration: Field Observations and Large-Scale Testing." MS Thesis. University of Texas at Austin, 2000.
17. Brown, M.D.; Sankovich, C.L.; Bayrak, O.; Jirsa, J.O.; Breen, J.E. and Wood, S.L. *Design for Shear in Reinforced Concrete Using Strut-and-Tie Models*. Austin: Center for Transportation Research, University of Texas at Austin, 2006. TxDOT Report 0-4371-2
18. Burgher, B.; Thibonnier, A.; Folliard, K.J.; Ley, T. and Thomas, M. *Investigation of the Internal Stresses Caused by Delayed Ettringite Formation in Concrete*. Austin: Center for Transportation Research, University of Texas at Austin, 2008. TxDOT Report 0-5218-1.
19. Chana, P.S. and Korobokis, G.A. *Structural Performance of Reinforced Concrete Affected by Alkali-Silica Reaction: Phase I*. Crowthorne: Transport and Road Research Laboratory, Department of Transport, 1991. Contractor Report 267.
20. Clark, L.A. *Critical Review of the Structural Implications of the Alkali-Silica Reaction in Concrete*. Crowthorne: Transport and Road Research Laboratory, Department of Transport, 1989. Contractor Report 169.
21. Clayton, N.; Currie, R.J. and Moss, R.M. "The Effects of Alkali-Silica Reaction on the Strength of Prestressed Concrete Beams." *The Structural Engineer* Vol. 68 No. 15 (1990): 287-292.
22. Cope, R.J. and Slade, L. "The Shear Capacity of Reinforced Concrete Members Subjected to Alkali-Silica Reaction." *Structural Engineering Review* Vol. 2 (1990): 105-112.

23. Den Uijl, J.A. and Kaptijn, N. "Shear Tests on Beams Cut from ASR-Affected Bridge Decks." *ACI SP-211-6*, 115-133.
24. Deschenes, D.J.; Bayrak, O. and Folliard, J.F. *ASR/DEF-Damaged Bent Caps: Shear Tests and Field Implications*. Austin: Ferguson Structural Engineering Laboratory, University of Texas at Austin, 2009. TxDOT IAC 12-8XXIA006.
25. Eskridge, A.E.; Klahorst, J.T.; Klingner, R.E. and Kreger, M.E. *Mitigation Techniques for In-Service Structures with Premature Concrete Deterioration: Project Summary Report*. Austin: Center for Transportation Research, University of Texas at Austin, 2005. TxDOT Report 0-4069-S.
26. Fan, S. and Hanson, J.M. "Effect of Alkali-Silica Reaction Expansion and Cracking on Structural Behavior of Reinforced Concrete Beams." *ACI Structural Journal* Vol. 95 No. 5 (1998): 498-505.
27. Farny, J.A. and Kerkhoff, B. *Diagnosis and Control of Alkali-Aggregate Reactions in Concrete*. Skokie: Portland Cement Association, 2007.
28. FIB. *Practical Design of Structural Concrete (Recommendations)*. International Federation for Structural Concrete, Lausanne, Switzerland, 1999.
29. FIB. *Structural Concrete, Textbook on Behaviour, Design, and Performance, Volume 2*. International Federation for Structural Concrete, Lausanne, Switzerland, 1999.
30. Folliard, K.J.; Barborak, R.; Drimalas, T.; Du, L.; Garber, S.; Ideker, J.; Ley, T.; Williams, S.; Juenger, M.; Thomas, M.D.A. and Fournier, B. *Preventing Alkali-Silica Reaction and Delayed Ettringite Formation in New Concrete: Project Summary Report*. Austin: Center for Transportation Research, University of Texas at Austin, 2006. TxDOT Report 0-4085-S.
31. Folliard, K.J.; Barborak, R.; Drimalas, T.; Du, L.; Garber, S.; Ideker, J.; Ley, T.; Williams, S.; Juenger, M.; Fournier, B. and Thomas, M.D.A. *Preventing ASR/DEF in New Concrete: Final Report*. Austin: Center for Transportation Research, University of Texas at Austin, 2006. TxDOT Report 0-4085-5.
32. Folliard, K.J.; Thomas, M.D.A. and Fournier, B. *Protocol for the Diagnosis and Prognosis of Concrete Structures Affected by Alkali-Silica Reaction and/or Delayed Ettringite Formation*. Austin: Concrete Durability Center, University of Texas at Austin, 2007.
33. Folliard, K.J.; Juenger, M.; Schindler, A.; Riding, K.; Poole, J.; Kallivokas, L.F.; Slatnick, S.; Whigham, J. and Meadows, J.L. *Prediction Model for Concrete Behavior—Final Report*. Austin: Center for Transportation Research, University of Texas at Austin, 2007. TxDOT Report 0-4563-1.

34. Folliard, K.J. and Drimalas, T. "Brief Summary of Evaluation of Houston Box Beams." Internal Report, March 2008.
35. Folliard, K.J.; Burgher, F.; Ley, T.; Thibonnier, A. and Thomas, M.D.A. *Extending Service Life of Large or Unusual Structures Affected by Premature Concrete Deterioration*. Austin: Research and Technology Implementation, Texas Department of Transportation, 2008. TxDOT Report 0-5218-S.
36. Folliard, K.J. Personal Communication, 2010.
37. Fournier, B.; Berube, M.A.; Thomas, M.D.A.; Smaoui, N. and Folliard, K.J. *Evaluation and Management of Concrete Structures Affected by Alkali-Silica Reaction: A Review*. Ottawa: CANMET Materials Technology Laboratory, Natural Resources Canada, 2004. Report Number MTL 2004-11.
38. Giaccio, G.; Zerbino, R.; Ponce J.M.; Batic O.R.; "Mechanical Behavior of Concretes Damaged by Alkali-Silica Reaction." *Cement and Concrete Research*, V. 38, No. 7, July. 2008, pp. 993-1004.
39. Hobbs, D.W., "Countering Alkali-Silica Reaction in Concrete." *Concrete Construction - World of Concrete*, V. 34, No. 11. 1989, pp. 948-50.
40. Inoue, S.; Oshita, H.; Sawai, K. and Hatano, Y. "Effect of Rupture of Shear Reinforcement on Shear Capacity of ASR Damaged Reinforced Concrete Beams." *Proceedings of the Thirteenth International Conference on Alkali-Aggregate Reaction*. Trondheim. 2008.
41. Institution of Structural Engineers. *Structural Effects of Alkali-Silica Reaction*. London: SETO, 1992.
42. Kapitan, J.G. "Structural Assessment of Bridge with Damage Similar to ASR and/or DEF." MS Thesis. University of Texas at Austin, 2006.
43. Kee, S.H. Personal Communication, 2010.
44. Larson, N.A. "Structural Performance of ASR/DEF Damaged Prestressed Concrete Trapezoidal Box Beams with Dapped Ends." MS Thesis. University of Texas at Austin, 2010.
45. Lawrence, B.L.; Moody, E.D.; Guillemette, R.N. and Carrasquillo, R.L. "Evaluation and Mitigating Measures for Premature Concrete Distress in Texas Department of Transportation Concrete Elements." *Cement, Concrete, and Aggregates* Vol. 21 No. 1 (1999): 73-81.
46. Mather, B., "New Concern over Alkali-Aggregate Reaction." 1975, National Sand and Gravel Association, NSGA Circular

47. Mikata, Y.; Maeda, S.; Hatano, Y. and Inoue, S. "Effect of Fractured Anchorage of Shear Reinforcements on Loading of PC Beams." *Proceedings of the Thirteenth International Conference on Alkali-Aggregate Reaction*. Trondheim. 2008.
48. Miyagawa, T.; Seto, K.; Sasaki, K.; Mikata, Y.; Kuzume, K. and Minami, T. "Fracture of Reinforcing Steels in Concrete Structures Damaged by Alkali-Silica Reaction - Field Survey, Mechanism, and Maintenance." *Journal of Advanced Concrete Technology* Vol. 4 No. 3 (2006): 339-355.
49. Monette, L.J.; Gardner, N.J. and Grattan-Bellew, P.E. "Residual Strength of Reinforced Concrete Beams Damaged by Alkali-Silica Reaction – Examination of Damage Rating Index Method." *ACI Materials Journal* Vol. 99 No. 1 (2002): 42-50.
50. Morgan, E. "UT ASR DEF Petrographic Analysis." Austin: Texas Department of Transportation., 30 March 2010, Unpublished Report.
51. Morgan, E. Personal Communication, 2010.
52. Schlaich, J.; Schäfer, K. and Jennewein, M. "Toward a Consistent Design of Structural Concrete." *PCI Journal* Vol. 32 No.3 (1987): 74-150.
53. Smaoui, N.; Bissonnette, B.; Berube, M.A.; Fournier, B. and Durand, B. "Mechanical Properties of ASR-Affected Concrete Containing Fine or Coarse Reactive Aggregates." *Journal of ASTM International* Vol. 3 No. 3 (2006): 1-16.
54. Stanton, T.E. "Expansion of Concrete through Reaction between Cement and Aggregate." *Proceedings of the American Society of Civil Engineers* Vol. 66 (1940): 1781-1811.
55. Swamy, R.N. and Al-Asali, M.M. "Engineering Properties of Concrete Affected by Alkali-Silica Reaction." *ACI Materials Journal* Vol. 85 No. 5 (1988): 367-364.
56. Thomas, M.D.A.; Folliard, K.J.; Drimalas, T. and Ramlochan, T. "Diagnosing Delayed Ettringite Formation in Concrete Structures." *Cement and Concrete Research* 38 (2008): 841-847.
57. Thompson, M.K.; Young, M.J.; Jirsa, J.O.; Breen, J.E. and Lingner, R.E. *Anchorage of Headed Reinforcement in CCT Nodes*. Austin: Center for Transportation Research, University of Texas at Austin, 2003. TxDOT Report 0-1855-2
58. Vecchiano, F.J. and Collins, M.J. "The Modified Compression Field Theory for Reinforced Concrete Element Subjected to Shear." *ACI Structural Journal* Vol. 83 No. 2 (1986): 219-231.

59. Wight, J.K.; Parra-Montesinos, G. "Use of Strut-and-Tie Model for Deep Beam Design as per ACI 318 Code." *ACI Concrete International* Vol. 25 No. 5 (2003): 63-70.

60. www.wunderground.com

VITA

Tz-Wei Wang attended Taipei Municipal Jianguo High School, Taipei, Taiwan. In 1999 he entered National Taiwan University in Taipei, Taiwan. He received the degree of Bachelor of Science from National Taiwan University in May, 2003. During the following two years he completed his military service in Taichung, Taiwan. In September, 2005, he entered the Graduate School at National Taiwan University. After completing his Master of Science degree in Structural Engineering in June of 2007, he began work on his Ph.D. under the supervision of James O. Jirsa.

Permanent address: 1F, No.16, Lane 55, Minle St., Yonghe, Taipei, Taiwan, R.O.C., 234

This dissertation was typed by the author.